A millimeter unilateral finline SIS mixer with a wide IF bandwidth

Yangjun Zhou

Merton College

University of Oxford

A thesis submitted for the degree of

Doctor of Philosophy

2013

Declaration

This thesis is a presentation of my original research work. Wherever contribution of others are involved, every effort is made to indicate this clearly, with due reference to the literature, and acknowledgement of collaboration and discussion. No part of this thesis has been accepted, or is currently being submitted, for any degree, diploma or any other qualification in University of Oxford or elsewhere. The total length of thesis does not exceed 250 pages.

Acknowledgement

My first debt of gratitude must go to my supervisor Ghassan Yassin who patiently provided the vision, encouragement, necessary advise and financial help to me through the Dphil program and the extremely careful checking on this thesis, to Jamie Leech who spent a lot of time in explaining the cryogenic tests of SIS mixers, guiding me through cryogenic experiment in my first year and also reading through my thesis, to Paul Grimes who patiently guided me through the whole process of mixer design and fabricated the devices in Cologne, also to Boon Tan Kok, who spent huge amount of time sharing his knowledge on SIS mixers with me. I am enormously grateful to Rik Elliot, the technician in our group who built up the electronics system and also encouraged me at my most difficult time. I should also thank Paul Pattinson for his intricate bonding jobs, which were essential steps towards the realization of the excellent mixer performance. I would also thank Mike Jones, Angela Taylor and Peter Huggard for their academic advise on GUBBINS cryogenic system and device handling. I also would like to thank my department mentor Jocelyn Bell Burnell, who is always one of the greatest female scientist in the world and meanwhile a great listener. Additionally I would like to thank the people in electronics workshop who always kindly gave me a hand during the Dewar cooling down. I would also like to give my thanks to Roger David, Lance Miller and Pat Roche for all these kind supports from the department in the past few years. Also I would like to thank Xiaosu Yi and Wen Xiao in Beihang Univerisity, who appreciated me and inspired me to see the world. I also would like to thank all the friends in Astrophysics, especially my lovely office mates. Additionally, I would like to thank all the friends I have met in Oxford, who shared the most fabulous years with me in Oxford. Also I am indebted to Chinese ministry of Education, University of Oxford and Merton College for the award of scholarship through my Dphil program.

Finally, after all these thanks, I should say 'Thank you, Dad and Mum', thank you for bringing me into this wonderful world and giving me the most generous love, support, trust and understanding.

Abstract

Superconductor-Insulator-Superconductor (SIS) tunnel junction mixers are now commonly used in astronomical receivers at (sub)millimeter wavelengths because of their superb sensitivity, high dynamic range and stability of operation. Niobium SIS mixers operating at frequencies well below the superconducting gap (∼680 GHz) have already achieved quantum limited sensitivity. Therefore to further enhance the receiver sensitivity, increasing the Intermediate Frequency (IF) bandwidth of SIS mixers has became crucial. This thesis focuses on the theoretical modeling, design and experimental verification of Nb SIS mixers operating around 230 GHz with a wide IF bandwidth of 1–15 GHz. These mixers were designed for a single baseline heterodyne interferometer (GUBBINS), which is being built to observe the Sunyaev-Zel'dovich effect in the Cosmic Microwave Background. The combination of wide IF bandwidth SIS mixers and complex analogue correlators will allow GUBBINS to feature high surface brightness sensitivity, that helps to distinguish the weak SZ effect from the background noise. The SIS mixer detector system was assembled inside the GUBBINS cryostat together with the IF electronics and RF/LO optical systems. Low noise temperatures of around 71 K were then measured in the GUBBINS system.

The Nb SIS mixer we have developed uses a unilateral finline and fully integrated planar circuits deposited on a silicon substrate, to couple the electromagnetic radiation from the waveguide into the SIS junction. The finline mixer allows a broad-band RF coupling, an easy integration of the on-chip planar circuits and an easy-to-fabricate mixer block. To achieve a wide IF bandwidth, the output impedance of the SIS mixer was well matched to the input impedance of the amplifier by a multi-stage microstrip circuit. Additionally, the planar circuit of the SIS mixer was also designed to have a small lumped inductance and capacitance. The SIS mixer chip was extensively simulated by rigorous electromagnetic software (HFSS) and the S-parameter was exported to a quantum mixing package SuperMix to produce a full-wave model of the mixer. Experimental testing yielded a best noise temperature of 50 K with an average noise temperature of 75 K over an RF bandwidth of 160 GHz–260 GHz. We have performed thorough experimental and computational investigation of the IF system in particular the constraints on the bandwidth caused by the lumped element capacitance of the mixer chip and the matching of the output impedance of the mixer to the IF amplifier. Our conclusion is that a bandwidth of 1–15 GHz could be achieved using our mixer design, subject to the performance of the amplifier. Finally, a variable temperature load system was successfully developed and tested inside the cryostat, to avoid the losses from the room-temperature optics. We have showed that the noise temperature of the SIS detector could be reduced by as much as 15 K by testing the mixer using a variable temperature load inside the cryostat.

Contents

Chapter 1

Introduction

The work in this thesis will focus on the development of SIS (Superconductor-Insulator-Superconductor) mixer technology for observation of the Sunyaev-Zel'dovich (SZ) effect in bright galaxies. We shall therefore start with a brief review of the CMB science and the SZ effect, followed by the description of a single baseline interferometer (GUBBINS) that will employ these mixers. This will be followed by a description of the underline physics of SIS mixers operation and a discussion of the methodology of SIS mixer design. At the end of the chapter we shall give the outline of this thesis.

1.1 Cosmic Microwave Background

The Cosmic Microwave Background (CMB) radiation is the left-over radiation from the Big Bang, consisting of a very uniform thermal radiation that fills the observable Universe. It was predicted by Ralph Alpher and Robert Herman as a test of the Big Bang Model [38][37][3] of the Universe, and accidentally discovered by Arno Penzias and Robert Woodrow Wilson [70]. The CMB radiation contains the most ancient photons that one can observe today, in which the information about the Universe at redshifts (z≈1000), much larger than the redshifts of visible galaxies or quasars, is encoded.

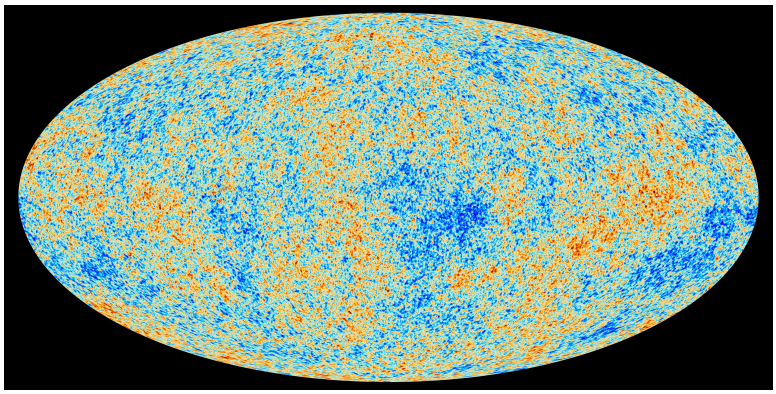

Figure 1.1: The CMB radiation distributions, captured by ESA's Planck satellite. The picture was extracted from [30].

Long before the formation of any celestial objects, the Universe was extremely hot and dense fog

consisting of hydrogen plasma and radiation photons. The photons were constantly scattered by the hot electrons, leading to a tight coupling between matter and radiation at thermal equilibrium. As the Universe kept expanding, the hydrogen plasma cooled down so there came a point where protons and electrons were cold enough ($\sim$ 3000 K) to form the simplest atoms. After this epoch of recombination which is called '*surface of last scattering*', the radiation photons were no longer absorbed or scattered by the ionized matter and could freely propagate through space. The CMB radiation we observe today originates from this '*surface of last scattering*'. As the photons travelled through space, the expansion of the Universe stretched out the photons wavelength by around 1000 times. Therefore today the photons from the relic of the Big Bang fall into the microwave part of the spectrum and thus are called the 'Cosmic Microwave Background' (CMB) radiation. The CMB is the most perfect blackbody radiation ever found in the Universe at a thermodynamic temperature of 2.725 K, and the spectral density peaks in the microwave region. Also, the CMB radiation is remarkably isotropic over large scales across the sky, apart from anisotropies which are the fluctuations of temperature at small angular scales [2]. In Fig 1.1 we present a CMB full-sky map, showing the anisotropies across the sky with very high resolution, which was captured by ESA's Planck satellite.

1.1.1 Sunyaev-Zel'dovich Effect

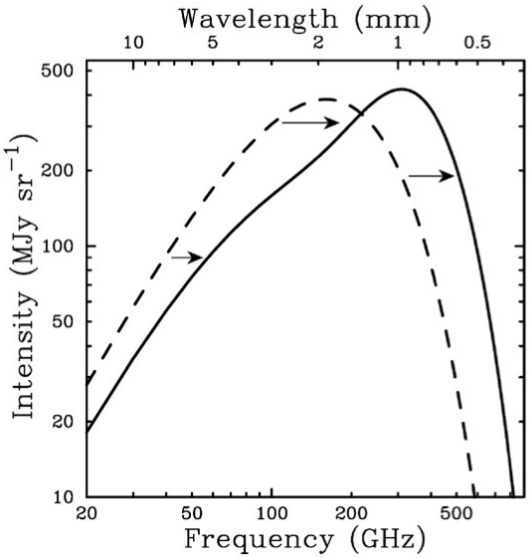

Figure 1.2: The spectral distortion of the CMB radiation due to the Sunyaev-Zel'dovich effect. The dashed line represents the undistorted CMB spectrum and solid line represents the CMB spectrum distortion by the SZ effect. To illustrate the effect, the SZ effect distortion shown here is for a fictional cluster 1000 times more massive than a typical galaxy cluster. The figure was extracted from Carlstrom's review on the SZ effect [29].

The Sunyaev-Zel'dovich (SZ) effect is one type of CMB anisotropy which occurs when the CMB photons are inverse Compton scattered by the hot ionized gas within the galaxy clusters, in which the low energy CMB photons are scattered by high energy electrons within the galaxy clusters. The scattered photons gain a substantial amount of energy from the relativistic electrons. Assuming that

the angle between the incident electron and the incident photon is φ_i and the angle between the incident electron and the scattered photon is φ_f, it can be shown that the ratio of scattered and incident photons energy can be written as [31]:

$$\frac{E_f}{E_i} = \frac{1 - \beta\cos\varphi_i}{1 - \beta\cos\varphi_f + \frac{\epsilon}{\gamma}(1 - \cos\theta)} \tag{1.1}$$

where θ is the angle between the incident and scattered photons, $\beta = u/c$, u is the initial speed of the electron, $\gamma = (1-\beta)^{-\frac{1}{2}}$ and $\epsilon = E_i/mc^2$ is the ratio between the initial energy of the photon and the rest energy of the electron. Assuming head-on collision for simplicity ($\varphi_i = 180°$ and $\varphi_f = 0°$) ,

$$E_f/E_i = \frac{1+\beta}{1-\beta+\frac{2e}{\gamma}} \tag{1.2}$$

For very fast electrons $\beta \sim 1$ and $\gamma \gg 1$, giving $E_\mathrm{f}/E_\mathrm{i} \sim 4\gamma^2$. For example, an electron with $\gamma \sim 10^4$ colliding with a CMB photon would generate an X-ray emission. The inverse Compton scattering by the high energy electrons increases the number of photons with high energy and deceases the number of photons with low energy.

Galaxy clusters are the largest gravitationally bound structures in the Universe, whose abundance and structure provides us with a rich resource to explore the Universe. A galaxy cluster is not simply a group of galaxies, instead most of the baryonic matter in a galaxy cluster is not in the galaxies themselves but in the highly ionized gas which occupies the space between them. Therefore if one observes the CMB radiation towards a galaxy cluster there would be fewer low energy photons and more higher energy photons than one would expect in the Cosmic Microwave Background. That is to say, the boost of CMB radiation energy results in a spectral shift of the blackbody spectrum towards higher frequencies as shown in Fig 1.2. At ∼217 GHz, known as the 'null frequency', there is almost no change in the intensity of the CMB spectrum. The exact null frequency varies with the temperature of the cluster gas (thermal SZ effect) and the peculiar velocity of the cluster (kinetic SZ effect). The shift in the null frequency due to the thermal SZ effect is approximated as 217+0.45 T GHz [13], where T is the temperature of the galaxy cluster in KeV. Therefore by measuring the SZ spectrum and finding the null frequency, we can measure the cluster temperature without requiring X-ray observation [44]. However observing such a continuum faint signal requires excellent control of systematic errors and also detector systems with good brightness sensitivities.

1.2 220-GHz Ultra-BroadBand INterferometer for S-Z (GUBBINS)

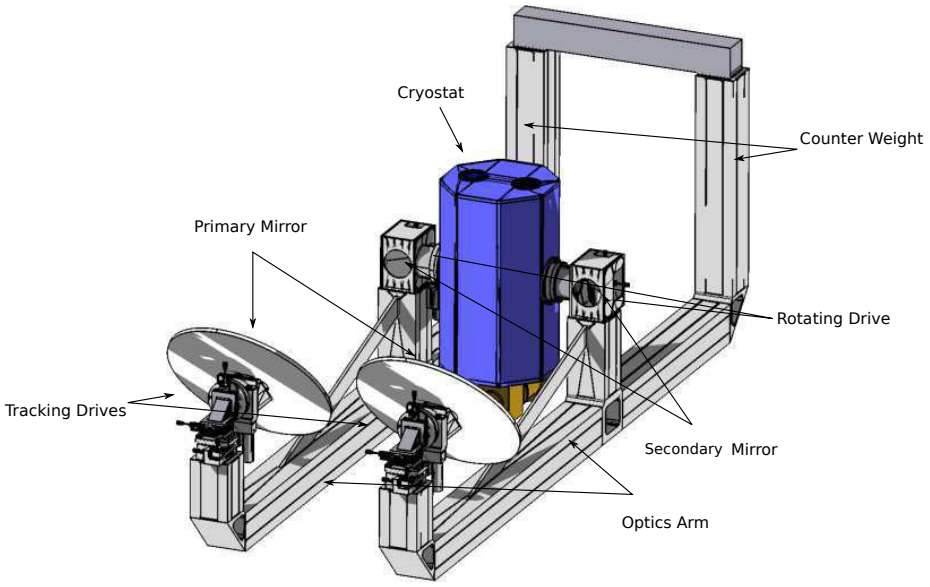

Figure 1.3: A schematic diagram illustrating the GUBBINS instrument.

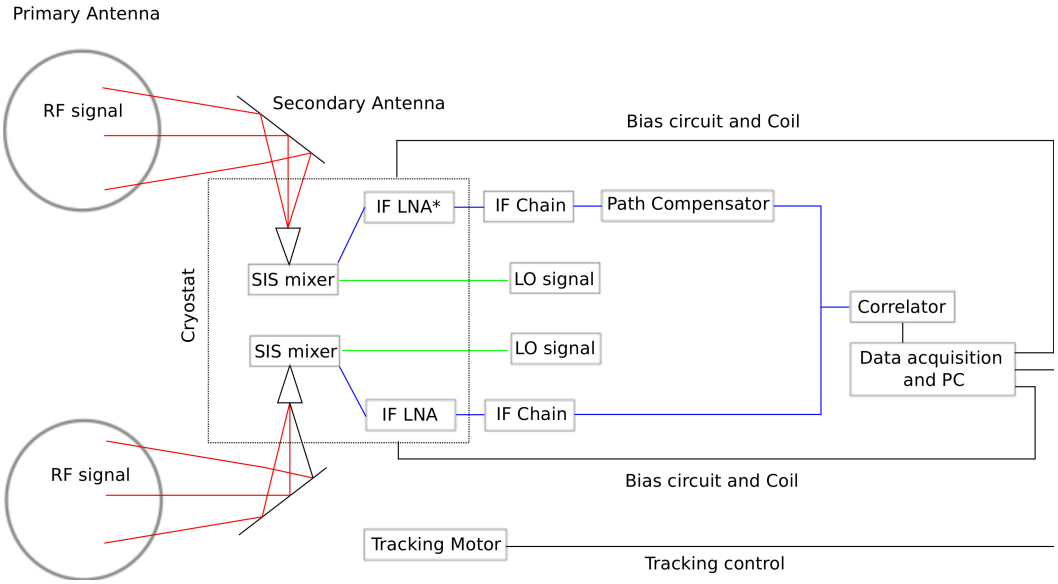

Figure 1.4: A schematic diagram illustrating the GUBBINS interferometer. Radio Frequency (RF) signals are shown in red color, Local Oscillator (LO) signals are shown in green color and Intermediate Frequency (IF) signals are shown in blue color. DC and data signals are shown in black color.

GUBBINS is a ground-based tracking heterodyne interferometer. It was designed to carry out demonstration observations of the Sunyeav-Zel'dovich effect in bright galaxy clusters, especially at the null frequency around 217 GHz. A CAD model of the GUBBINS instrument is shown in Fig 1.3. Unlike

other conventional interferometers which mostly feature high spatial resolution, GUBBINS interferometer features high surface brightness sensitivity for the observation of weak continuum sources (CMB radiation), which is achieved by wide IF bandwidth SIS mixers and analogue correlators. GUBBINS is a two-dish interferometer, with a 0.5 m length baseline and two small antennas each with an aperture of 0.4 m. This special optical design provides GUBBINS a maximum filling factor with no shadowing between two antennas and a moderate spatial resolution just fitting the angular size of the brightest galaxy clusters (primary beam: 11.4' FWHM).

Since the frequency of the incoming astronomical radiation is too high to be processed by the amplifiers, a mixer is used as the first stage of the receiver chain, to down-convert the radio frequency signal to an intermediate frequency signal (below ∼20 GHz). As the most sensitive heterodyne detectors, Superconductor-Insulator-Superconductor (SIS) mixers are used in the GUBBINS interferometer with quantum-limited sensitivity. SIS mixers mix the astronomical **R**adio **F**requency signal (**RF** signal) with the **L**ocal **O**scillator signal (**LO** signal) at nearby frequency, and generates an **I**ntermediate **F**requency signal (**IF** signal) at their difference frequency ($f_{\rm IF} =\mid f_{\rm RF} - f_{\rm LO} \mid$). The astronomical radiation is coupled to the SIS mixer subsequently through the primary mirror, the secondary mirror, the side window of the cryostat and a horn-reflector inside the cryostat. The frequency down-converted IF signals in both channels are then further amplified by the 4 K and 30 K amplifiers, and then cross-correlated to produce the complex visibility function which directly relates to the source brightness I_s through the Fourier transform. A block diagram of GUBBINS interferometer is shown in Fig 1.4.

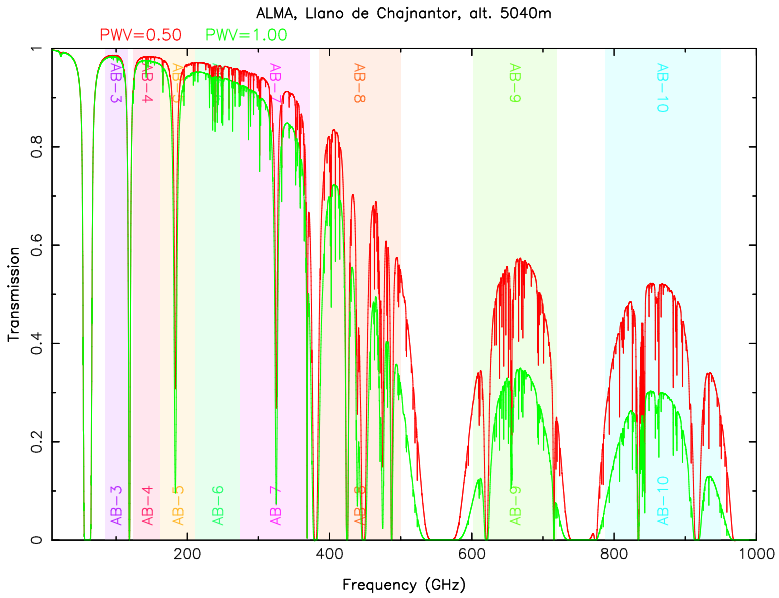

Figure 1.5: Atmosphere transmission below 1 THz at the Chajnator Plain. The RF bandwidth of GUBBINS interferometer covers band 6 and part of band 5, both of which are clear atmospheric windows. 'PWV' denotes Precipitable Water Vapor.

A possible site for GUBBINS is the Chajnantor plain of the Chilean Andes at an elevation of about 5000 m, adjacent to ALMA. CMB observation is not only limited by the availability of highly sensitive detectors, but also by the atmospheric transmission. Large amount of water vapor and other

absorbing molecular species exist in the earth atmosphere, which attenuate the incoming radiation and also add thermal noise. Therefore only sites at high altitude with extremely dry and stable atmosphere are suitable for CMB observation, i.e the Chajnantor Plain, Chile or Mauna Kea, Hawaii. The atmospheric transmissions from ALMA site on the Chajnator Plain is plotted in Fig 1.5.

1.2.1 The SIS heterodyne receiver

To down-convert the frequency of the incoming weak astronomical RF signal, the RF signal is coupled with a strong LO signal at a slightly different frequency at the SIS junction. The signals at the sum or difference frequencies of the RF and LO signals are then generated at the mixer output, preserving both the phase and amplitude information of the RF signal. The IF (Intermediate Frequency) signal with the difference frequency is usually of the greatest interest, therefore the mixing process is usually referred to as a frequency '*down-conversion*' process. The heterodyne principle, that explains how the mixer works, is schematically illustrated in Fig 1.6. Mixers which are sensitive to the RF signals on both sides of LO signal are defined as double sideband (DSB) mixers and the mixers only sensitive to one side band are defined as single sideband (SSB) mixers. For detection of narrow spectral lines, SSB may be preferred since the image band will only contribute noise but no signal. However in a continuum source observation (i.e CMB radiation), a DSB mixer is preferred which can observe with broad RF bands at both sides of the LO frequency.

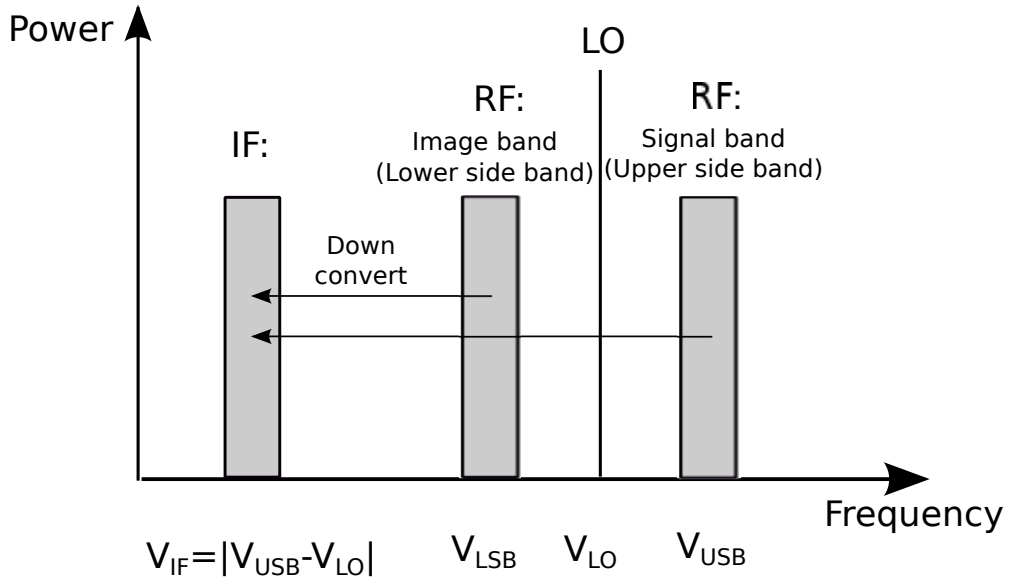

Figure 1.6: In a DSB mixer, the RF signals at both sides of the LO signal can be down-converted to the IF signal with equal or similar efficiency. The bandwidth of the IF signal is determined by the IF bandwidth of the mixer itself.

In a mixer the output current is nonlinearly related to the input RF/LO voltages and the non-linearity varies from one to another for different kinds of mixers. For the simplest form, the output current of a mixing element is proportional to the square of the total applied input voltages as,

$$
\begin{aligned}
I(\omega) &\propto (V_0 + V_{\mathrm{RF}}\mathbf{sin}(\omega_{\mathrm{RF}}t) + V_{\mathrm{LO}}\mathbf{sin}(\omega_{\mathrm{LO}}t))^2 \\
&\propto (\frac{V_{\mathrm{RF}}^2}{2} + \frac{V_{\mathrm{LO}}^2}{2} + V_0^2 + V_{\mathrm{RF}}V_{\mathrm{LO}}\mathbf{cos}(\omega_{\mathrm{LO}} - \omega_{\mathrm{RF}})t \\
&\quad -V_{\mathrm{RF}}V_{\mathrm{LO}}\mathbf{cos}(\omega_{\mathrm{LO}} + \omega_{\mathrm{RF}})t - \frac{V_{\mathrm{RF}}^2}{2}\mathbf{cos}2\omega_{\mathrm{RF}}t - \frac{V_{\mathrm{LO}^2}}{2}\mathbf{cos}2\omega_{\mathrm{LO}}t \\
&\quad +2V_{\mathrm{LO}}V_{\mathrm{RF}}\mathbf{sin}(\omega_{\mathrm{RF}})t + 2V_0V_{\mathrm{LO}}\mathbf{sin}(\omega_{\mathrm{LO}}t))
\end{aligned}
\tag{1.3}
$$

In the above equation, the output current $I(\omega)$ includes the IF signal with difference frequency $V_{\mathrm{RF}}V_{\mathrm{LO}}\mathbf{cos}(\omega_{\mathrm{LO}} - \omega_{\mathrm{RF}})t$ and some other higher order harmonics. The IF signal $V_{\mathrm{RF}}V_{\mathrm{LO}}\mathbf{cos}(\omega_{\mathrm{LO}} - \omega_{\mathrm{RF}})t$ which contains both the amplitude and phase information of the RF signal, would then be bandpass filtered and amplified before they are processed in the correlator or spectrometer. In a real SIS mixer, the nonlinearity of the heterodyne detector would generate many more higher harmonics, however most of which are shorted by the junction capacitance.

Apart from the heterodyne detection, direct detection has also been widely used in astronomy from optical to infrared wavelengths. The direct detector, as a total power detector, might have extremely high sensitivity to incoming photons, but does not preserve the phase and spectral information. The difficulties in detecting both the amplitude and the frequency information with arbitrary sensitivity is a consequence of the Heisenberg uncertainty principle, which prevents the simultaneously accurate measurement of photon energy E and their characteristic time τ in an electromagnetic wave to arbitrary precision [47]

$$\Delta E \Delta\tau \geq \frac{\hbar}{2} \tag{1.5}$$

The restriction arises since the phase of the wave is given by $\Phi = \omega\tau$. A well known type of direct detector is the bolometer, in which the detected (or absorbed) photons change the resistance of a temperature-sensitive element. However, if the spectral and phase information is essential in the observation (i.e high resolution spectroscopy), heterodyne receivers based on SIS mixers are commonly used between 100 GHz and 1 THz.

In the process of heterodyne detection, there are two parameters to judge the performance of the mixing, one is the noise power P_{r} added by the receiver and the other is the ratio of output IF signal power to the RF input signal power, namely the conversion gain G_{r}. The noise temperature T_{r} is related to noise power by $P_{\mathrm{r}} = k_{\mathrm{B}}T_{\mathrm{r}}$, where k_B is the Boltzmann constant. The minimum noise temperature T_{r} of any heterodyne receiver is also restricted by the Heisenberg uncertainty principle, as explained above such that

$$T_r > \frac{\hbar\omega}{k_B} \tag{1.6}$$

The invention of the Superconductor-Insulator-Superconductor (SIS) junction has brought an unprecedented progress in the development of heterodyne detection in the (sub)millimeter band. Nowa-

days the SIS mixer has became the almost unique choice for the heterodyne detectors for high sensitivity observation at frequencies below 1 THz at many ground-based radio observatories and space telescopes. Since the SIS mixer is a quantum mixer, the photon step of the incoming RF radiation at the operating frequency is much larger than the voltage range where the current-voltage characteristic is nonlinear. The photon step on the DC current-voltage characteristic curve is a consequence of the extra quasi-particle tunneling that assisted by the incoming radiation photons. As predicted by Tucker's theory, the SIS mixer can actually achieve quantum limited noise $\hbar\omega/k_B$ and conversion gain G_{r} of more than unity, provided the RF/LO power can be effectively coupled to the SIS junction [55]. However the noise temperature of a heterodyne receiver chain is not only determined by the SIS device itself, but also by all the other components before and after the SIS mixer. The key components in a typical heterodyne receiver are illustrated in Fig 1.7: the local oscillator source, the feed horn, the SIS mixer and the IF amplifier chain. Under most circumstances, the gain of the SIS mixer is less than unity, therefore to minimize the receiver noise, the cryogenic LNA (Low Noise Amplifier) must contribute as little noise as possible. Also, the LNA has to provide sufficient gain (usually $>$ 30 dB), to make the noise contributed by the subsequent warm electronics to the overall noise temperature negligible.

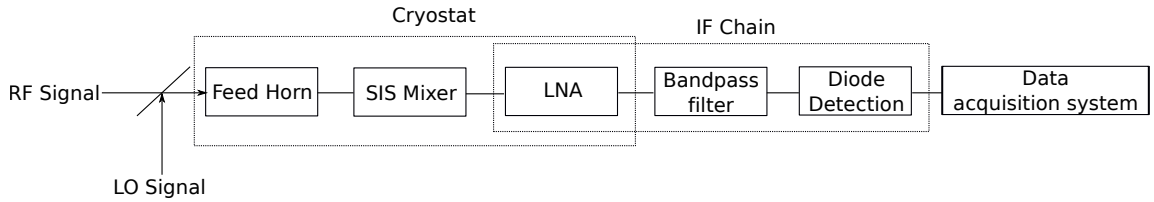

Figure 1.7: The heterodyne layout widely used in SIS mixer receivers. The RF and the LO signals are combined together by a dielectric beamsplitter or a duplexer, and then coupled to the SIS mixer through a feed horn antenna. The generated IF signals from the SIS mixer are amplified by a few stages of amplification and then detected by the data acquisition system.

The minimum detectable temperature ΔT of a receiver is related to the system noise temperature T_{sys} by the Dicke radiometer equation as [16],

$$\Delta T = \frac{T_{\mathrm{sys}}}{\sqrt{\Delta t \Delta \nu}} \tag{1.7}$$

where Δt represent the integration time and $\Delta\nu$ the IF bandwidth of the detector chain. The total system noise T_{sys} is contributed from the receiver, the atmosphere, the ground noise and the CMB background noise. As can be easily seen, the IF bandwidth of the detector chain $\Delta\nu$ is essential in enhancing the sensitivity of the heterodyne detector for the observation of very faint continuum source, i.e the CMB. Also, for a spectroscopic observation, increasing the IF bandwidth could effectively save observation time without sacrificing the sensitivity, as it would cover several spectral lines in a single observation. As the development of state-of-art SIS mixers, especially at low frequency ($<$ 500 GHz), has already pushed the mixer noise temperature to a few times of the quantum limit, increasing the IF bandwidth becomes crucial in further enhancement of the instrument sensitivity ΔT. Alternatively, multiple pixel focal planar arrays can also be used to enhance sensitivity [79].

1.3 SIS mixers

1.3.1 The SIS junction

The key component performing the frequency down-conversion in the SIS mixer is the SIS tunnel junction. The SIS junction consists of two superconducting layers separated by a very thin insulating thin films ($\sim$ few tens of $\mathring{A}$). A schematic diagram of the layout and energy diagram are shown in Fig 1.8. The two superconductor layers are usually made from the same material, but in principle they could be different material. As a result of the sandwich structure, the SIS junction has an intrinsic capacitance which is proportional to the junction surface area. The intrinsic capacitance prevents the incoming RF signal from coupling efficiently to the SIS junction, hence tuning circuits are always fabricated around the SIS junction to tune out the capacitance.

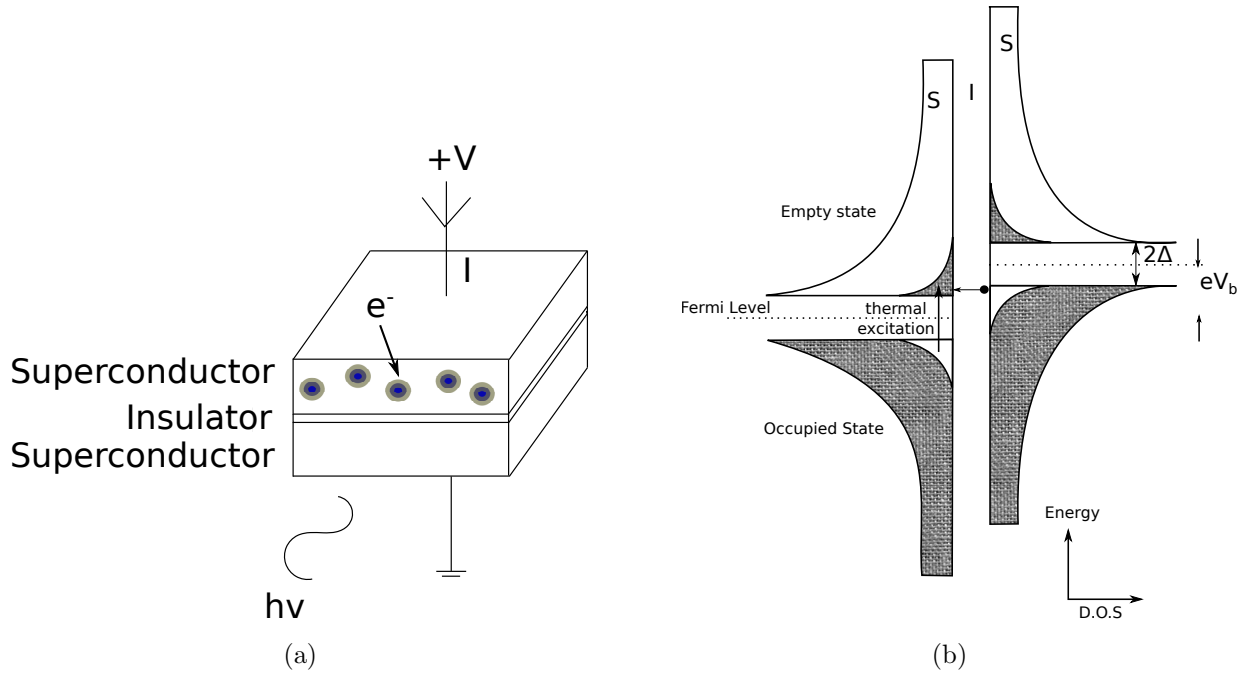

Figure 1.8: (a) A schematic diagram illustrating the SIS junction. (b) A schematic diagram illustrating the density of states of the SIS junction.

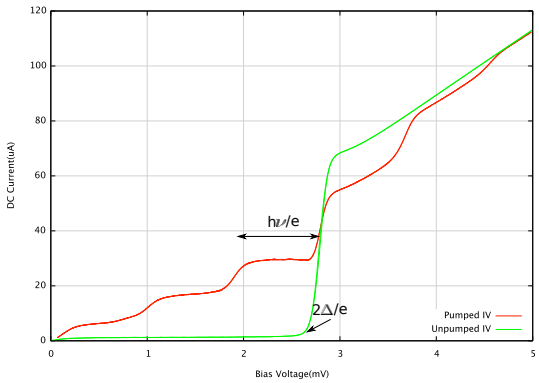

Figure 1.9: The pumped IV characteristic curve superimposed on an unpumped IV curve. The SIS junction is illuminated by LO signal at frequency of ν=219 GHz and photon steps with width hν/e = 0.905 mV are generated on the I-V characteristic curve. The unpumped current-voltage (I-V) characteristics curve shows very high nonlinearity at bias voltage $2\Delta/e$, where 2Δ is the gap energy for the superconductor.

In principle, any type of nonlinear device can be used as a mixer (i.e Schottky diode). However the SIS junction has a very strong nonlinearity in the I-V (current-voltage) characteristic compared with other devices used as mixers. The nonlinearity of SIS junction is due to the quantum tunneling of quasiparticles from one superconductor to another across the insulator barrier. Below the transition temperature, the electron gas in the superconductor consists of highly correlated pairs of electrons, named 'Cooper pairs'. The weak binding energy of a Cooper pair is 2Δ, in the order of meV. When biasing the SIS junction with DC voltage $V_{\text{gap}} = 2\Delta/e$ across the tunnel junction, Cooper pairs are broken into single quasiparticles that can tunnel to the opposite electrode, shown in Fig 1.8 (b). The quasiparticles are therefore normal electrons that have an energy gap of 2Δ in their density of states. The infinite density of states at energy levels $\pm\Delta$ for the quasiparticles allows a large increase in tunneling current at bias voltage $V_{\text{gap}} = 2\Delta/e$ leading to a large nonlinearity feature in the IV curve. The detection of the external radiation is realized by the photon-assisted quasi-particle tunneling. Under external radiation with energy $h\nu$, a quasi particle can tunnel through the barrier if $eV_{\text{bias}} + nh\nu > eV_{\text{gap}}$, where ν is the frequency of the incident photon, n is number of the absorbed photons, h is the Planck's constant and V_{bias} is the DC bias voltage. Examples of the unpumped I-V characteristic curve showing the nonlinearity of the SIS junction and a pumped IV curve when the device is illuminated by an electromagnetic wave with frequency ν is shown in Fig 1.9.

1.3.2 SIS mixer design and fabrication

A typical SIS mixer tunnel junction has an area of $\sim$1 μm^2. Since its size is much smaller than the wavelength of the detected signal, an antenna or other kinds of coupling circuitry are needed to couple the incoming RF/LO radiation to the SIS junction. Therefore the performance of an SIS mixer is not only determined by the nonlinearity of the SIS junction, but also by all the components used in the SIS mixer chip. These components, especially the mixer feed and the on-chip planar circuits,

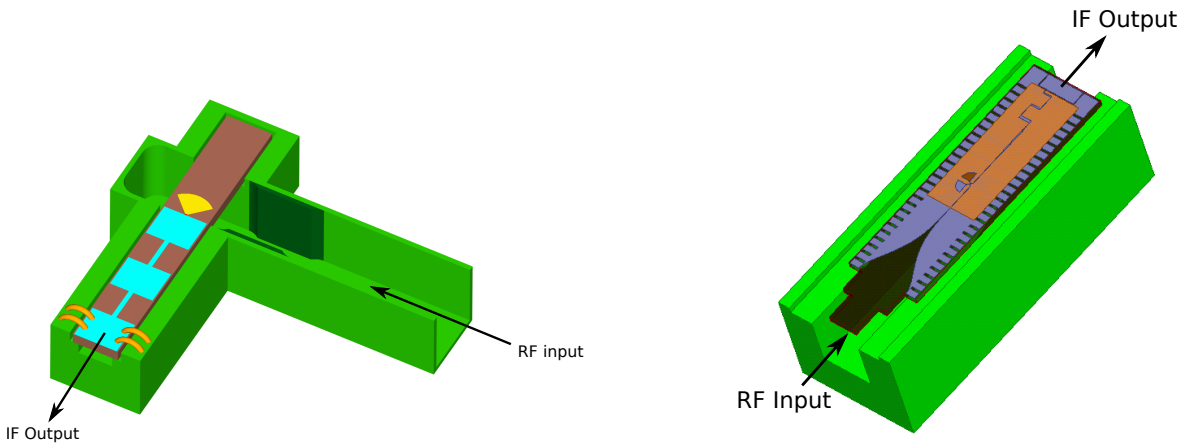

(a) (b)

Figure 1.10: (a) A schematic view of a probe mixer (Figure is extracted from [59]). (b) A schematic view of a finline mixer.

determine the LO/RF power coupling efficiency to the SIS junction and eventually the gain and the noise temperature of the SIS mixer. SIS mixers may be classified into two types: the quasi-optical SIS mixer and the waveguide SIS mixer. The quasi-optical mixer [102] employs an integrated planar antenna fed by a hemispheric dielectric lens to couple the radiation onto the mixer chip which is glued at the back of the lens. Quasi-optics mixers are easy to fabricate but have the disadvantages of poor beam pattern, which becomes important in focal plane mixer arrays. Waveguide mixers, however use a horn to collect the incoming radiation into a single-mode waveguide. Once the radiation is coupled to the waveguide, a planar circuit fabricated on a thin substrate couples the signal from the waveguide to a transmission line (i.e microstrip) where the SIS junction is fabricated. Compared to the quasi-optical mixers, waveguide mixers provide a much better beam-pattern characteristic (low sidelobes and cross polarization levels) [97], especially the ones operating at low frequencies below 500 GHz. The transition from the waveguide to the microstrip can be accomplished in either a waveguide probe [93][91] or a finline transition [83][97]. In Fig 1.10 we plot the schematic diagrams for a probe mixer and a finline mixer.

All mixers investigated in this thesis employ finline tapers to couple the signal from the waveguide mode to the microstrip/slotline mode. Fig 1.11 shows two types of finline transitions and Fig 1.12 shows an example of the finline mixer. The finline transition and all the other planar circuits are deposited on thin silicon substrate, which is mounted in the E-plane of the waveguide. The finline transition provides a large space for on-chip planar circuits, so that all the superconducting circuitry can be fabricated using planar circuit technology during the device deposition. This simplifies the requirement on the mixer block (i.e no back short or E-plane tuner). Also, the large substrate area allows an elegant and simple integration of the additional planar circuits (i.e hybrid or power divider) for upgrading, i.e to a single sideband mixer. Last but not least, the finline transition has a very broad band RF coupling, up to 40% of the operating frequency.

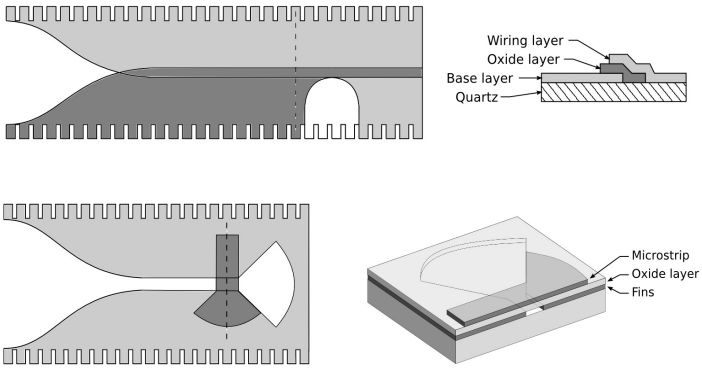

Figure 1.11: A graphic representation of (Top) an antipodal finline and (Bottom) a unilateral finline with their cross-section views. Both figures were extracted from [96].

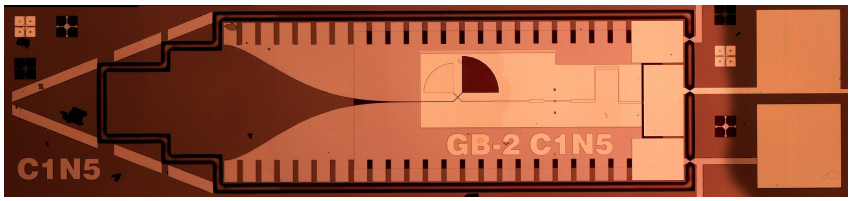

Figure 1.12: A photo of one finline SIS mixer. The RF/LO radiation is coupled from the SIS mixer (left hand side of the picture) and the IF signal is extracted to the following IF chain from the bond pad (right hand side of the picture).

1.3.3 State-of-art for SIS mixers

The best performance that an SIS mixer could achieve is the quantum limited noise $h\nu/k_{\mathrm{B}}$, where k_B is the Boltzmann constant. With current technology, SIS mixers operating at frequencies below 500 GHz have routinely achieved sensitivity approaching the quantum limit. The noise temperatures measured for the SIS mixer receivers in several world-class laboratories are plotted in Fig 1.13. Receiver noise temperatures (includes the noise from the optics, the SIS mixer and the IF chain) between $3\times h\nu/k_{\mathrm{B}}$ and $5\times h\nu/k_{\mathrm{B}}$ has already been achieved. As the noise temperature of the mixer at frequencies below 500 GHz have been pushed to this limit, the main attention has recently shifted towards expanding the IF bandwidth, and also widening the RF bandwidth to which the receiver is sensitive. A variety of solutions have been tried to reduce the lumped capacitance and inductance of the mixer planar circuit to expand the IF bandwidth, i.e multiple SIS junctions [99], integrated-preamp, SOI (Silicon On Insulator) devices with beam-leads and IF matching network. The widest IF bandwidth ever reported was from Tong's group with a 10.5 GHz IF bandwidth operating at around 300 GHz RF frequency [99]. To achieve this wide IF bandwidth, a number of SIS junctions were embedded in a distributed network to reduce the chip capacitance, and beam-lead technology was used to reduce the chip inductance. However this complicated design makes the fabrication process to be challenging, especially that all the fabricated SIS junctions have to be nearly identical.

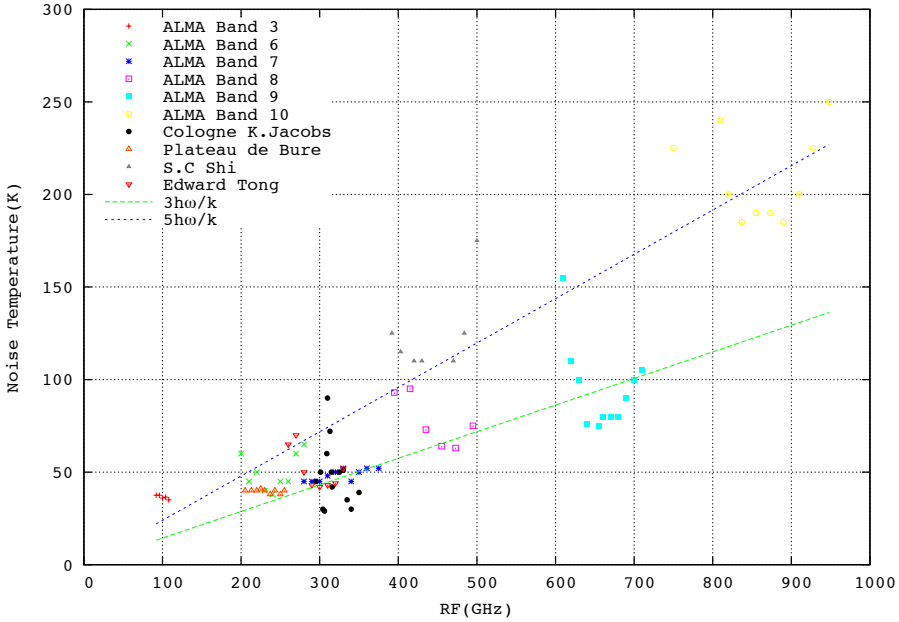

Figure 1.13: The noise temperatures as a function of RF frequency for several SIS mixers built by a selection of research groups (IF bandwidth shown in bracket in the caption). ALMA Band 3 (IF: 4-8 GHz) [26]. ALMA Band 6 (IF:4-12 GHz) [8]. ALMA Band 7 (IF:4-8 GHz) [66]. ALMA Band 8 (IF:4-8 GHz) [77]. ALMA Band 9 (IF:4-12 GHz) [10]. ALMA Band 10 (IF:4-12 GHz) [89]. Cologne K.Jacobs (4-12 GHz) [5]. Plateau de Bure [56]. S.C Shi (IF: 4-8 GHz) [64]. Edward Tong (IF:6-16 GHz) [99].

In this thesis, we extend the IF bandwidth by using a series of microstrip transmission lines to match the complex output impedance of the SIS mixer to the 50 Ω LNA, while carefully designing the planar circuits of the mixer chip to present as low lumped capacitance and inductance as possible. By using only one SIS junction and planar circuits, the mixer chip is easy to design and fabricate. In this way, an IF bandwidth of 2–15 GHz was achieved over an operating RF bandwidth of ∼80 GHz.

1.4 Thesis outline

The contents of this thesis are as follows:

- **Chapter 2: SIS mixer theory and simulation techniques** describes the quantum mixing theory and the underlying physics associated with quantum tunneling in an SIS junction. The theory developed by Tucker [55] has provided a solid framework to understand and predict the behavior of SIS mixers. Large and small signal analysis are explained, as well as the embedding impedance recovery method.

- **Chapter 3: SIS Mixer Design** discusses the design methodology of the SIS mixer. The electromagnetic simulation software HFSS and the quantum mixing package SuperMix are extensively used to predict the behavior of the mixer.
- **Chapter 4: SIS Mixer RF performance tests** describes the experimental setup and discusses the measured RF performance of the finline mixer operating around 230 GHz. The measured performance of several devices are discussed in this chapter. The losses contributed by the individual components of the mixer circuits are analyzed. A comparison is also made between the RF experiments carried out in two independent test systems.
- **Chapter 5: SIS Mixer IF performance tests** investigates the IF performance results of the SIS mixer between 2–15 GHz, which were measured by either a spectrum analyzer or a diode detector. The performance of the IF matching circuits are investigated and evaluated. An upgraded mixer design with a better IF performance is presented.
- **Chapter 6: 220 GHz Ultra-BroadBand INterferometer for S-Z effect (GUBBINS)** describes a novel heterodyne interferometer (GUBBINS) that employs SIS mixers with an ultra-wide IF bandwidth. The GUBBINS instrument was designed to detect the Sunyaev-Zel'dovich effect in the Cosmic Microwave Background, with a very high brightness sensitivity. In this chapter, the scientific background for the CMB and the SZ effect are reviewed, and the design of the instrument, in particular the front end is described.
- **Chapter 7: Variable Temperature Load** describes the development of a variable temperature load installed inside the cryostat. With the blackbody load inside the cryostat, the optical loss introduced by the cryostat window can be avoided. The performance of the SIS mixer working in conjunction with this variable temperature load will be discussed and analyzed.
- **Chapter 8: Summary and Future Work** summaries the work in this thesis and proposes further development.

Some of the work presented in this thesis was completed in a collaborative way. Therefore I list the part of work that has been contributed by other people:

- FTS measurement of LO harmonics: Dr. Jamie Leech
- GUBBINS mixer fabrication: Dr. Paul Grimes
- GUBBINS optics design and fabrication: Dr. Jamie Leech and the mechanical workshop in the Department of Physics, Oxford
- GUBBINS backend: Adam Coat, Dr. Angela Taylor, Prof. Mike Jones
- GUBBINS electronics: Rik Elliot
- Temperature load design and fabrication: Dr. Paul Grimes

Chapter 2

SIS mixer theory and simulation techniques

Overview: In this chapter, we discuss the underlying physics of quantum tunneling in SIS junctions and the quantum theory of the SIS mixer as a supporting theoretical backgrounds for the subsequent studies presented in this thesis. We will also present the computational analysis tools (embedding impedance recovery method, SuperMix, commercial software *Ansoft* HFSS and *Ansoft* Designer) for predicting the performance and the characteristics of the SIS mixer. Several simulation examples are also given.

2.1 SIS mixer theory

When a superconductor is cooled below the critical temperature T_c, the electron gas that characterizes the normal conducting state is transformed into a different type of fluid of highly correlated pairs of electrons, named Cooper pairs. Cooper pairs are formed by weakly coupled electrons of given momentum and opposite spin. The coupling is provided by the quantized vibration waves within the lattice.

In a normal metal, all the electrons are fermions and obey the Fermi-Dirac statistics and the Pauli exclusion principle. But in a superconductor, Cooper pairs are quasi-bosons and obey the Bose-Einstein statistics. There are many Cooper pairs in the superconductor, and their wavefunctions overlap with each other strongly. Thus the Cooper pairs form a highly collective condensate, condensing to the lowest energy state, which is described by a single wave function as

$$\Psi(\mathbf{r}) = \sqrt{n_s} e^{i\varphi(r)} \tag{2.1}$$

where n_s is considered as the number of Cooper pairs and $\varphi(r)$ is the phase factor for the Cooper pairs. The binding energy of Cooper pairs 2Δ is quite weak, only of the order of 10^{-3} eV, preventing Cooper pairs existing above a critical temperature T_c. Below the critical temperature T_c, some Cooper pairs can be easily broken into single electrons, after absorbing energy equal or higher than the Cooper pair binding energy 2Δ. These particles, called quasi-pariticles, have different effective masses or effective charge, behave similarly as normal electrons, but have an energy gap of 2Δ in their density of states around the Fermi level, see Fig 2.3.

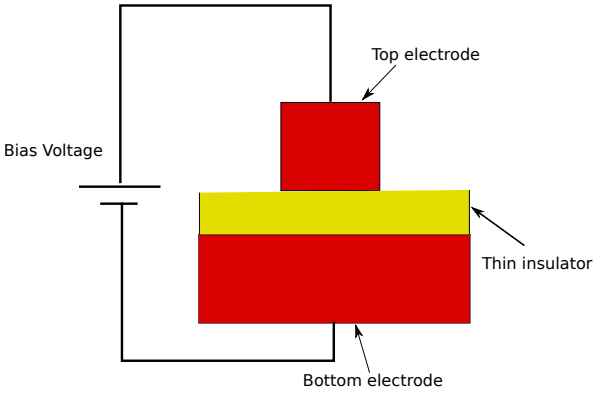

Figure 2.1: Schematic cross section of an SIS tunnel junction. DC bias voltage is applied to the junction through the on-chip circuit. The area of the SIS junction is determined by the size of the top electrode ($\sim$1 μm^2).

The Superconductor-Insulator-Superconductor (SIS) junction consists of a thin insulating barrier with a typical thickness of 10-20 $\mathring{A}$, sandwiched between two superconducting films, Fig 2.1. The insulating barrier is thin enough that the wave function (Eq 2.1) describing the particles on one side of the electrodes can have a finite probability amplitude on the opposite electrode, which enables large number of quasi-particles or Cooper pairs to tunnel through the barrier. The tunneling current of the SIS junction includes two types of particles, one is the Cooper pair tunneling, described by the AC and DC Josephson effect and the other is the quasi-particle tunneling. The quasi-particles current arises from the breaking of Cooper pairs by either a DC bias voltage eV exceeding 2Δ across the SIS junction, by thermal promotion of the quasiparticles above the gap, or by excitation by external photons. The DC gap voltage across the SIS junction may be written as,

$$V_{\text{gap}} = \frac{\Delta_1 + \Delta_2}{e} \tag{2.2}$$

where Δ_1 and Δ_2 are the gap energies of the superconductors on either side of the barrier of the SIS junction. For identical electrodes Δ_1=Δ_2, the gap voltage is simplified as $2\Delta/e$. For the most commonly used Nb/AlO_x/Nb SIS junction, V_{gap} is approximately 3.0 mV at $T = 0$ K. The dependence

of V_{gap} on the ambient temperature can be calculated using the BCS theory as shown in section 2.3.

2.1.1 DC characteristics of the unpumped SIS junction

An overview of the DC characteristics of an unpumped SIS junction is given in Fig 2.2. The tunneling of cooper pairs is called Josephson tunneling, was first theoretically predicted by B.D.Josephson in 1962 [53][54] and later confirmed experimentally by P.W.Anderson and J.M.Rowell [4]. With zero bias voltage, Cooper pairs from either side of the superconductor, of SIS junction, can flow to the other side without any dissipation. Therefore a DC current I_{s} exists in the I-V characteristics at zero bias voltage, known as the 'DC Josephson current', or the 'Super Current'. For two bulk superconductors in close proximity, the wave function of one electrode overlaps with the wave function of the opposite electrode. Assuming a phase difference $\Delta\phi$ between the two electrodes, the super current I_s can be written as

$$I_s = I_c \mathbf{sin} \Delta\phi \tag{2.3}$$

where I_c is a the critical current of the SIS junction, related to the gap voltage V_{gap} and the junction area [69] as

$$I_c = \frac{\Delta\pi}{2eR_n} \mathbf{tanh}\left(\frac{\Delta}{2K_BT}\right) \approx \frac{\pi}{4}\frac{V_{\text{gap}}}{R_n} \tag{2.4}$$

where R_n is the junction normal resistance which is dependent on the junction area (see Sec 2.3.2. Thus the DC Josephson current oscillates between $\pm I_c$, shown by a vertical line at zero bias voltage in Fig 2.2.

If a fixed DC voltage V is applied across the SIS junction, the phase difference across the SIS junction $\Delta\phi$ will change linearly with time as,

$$\frac{d}{dt}\Delta\phi = \frac{2eV}{\hbar} \tag{2.5}$$

If we substitute Eq 2.5 into Eq 2.3, we find that an AC tunneling current at a frequency of $2eV/\hbar$, ~484 GHz/mV flows across the SIS junction. This AC tunneling current is named the '*AC Josephson current*'.

When an AC tunneling current passes across the SIS junction, the higher frequency components will be shorted by the intrinsic capacitance of the SIS junction. But for an SIS junction connected to a tuning circuit, one particular AC component f_{tune} is transmitted corresponding to the case when the capacitance of the SIS junction is tuned out. Therefore at a fixed bias voltage V_{Fiske}, there is an

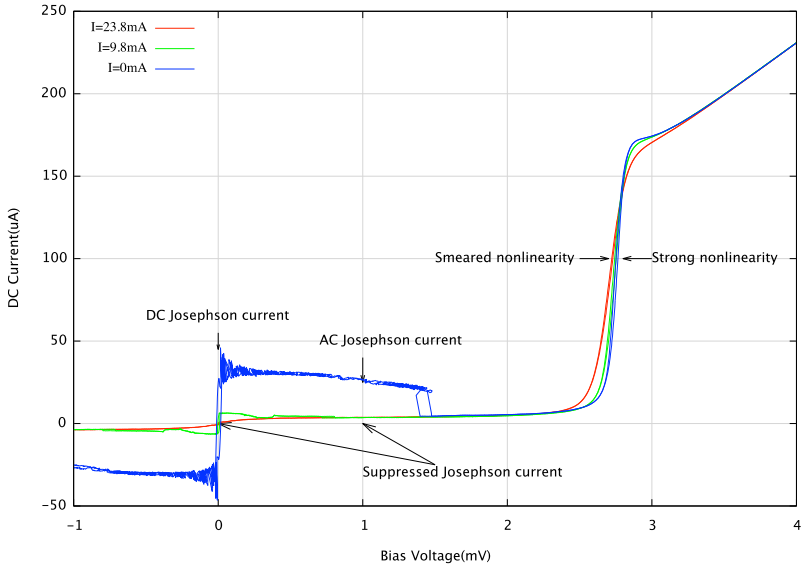

Figure 2.2: Measured unpumped I-V curves of the SIS junction with and without applied magnetic field. Both AC and DC Josephson effects are suppressed by the external magnetic field. The extent of the rounding of the nonlinearity and suppression of the gap voltage around 2.75 mV is dependent on the amplitude of the applied magnetic field.

abrupt rise in current oscillating at a frequency f_{tune}, called the '*Fiske step*'. The bias voltage V_{Fiske} is related to the resonant frequency f_{tune} by $2eV_{\text{Fiske}}/\hbar = f_{\text{tune}}$, equivalent to 0.475 mV for an SIS mixer tuned at 230 GHz. This allows the Fiske step to be used to estimate the tuning frequency of the SIS mixer in a simple DC test. Given the sharpness of the Fiske step, it can only be observed in the current-bias mode as the DC voltage across the junction is swept by the bias circuit. To identify correctly tuned devices, the whole SIS mixer wafer prior to dicing is mounted on a specially-made jig, and dipped into the liquid helium until the ambient temperature of the SIS mixer is well below the critical temperature T_c. The unpumped IV characteristics of each device is recorded and the Fiske step is estimated, along with other crucial parameters. The selection of the high performance devices from the hundreds of devices on the wafer, depends mostly on this testing results, meaning the IV curve sharpness, the junction normal resistance (Sec 2.3) and the location of the Fiske step.

Since the Josephson current adds unwanted noise to the quasi-particle tunneling, both AC and DC Josephson tunneling currents are suppressed during operation of the SIS mixer by applying a weak magnetic field across the SIS junction. This relies on the fact that the critical current I_c of the tunnel junction is a strong function of the magnetic field penetrating the barrier [25], as given by the relation

$$\begin{aligned} I_c &= I_c(0)\left|\frac{J_1(x)}{x}\right| \\ x &= \frac{\pi\Phi}{\Phi_0} \end{aligned} \tag{2.6}$$

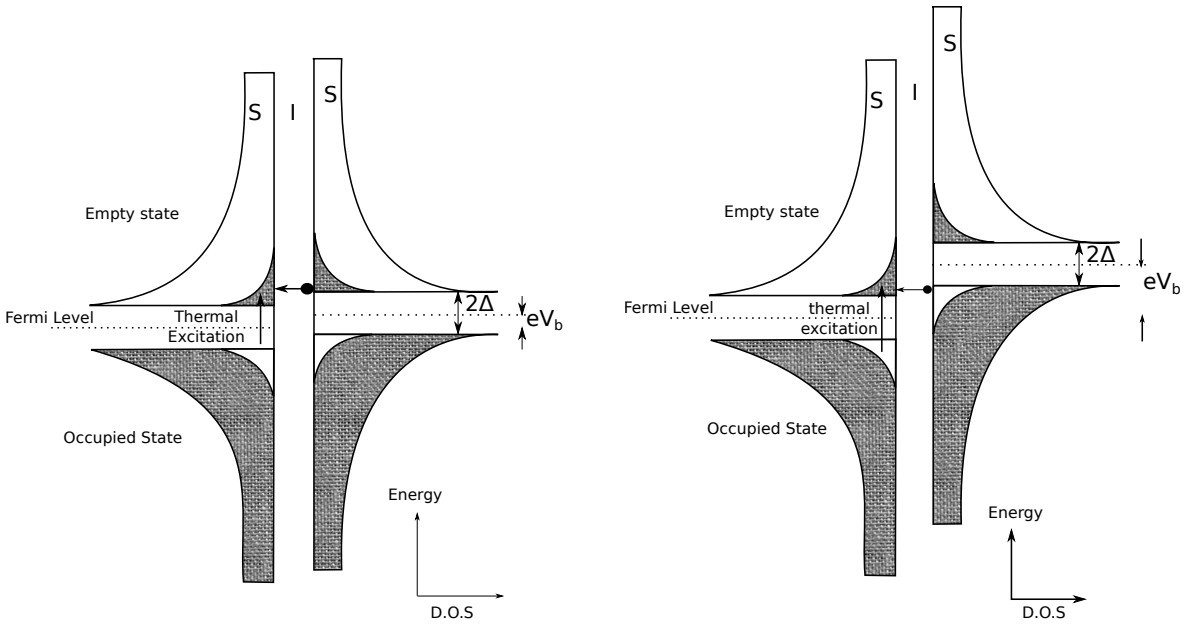

Figure 2.3: (a) Density of states diagram for an SIS junction at $0 < T < T_c$, with $V_{\text{bias}} < 2\Delta/e$. Thermally excited quasi-particles tunnel across the barrier, giving rise to a sub-gap current. (b) Density of states diagram for SIS junction with bias voltage at $V_{\text{gap}} \sim 2\Delta/e$ at $0<T<T_c$, an abrupt increase of tunneling current occurs in the SIS junction due to the large quasiparticle density of states at $\pm\Delta$.

where $I_c(0)$ is the critical current at zero magnetic field, J_1 is a Bessel function of its first kind and Φ_0 is the magnetic flux quantum $h/2e$. The magnetic field strength required to generate an equivalent magnetic quantum flux is approximately $B = \frac{\Phi_0}{l(d+2\lambda)}$, where l is the length of the junction size perpendicular to the direction of B-field, d is the barrier thickness, and λ is the magnetic penetration depth [82] [1]. From Eq.2.4 and Eq 2.6, we see that a bigger junction allows suppression of Josephson current at lower magnetic field.

From Eq 2.6, we notice that the critical current I_c is modulated by applying a magnetic field Φ in terms of Bessel function. So a zero critical current I_c, hence zero AC/DC Josephson currents can be achieved by applying a magnetic filed Φ that allows x to be the n^{th} null in Eq 2.6. The Josephson currents can be suppressed more efficiently if a higher null corresponding to stronger magnetic field is employed. A higher magnetic field however can smear the nonlinearity of the SIS junction and suppress the gap voltage as can be seen by Fig 2.2. Thus a compromise has to be made between the suppression of Josephson currents and the sharpness of the IV curve near the gap. In practical receivers, the second or third magnetic nulls are usually chosen to operate the SIS mixer.

The 'semiconductor' model showing the density of states of quasiparticles in a superconductor at

finite temperature is shown in Fig 2.3. According to BCS theory [9], the distribution of density of state $\rho(E)$ is given by,

$$\rho(E) = \begin{cases} 0 & \text{if } |E| < \Delta \\ N(0)\frac{|E|}{\sqrt{E^2-\Delta^2}} & \text{if } |E| > \Delta \end{cases} \tag{2.7}$$

Here $N(0)$ is density of states at the Fermi level in normal metal above the transition temperature and E is the energy of the quasi-particles given as

$$E = \sqrt{\varepsilon^2 + \Delta^2} \tag{2.8}$$

where ε is the normal-state quasi-particle energy measured from the Fermi level, E_F. The current tunneling through the insulator barrier, as a function of the external bias voltage V_b can be written as [87]

$$I(V_b) = G_n/e \int_{-\infty}^{\infty} \rho(E)\rho(E + eV_b)[f(E + eV_b) - f(E)]dE \tag{2.9}$$

where G_n is a constant representing the conductance of the superconductor at normal metal state, $\rho(E)$ is given by Eq 2.7 and f(E) is the Fermi-Dirac distribution function at temperature T

$$f(E) = \frac{1}{e^{E/k_BT} + 1} \tag{2.10}$$

At $T = 0$ K and bias voltage below V_{gap}, there is no quasi-particles tunneling current because all of electrons in the superconductor are bound together as Cooper pairs. But at finite temperature $0 < T < T_c$, a number of Cooper pairs are thermally broken into quasi-paricles and can be excited to a higher energy level and then tunnel to the empty state on the opposite electrode, giving rise to a leakage current, which is shown in Fig 2.3 (a).

From the semiconductor model shown in Fig 2.3 (b), it can be seen that at bias voltage equal or greater than $V_{\text{gap}} = 2\Delta/e$, there is enough energy for Cooper pair to be broken into quasi-particles that tunnel across the barrier. The large density of state just above and below the energy gap, on both side of the electrodes, causes a sharp increase in the current to tunnel across the barrier. At bias voltage above V_{gap}, the tunneling current becomes proportional to V_{bias}.

As the temperature increases, more quasi-particles are thermally excited and can tunnel to the empty state on the counter electrode below V_{gap}, occupying additional empty states. This decreases the nonlinearity and the mixer conversion gain. For this reason, the SIS mixer has to be operated at temperature well below transition temperature T_c. For Niobium, $T_c = 9.4$ K and $2\Delta/h$ ~700 GHz.

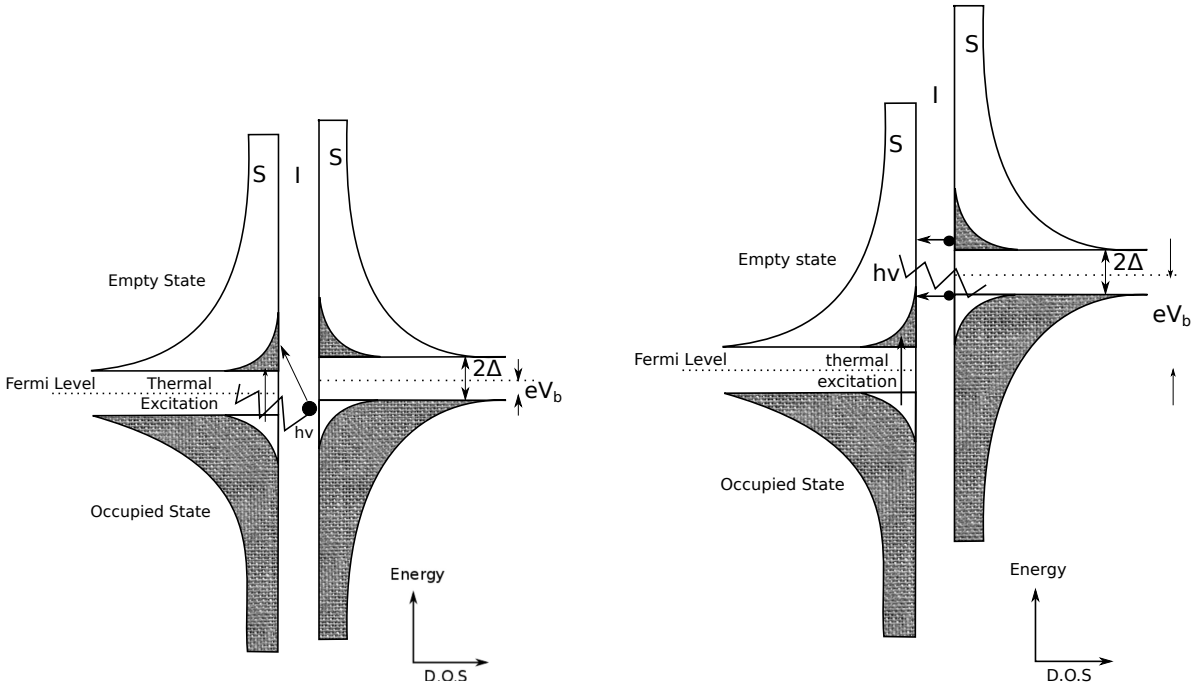

Figure 2.4: (a) Density of states diagram for SIS junction at $0 < T < T_c$, with $V_{\text{bias}} < 2\Delta/e$, irritated with external RF radiation, photon assisted tunneling occurs before gap voltage V_{gap} is reached (b) Density of states diagram of an SIS junction at $0<T<T_c$ with external RF radiation, at bias voltage eV_0 larger than 2Δ.

The mixer described in this work was operated at 230 GHz, hence liquid helium temperature 4.2 K was sufficient for good performance operation of SIS mixer. Mixers operating at frequencies near the gap are often cooled well below 4 K.

2.1.2 DC characteristics of the pumped SIS junction

The photon assisted tunneling effect is illustrated in Fig 2.4, which explains the principle of photon detection in an SIS junction. Incident photons on the SIS junction with energy $h\nu$ can help break the Cooper-pair and assist quasi-particles to tunnel through the barrier. For this to happen, energy of the photons must be high enough to satisfy: $nh\nu + eV_b > 2\Delta$, where n is the number of photons absorbed in the tunneling process. Photon-assisted tunneling therefore causes the sharp increase in current at bias voltage below V_{gap}, producing the pumped current-voltage steps of width $\hbar\omega/e$ shown in Fig 2.5

.

Fig 2.5 shows the current-voltage characteristic of the SIS mixer below the gap voltage, occurring at bias voltages $V_{\text{gap}} - nh\nu/e$ with $n \geq 1$, due to the radiation of the incoming photons. Multi-photon assisted tunneling ($n > 1$) occurs but with much smaller probability than the single photon assisted

tunneling. This leads to photon steps of decreasing height, depending on the number of photons absorbed in the process.

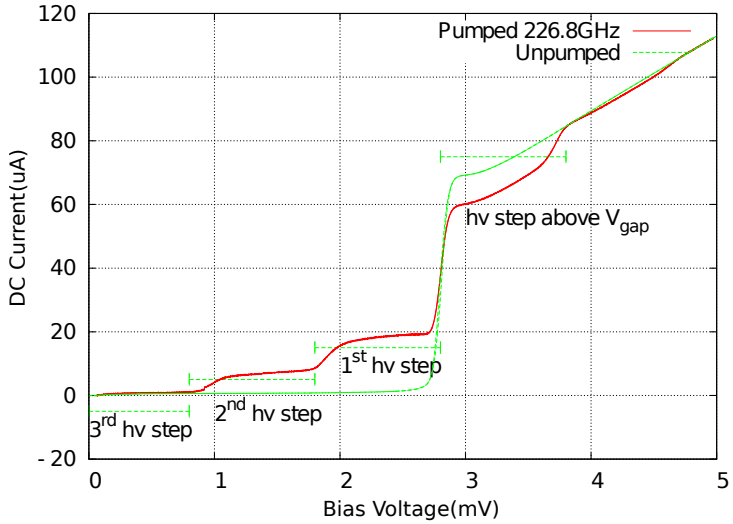

Figure 2.5: The pumped IV characteristic curve superimposed on an unpumped IV curve. The SIS junction is illuminated by an LO signal at frequency of 226.8 GHz. Photon steps of width $h\nu/e = 0.938$ mV are generated.

Above the bias voltage V_{gap}, photons can still break the Cooper pair and assist the quasi-particle to tunnel, hence photon steps can also be seen above the gap. However since above the gap, density of states decreases as a function of energy, the photon steps above the gap voltage appear as a decrement in the tunneling current as shown in Fig 2.5.

2.2 Device Fabrication

The GUBBINS SIS devices were fabricated in I. Physikalisches Institut, University of Cologne, Germany by Dr. Grimes based on the design developed by the author. He thoroughly described the fabrication process of the Nb/AlO_x/Nb SIS junction in his PhD thesis [43]. Four fabrication masks were required for fabricating the mixer chip that included the dimension information of the SIS tunnel junction and the mixer planar circuits. Here we will only give a brief description of the process, in order to understand the mixer design strategy.

- Deposition of the Nb/AlO_x/Nb trilayer structure by the ultraviolet (UV) lithography techniques on a 200 μm silicon substrate. The formed pattern is shown in Fig 2.6 (a), including the finline transition, the ground plane for the microstrip transmission lines and the ground bonding pad.
- Define the pattern of the SIS junction using Reactive Ion Etching (RIE) by removing the top niobium electrode across the ground plane, apart from the SIS junction area. A cross-section

view of the deposition through SIS junction is shown in Fig 2.6 (a). It is worthwhile pointing out that UV lithography is not sufficiently accurate to define the SIS junction with the desired tolerance, hence 'RIE' is employed.

- Two insulator layers (Fig 2.6 (b)(c)) (thickness: 240 nm and 250 nm) are deposited on top of the Nb ground plane. A 10 μm×10 μm window is left on the top SiO insulator so that the Nb Wiring layer fills in the window and has a firm contact with the top electrode of the SIS junction. The junction is protected by the photoresist.

- Nb wiring layer including the slotline-to-microstrip transition, the tuning circuit and the signal bonding pad, are finally deposited on top of the SiO layer using standard UV lithography techniques (Fig 2.6 (d)). A thin (∼25 nm) gold protection layer is finally sputtered on the wiring layer, to prevent the Nb, especially the bonding pads from oxidation.

2.3 Characteristic parameters of an SIS Junction

The parameters of the SIS device, which are essential to the device selection, are described below.

2.3.1 Gap-voltage V_{gap}

The gap voltage at $T = 0$ of an SIS junction is the sum of the energy gaps of both junction electrodes divided by the electron charge e, i.e,

$$V_{\mathrm{gap}}(\mathrm{T}) = 2\Delta(\mathrm{T})/\mathrm{e} \tag{2.11}$$

where the gap energy Δ(T) depends on the quality of the junction barrier, and also the ambient temperature T through the BCS-integral equation [9][87],

$$\frac{1}{VN(E_F)} = \int_0^{\hbar\omega_D} d\xi(\xi^2+\Delta^2)^{-1/2}\mathbf{tanh}[\frac{1}{2k_BT}(\xi^2+\Delta^2)^{1/2}] \tag{2.12}$$

The dimensionless parameter $VN(E_F) = \lambda_{ep}$ is the product of the density of states at the Fermi level $N(E_F)$ and the attractive energy V. The theoretical and experimental values of λ_{ep} for conventional superconductors are displayed in Table 2.1. ω_D is Debye frequency that describes the maximum possible frequency for atom vibration in crystal and has typical values between 10^{12} and 10^{13} Hz. ξ represents energy, which should be integrated from the Fermi energy level to the energy level that corresponds to Debye frequency $\hbar\omega_D$.

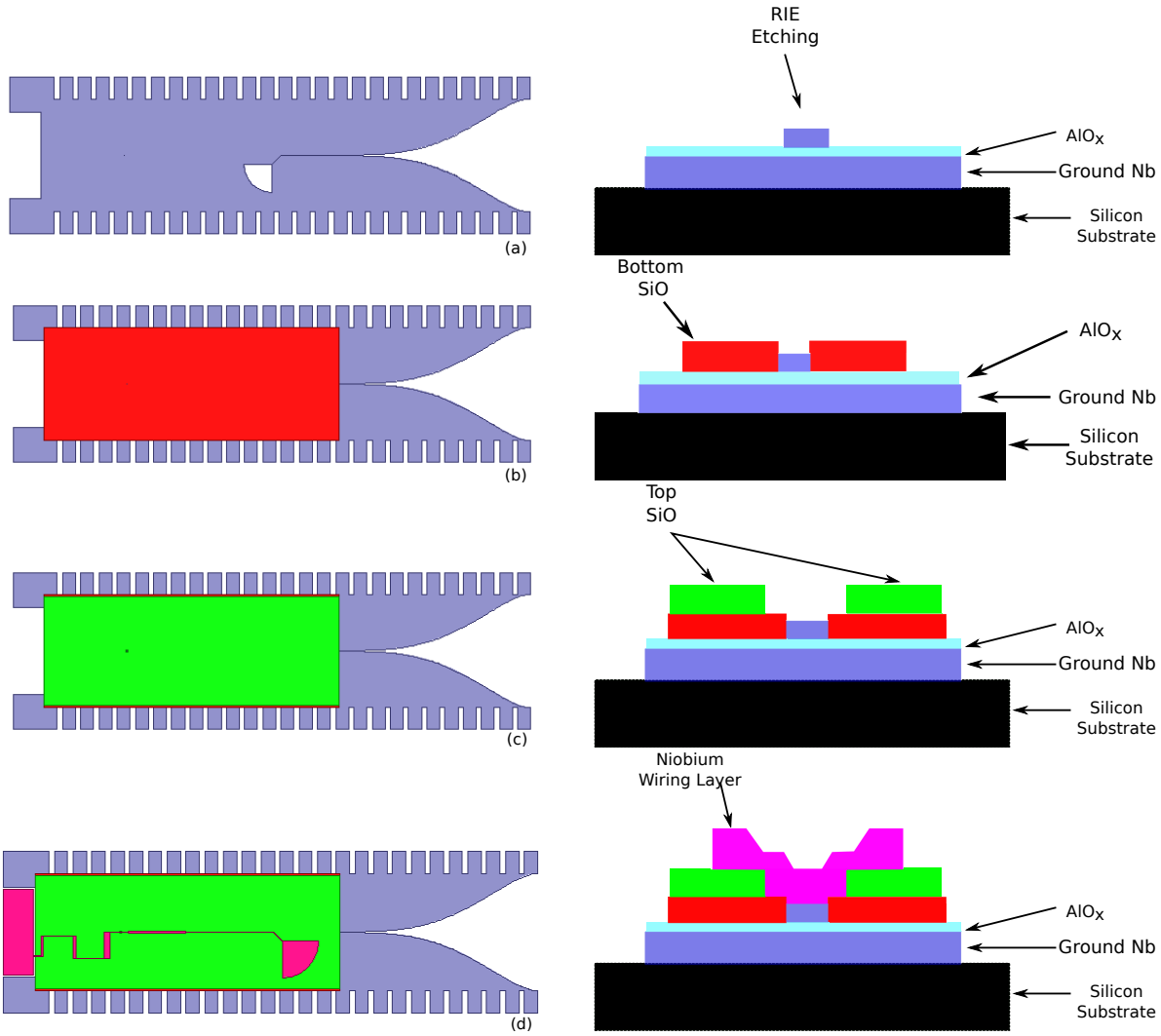

Figure 2.6: Building up of the fabrication process. (Left) The left column shows the fabrication sequences for the different layers of the device. The SIS junction is too small to be seen and the silicon substrate is not shown here. (Right) The right column shows a schematic cross-section view of the deposition through SIS junction sandwich structure.

A useful approximate expression for the energy gap as an alternative to the above integral equation is given by [87]

$$V_{\mathrm{gap}}(T) = V_{\mathrm{gap}}(0)\sqrt{\cos(\frac{\pi}{2}\frac{T^2}{T_{\mathrm{c}}^2})} \tag{2.13}$$

where T_{c} is the critical temperature and T is the ambient temperature. The gap voltage at T=0 K is related to the critical temperature T_c through BCS theory by [9],

$$2\Delta(0) = 3.52 \cdot k_B \cdot T_{\mathrm{c}} \tag{2.14}$$

We have calculated the gap voltage by both solving the integral equation in Eq 2.12 and the

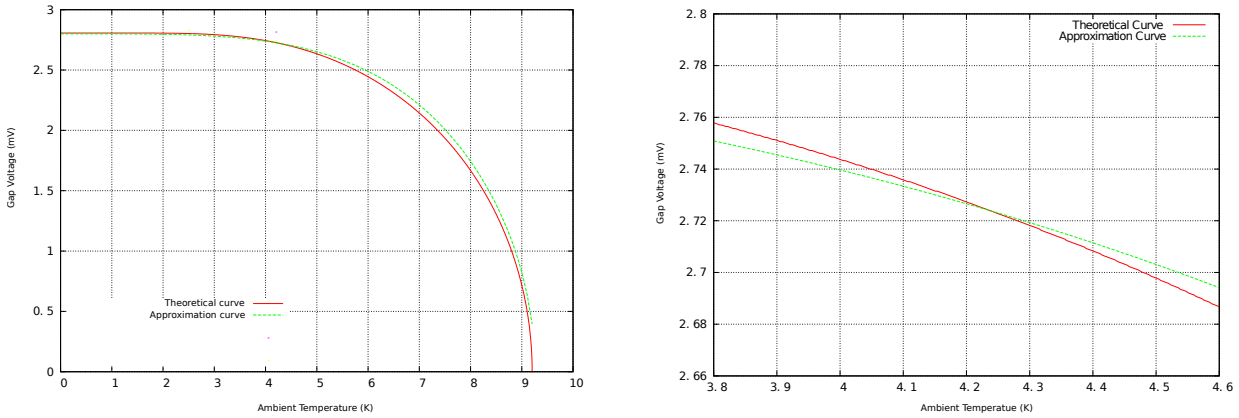

(a) (b)

Figure 2.7: (a) Gap voltage as a function of the ambient temperature, calculated from both BCS theory (Eq 2.12) and from the approximate equation (Eq 2.13). In the calculation from Eq 2.12, the values of $\omega_D = 1.85 \times 10^{13}$, λ_{ep}=0.35 were used. (b) The same figure zoomed on temperature ranging from 3.8 K to 4.2 K.

approximate expression in Eq 2.13. In Fig 2.7, the temperature dependence of the voltage gap V_{gap} from both expressions are compared. It can be shown that at $T < 5$ K the approximate expression gives accurate values for Δ but for 5 $K < T < 8$ K, the exact solution must be used. The temperature of the SIS mixer affects the performance of the device in several ways. A lower temperature gives higher V_{gap} ($V_{\text{gap}} < V_{\text{gap}}(0)$), and lower subgap current. Devices with gap voltage significantly lower than the value predicted by theory will not perform as good mixers.

Metal	Calculated λ_{ep}	Experimental λ_{ep}
Al	0.23	0.175
Nb	0.35	0.32

Table 2.1: Values for $\lambda_{ep} = N(E_F)V$ for Al and Nb [87][23].

2.3.2 Normal resistance R_{N}

The value of the normal conductive state of the SIS tunnel junction R_{N} can be easily measured during DC testing by calculating the ratio for ΔV/ΔI for V>> V_{gap}. For a given junction cooled well below the critical temperature T_c, with junction area A_{J}, gap voltage V_{gap} and current density j_c, R_{N} can be expressed as,

$$R_{\text{N}} = \frac{V_{\text{gap}}}{j_c \cdot A_{\text{J}}} \tag{2.15}$$

Due to the sandwich structure of the SIS junction, it has an intrinsic capacitance C_{J} which is

proportional to junction area A_J. The intrinsic capacitance C_J is determined by the dielectric barrier thickness and material properties. The successful operation of an SIS mixer requires the parasitic capacitance of the tunnel junction C_J, to be tuned out across a certain bandwidth to prevent shorting of the detected RF and LO signals. Based on transmission line theory, the input impedance of a transmission line (characteristic impedance Z_0, electric length βl) terminated by a load (characteristic impedance Z_l) is given by,

$$Z_{\text{in}} = Z_0 \frac{Z_l + jZ_0 \tan\beta l}{Z_0 + jZ_l \tan\beta l} \tag{2.16}$$

So the input impedance of a short-ended microstrip line with the electrical length βl and characteristics impedance Z_0 is $j\tan\beta l$, which can cancel the capacitive part of an SIS junction ($1/j\omega C_J$) over a narrow RF band around frequency ω, as indicated by the following equation

$$\tan\beta l = Z_0 \omega C_J \tag{2.17}$$

where $\beta = 2\pi/\lambda$ is the guided wave-number and C_J is the intrinsic capacitance of the SIS junction. Fig 2.8 depicts the equivalent circuit of an SIS junction being tuned out by a single microstrip tuner.

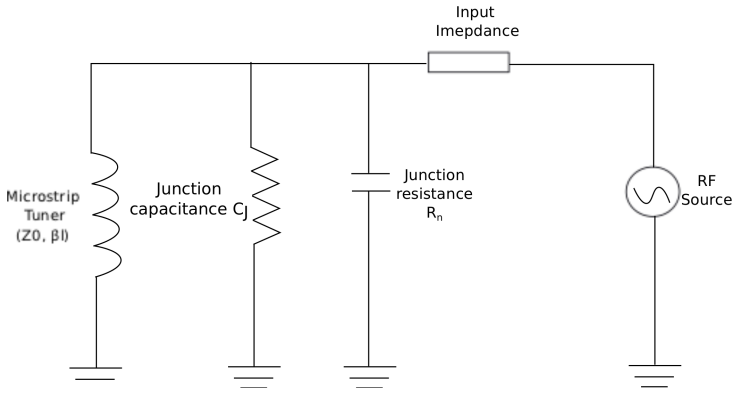

Figure 2.8: The equivalent circuit showing a single microstrip tuner as an inductance to tune out the junction parasitic capacitance C_J at frequency ω, which satisfies the relation $\tan\beta l = Z_0 \omega C_J$. The RF source denotes the incoming RF signal and the input impedance is determined by the finline transition and the slotline-to-microstrip transition.

where $\beta = 2\pi/\lambda$ is the guided wavelength. $\tan\beta l$ can be approximated to βl due to the short length l, so

$$\beta l \approx Z_0 \omega C_J \tag{2.18}$$

As the intrinsic capacitance C_J of the SIS junction is proportional to its area A_J, substitute Eq 2.18

to Eq 2.15, we can find that the normal resistance R_N is proportional to the tuned frequency ω.

The area of the SIS junctions used in this work is approximately 1 μm^2, and variances in junction area result in variances of capacitance and therefore the tuned frequency ω. For GUBBINS devices, 10% of the devices have less than ±5% offset in normal resistance, shifting the expected 230 GHz tuned frequency to 218.5 GHz–241 GHz. Since the tuned frequency ω determines the center of the RF band of the SIS mixer, measuring R_N is an important step in selecting good quality SIS devices.

2.3.3 Critical current density j_c

The critical current density is defined as the largest amount of the current that can flow per unit area before superconductivity disappears. In an SIS junction, it is determined by the physical properties of the insulating barrier such as the thickness and the quality of the AlO_x. A high current density is required for the purpose of RF broadband SIS mixer. However, this requires a thin barrier, which can cause higher sub-gap current and a higher chance on barrier defects, such as pinholes [46].

2.3.4 Subgap Leakage current I_{sub} and junction quality factor Q

The sub-gap leakage current caused by the thermal excitation of quasiparticles, is a major source of shot noise in SIS device, and the lower this value, the better the mixer performance. Theoretically sub-gap current is inversely proportional to the normal resistance R_N and can be written as [12],

$$I_{\text{sub}} = \frac{2}{R_N \cdot e} \cdot e^{-\frac{\triangle}{k_B T}} \cdot \sqrt{\frac{2\triangle}{eV + 2\triangle}} \cdot (eV + \triangle) \cdot \sinh(\frac{eV}{2k_B T}) \cdot K_0(\frac{eV}{2k_B T})$$

where K_0 is the 0^{th} order modified Bessel function. In Sec 2.4.4, we will show the influence of the leakage current on the conversion gain and the noise temperature of the SIS mixer.

The junction quality factor Q is defined as the ratio I_g/I_{sub} of tunneling currents when the junction is biased just above and below the gap voltage. High Q factor is a prerequisite for an SIS devices with good performance.

2.4 Mixer Theory and Computations

In SIS mixer operation, a strong LO radiation is coupled to the SIS junction causing photon-assisted quasi-particle tunneling through the barrier. The I-V curve of an SIS junction in the presence of an LO radiation at frequency ν_{LO} creates photon steps at integral multiples of $h\nu_{LO}/e$ below and above V_{gap}. The main role of the SIS mixer is to achieve frequency down-conversion of a weak RF signal

at a frequency ν_{RF} by coupling both the RF signal and a strong LO radiation at frequency ν_{LO} to the SIS junction. This produces an IF signal with their difference frequency $\nu_{IF} = |\nu_{LO} - \nu_{RF}|$. The quality of the SIS mixer depends on the conversion gain (amplitude ratio of P_{IF} to P_{RF}), the noise added in the down-conversion process, and the instantaneous bandwidth of the generated IF signal. The Tucker quantum mixing theory is able to predict the full performance mentioned above [55] and has been extensively verified [45] [97] [84]. Tucker's theory uses a quantum mechanical formulation of the behavior of the SIS junction under illumination by radiation with photon energy comparable to the energy gap of the superconductor, and predicts that SIS mixers can achieve quantum limited noise performance, and a conversion gain equal to or even greater than unity. A computational model based on Tucker theory has been constructed here to predict the performance of our SIS mixer. The large signal analysis describes the strong LO coupling, and the small signal analysis including both the LO and RF signals calculates the mixer conversion gain and noise correlation matrix between the RF and IF sidebands under the assumption that the signal levels in the sidebands are small [43]. Following the mixer theory description we will show how the large signal analysis can be used to estimate the embedding impedance seen by the device in the mixer chip using the experimentally measured IV curve. Finally we introduce the SuperMix software package, developed by Caltech [34], based on the Tucker Theory. SuperMix can perform rigorous calculation and optimizations of high-frequency circuits, incorporating superconducting microstrip transmission lines and multiple SIS tunnel junctions. Used in combination with HFSS, SuperMix is a valuable tool in designing and predicting the performance of the SIS mixer chips.

2.4.1 Large Signal Analysis

The quantum tunneling phenomenon in SIS junction has been described by several authors [52][33]. The widely accepted concept is to introduce an extra transfer Hamiltonian term to the total system Hamiltonian. Inspired by the observations of superconducting energy gap in tunneling experiments by Giaever [49][48], and the treatment by Bardeen [50] in which the barrier is considered to weakly couple two many-body systems, Cohen, Falicov, and Phillips [68] constructed a transfer Hamiltonian H_{T} formulation of tunneling theory. In this theory, the barrier is represented as a perturbation H_T to the original system Hamiltonian, as

$$H = H_R^0 + H_L^0 + eV(t)N_L + H_T \tag{2.21}$$

where $H_{L,R}^0$ are the full many-body Hamiltonian for the left hand and right hand side electrodes, assuming no existence of barrier hence no coupling at all. The DC voltage applied across the SIS

junction, shifting the electric potential of one electrode with respect to the opposite-electrode, characterized by $eV(t)$, multiplied by the number operator of un-grounded electrode N_L. The applied voltage $V(t)$ includes the AC field of the incident radiation.

If the SIS junction is illuminated by an external local oscillator with frequency ω, the voltage applied across the SIS junction can be in the form,

$$V(t^{'}) = V_0 + V_{LO}\cos(wt^{'}) \tag{2.22}$$

with DC bias voltage V_0 and LO signal amplitude V_{LO}. The Fourier transform W($\omega^{'}$) of the time-varying potential $V(t^{'})$ can be calculated as,

$$\int_{-\infty}^{\infty} dw^{'} W(w^{'}) e^{-iw^{'}t} = \exp[-\frac{-ie}{\hbar}\int_{0}^{t} dt^{'}[V(t^{'}) - V_0]] \tag{2.23}$$

and substituting Eq 2.22 into Eq 2.23 leads to a phase modulation of the single particle operators with the form,

$$\begin{aligned} \exp\left\{-\tfrac{ie}{\hbar}\textstyle\int^{t} dt^{'} V_{LO}\cos\omega t^{'}\right\} &= \exp\left\{-i\left(\tfrac{eV_{LO}^{'}}{\hbar\omega}\right)\sin\omega t\right\} \\ &= \textstyle\sum_{n=-\infty}^{\infty} J_n(eV_{LO}/\hbar\omega)e^{-in\omega t} \end{aligned} \tag{2.24}$$

The Fourier transformer of the time-dependence phase factor of Eq 2.24 can be expressed as,

$$W(\omega^{'}) = \sum_{n=-\infty}^{\infty} J_n(\alpha)\delta(\omega^{'} - n\omega) \tag{2.25}$$

where the factor α is the normalized and the magnitude of the applied LO signal is given by,

$$\alpha = eV_{LO}/\hbar\omega \tag{2.26}$$

The time-depedent tunneling current through an SIS junction was originally derived by Werthamer [69], and based on the calculation done by Ambegaokar and Baratoff [90] of the Josephson effect, can be expressed as,

$$\langle I(t)\rangle = \mathrm{Im}\int_{-\infty}^{\infty} dw^{'} dw^{''} W(w^{'}) W^{*}(w^{''}) e^{-i(w^{'}-w^{''})t} j(V_0 + \hbar w^{'}/e) \tag{2.27}$$

where V_0 is the DC bias voltage of the SIS mixer, $W(w)$ is the Fourier transform of the varying part of the time-dependent bias voltage $V(t)$ and $j(V)$ is the response function related to the DC unpumped IV characteristic $I_{dc}^{0}(V_0)$. By putting in Eq 2.27, it can be seen that the imaginary part of $j(V_0)$ is simply the DC-IV characteristic. The real part of $j(V_0)$ is related to the imaginary part by the Kramers-Kronig relation

$$\begin{aligned} \mathrm{Re}[j(V_0)] &= P\int_{-\infty}^{\infty} \frac{dV'}{\pi} \frac{I^0_{dc}(V') - V'/R_n}{V' - V_0} = I_{KK}(V_0) \\ \mathrm{Im}[j(V_0)] &= I^0_{dc}(V_0) \end{aligned} \tag{2.28}$$

where R_n denotes the normal resistance of the SIS junction and P denotes the Cauchy principle value of the integral. The complex function $j(V_0)$ therefore represents the physical behavior of the SIS tunnel junction. The tunneling current through the SIS junction in the presence of a time-varying AC potential may, therefore, be expressed in terms of its DC I-V characteristics and its corresponding Kramers-Kronig transform.

By substituting Eq 2.25 into Eq 2.27, the current tunneling through the SIS junction under the illumination of the LO signal can be written as,

$$\begin{aligned} I_{LO}(t) &= \mathrm{lm}\sum_{n,m=-\infty}^{\infty} J_n(\alpha) J_{n+m}(\alpha) e^{+imwt} j(V_0 + n\hbar w/e) \\ &= a_0 + \sum_{m=1}^{\infty} [2a_m \mathrm{cos} m\omega t + 2b_m \mathrm{sin} m\omega t] \end{aligned} \tag{2.29}$$

where J_n is the n-th order Bessel function of the first kind. The tunneling current induced by the local oscillator in Eq 2.29 contains harmonic signals with amplitudes,

$$\begin{aligned} 2a_m &= \sum_{n=-\infty}^{\infty} J_n(\alpha) \left[J_{n+m}(\alpha) + J_{n-m}(\alpha)\right] I_{dc}(V_0 + n\hbar\omega/e) \\ 2b_m &= \sum_{n=-\infty}^{\infty} J_n(\alpha) \left[J_{n+m}(\alpha) - J_{n-m}(\alpha)\right] \mathrm{Re}(j(V_0 + n\hbar\omega/e)) \end{aligned} \tag{2.30}$$

Eq 2.29 can be expanded into a Fourier series, and taking only the m=0,1 components we obtain,

$$I_{LO}(t) = I^0_{LO} + I^{\omega}_{LO} e^{i\omega t} \tag{2.31}$$

we have neglected the higher order harmonic signals assuming that they are shorted by the intrinsic capacitance of the SIS tunnel junction. The m=0 component is the DC pumped I-V curve given by,

$$I_{dc}(V_0, V_{LO}) = I^0_{LO} = a_0 = \sum_{n=-\infty}^{\infty} J^2_n(\alpha) I^0_{dc}(V_0 + n\hbar\omega/e) \tag{2.32}$$

The components $I^{\omega}_{LO} e^{i\omega t}$ in Eq 2.31 are the complex amplitudes of the AC tunneling current acoss the SIS junction, and can be expressed as $I^{\omega}_{LO} = I^{'}_{LO} + iI^{''}_{LO}$ and it can be easily shown that,

$$\begin{aligned} I^{'}_{LO} &= \sum_{n=-\infty}^{\infty} J_n(a)[J_{n-1}(\alpha) + J_{n+1}(\alpha)] I_{dc}(V_0 + n\hbar\omega/e) \\ I^{''}_{LO} &= \sum_{n=-\infty}^{\infty} J_n(a)[J_{n-1}(\alpha) - J_{n+1}(\alpha)] I_{KK}(V_0 + n\hbar\omega/e) \end{aligned} \tag{2.33}$$

The equivalent Norton circuit representing the SIS mixer under the illumination of the LO source

is shown in Fig 2.9 (a). The LO source is represented by a current source with a complex amplitude ξ_{LO}, in parallel with an effective source admittance $Y_\omega = G_\omega + iB_\omega$. The embedding admittance Y_ω seen by the junction in the mixer chip hence depends on the details of the waveguide transition, tuning circuit etc. The susceptive part B_ω includes the contribution from the intrinsic capacitance of the SIS junction C. It is essential to be able to estimate the value of embedding impedance seen by SIS tunnel junction in order to assess how complete the capacitance of the SIS junction is tuned out.

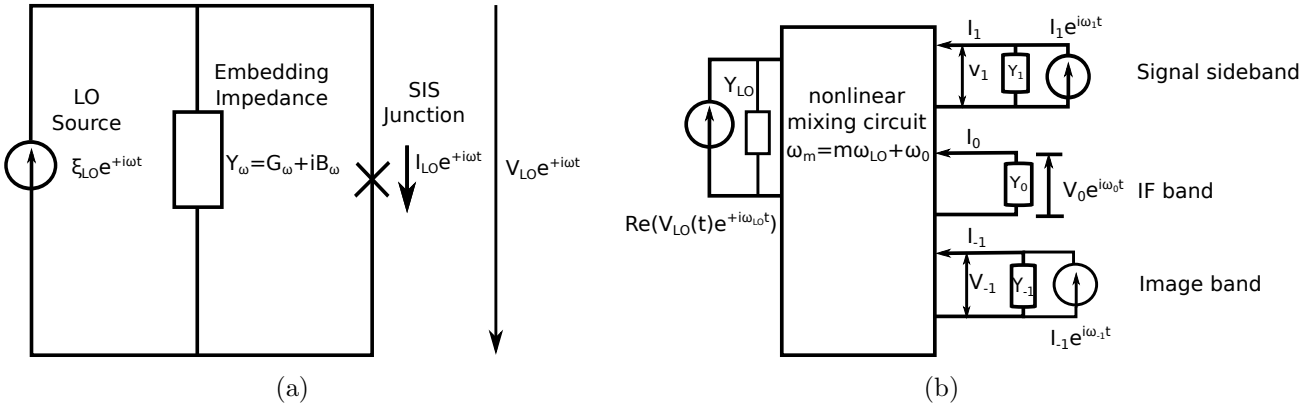

Figure 2.9: (a) The equivalent circuit for the large-signal analysis of an SIS mixer under the illumination of an external LO source. (b) The equivalent circuit for the small-signal analysis illustrating the strong pumping at the LO frequency ω mixing with the sideband signal at frequencies ω_1, ω_{-1}, etc.

2.4.2 Small Signal Analysis

We shall now discuss the case when an RF weak radiation is incident on the sideband ports of the mixers in the presence of a strong local oscillator power. The schematic diagram illustrating the relationship between the small signals in various ports and the large signal from the LO source is shown in Fig 2.9 (b). The heterodyne mixer combines all the small signal sidebands ω_m with the LO source ω and delivers the output IF signal ω_0, by Eq 2.34, at frequencies

$$\omega_m = m\omega + \omega_0 \tag{2.34}$$

The equivalent circuit for the small signal analysis in Fig 2.9 has been simplified to a 3-port model, that only takes into account the m=-1,0,1 components assuming all the higher harmonics are shorted out by the capacitance of the SIS tunnel junction. The RF signal in the signal-sideband at frequency ω_1 is shown as a current source with amplitude I_1 shunted by an admittance Y_1, while the RF signal in the image-sideband is represented by a current source with amplitude I_{-1} shunted by an admittance Y_{-1}. The purpose of mixing is to convert the incoming RF power in the image sideband and the signal

sideband into the low frequency IF port, terminated by admittance Y_0.

The current and voltage across all the sidebands can be represented by the sum of currents and voltages in each port,

$$\begin{aligned} v_{sig}(t) &= \mathrm{Re}\sum_{m=-\infty}^{\infty} v_m e^{+i\omega_m t} \\ i_{sig}(t) &= \mathrm{Re}\sum_{m=-\infty}^{\infty} i_m e^{+i\omega_m t} \end{aligned} \tag{2.35}$$

The small signal currents and voltages are related to each together by an admittance matrix $Y_{mm'}$ with elements given by

$$i_m = \mathrm{Re}\sum_{m'} Y_{mm'} v_{m'} \tag{2.36}$$

The admittance matrix $Y_{mm'}$ is strongly dependent on the quality of the SIS junction, e.g the nonlinearity of the I-V characteristic and also the strength of the LO signal. The value of $Y_{mm'}$ can be calculated by finding the tunneling current across the SIS junction (Eq 2.27) according to the sideband voltage v_m and their ratio will be $Y_{mm'}$. The tunneling current contribution from the small signals $v_{sig}(t)$ is calculated in the same method as in the large signal analysis. The total voltage and current applied across the SIS mixer can be expressed as,

$$V(t) = V_0 + V_{LO}(t) + v_{sig}(t) \tag{2.37}$$

$$\langle I(t)\rangle = I_{LO}(t) + I_{sig}(t) \tag{2.38}$$

Substituting Eq 2.37 into Eq 2.24, and comparing with the large-signal analysis , the inclusion of $v_{sig}(t)$ multiplies the time-dependent phase factor in Eq 2.24, by a ratio related to $v_{sig}(t)$. The Fourier transform of the time-dependent factor in the small-signal analysis scenario can therefore be written as [55],

$$W(\omega') = \sum_{n=-\infty}^{\infty} J_n(eV_0/\hbar\omega)\left[\delta(\omega'-n\omega) + \sum_{m'=-\infty}^{\infty}\frac{e}{2\hbar\omega_{\omega'}}\left[v^{\star}_{m'}\delta(\omega'-n\omega-\omega_{m'}) - v_{m'}\delta(\omega'-n\omega+\omega_{m'})\right]\right] \tag{2.39}$$

Combining the Fourier transform factor $W(\omega')$ with Eq 2.27, and only reserving the part that is linearly proportional to the sideband voltage v_m, the admittance matrix could be obtained and expressed in the form,

$$Y_{mm'} = G_{mm'} + iB_{mm'} \tag{2.40}$$

where

$$G_{mm'}(V_0, V_{LO}) = \frac{e}{2\hbar\omega_{m'}} J_n(\alpha) J_{n'}(\alpha) \delta_{m-m',n'-n} \times \Big\{ \Big[I^0_{dc}(V_0 + n'\hbar\omega/e + \hbar\omega_{m'}/e) - I^0_{dc}(V_0 + n'\hbar\omega/e) \Big] + \big[I^0_{dc}(V_0 + n\hbar\omega) - I^0_{dc}(V_0 + n\hbar\omega/e - \hbar\omega_{m'}/e) \big] \Big\} \tag{2.41}$$

and

$$B_{mm'}(V_0, V_{LO}) = \frac{e}{2\hbar\omega_{m'}} J_n(\alpha) J_{n'}(\alpha) \delta_{m-m',n'-n} \times \Big\{ \Big[I^0_{KK}(V_0 + n'\hbar\omega/e + \hbar\omega_{m'}/e) - I^0_{KK}(V_0 + n'\hbar\omega/e) \Big] + \big[I^0_{KK}(V_0 + n\hbar\omega/e) - I^0_{KK}(V_0 + n\hbar\omega/e + \hbar\omega_{m'}/e)) \big] \Big\} \tag{2.42}$$

The admittance matrix $Y_{mm'}$ components $G_{\mathrm{mm'}}$ and $B_{\mathrm{mm'}}$ are associated with the measured dc I-V characteristic of the SIS junction $I_{dc}(V)$ and its Kramers-Kronig components $I_{KK}(V)$ and they are strongly dependent on the LO signal strength $\alpha = eV_{\mathrm{LO}}/\hbar\omega$. While the admittance matrix $Y_{mm'}$ for the required sideband are determined, the calculation of the mixer conversion gain for the various sidebands is rather straightforward. Referring to Fig 2.9, each sideband port with frequency ω_m can be represented by the current source I_m, which produces small-signal voltage and current across the SIS junction satisfying,

$$\begin{aligned} I_m &= i_m + Y_m v_m \\ &= \textstyle\sum_{m'} (Y_{mm'} + Y_m \delta_{m,m'}) v_{m'} \end{aligned} \tag{2.43}$$

To obtain the mixer conversion gain, we need to know the power delivered to the IF load (Y_0), V_0. Eq 2.43 cab be converted to the following form,

$$v_m = \sum_{m'} Z_{mm'} I_{m'} \tag{2.44}$$

and defining the impedance matrix $Z_{mm'}$ as,

$$\left\| Z_{mm'} \right\| = \left\| Y_{mm'} + Y_m \delta_{m,m'} \right\|^{-1} \tag{2.45}$$

The IF small signal voltage v_0 can be written as,

$$v_0 = \sum_{m'} Z_{0m'} I_{m'} \tag{2.46}$$

In a standard Single-SideBand mixer (SSB) mixer, the incoming signal from the signal sideband can be expressed as $I_1 = I_s$ at frequency $\omega_s = \omega_{LO} + \omega_0$, with power input given by,

$$P_{in} = |I_s|^2 / 8G_s, \tag{2.47}$$

where G_s is the real part of the source admittance Y_s

The frequency down-converted signal at the IF output port can be expressed as,

$$P_{out} = \frac{1}{2} G_L |v_0|^2 = \frac{1}{2} G_L |Z_{01}| |I_s|^2 , \tag{2.48}$$

Where G_{L} is the real part of the load admittance Y_{L}. Hence the conversion gain is given by,

$$L_{-1} = \frac{P_{out}}{P_{in}} = 4G_s G_L |Z_{01}|^2 \tag{2.49}$$

For the DSB mixer, the conversion gain is

$$L_{-1} = \frac{P_{out}}{P_{in}} = 2G_s G_L |Z_{01}|^2 \tag{2.50}$$

2.4.3 Embedding Impedance Recovery

Embedding impedance is the effective impedance that is seen by the SIS junction when the mixer chip is mounted in the mixer block and is illustrated in the mixer circuit shown in Fig 2.9 by $Y_\omega = G_\omega + jB_\omega$. The embedding impedance is strongly influenced by the parasitic capacitance of the SIS junction and its tuning circuit, and is independent on the DC bias voltage. On the other hand, the junction RF admittance/impedance is a strong function of the DC bias voltage. A good knowledge of the embedding impedance is of great importance, because the match between the embedding impedance and the SIS junction determines the coupling of the LO and RF power into the SIS junction, and hence the sensitivity of the SIS mixer. Even though without performing a rigorous embedding impedance recovery calculation, the susceptance part B_ω of the embedding admittance Y_ω can be roughly estimated by observing slope of the first photon step. A positive slope of the first photon step indicates a capacitive embedding impedance, while a negative one indicates an inductive one, and a flat slope indicates a perfectly tuned SIS junction [82]. The embedding impedance calculation requires the use of experimental pumped and unpumped IV curves of the device. However to illustrate the embedding impedance calculation, the unpumped IV characteristic $I^0_{dc}(V_0)$ expressed in Eq 2.28 could be replaced by a polynomial expression,

$$I_{DC}(\widetilde{V_0}) = \frac{\widetilde{V_0}^{2n+1}}{1 + \widetilde{V_0}^{2n}} \tag{2.51}$$

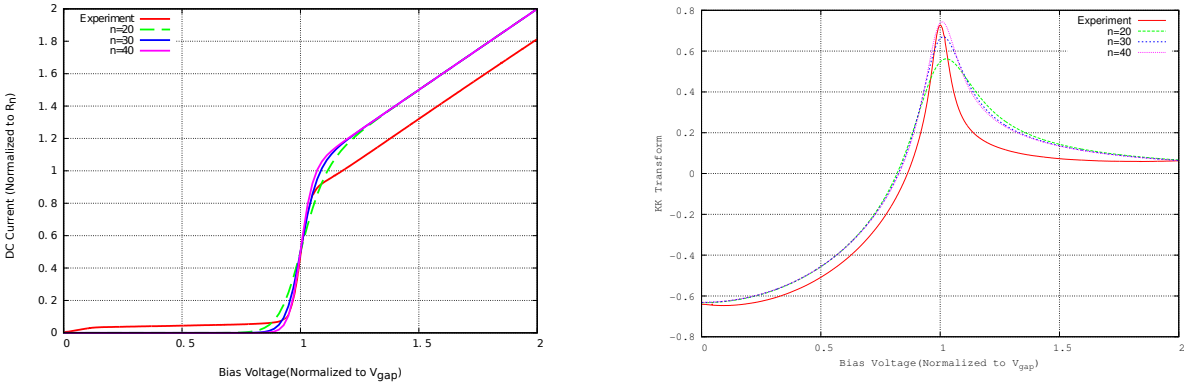

(a) (b)

Figure 2.10: (a) Red: the experimental IV curves normalized to the gap voltage $V_{\rm gap}$ and normal resistance $R_{\rm n}$. Other colors: the IV curves produced by the polynomial equation Eq 2.51 with n=20, 30, 40. (b) The corresponding Kramers-Kronig transforms of each IV curve shown in the left.

where n control the nonlinearity in the I-V curve. The tildes on top of the letter indicates that the quantity has been normalized. The voltage is normalized to the gap voltage $V_{\rm gap}$ and the current is normalized to $V_{\rm gap}/R_{\rm n}$, where $R_{\rm n}$ is the normal resistance for the SIS junction. In Fig 2.10, the unpumped DC IV curves obtained from both the experiment and the polynomial approximations are displayed, together with their corresponding Kramers-Kronig transform.

Using the equivalent circuit shown in Fig 2.9 for a single frequency ω, the current running through the SIS junction I^{ω}_{LO} is related to the current generated by the LO source ξ_{LO} by,

$$\xi_{\rm LO} = I^{\omega}_{\rm LO} + Y_{\omega} V_{\rm LO} \tag{2.52}$$

where I^{ω}_{LO} is the complex AC current tunneling through the SIS junction (Eq 2.32 and Eq 2.33), V_{LO} is the voltage drop across the SIS junction, Y_{ω} is the embedding admittance and $\xi_{\rm LO}$ is the current from the LO source. Substituting the experimental pumped IV curve to Eq 2.52, we obtain rough estimation for the values of Y_{ω} and ξ_{LO} according to the pumping level and the slope of the first photon step. The estimated Y_{ω} and ξ_{LO} values are substituted into the Eq 2.52 to solve for $V_{\rm LO}$ at each bias points V_0. The calculated $V_{\rm LO}$ is then converted to α and substituted to Eq 2.32 to calculate the pumped IV curve. The calculated pumped IV curve is then compared with the experimental IV curve at each bias voltage point, especially on the first photon stop, to determine the next estimated values for Y_{ω} and ξ_{LO}, in order to minimize the difference between the experimental and simulated pumped IV curves. Several iterations have to be performed before the exact Y_{ω} and ξ_{LO} values can be found. In Fig 2.11, we show a range of simulated pumped IV curves with varied embedding admittance (G+jB) values, especially the susceptance part B. The admittance is normalized to mixer normal resistance

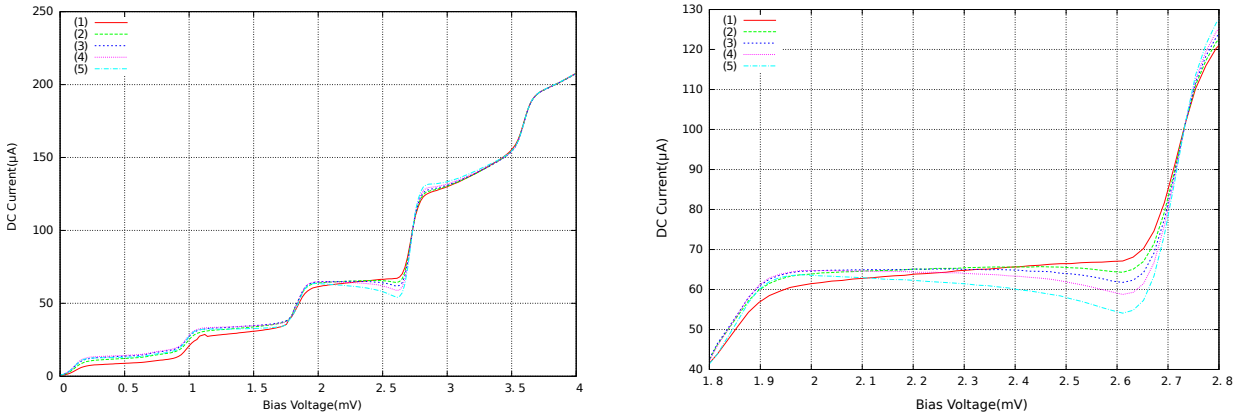

Figure 2.11: (a)The simulated pumped IV characteristics based on various value of B ranging from 0.5, 0.2, 0. -0.2, -0.5 from curve(1) to curve(5). (b)The enlarged picture of the first photon steps, indicating the changes of the slopes of the first photon step as a function of the embedding reactance.

R_{n}. As the embedding impedance is a strong indication of how well the SIS junction is tuned, it determines the slope on the first photon step. As can be easily seen, with the susceptance part B changing from 0.5 to -0.5, the slopes on the first photon step change from positive to negative. We compare a simulated pumped IV curve based on the recovered embedding impedance at 216 GHz with its experimental pumped IV curve in Fig 2.12 (b), that the experimental and simulated IV curves overlap with each other over most part of the first photon step. The recovered normalized embedding admittance here is 1.1+0.12j with an α value equal to 1.25. The real part of the embedding impedance is therefore close to the normal resistance of the tunnel junction and the imaginary part is small. This device is therefore well tuned at this frequency.

2.4.4 SuperMix Simulation

SuperMix is an extensive C++ software library written to aid the design and optimization of high-frequency circuits, in particular those with an SIS mixer. Its complete set of circuit element allows the user to perform frequency-domain simulation from DC to THz domain. Due to the object oriented nature of the SuperMix library, it allows the user to add new circuit elements and to tailor the optimization function without re-writing the code required in the simulation.

SuperMix includes full Tucker theory based models of the SIS quasi-particle tunnel junctions and superconducting transmission line components such as microstrip and CPW lines. This allows SuperMix to perform full harmonic calculation of SIS quasiparticle receiver designs of arbitrary complexity. Mixer conversion gain, noise properties can be analyzed using any number of harmonics and including any number of superconducting tunnel junctions [18]. Also, the successful integration of the RF

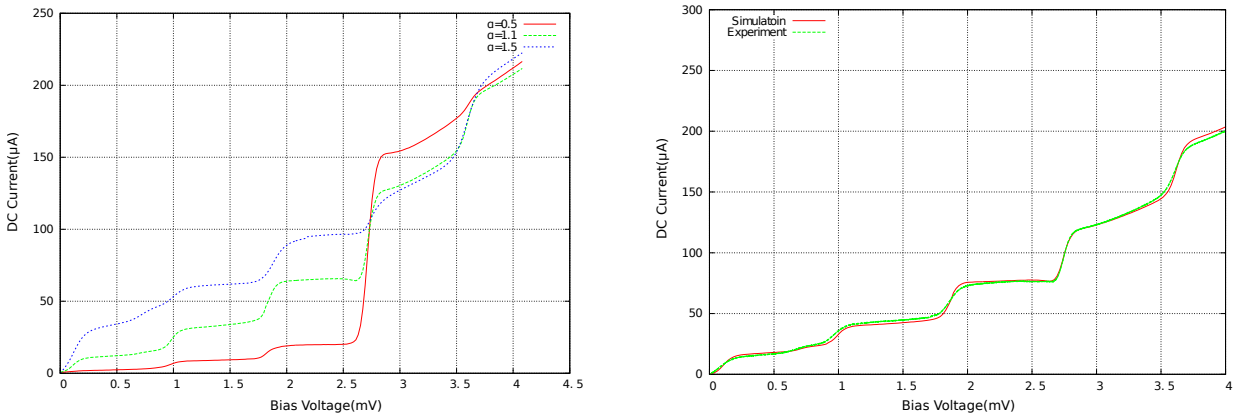

(a) (b)

Figure 2.12: (a) The pumped IV curves as a function of the bias voltage under various LO input power. (b) A simulated pumped IV curve matches to the experimental pumped IV curve at 216 GHz, assuming normalized embedding admittance to be 1.1+0.12j and LO power α to be 1.25.

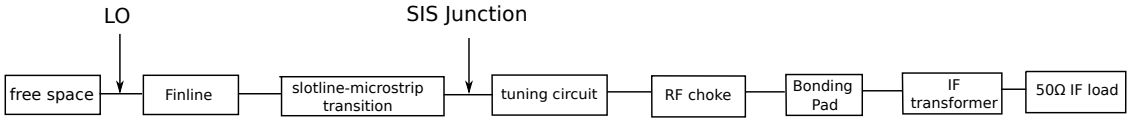

Figure 2.13: The block diagram illustrating the structure of the SIS mixer being simulated in SuperMix. Each electromagnetic component, like finline or slotline-microstrip transition, can be simulated individually in HFSS (see Sec 2.4.5).

feed, RF/IF matching circuit allows SuperMix to perform a complete analysis of an SIS mixer based receiver. As SuperMix uses a scattering matrix representation to perform circuit calculation, the conversion between wave and impedance or admittance representation can easily be carried out.

However the electromagnetic calculations in SuperMix are restricted to planar structure with negligible thickness, hence it will not be used for our passive mixer circuits. The scattering matrices for each of the electromagnetic components of the SIS mixer can be rigorously calculated in HFSS (see section 2.4.5) and exported into SuperMix to assess the gain, noise temperature and other heterodyne properties of the mixer by performing the quantum mixing calculation. Due to the limited memory available in HFSS, the passive circuit for the SIS mixer is often split into various separate components, e.g, finline, tuning circuit, IF choke, etc, and simulated separately. These various components can then be cascaded together in SuperMix. The block diagram showing the equivalent circuit of the SIS mixer simulation in SuperMix is shown in Fig 2.13.

Examples of the SuperMix simulation performed for the SIS mixers as a function of the bias voltage are listed in Fig 2.14, Fig 2.15, Fig 2.16 with some mixing operators as the variables to explore the behavior of the SIS junction. The noise temperature shown is the pure noise temperature generated

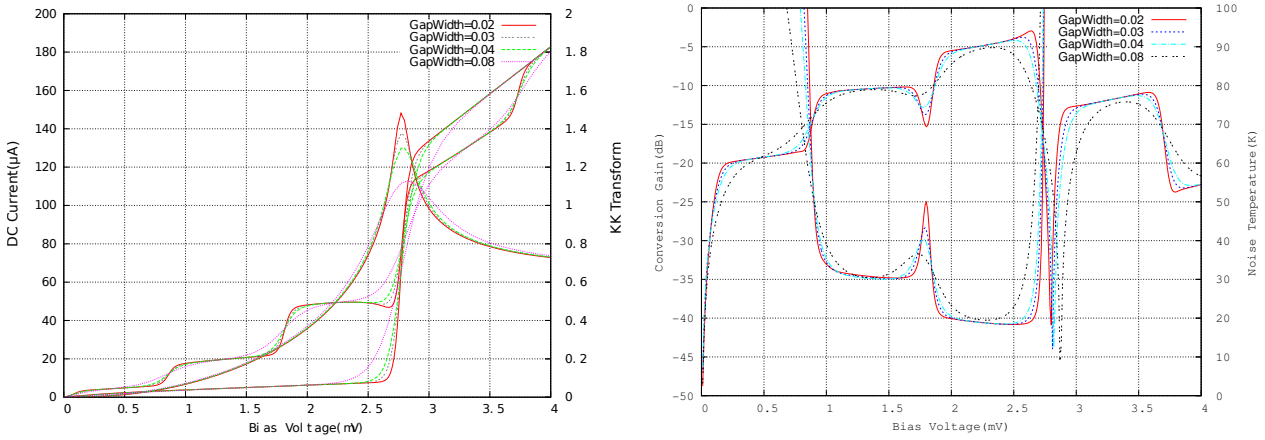

(a) (b)

Figure 2.14: Mixer performance as a function of the DC bias voltage at LO frequency of 230 GHz, for the SIS junctions with various nonlinearities. (a) The unpumped IV characteristic curves are produced using a package in SuperMix with the nonlinearity being parameterized and their KK transform curves are also shown. (b) The simulated noise temperature and conversion gain as function of the bias voltage, based on IV curves presented in the left hand side.

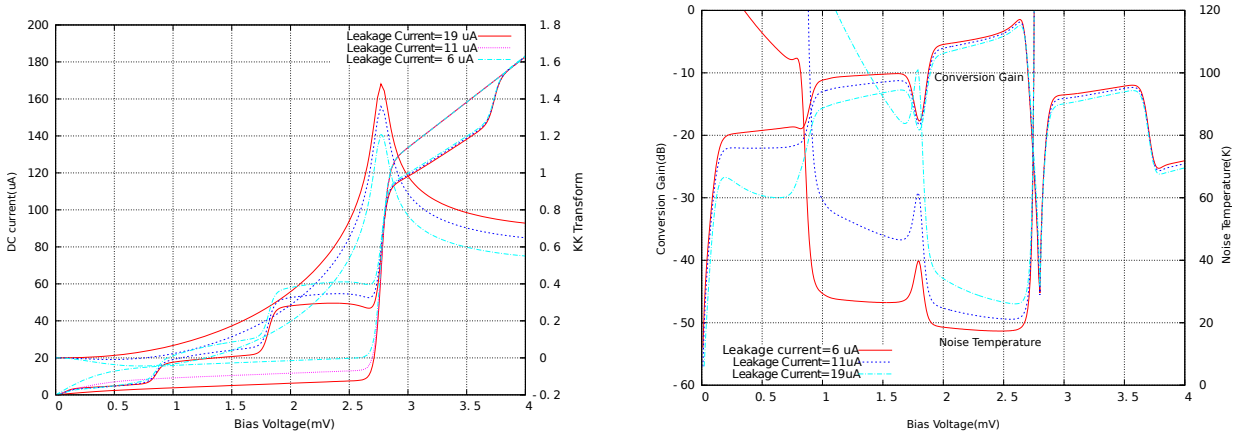

(a) (b)

Figure 2.15: Mixer performance as a function of the DC bias voltage with LO frequency at 230 GHz, for the SIS junction with various leakage currents. (a) The unpumped IV characteristic curves are produced using a package in SuperMix with the leakage current being parameterized and their KK transform curves are also shown. (b) The simulated noise temperature and conversion gain as function of the bias voltage.

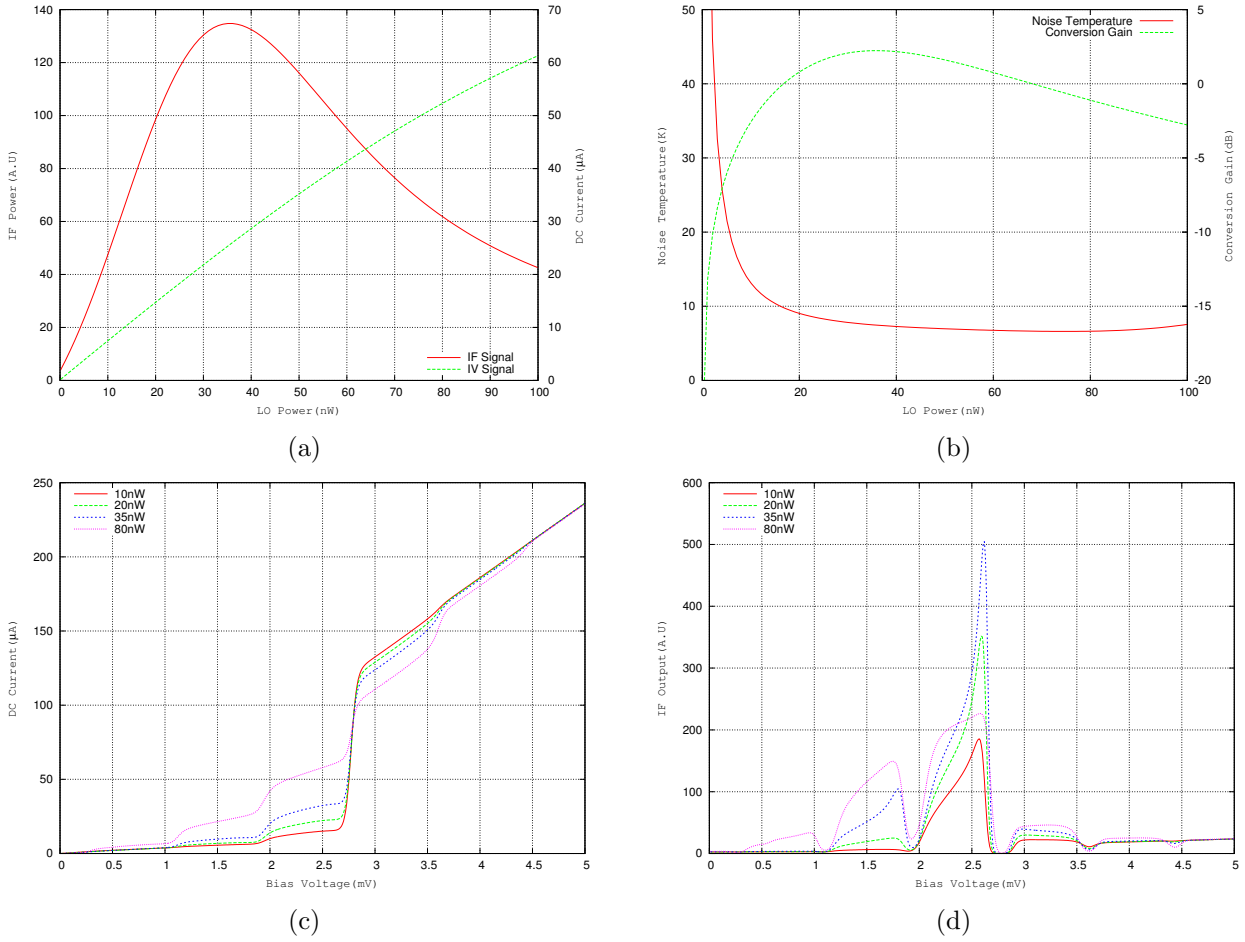

Figure 2.16: (a) The IF and IV output at the center of the first photon step below V_{gap} as a function of the LO power at fixed bias point. (b) The simulated conversion gain and noise temperature for the SIS mixer biased at the center of the first photon step below V_{gap}, as a function of the LO power.(c) The pumped IV curves under varied LO power. (d) The pumped IF curves under varied LO power.

by the SIS mixer itself, and should therefore be comparable to $\hbar\omega/k_B$, ~11 K at 230 GHz. The unpumped IV curves used in the above calculation were generated by a built-in package in SuperMix which can parameterize the nonlinearity, the leakage current, and the Q-factor for the unpumped IV characteristic curve. When we use the package to analyze our experimental mixer results, we will obviously use the measured IV curves.

In Fig 2.14, we show that the effect of the SIS junction nonlinearity on the mixer performance. Here the sharpness of the SIS junctions has been parameterized in terms of the width of the gap nonlinearity, with gap widths of 0.02 mV, 0.03 mV, 0.04 mV, 0.08 mV. It can be seen that as long as the junction gap width is reasonably small (0.02 mV, 0.03 mV, 0.04 mV), the gain and noise temperature on the first photon step are not degraded by much, however the nonlinear curve with gap width of 0.08 mV exhibits an obvious increase in the noise temperature and decrease in the conversion

gain.

In Fig 2.15, the leakage current of the unpumped IV curves has been manipulated to provide leakage current (measured at 2 mV) of 6, 11 and 19 μA. We can observe a clear increase in noise temperature and slight decrease in conversion gain with high leakage currents. This is to be expected since the leakage current is a major source for the shot noise of the SIS junction.

The saturation property of the SIS mixer under a strong LO radiation is investigated in Fig 2.16. The amplitude of the IF and IV signals measured at the center of the first photon step under various LO power are plotted. Before the LO is increased to the point of mixer saturation, the tunneling current at the center of the first photon step (IV curve) increases linearly with the incoming LO signal. However after saturation is reached, the increasing rate of IV signal measured on the first photon step starts to decrease. Since the IF curve is a differential equation of the IV curve, the IF amplitude peaks around saturation and then falls with increasing power. The saturation of SIS mixers by the LO power is not only characterized by a peak power in the IF signal, but also by significant gain of the mixer gain. The noise temperature and conversion gain are simulated as a function of the LO power with the SIS mixer biased at the center of the first photon step. The noise temperature is relatively flat across a wide range of LO power around saturation but the conversion gain suffers severe suppression above the saturation leading to substantial deterioration in the receiver performance.

2.4.5 HFSS Software Package

Ansoft HFSS is a simulation tool for 3-D full-wave electromagnetic field simulation, based on the finite element method. It can be used to rigorously compute basic electromagnetic field quantities, calculate the characteristic port impedances and propagation constant and also compute the S-parameters. Through this thesis, HFSS has been used extensively in simulating the electromagnetic performance of the SIS mixer passive circuits. The SIS mixer chip embedded in the WR-4 waveguide is simulated in HFSS, with the SIS junction being replaced by a lumped element circuit consisting of a resistor in parallel with a capacitor. The resistance is determined by the normal resistance of the SIS junction, while the capacitance is determined by the intrinsic capacitance. The scattering parameters calculated by HFSS as a function of the RF signal are of the greatest importance in designing and optimizing the SIS mixer circuit. Also as mentioned above, SuperMix package can import the rigorous scattering matrix data calculated by HFSS for each individual component in the SIS mixer, and perform the quantum mixing calculation based on these S-parameter results. The combination of rigorous electromagnetic HFSS simulations and Tucker theory description of the SIS device allows us to predict accurately the experimental behavior of the mixer. More importantly, comparing the experimental

result with their precise simulations allows us to recover the detailed sub-micro dimensions of the mixer circuit and hence to improve the design and fabrication of the subsequent mixers.

Chapter 3

SIS Mixer Design

Overview: In this chapter, I discuss the design of an SIS unilateral finline mixer operating at around 230 GHz with both wide IF and RF bandwidths. The mixer is intended for use in a heterodyne interferometer (GUBBINS) with the scientific aim of observing the Sunyaev Zel'dovich effect. The key feature of this design is the employment of a unilateral finline taper on a thin and wide silicon substrate. The finline taper is used to transform the electromagnetic field from the waveguide mode to the microstrip mode, as the SIS junction is embedded in the microstrip line. The unilateral finline is easier in design and fabrication than the conventional antipodal finline, since the fins do not overlap at any stage. The unilateral finline allows wide band coverage in both radio frequency (RF) and intermediate frequency (IF), and also offers large area for the complex on-chip planar circuits. The mixer is designed to work in conjunction with a circular 1 μm^2 Nb/AlO$_x$/Nb (Niobium/Aluminium-Oxide/Niobium) SIS (Superconductor-Insulator-Superconductor) junction embedded in a microstrip line with width of 2-3 μm. A wide RF band tuning circuit is developed to tune out the junction capacitance, so that the RF power over maximum bandwidth can be coupled to the junction. To achieve wide IF bandwidth performance, the device has been carefully designed to present a minimum lumped capacitance and inductance. Each individual component of the planar circuits was separately simulated by the rigorous electromagnetic software HFSS before they were combined and simulated as a whole to evaluate the full device performance.

3.1 General description

A magnified figure showing one fabricated device on the sub-wafer, prior to separation, is displayed in Fig 3.1. In the direction of the RF propagation, the components comprising the device are: silicon notches, unilateral finline, slotline-to-microstrip transition, tuning circuit, SIS junction, RF choke and

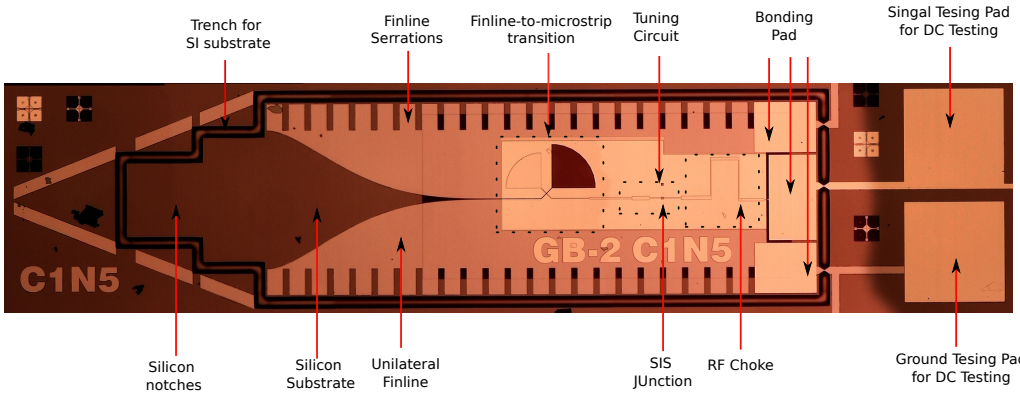

Figure 3.1: An overview of the fabricated SIS mixer device. The mixer chip comprises the finline transition, the finline-to-microstrip transition, the tuning circuit, the SIS junction, the RF choke and the bonding pads. The planar circuits of the SIS mixer are deposited on a 60 μm silicon substrate. Trenches are formed around the silicon substrate to simplify the thinning and separation process. Notches are designed in the front end of the silicon substrate to minimize the impedance mismatch between the free space waveguide and the waveguide loaded by the silicon substrate.

bonding pads. The SIS junction designed here is a Nb/AlO_x/Nb trilayer junction with a circular area of 1 μm^2. The junction has a normal resistance of 20 Ω, a specific intrinsic capacitance of 75 fF/μm^2, and a current density of 14 mA/μm^2. The planar circuits are deposited on a 60 μm silicon substrate. Two stage silicon notches are formed in the front end of the substrate to minimize the impedance mismatch between the free-space waveguide and loaded waveguide. The ground and wiring layers for the planar circuits are both made of Nb film with thickness of 250 nm and 400 nm respectively. A SiO layer (ε_r=5.8) with thickness of 490 nm acts as the dielectric layer for the microstrip lines. The smallest dimensions involved in the design are 2.2 μm for the microstrip and 2.5 μm for the slotline. With such demanding requirements on the fabrication precision, we managed to receive only a limited number of good devices that gave reasonable noise performance. Following the device, the IF transformer board is an independent component that connects to the IF bonding pad of the device by aluminum wires. The IF transformer is used to match the IF output impedance of the SIS mixer with the 50 Ω input resistance of the cryogenic Low Noise Amplifier (LNA). In the following section, we will discuss the detailed design methodology and the simulation results for each component of the mixer.

3.2 Finline Transition

The idea of using a finline as the quasi-planar transmission line structure was raised by Yassin [45] as an alternative to the ridged waveguide and introduced to be used in SIS mixers. Compared to the conventional probe SIS mixer and the quasi-optics SIS mixer, both of which have produced state-

of-the-art performance, the finline mixer allows elegant integration of the complex on-chip planar circuits as the silicon substrate dimensions are large relative to the microstrip width. In addition, the finline mixer eases both the design and the fabrication of the mixer block since no mechanical tuner is needed. The planar circuits fabricated on the mixer chip tune out the junction capacitance. This is of particular importance when fabricating large number of SIS mixers used in arrays in a cheap and time-saving way.

Successful operation of the finline SIS mixers working at 230 GHz [45], 350 GHz [97] and 700 GHz [73][71] have already been reported, mostly are in conjunction with antipodal finline tapers. The schematic diagrams for an antipodal finline and a unilateral finline are compared in Fig 3.2. The electric field distribution in the cross section of both types of finlines are shown in Fig 3.3 and Fig 3.4. Antipodal finline contains a section of overlapping fins to feed the SIS junction embedded in the microstrip line. The top and bottom fins are made out of Niobium and separated by a thin insulator layer ($\sim$400 μm). Before the fins overlap, the thickness of the insulator layer is much less than that of the silicon or quartz substrate. The antipodal finline then behaves as a unilateral finline while the impedance in this section can be brought down from few hundreds to $\sim$60 Ω (see section B in both Fig 3.2 (a) and Fig 3.3). As the fins start to overlap, this sandwich structure behaves approximately as a parallel-plate waveguide with effective width equal to that of the overlapping region (see section C in both figures). When the width is large enough that the fringing effect can be ignored, the waveguide-to-microstrip transition starts to form. After this, the top and bottom fin layers are tapered to form a microstrip line with the desired width (see sections D, E and F in both figures [45]). Whenever the microstrip structure is formed, the silicon (or quartz) substrate thickness is no longer important, instead the thickness of the insulator layer between the two fins determines the electromagnetic performance of the planar circuit. Ideally, the antipodal finline can be directly tapered to a microstrip with any required width. This feature allows the antipodal finline to be matched to the tuning circuit without additional complicated matching circuits, greatly simplifying the design of the tuning mixer chip.

Although the antipodal finline exhibits wide RF and IF bandwidth and other attractive features, it has several intrinsic disadvantages. Firstly, with regards to design, a rigorous simulation is difficult for an antipodal finline particularly at the point where the fins start to overlap, because at this point the field is influenced by the thickness of both the silicon substrate and the insulator layer between the two fins. Secondly, from the point of fabrication, extreme attention has to be paid to the location where the top and bottom fins start to overlap, to avoid shorting the top fin to the bottom fin where their overlap width is small. Also, the antipodal finline chip is usually very long and consequently reduces the amount of devices that can be fabricated on a single wafer, and also increases the loss due

to its long transmission lines, especially for the devices operating near the gap frequency.

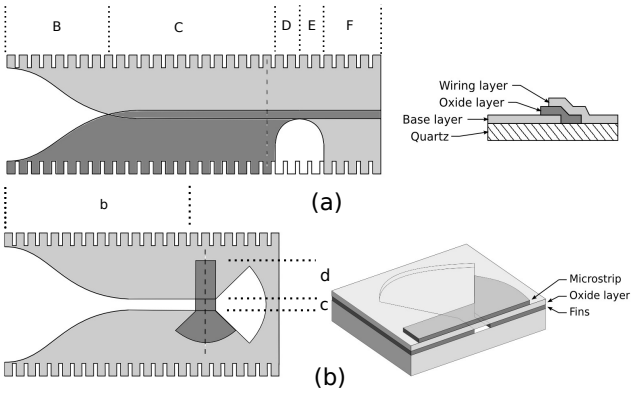

Figure 3.2: (a) A schematic representation of an antipodal finline and its cross-section view. The electric field distribution of the cross-section along the antipodal finline is shown in Fig 3.3 [96]. (b) A schematic representation of a unilateral finline and its cross-section view. Both figures were extracted from [96].

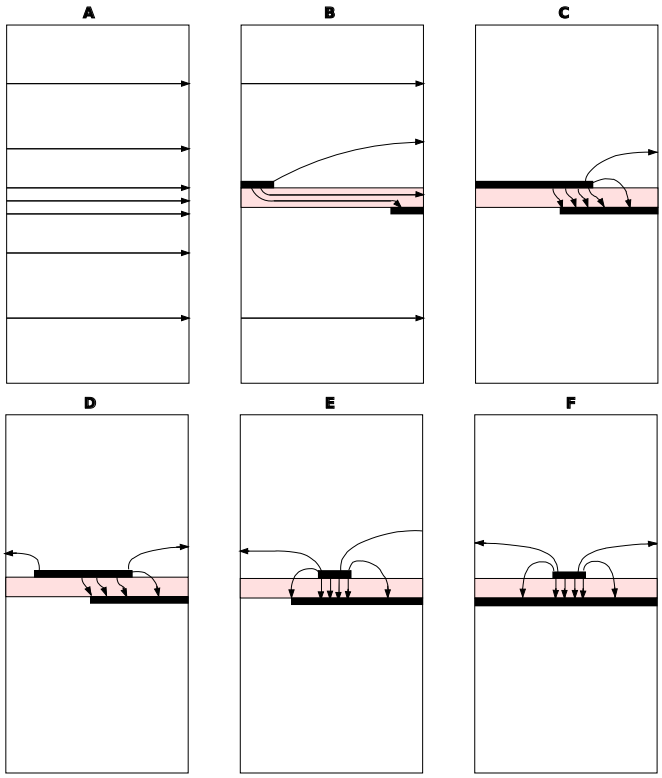

Figure 3.3: The electric field distribution of cross sections along antipodal finline. The pink layer denotes the substrate for the microstrip lines. Plot A represents an empty waveguide. The figure was extracted from [72].

In the context of the mentioned disadvantages of the antipodal finline, unilateral finline was developed as an alternative, as it preserves the advantages of the antipodal finline, but eases both design

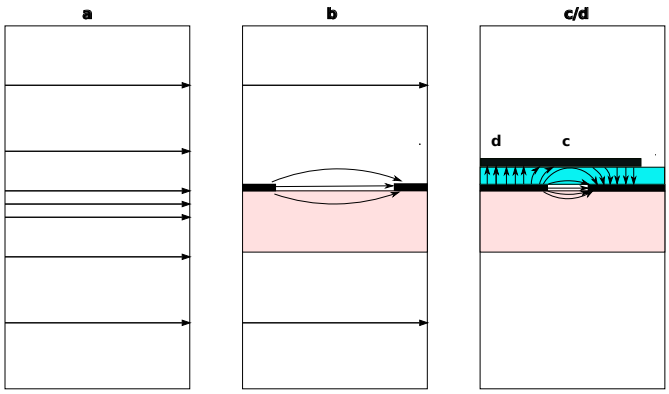

Figure 3.4: The electric field distribution of the cross section along unilateral finline. The pink layer denotes the silicon substrate and the blue layer denotes the dielectric insulator. Plot a denotes an empty waveguide.

.

and fabrication. In the unilateral finline, we totally remove the overlapping fins structure and retain only a single slotline layer. To couple the RF power from the unilateral finline to the microstrip, we bridge one section of microstrip directly on top of the finline, as shown in Fig 3.2 (b). Considering an SIS junction with normal resistance of 20 Ω, it should be embedded in a microstrip with width of $\sim$ 2.5 μm, giving a characteristic impedance of $\sim$20 Ω. So the width of the finline slot should be tapered as narrow as possible to match to 25 Ω microstrip line, because slotline has intrinsically high characteristic impedance. Limited by the state-of-the-art photolithography techniques, the minimum width we could guarantee for the slotline is about 2.5 μm, giving a characteristic impedance of $\sim$40 Ω. So at the transition area, 90° quarter-wavelength microstrip/slotline radial stubs are required to connect to the microstrip/slotline to maximize the power coupling. In such a circumstance, the free space impedance of several-hundred Ohms can smoothly be brought down to 20-30 Ω, which is just about the characteristic impedance of the narrow microstrip where the SIS junction is fabricated. As the mixer was designed to have a wide IF bandwidth ($\sim$ 10 GHz), which is a good fraction of the operating RF frequency (230 GHz), an RF bandpass filter is needed between the finline and the SIS junction to block any IF signal from leaking into the RF port. However since the unilateral finline has a natural cutoff frequency above the IF frequency, no RF bandpass filter was required between the finline and the tuning circuit, which reduces the total length of the device. The profile of the unilateral finline can be rigorously synthesized by a code developed by our group, employing the theory of the transverse resonance technique in conjunction with the Optimum Taper Method (OTM) [20]. OTM method allows the length of the finline taper to be kept as short as possible while giving a wide-band performance. As the mixer is mounted in the E-plane of the waveguide, supported by the grooves in the waveguide wall, quarter-wavelength serrations are added to both sides of the unilateral finline, to

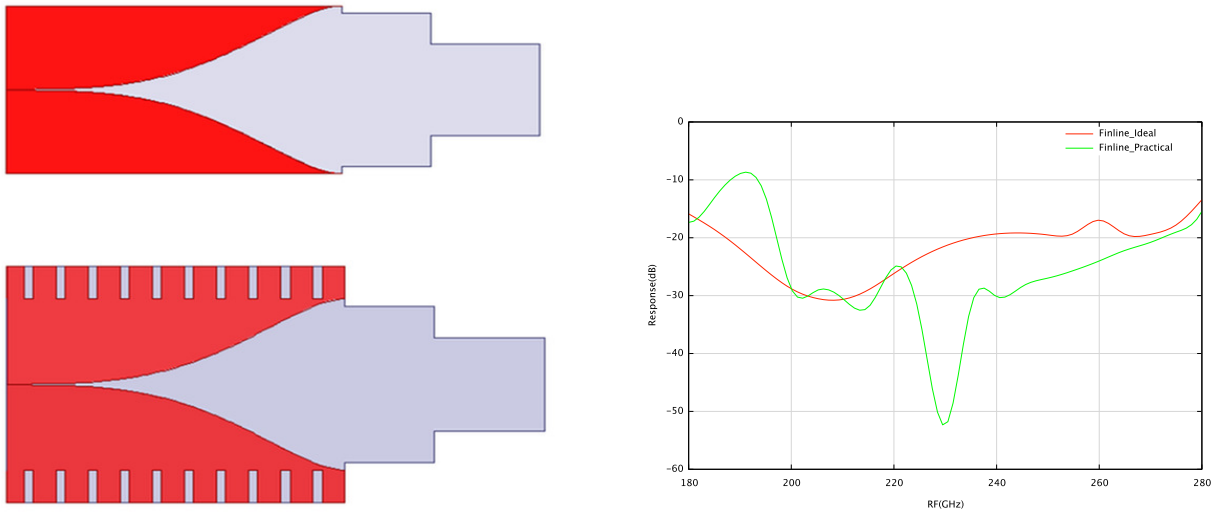

(a) (b)

Figure 3.5: (a) The schematic view of the model constructed in HFSS for the an ideal unilateral finline and a practical finline which sits in the waveguide groove. (b) The HFSS simulated performance for both the ideal finline and the practical finline.

prevent RF power propagating in the grooves. A 3-D full-wave electromagnetic software (HFSS) was used, we simulate the performance of an ideal unilateral finline taper, without serrations, mounted in a waveguide, without grooves (Fig 3.5 (a) (Top)). We then simulated the performance of a practical unilateral finline, with serrations on both sides, mounted in a waveguide supported by grooves ((Fig 3.5 (a) (Bottom))). We compare the results of the above two simulations in Fig 3.5 (b) which show that the performance of the practical finline transition is almost as good as the ideal finline, giving a return loss below -20 dB over RF bandwidth of 80 GHz. The above simulations demonstrate the good performance for the unilateral finline working in conjunction with serrations.

The planar circuits of the SIS mixer including the unilateral finline were deposited on a 60 μm silicon substrate. Notches were designed at the front end of the silicon substrate to match the free space waveguide to the waveguide loading the substrate. Due to the high dielectric constant ($\varepsilon_r = 11.8$) of silicon, two-stage rectangular notches were used to perform the transition, while for smaller dielectric constant material (i.e Quartz $\varepsilon_r = 5.8$), triangular taper notches were sufficient. Usage of silicon as the substrate, rather than the normally used Quartz, has several benefits in the design and fabrication. Firstly, the high ε_r of silicon substantially reduces the characteristic impedance of the slotline, hence becomes similar to the characteristic impedance of the microstrip line at the finline-to-slotline transition area. Secondly, the silicon material is more robust than the quartz material, reducing the chances of device breaking during the process of devices handling. Thirdly, trenches are allowed to be fabricated around the silicon device, so that the devices can be automatically separated after polishing

to the right thickness, easing the process of device separation and avoiding the potential damage to the delicate SIS junction during dicing.

3.3 Slotline-to-microstrip Transition

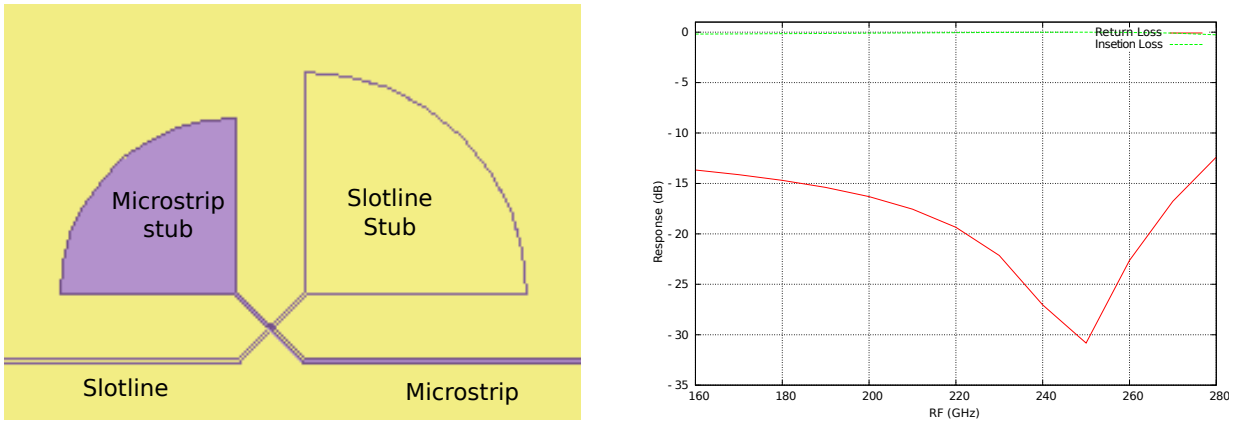

(a) (b)

Figure 3.6: (a) A drawing for the slotline-to-microstirp transition (b) HFSS calculated S-parameter performance for the transition.

The RF signal is coupled from the 2.5 μm width slotline at the end of the finline, to a 2.5 μm width microstrip by employing a double radial-stub structure fabricated across the dielectric layer. On top of the 2.5 μm slotline where the finline transition is terminated, a 490 nm SiO insulating layer and a 2.5 μm microstrip line is deposited with the microstrip on top of the insulator. This allows the RF power to be directly coupled from the slotline to the microstrip line, via the SiO layer. To optimise the coupling, the microstrip stub is terminated by an open-ended 90° quarter-wave radial stub, while the slotline is terminated by a short-ended 90° quarter-wave radial stub. According to the transmission line equation

$$Z_{\text{in}} = Z_0 \frac{Z_l + jZ_0 \tan\beta l}{Z_0 + jZ_l \tan\beta l} \tag{3.1}$$

the input impedance Z_{in} of a quarter wavelength transformer ($l = \lambda_g/4$) is Z_0/Z_l, where Z_0 is the characteristic impedance of the quarter wavelength transformer and Z_l is its load impedance. Thus a quarter wavelength transformer can transfer a short-ended circuit ($Z_l = 0$) into an open-ended circuit ($Z_{\text{in}} = \infty$) and vice versa. As both the microstrip/slotline radial stubs are designed to be $\lambda_g/4$ long, at the crossing point the short-ended slotline stub ends up as an open circuit, whilst the open-ended microstrip ends up as a short circuit. When the RF signal in the slotline propagates to the crossing

point, it sees an open-circuit in the slotline layer which stops its propagation. Then the signal is shorted to the microstrip layer and propagating in the microstrip line due to the $\lambda_g/4$ microstrip radial stub. This double-stub crossing design ensures the signal coupling from the slotline to the microstrip with the minimum mismatch. At the crossing point the minimum width of both the microstrip and the slotline, fabricated using photolithography, is only 2.5 μm. If the width of the slotline and the microstrip could be further reduced or the thickness of the SiO insulator could be further increased, better coupling would be obtained since the characteristic impedance of the slotline becomes more similar to the microstrip, making the matching easier. The 90° angles for both the slotline and microstrip radial stubs ensure that the RF signal is completely blocked at the end of slotline and shorted to the microstrip over the maximum RF bandwidth. The schematic diagram of the double radial-stub transition is illustrated in Fig 3.6 (a) and its simulated return loss is plotted in Fig 3.6 (b).

3.4 Tuning Circuit

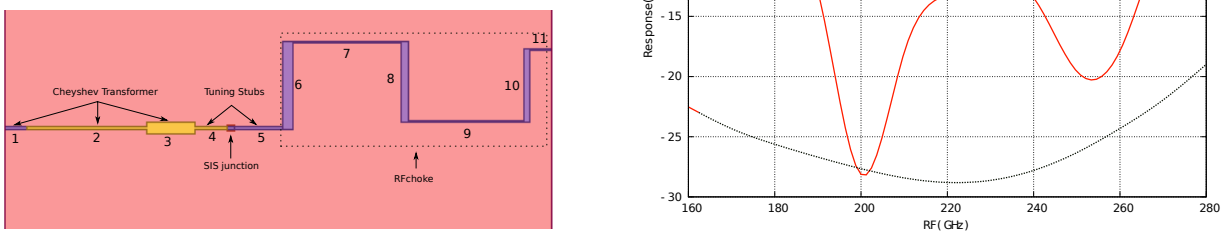

(a) (b)

Figure 3.7: (a) A schematic drawing of the tuning circuits. (b) The HFSS simulated performance of the tuning circuits.

The sandwich structure of the SIS junction presents an inherently parasitic capacitance of an order of 100 fF. The capacitance of this magnitude happens to short out the unwanted higher order harmonics produced by the SIS junction, but also short out the incoming RF radiation. Tuning circuits have therefore to be employed to tune out the capacitance over the desired RF bandwidth, as wide as possible. Kerr has predicted that the achievable bandwidth is determined by the $\omega R_n C$ product, if a

single microstrip stub tuner is applied [57]. From the previous experiences [57][58], we have developed a wide-RF band tuning circuit employing two microstrip stubs to tune out single SIS junction over 30% of the RF band. The schematic diagram for the tuning circuit and the HFSS simulated response are illustrated in Fig 3.7. The tuning circuit comprises three components: a three-stage Chebyshev transformer (stubs 1, 2, 3), double-stub inductive tuner strips before/after the SIS junction (stubs 4, 5) and an RF choke (stubs 6, 7, 8, 9, 10, 11). The procedure of the tuning circuit design has been constructed as follows:

- Design two inductive microstrip stubs (stub 4 and stub 5 in Fig 3.7 (a)) in series before/after the SIS junction to tune out the junction capacitance sharply at two frequency poles, ω_1 and ω_2, around the central frequency $\omega_0 = 230$ GHz. The double-stub tuning broadens the RF bandwidth compared to the single-stub tuning. Stub 4 with length l_4 tunes out the capacitance C_{J} at frequency $\omega_1 > \omega_0$, that $\tan\beta l_4 = Z_0\omega_1 C_{\mathrm{J}}$, where Z_0 is the characteristic impedance of stub 4 which is normally chosen to approach the normal resistance of the junction and C_J is the junction capacitance.

- Stub 5 is located after the SIS junction with the same characteristic impedance Z_0. Stub 5 tunes out any residue capacitance left by stub 4 and the SIS junction at frequency $\omega_2 < \omega_0$, by forcing the imaginary part of the source impedance Z_s at frequency ω_2 to be zero:

$$Z_{\mathrm{in}} = Z_0 \frac{Z_l + jZ_0 \tan\beta l_5}{Z_0 + jZ_l \tan\beta l_5} \tag{3.2}$$

  where Z_l is the output impedance of the combination of stub 4 and the SIS junction at frequency ω_2, and βl_5 is the electric length of stub 5. With the knowledge of Z_0 and Z_l, $\tan\beta l$ could be easily calculated. Z_0 and $\tan\beta l$ can be easily transferred to width and length of the microstrip line. By connecting both inductive tuners to the SIS junction, the imaginary part of Z_{in} would pass through zero at frequency $\sim \omega_1$ and $\sim \omega_2$.

- A Chebyshew or quarter wavelength transformer is then designed to match the output impedance of the slotline-to-microstrip transition to Z_{in}.

- A six-stage RF choke made of low and high alternating impedance is designed after the tuning circuit to block the RF signal from leaking into the IF port of the SIS mixer. The RF choke ensures no RF power leaking to the IF port, while maintaining the maximum signal transition in IF band. The six-stage RF choke could be cut down to four-stage to reduce the output inductance so as to maximize the IF bandwidth, with a little sacrifice on the SIS junction coupling, while

a two-stage RF choke could further increase the IF bandwidth but reduces the RF coupling performance to an unacceptable level.

- Finally, the tuning circuit design is tailored and optimized by HFSS, while taking the superconducting surface impedance and other electromagnetic factors into account. The double-stub tuning circuit offers a return loss pattern with two dips resonating before and after 230 GHz with an RF bandwidth of over 30%.

3.5 Bonding Pads

The IF signal carried by the RF choke is transmitted to the bonding pads. Three bonding pads located at the rear of the SIS device are used to conduct the IF signal to the Duroid 6010 IF transformer by bonding wires. The signal bonding pad (the central pad in Fig 3.8(a), dimension: 0.25 mm×0.35 mm) is connected to the wiring layer of the microstrip while the ground bonding pads (the side pads in Fig 3.8(a)) are connected to the ground plane. The signal bonding pad is bonded to the IF board and the ground bonding pads are bonded to the mixer block, both through bonding wires (bonding wire diameter: 25 μm, average length: 200 μm). The gap between the signal bonding pad and the ground bonding pad, W_{gap} (see Fig 3.8(a)), is carefully simulated to minimize the IF mismatch between the last stage RF choke and the aluminum bonding wires. For the widest possible IF bandwidth, the inductance brought by the aluminum bonding wires should be kept as small as possible, to reduce the impedance mismatch between the mixer and the 50 Ω LNA, therefore the bonding wires should be as short as possible. If possible, multi bonding wires should be bonded simultaneously to reduce the inductance. The HFSS simulated S-parameters for the bonding pad and the schematic drawing are shown in Fig 3.8.

3.6 Full Device

All the components mentioned above (excluding the bonding pad), are combined together to form a complete SIS mixer chip, and is simulated as a 3-D full wave model in HFSS as function of RF and IF frequency. Subtleties are taken into account in the final simulation, such as the superconductive surface impedance, the curvature in the SiO layer around the junction, the radiation shield for the waveguide air box and the bending of the stepped RF choke. The whole mixer device, including the bonding pads and the finline serrations, is schematically shown in Fig 3.9, with the critical dimensions tabulated in Tab 3.1. The HFSS simulated S-parameter performances in both RF and IF band are shown in Fig 3.10. The mixer shows good RF performance over 80 GHz RF bandwidth. We would like

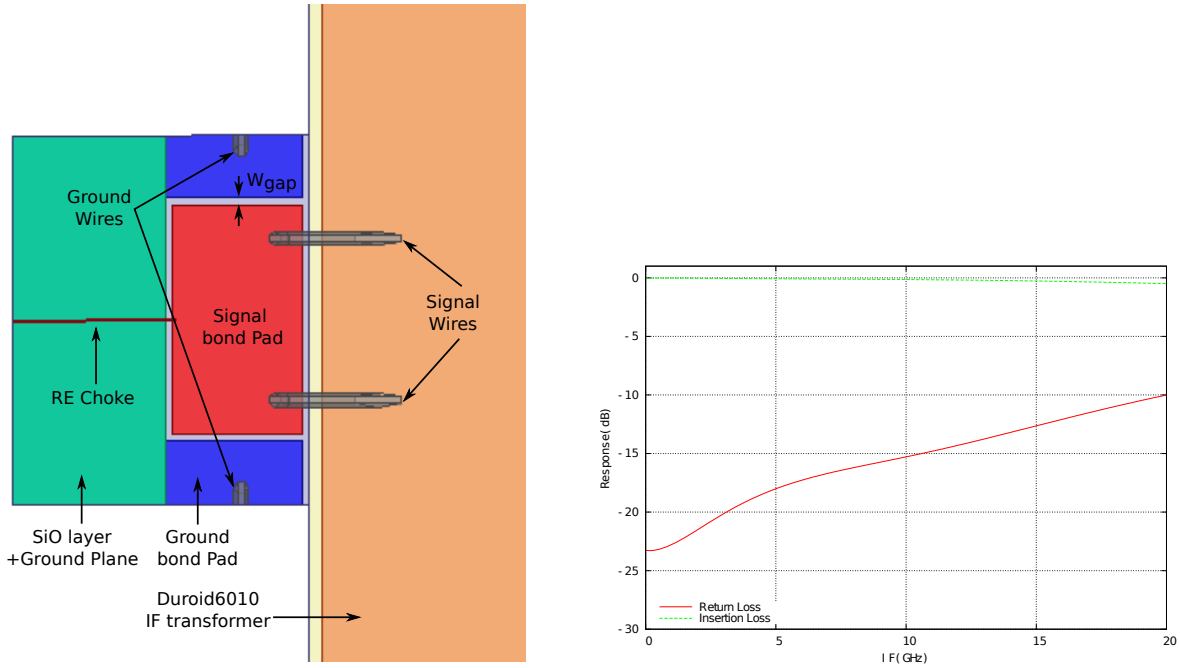

(a) (b)

Figure 3.8: (a) A schematic view of the bonding pad at the rear of the mixer chip. (b) The HFSS simulated performance for the bonding pad as a function of IF band.

to emphasize however that the IF performance of the mixer is not determined by the plots given in Fig 3.10(b) alone since the chip output impedance is not matched to the amplifier with the matching circuit fabricated on the IF board yet. In Fig 3.11 we show the IF performance of the mixer optimized between 2 - 6 GHz. In the IF plot in Fig 3.10 (b), we notice the evidence of a resonant circuit whose resonance frequency is at 8 GHz. The influence of the 8 GHz resonance on the mixer performance is investigated in details in Chapter 5.

	TranA	TranB	TranC	Tuner1	Tuner2	ChokeA	ChokeB	ChokeC
width/length	2.2/150	6.38/172	14.8/68.7	2.5/52	2.5/75	14.25/120	2.2/154	11/110
	ChokeD	ChokeE	ChokeF	Notch1	Notch2	Serration	Slot	
width/length	2.2/165	9.48/100	2.5/30	300/300	500/247	63.3/105.4	2.6/160	
	SlotStub	MicroStub						
radius/angle	171/90°	136/90°						

Table 3.1: Dimensions for mixer design. Dimensions are in unit of μm.

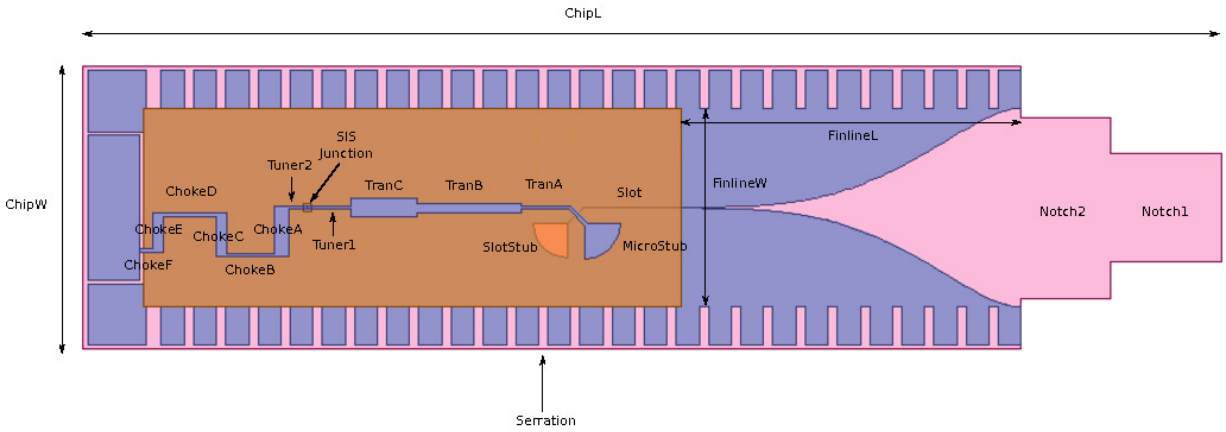

Figure 3.9: A schematic drawing for the whole device, including the bonding pad and the serrations. For the convenience of display, the planar circuit components in the figure are not to scale. The thickness of the silicon substrate is 60 μm, of the SiO dielectric layer is 490 nm, of the signal layer is 400 nm and of the ground layer is 250 nm.

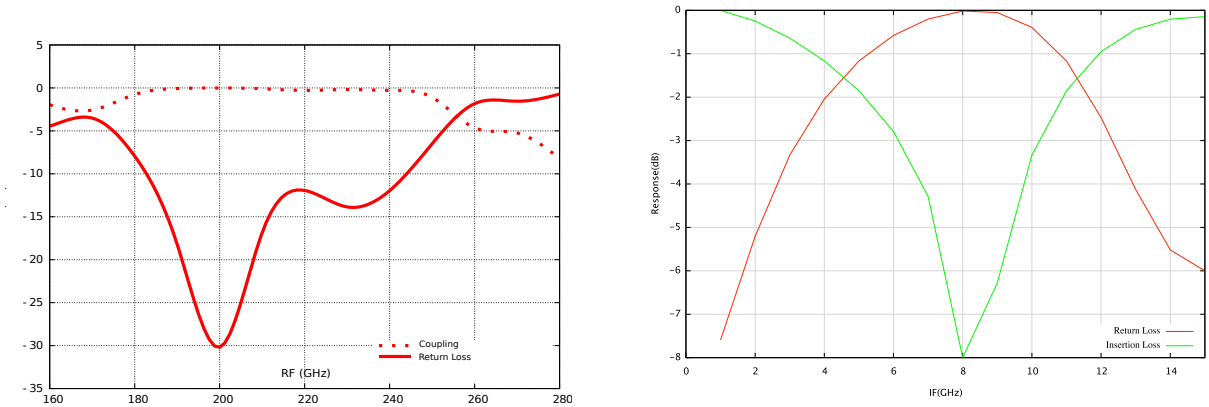

(a) (b)

Figure 3.10: (a) The HFSS simulated performance for the full mixer chip in the RF band. (b) The HFSS simulated performance for the full mixer chip in the IF band.

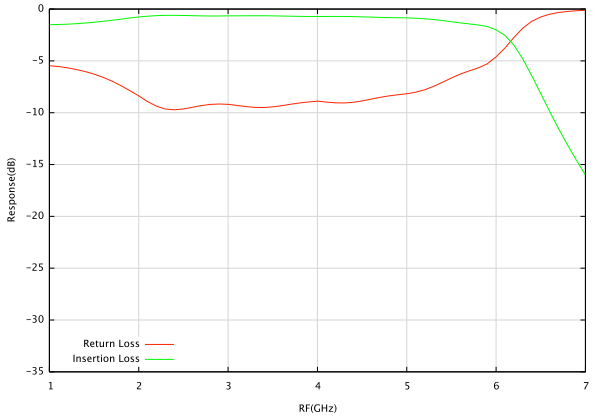

Figure 3.11: The HFSS simulated IF performance for the device incorporating an IF transformer. The performance over IF bandwidth 2 - 6 GHz was optimized by the IF transformer.

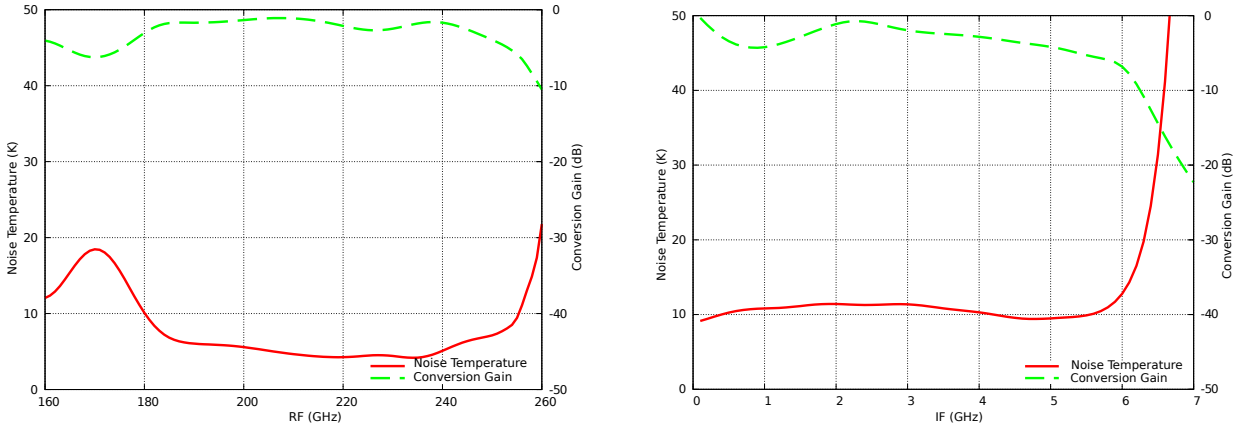

(a) (b)

Figure 3.12: (a) The SuperMix simulated RF performance for the finline SIS mixer device. The bias voltage (2.55 mV), LO power (80 nW) and IF frequency (2 GHz) has been optimized to obtain the best RF performance. (b) The SuperMix simulated IF performance for the finline mixer device incorporating an IF transformer, that optimizing the performance over bandwidth 2 - 6 GHz.

To complete the mixer design, the rigorous HFSS electromagnetic designs described above were then exported into the quantum mixing software SuperMix to predict the mixer gain and noise temperature. In Fig 3.12 we present the SuperMix simulation results in both RF and IF band. The SuperMix predicts conversion gains above -2 dB and reasonably low noise temperatures across most of the RF band. And SuperMix predicts an optimized IF performance over bandwidth 2-6 GHz, with the incorporation of an IF transformer.

Chapter 4

SIS Mixer RF performance tests

Overview: This chapter focuses on the experimental investigation of SIS finline mixers operating around 230 GHz. The experimental setups are described and the techniques for assessing and analyzing the RF performance of the mixers are discussed. Two separate and independent test systems were employed through the mixer testing: a wet cryostat system and a G-M (Gifford-McMahon) cooler system. The RF tests for several representative devices are presented and analyzed. The receiver noise temperatures are broken down to different contributions from various components in the receiver chain to highlight the performance of each component and facilitate the improvement of the mixer. HFSS (a 3-D electromagnetic simulation software) simulations were performed to predict the mixer performance. The simulations are compared with the experimental results, to investigate the influence of different parameters of the SIS mixer, e.g normal resistance, substrate thickness, etc. on the mixer performance. The embedding admittance was also recovered across the RF band to examine the performance of the tuning circuit. Most of the tested devices showed promising performance. For the best device, a lowest noise temperature of 50±2 K was measured at 219 GHz and an averaged noise temperature of 75 K was measured over RF bandwidth 162 GHz - 258 GHz.

4.1 SIS mixer testing system

The testing apparatus comprises the following subsystems: 1) an optical system to inject the LO and hot/cold load RF signals into the SIS mixer, 2) a wet cryogenic Dewar or a mechanical cooler to cool the SIS mixer and other cold electronics, 3) a room temperature IF amplifier chain and an IF power detection system, 4) a data acquisition system, 6) the control electronics.

Two independent cryogenic systems have been used to cool the SIS mixer and other cold electronics : 1) a Wet Dewar, 2) a G-M cooler system (GUBBINS). The essential equipment used in these two

systems are slightly different, as shown in Tab 4.1. In the tests carried out in the Wet Dewar, both the double-ended and single-ended mixer blocks had been used to hold the SIS mixer devices and both the GUBBINS multiplier chain LO and the Gunn LO were used as the LO sources. In addition, the LO power was coupled to the SIS mixer through the reflection of a Mylar beamsplitter. In the GUBBINS system, only the double-ended mixer block was used to hold the mixer and only the GUBBINS LO was employed as an LO source. A waveguide LO coupler which was mounted inside the mixer block coupled the LO power into the SIS mixer in the GUBBINS system.

	Wet Dewar	GUBBINS system
Mixer Block	Double-ended / Single-ended block	Double-ended block
LO Source	GUBBINS LO / Gunn LO	GUBBINS LO
LO Coupling	Mylar Beamsplitter	LO Coupler

Table 4.1: An overview of the essential equipments used in either the Wet Dewar or in the GUBBINS system

4.1.1 The experimental Setup in the Wet Dewar

The schematic layout of the testing setup in the Wet Dewar is shown in Fig 4.1. The Wet Dewar itself and inner working area are shown in Fig 4.2. The wet cryogenic Dewar houses all the cold electronics and the SIS mixer block assembly, which are all attached to the 4.2 K cold plate.

The LO radiation is focused into the smooth-walled horn of the SIS mixer block using two off-axis parabolic mirrors. The Gunn LO source comprises a Gunn oscillator operating in range of 72–85 GHz, driving a varactor tripler, giving a final operating band of 215–255 GHz of average power 100–500 mW. A mechanical modulator is placed between the Gunn and the varactor tripler, allowing the power output to be continuously controlled without detuning the system. A second LO source we used (GUBBINS multiplier chain LO) is a $\times 18$ (3×6) frequency multiplication chain LO which is driven by an external RF power generator operating around 10.8–14.5 GHz, and producing $\sim$150 mW LO power in the range of 195–260 GHz. A mechanical modulator is placed between the $\times 3$ and $\times 6$ multiplier to control the amplitude of the output LO power.

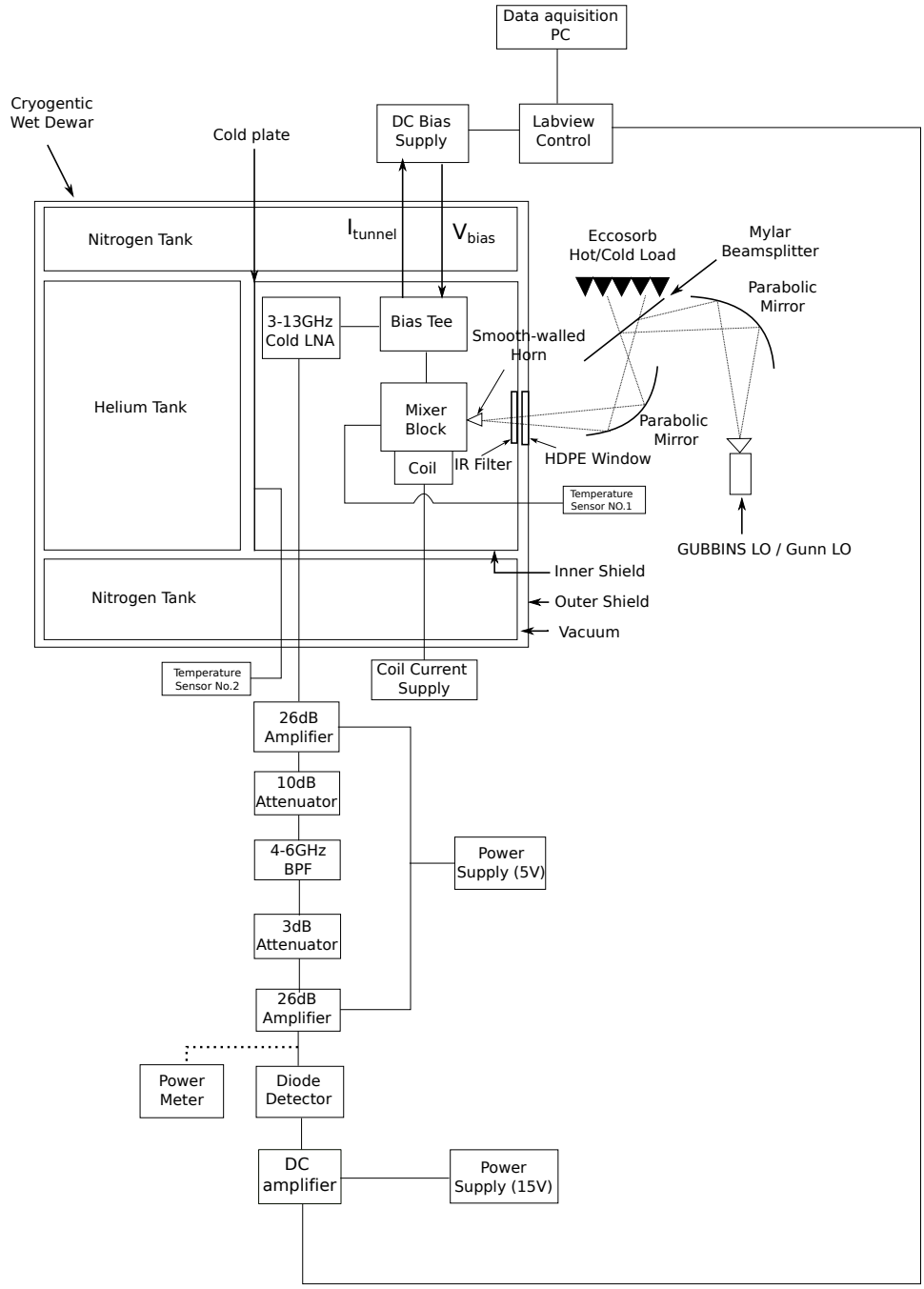

Figure 4.1: Block diagram showing the experimental setup for testing the behavior of the mixer in a wet cryogenic Dewar. The cold load is made of an open bucket filled with liquid nitrogen and lined with Eccosorb AN-72 microwave absorber. The hot load is provided by blocking the cold load with a few layers of stacked Eccosorb at room temperature.

In the mixer tests, the RF signal and the LO beams are incident from orthogonal directions on a Mylar beamsplitter which intersects both beams at 45°, directing the RF and LO beam into the mixer feed (Fig 4.2 (a)). The percentage of the RF power transmitted through the beamsplitter depends

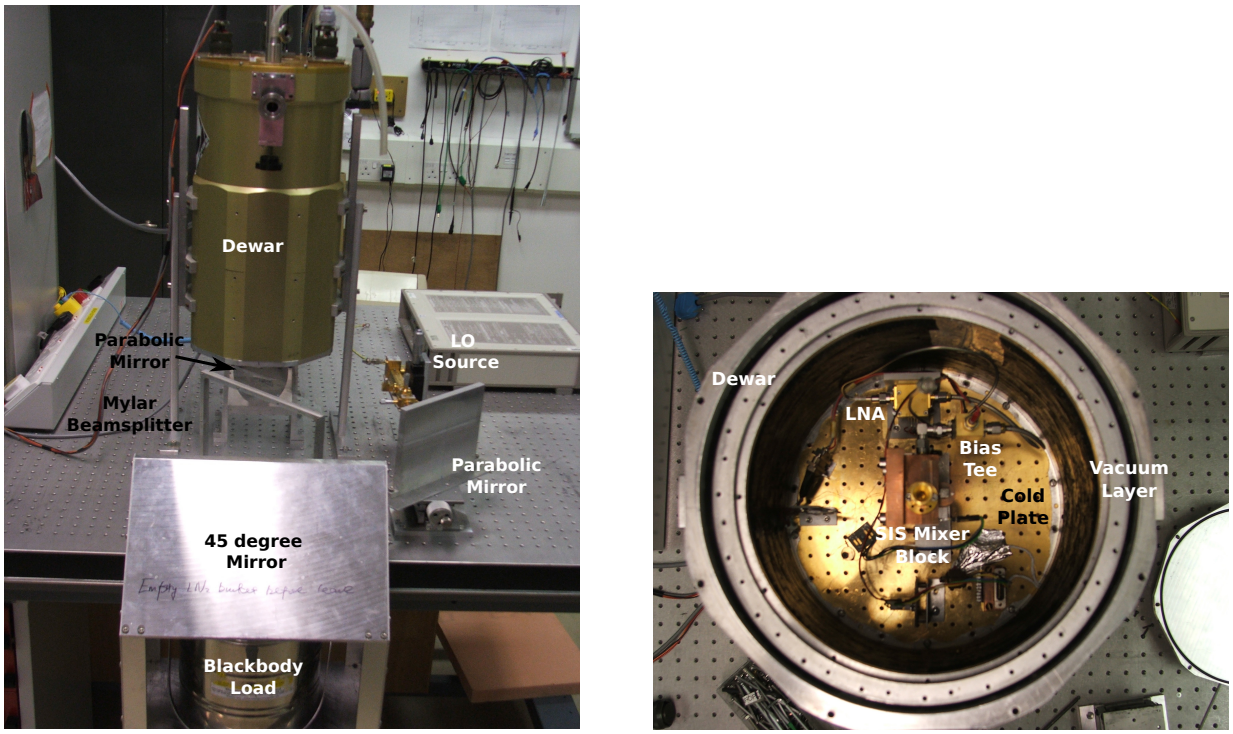

(a) (b)

Figure 4.2: (a) The experimental layout for measuring the noise characteristics of an SIS finline mixer. (b) Working area inside the Dewar.

on the thickness of Mylar beamsplitter, which is generally around a few tens of microns. A thicker beamsplitter reflects more LO power into the mixer, but also reflects more LO noise into the mixer. In addition, a thicker beamsplitter would also reflect or absorb more RF hot/cold load signal, which would increase the optical losses. Therefore a thicker beamsplitter would lead to a higher receiver noise temperature. The transmission losses for Mylar beamsplitters with various thicknesses are plotted as a function of RF frequency in Fig 4.3.

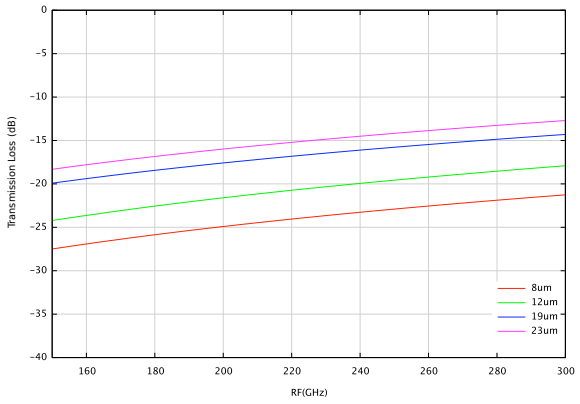

Figure 4.3: Transmission losses of Mylar beamsplitters with various thickness.

Before being coupled to the feed horn of the SIS mixer block, the combined RF and LO signals from the Mylar beamsplitter pass through a LD 45 Zotefoam® vacuum window mounted on the outer shield of the Wet Dewar, and then three layers of Zitex® PTFE G-110 IR filters mounted on the inner shield to reduce the heat load of the cold plate. The SIS mixer block is mounted on a copper L-shaped bracket and tightly bolted to the cold plate. Both the double-ended and single-ended mixer blocks were employed in the Wet Dewar. The finline mixer device (Fig 4.4) is mounted inside the mixer block. Two Lakeshore temperature sensors are respectively mounted on the cold plate and the mixer block to monitor the temperature variations during the experiment. The mixer tests performed in the Wet Dewar were undertaken with a block temperature of 4.6 K.

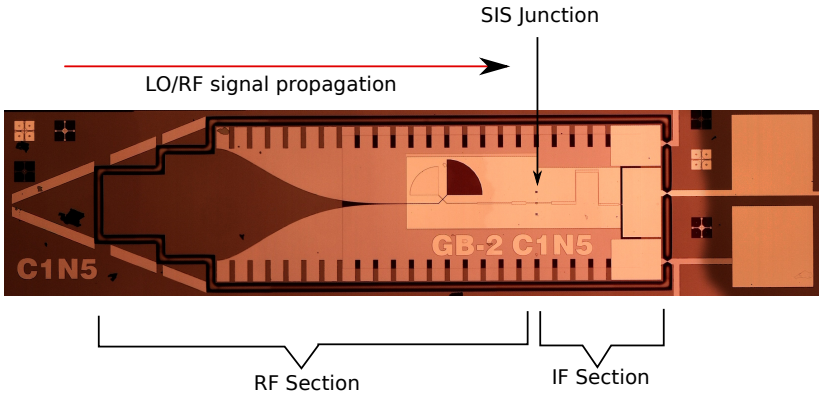

Figure 4.4: A picture of a SIS mixer device. The direction of LO/RF signal propagation is indicated by an arrow. All the planar circuits prior to the SIS junction belong to the RF section and all the circuits after the SIS junction belong to the IF section.

The IF output of the SIS mixer block connects to a commercial bias tee, which supplies the DC bias voltage for the SIS mixer. The IF signal is then amplified by a 3-13 GHz LnP LNA (Low Noise Amplifier) supplied by S.Weinreb in Caltech (Batch Number: 111-CIT-4254-077) [81]. The performance of the LNA provided by the manufacture is shown in Fig 4.5. The average noise temperature (NT) of the LNA within IF band 4-12 GHz is ∼4 K, and the gain is ∼35 dB. The noise temperature (NT) over IF band 4-6 GHz (the most frequently used IF bandwidth in the mixer tests) is below 3 K at ambient temperature of 9 K.

Attenuators were used in the warm IF chain to prevent saturating the warm IF amplifier and also to ensure that the diode detector was operated within its most linear region (<-25 dBm). To investigate the IF performance of the SIS mixer, IF bandpass filters with bandwidth 3-4 GHz, 3.75-4.25 GHz and 4-6 GHz were used in the testing (See Chapter 5). The IF power was measured as a function of the bias voltage by the data acquisition PC, sweeping in the range of -10 mV and 10 mV with a sweeping

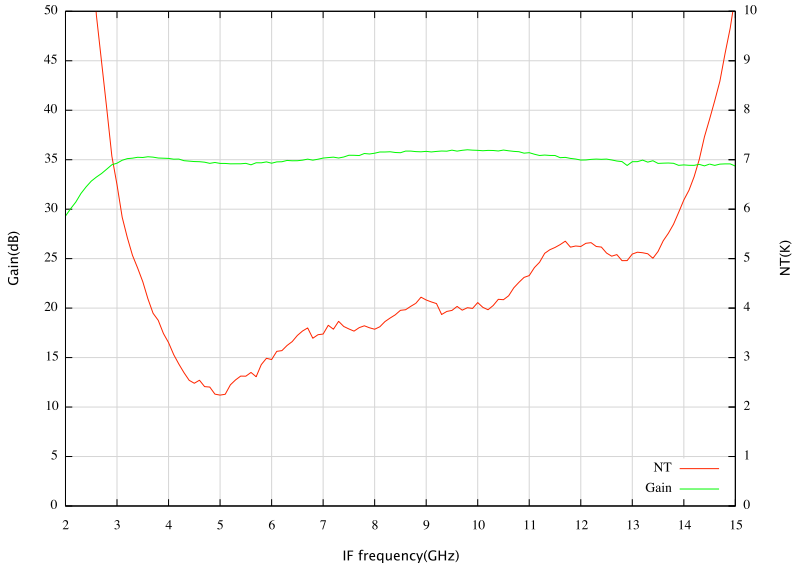

Figure 4.5: The expected noise temperature and gain measured for the LNA at ambient temperature of 9 K [81].

frequency of ∼20 Hz. The LO power level and the magnetic field were adjusted by observing the DC current and IF output power as a function of the bias voltage. The Y-factor measurement was accomplished by recording the IF output power against the bias voltage with either hot or cold loads placed in front of the Dewar window.

4.1.2 The experimental setup in the GUBBINS cryostat

The schematic layout for the experimental setup of GUBBINS system is shown in Fig 4.6 and the mixer block assembly is shown in Fig 4.7. The double-ended mixer block is used in the GUBBINS system. The LO radiation is coupled to the SIS mixer through an LO horn and an internal LO waveguide coupler. The RF radiation is coupled to the SIS mixer through a horn reflector antenna. The LO horn and the RF horn are placed on either side of the mixer block. The LO horn is a smooth-walled horn and the RF horn is a corrugated horn. The IF output connects to the bias tee and then is amplified by a broad band LNA. All the cold electronics and the SIS mixer block assembly are mounted on copper brackets, which are connected to the 4 K stage of the G-M cooler. The mixer tests performed in the GUBBINS system were taken at a temperature below 4.0 K. More information concerning GUBBINS system can be found in Chapter 6.

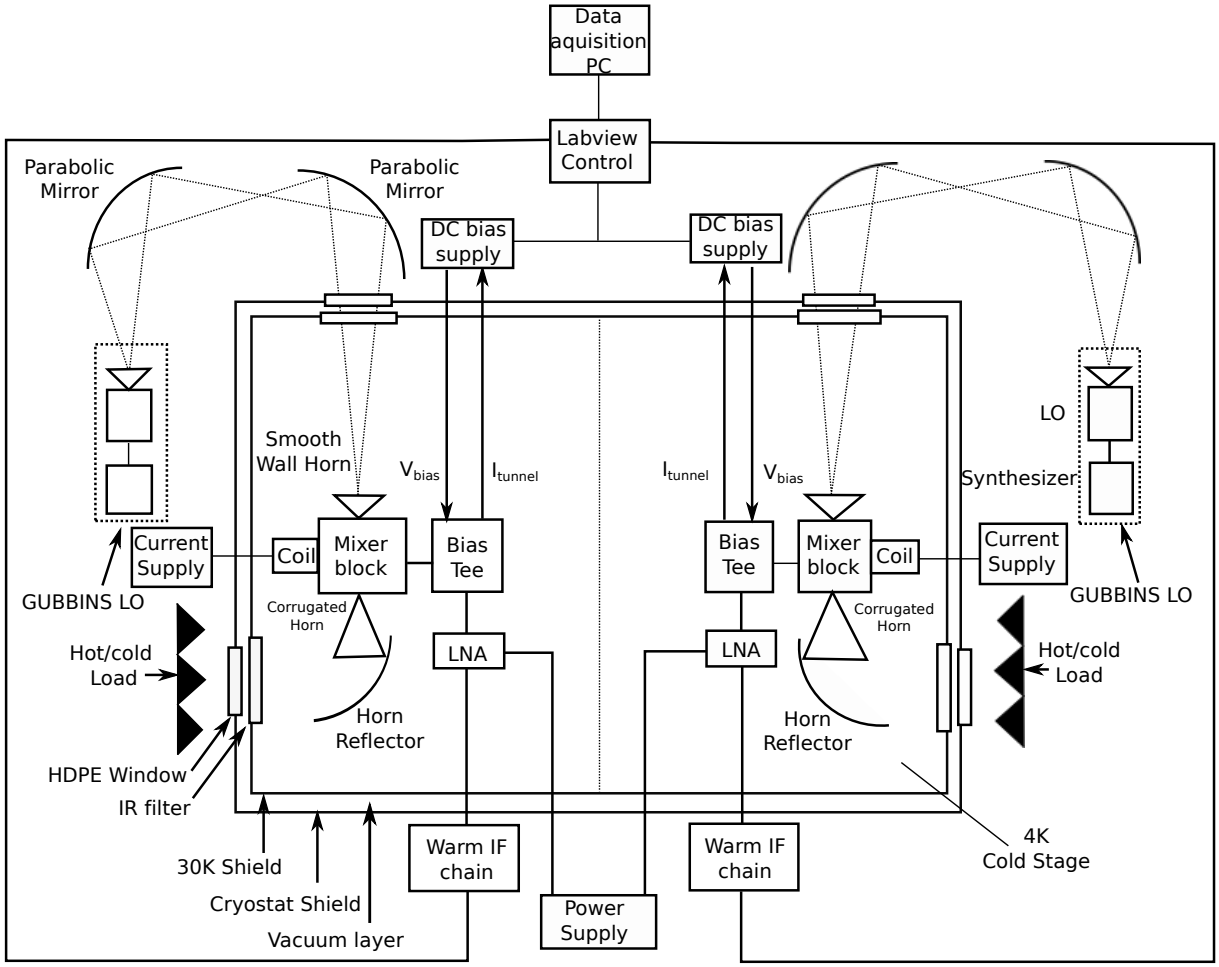

Figure 4.6: A block diagram showing the experimental setup of the GUBBINS system. The double-layer black frame denotes the cryostat, housing the G-M cooler and two identical SIS mixer receivers located in the left and right channels. These two channels are separated by a dashed line in the picture. For convenience of display, optical mirrors for coupling the LO radiation into the SIS mixers are rotated by $\pm 90^{\circ}$ clockwise into the paper.

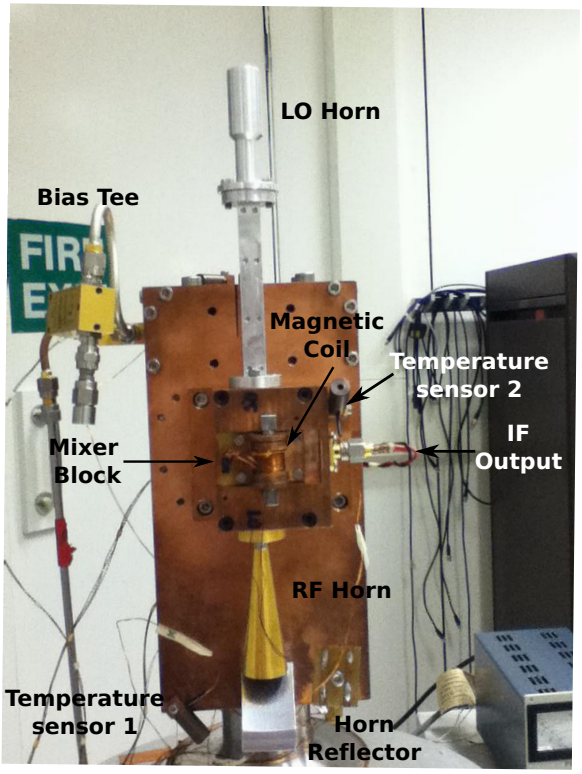

Figure 4.7: The assembly of SIS mixer block in GUBBINS system.

4.1.3 The mixer Block

The Double-ended mixer block was designed by Dr. Paul Grimes [44] and fabricated at the School of Earth and Space Exploration, Arizona State University, using a six-axis Computer Numerical Control micro-machine [85]. The block was split into two halves along the E-plane of the rectangular waveguide for ease of fabrication (Fig 4.8). The waveguide was a standard WR-4 type (1.1 mm height and 0.55 mm width) with grooves (0.25 mm height and 0.25 mm width) recessed on both side walls of the waveguide in the lower half block, to support the silicon substrate of the SIS mixer. In Fig 4.9 (b), we show an example of a silicon device mounted in the mixer block. The substrate, which carries the mixer chip, is located in the E-plane of the waveguide near the rear end. Aluminum bond wires (diameter: 25μm) are used to connect the signal bonding pad to the IF transformer. To form a good thermal and mechanical contact between the device and the block, we used both crystal bond and superglue to hold the mixer chip in the block.

The waveguide layout in the bottom half of the mixer block is shown in Fig 4.9 (a). The LO and RF signals are fed to the SIS mixer block through separate waveguides, before the LO signals being coupled to the RF signal by a directional waveguide coupler. This -17dB directional coupler [44] uses three 0.4 μm thick gold radial probes connected by suspended stripline deposited on 65 μm thick

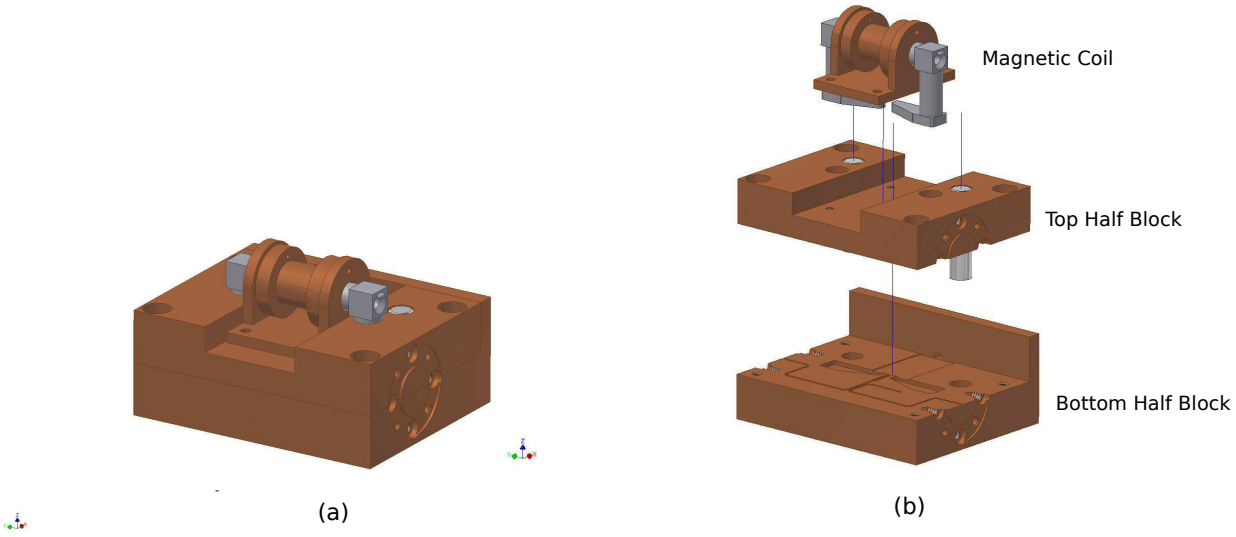

Figure 4.8: (a) A CAD model of double-ended block, enclosing a unilateral finline mixer. (b) A CAD model of exploded double-ended block [44].

quartz chips to couple power between the waveguides (Fig 4.10). Each chip and suspended stripline are approximately one quarter wavelength long. The chips were glued into shallow slots between the waveguides, spaced at quarter wavelengths along the waveguides. At the end of the LO waveguide, there is a wedge shaped Eccosorb MF 12 load to absorb the uncoupled LO signals. The mixer block also holds an IF transformer board used to transform the complex output impedance of the SIS mixer to the 50 Ω input impedance of the IF amplifier. The IF transformer circuits were fabricated on 0.254 mm thick RT/Duroid 6010 PCB board. A magnetic coil mounted on the surface of the SIS mixer block supplied the magnetic field to suppress the Josephson tunneling current. A 'butterfly-wing' structure (Fig 4.8) is used to hold the magnetic shoes, that could direct the magnetic field from the coil to the SIS junction.The coil was made from 2000 turns of 50 μm diameter copper-clad NbTi superconducting wire on a former of 7.0 mm diameter [82]. The magnetic coil was able to supply a magnetic field as much as 200 mA, which is sufficient to sweep the tunnel junction through several Josephson nulls. The second magnetic null was usually chosen to maintain a balance between the SIS junction nonlinearity and the stable operation of the SIS mixer Josephson tunneling.

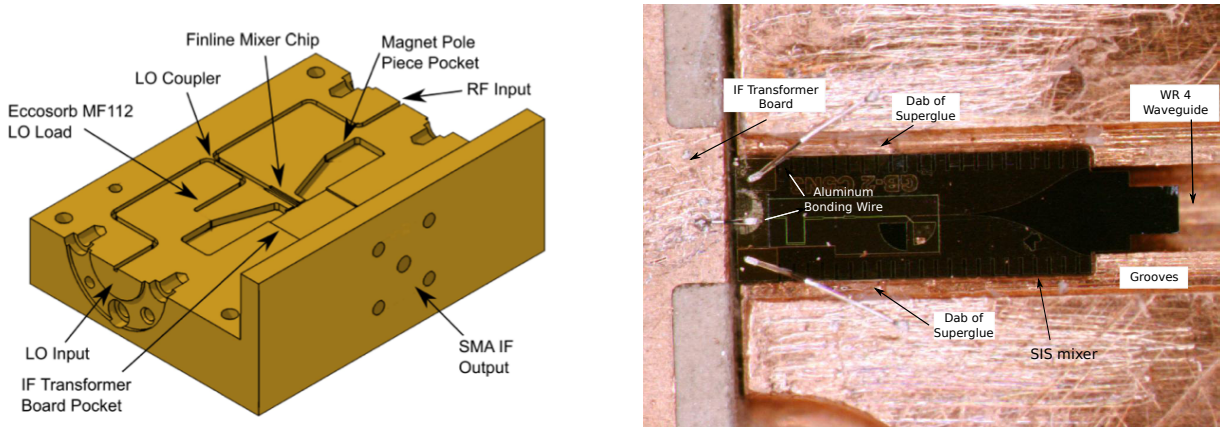

(a) (b)

Figure 4.9: (a) The waveguide layout in the bottom half of the double ended block [42]. (b) Photo showing the mixer chip sitting in the groove of the waveguide inside the mixer block. One bond wire connected the mixer chip bonding pad to the IF transformer. Another two bond wires connected the mixer chip ground pads to the block.

Figure 4.10: The LO directional waveguide coupler sitting in the shallow slot between the LO signal waveguide and the RF signal waveguide.

4.2 Y-factor Measurement

4.2.1 Receiver noise temperature

A direct way of quantifying the sensitivity of an SIS mixer receiver is to measure the noise power (P_{rec}) generated by the mixer device and the mixer conversion gain (G_{mix}). The noise power (P_{rec}) is related to its equivalent noise temperature (T_{rec}) by $P_{\mathrm{rec}} = k_{\mathrm{B}} T_{\mathrm{rec}} B$, where B is the bandwidth of the receiver and k_{B} is the Boltzmann constant. The noise power P_{rec} can be determined from the receiver output powers measured at two input power levels P_h and P_c, corresponding to two loads temperatures T_h and T_c respectively:

$$P_{\mathrm{rec}} = \frac{P_{\mathrm{h}} - YP_{\mathrm{c}}}{Y-1} \tag{4.1}$$

or equivalently

$$T_{\mathrm{rec}} = \frac{T_{\mathrm{h}} - YT_{\mathrm{c}}}{Y-1} \tag{4.2}$$

where $Y = P_{\mathrm{h}}/P_{\mathrm{c}}$ is the ratio of the two output powers. In the Rayleight-Jeans (R-J) approximation, the thermal noise temperature radiated by the blackbody at physical temperature T can be approximated as T, if $h\nu/k_{\mathrm{B}}T \ll 1$. The two input power sources in our case were matched to blackbody loads at ambient temperature T_{h}=293 K (room temperature) and at T_c=77 K (the boiling point of liquid nitrogen). Both blackbody loads satisfy the $h\nu/k_{\mathrm{B}}T \ll 1$ condition, therefore Rayleigh-Jeans approximation can be applied. However if the blackbody loads with much lower temperature, which violate the $h\nu/k_{\mathrm{B}}T \ll 1$ condition, other more accurate expressions should be used to relate the noise temperature and the physical temperature (Chapter 7).

4.2.2 Noise temperature of the receiver chain

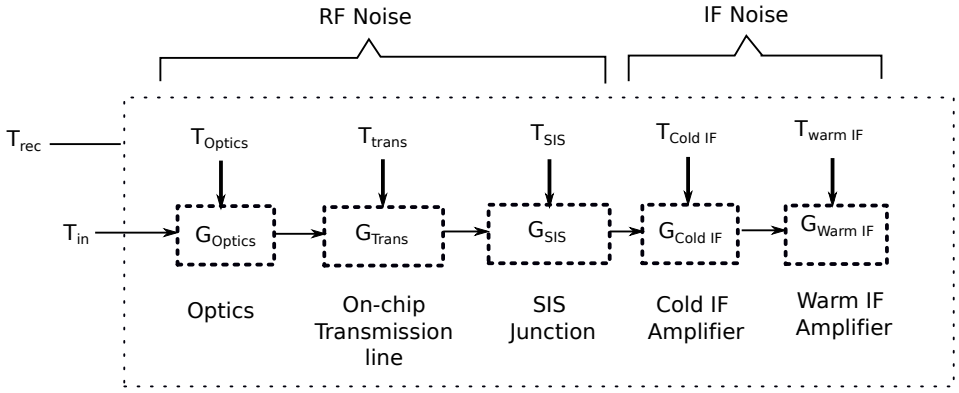

Figure 4.11: Cascaded components used to analyze the noise contribution of the mixer receiver. T_{x} and G_{x} respectively denote the equivalent noise temperature and gain added by each component. T_{rec} is the total equivalent noise temperature contributed by all the components in the receiver shown in the above frame. T_{in} is the noise temperature of the matched RF load (T_{h} or T_{c}). The IF transformer which would be discussed in Chapter 5 is included in the Cold IF block.

The receiver noise T_{rec} measured by the Y-factor method does not only include the noise contributed by the SIS junction, but also include the optical loss, the transmission lines loss and the IF loss of the receiver. To understand the noise contribution from various components, we break down the receiver noise T_{rec} into the contribution of various components. For a receiver chain consisting of noisy electrical components, the receiver noise temperature can be expressed by Friis formulae for noise [35],

$$T_{\rm rec} = T_1 + \frac{T_2}{G_1} + \frac{T_3}{G_1 G_2} + ... + \frac{T_{\rm N}}{G_1 G_2 ... G_{\rm N-1}} \tag{4.3}$$

where T_1, $T_2 ... T_{\rm N}$ and G_1, $G_2 ... G_{\rm N}$ are the noise temperature and the gain of each component respectively, assuming the impedance matches between each component are perfect. For passive component the effective noise temperature is given as $T = (\frac{1}{G} - 1)T_{\rm phys}$, where $T_{\rm phys}$ is the physical temperature and G is the gain of the passive component which is usually smaller than unity. The receiver noise temperature $T_{\rm rec}$ for SIS receiver can therefore be written as,

$$T_{\rm rec} = (1/G_{\rm optics} - 1)T_{\rm phys} + \frac{T_{\rm trans}}{G_{\rm optics}} + \frac{T_{\rm SIS}}{G_{\rm optics} G_{\rm trans}} + \frac{T_{\rm IF}}{G_{\rm optics} G_{\rm trans} G_{\rm SIS}} + \frac{T_{\rm hotIF}}{G_{\rm optics} G_{\rm trans} G_{\rm SIS} G_{\rm IF}} \tag{4.4}$$

The noise contributed by the warm IF amplifier $\frac{T_{\rm hotIF}}{G_{\rm optics} G_{\rm trans} G_{\rm SIS} G_{\rm IF}}$ can be ignored, if the cryogenic LNA provides a very large gain (i.e $G_{\rm IF}$>30 dB) and the warm IF amplifier has a reasonably low noise temperature (i.e $T_{\rm hotIF}$<500 K). As indicated in Fig 4.11, the RF noise is contributed from various optics components (i.e the Mylar beamsplitter, the Dewar window, the optical horn), the transmission lines and the SIS junction. The loss of the Mylar beamsplitter can be calculated using the analysis described by [40] where the beamsplitter is treated as a Fabry-Perot interferometer. The transmission loss of the Mylar beamsplitters with various thickness are plotted in Fig 4.3. The loss of the Dewar window is mainly due to the absorption in the LD 45 Zotefoam window and the Zitex layers, which is assumed to be -30 dB at 230 GHz. The noise contribution of the transmission lines is ∼0.2 dB/mm [98] at 230 GHz. The noise contribution of the SIS junction is caused by the shot noise due to the tunneling of quasiparticles across the SIS junction and the thermal noise that includes the zero-point fluctuation [55]. To calculate the noise contribution from the tunnel junction, we need to use Tucker quantum theory described in Chapter 2. For a good and well designed SIS mixer, the noise contribution of the SIS junction should be comparable to the quantum limited noise $h\nu/k_{\rm B}$, where ν is the LO frequency. The IF noise is contributed from various amplification stages, other IF components which are after the junction, i.e the IF board, the isolator, etc. and of course the IF mismatch.

There exist several techniques for estimating the noise contribution of the RF and IF components from experimental measurements, which we shall describe below [75][94].

4.2.3 Determination of the RF Noise Contribution

To distinguish between the RF and IF contributions, Eq 4.4 can be simplified as,

$$T_{\mathrm{rec}} = T_{\mathrm{RF}} + \frac{T_{\mathrm{IF}}}{G_{\mathrm{RF}}} \tag{4.5}$$

where

$$T_{\mathrm{RF}} = (1/G_{\mathrm{optics}} - 1)T_{\mathrm{phys}} + \frac{T_{\mathrm{trans}}}{G_{\mathrm{optics}}} + \frac{T_{\mathrm{SIS}}}{G_{\mathrm{optics}}G_{\mathrm{trans}}} \tag{4.6}$$

The IF output power per unit bandwidth of the receiver chain can be written as,

$$P_{\mathrm{out}} = k_{\mathrm{B}}(T_{\mathrm{rec}} + T_{\mathrm{in}})G_{\mathrm{RF}}G_{\mathrm{IF}} \tag{4.7}$$

where $G_{\mathrm{RF}} = G_{\mathrm{optics}}G_{\mathrm{trans}}G_{\mathrm{SIS}}$ is the mixer conversion gain and G_{IF} is the equivalent gain in the IF amplifier chain. T_{in} is the temperature of a matched load placed at the receiver input (this may be T_{h} or T_{c}) and k_{B} is the Boltzmann constant. Substituting for T_{N} yields,

$$P_{\mathrm{out}} = k_{\mathrm{B}}(T_{\mathrm{RF}} + T_{\mathrm{in}})G_{\mathrm{RF}}G_{\mathrm{IF}}B + k_{\mathrm{B}}T_{\mathrm{IF}}G_{\mathrm{IF}}B \tag{4.8}$$

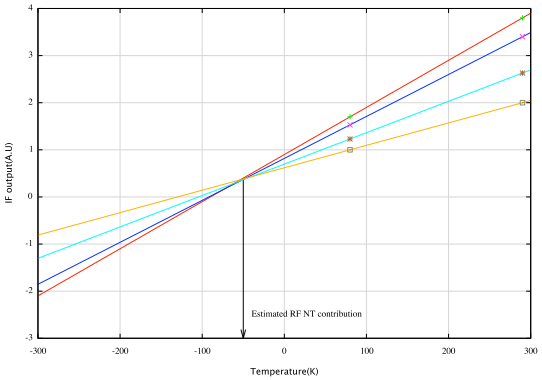

Figure 4.12: The intersecting line method for estimating the contribution of RF losses to the mixer noise temperature for device C3N1 at frequency 208.8 GHz. IF power data is taken for hot and cold loads at several IF power levels.

Eq 4.8 states that if P_{out} is plotted as a function of T_{in}, a straight line is obtained with a slope proportional to G_{RF}, hence proportional to the conversion gain of the SIS mixer G_{SIS}. Calculations based on Tucker's theory of mixing indicates that large variations in mixer conversion loss can be induced by simply changing the local oscillation (LO) drive level. Furthermore, it can be shown that under reasonable LO drive condition, T_{M} is varying very slowly as a function of LO drive. We has investigated the variation of the mixer noise and conversion gain theoretically in Fig 2.16. Additionally $k_{\mathrm{B}}T_{\mathrm{IF}}G_{\mathrm{IF}}$ is independent of the applied LO power. Thus by defining a straight line for P_{out} using T_{in} equal to either 77 K (liquid Nitrogen) or 290 K (room temperature), a series of straight lines can be

plotted by varying the LO power levels. All the lines intersect at $T_{\mathrm{RF}} = -T_{\mathrm{in}}$, with $P_{\mathrm{out}} = k_{\mathrm{B}} T_{\mathrm{IF}} G_{\mathrm{IF}}$. This graphical method, as illustrated in Fig 4.12, provides a convenient method to estimate the RF noise.

4.2.4 Determination of the mixer conversion gain and the IF noise contribution

This method is based on the fact that the SIS junction biased above V_{gap} behaves similar to a resistive shot noise source [94]. For an SIS junction, the shot noise spectrum density can be expressed as an equivalent noise temperature [27],

$$T = \frac{eI_{\mathrm{DC}} R_{\mathrm{n}} \coth(eV_{\mathrm{b}}/2k_{\mathrm{B}}T_{\mathrm{phy}})}{2k_{\mathrm{B}}} \tag{4.9}$$

where I_{DC} is the unpumped I-V characteristic of the SIS junction, R_{n} is the normal resistance of the SIS Junction, T_{phy} is the ambient temperature of the SIS junction and k_{B} is the Boltzmann constant. For an SIS junction biased well above the gap voltage, where the DC tunneling current rises linearly with the bias voltage, the shot noise contribution from the SIS junction can be simplified as,

$$T = \frac{eI_{\mathrm{DC}} R_{\mathrm{n}}}{2k_{\mathrm{B}}} \approx 5800 \times V_{\mathrm{b}} + \text{constant} \tag{4.10}$$

where V_{b} equals to $I_{\mathrm{DC}} R_{\mathrm{n}}$. The gradient of the shot noise T approximates to 5.8 K/mV. The gain of the IF components G_{IF} can be obtained by dividing the gradient measured from the unpumped IF curves well above the gap voltage with 5.8 K/mV. The output receiver noise temperature is given as,

$$P^{\mathrm{out}} = k_B(T_{\mathrm{in}} + T_{\mathrm{rec}}) G_{\mathrm{RF}} G_{\mathrm{IF}} \tag{4.11}$$

By measuring the IF output power with hot (T_{h}=290 K) and cold (T_{c}=80 K) loads, the gain of the RF system G_{RF} can be written as,

$$G_{\mathrm{RF}} = \frac{(P_{\mathrm{h}}^{\mathrm{out}} - P_{\mathrm{c}}^{\mathrm{out}})}{(T_{\mathrm{h}} - T_{\mathrm{c}}) * G_{\mathrm{IF}} k_{\mathrm{B}}} \tag{4.12}$$

The linear portion of the DC I-V characteristic for the SIS mixer does not pass through the origin, instead the DC current does not start to flow until the bias voltage reaches a value $V = V_1$ (Fig 4.13). So at $V = V_1$ (Fig 4.13), there is no noise contribution from the SIS junction shot noise, hence the IF output power from the SIS junction is zero and all the remaining noise power therefore must have came from the IF amplifiers chain. The IF noise temperature can be obtained by converting the IF power output at bias voltage $V = V_1$ to the noise temperature using the IF system gain G_{IF}. The

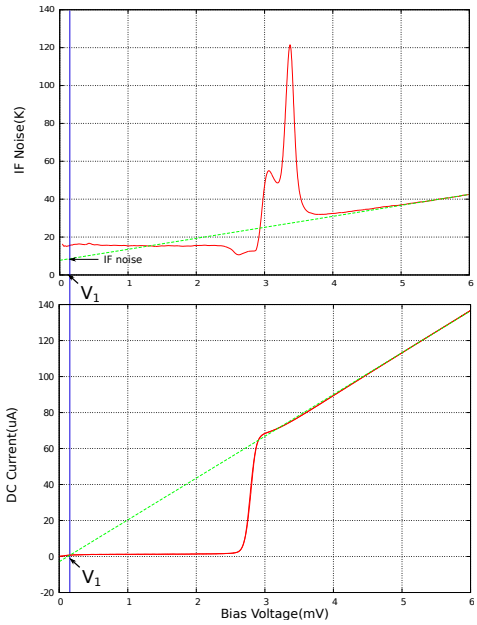

Figure 4.13: An example demonstrating the method of the estimating the IF noise contribution for device C5N1 at 219 GHz. (Top) red curve: the unpumped IF curve; green curve: the extrapolation of the linear portion of the unpumped IF curve. (Bottom) red curve: the unpumped DC IV curve; green curve: the extrapolation of the linear portion of the unpumped DC IV curve.

method for estimating the IF noise temperature is graphically illustrated in Fig 4.13.

4.3 Device DC tests

The SIS junctions fabricated at Cologne for our mixer were designed to be circular with a surface area of 1 μm^2, a normal resistance of 20 Ω and an intrinsic specific capacitance of 75 fF/μm^2. A crucial parameter determining the performance of SIS mixer is the junction area. The deposition of the Nb/AlO_x/Nb tri-layer structure for the SIS junction and all the transmission line structures are done by UV lithography but the SIS junction itself is defined by E-beam lithography [43]. The E-beam lithography and developing process has a tolerance of $\sim$0.1 μm, giving an SIS junction area tolerance of $\pm$20 %. If we assume that the thickness of the tunnel barrier is same across the whole wafer, the current density j_c would be homogeneous across the whole wafer. The normal resistance is given by

$$R_{\mathrm{N}} = \frac{V_{\mathrm{gap}}}{j_{\mathrm{c}} \cdot A_j} \tag{4.13}$$

where R_{N} is the normal resistance, V_{gap} is the gap voltage, j_{c} is the current density and A_j is the area of the SIS junction. The normal resistance R_{N} therefore allows us to determine the junction area A_{j}.

All the SIS mixers were fabricated together on a single wafer, and the devices are needed to be

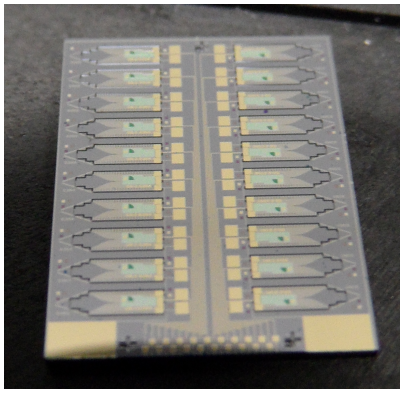

Figure 4.14: A photograph showing the layout of mixer devices on the silicon sub-wafer before separation. Since trenches are fabricated at the edge of the devices, which allow the device to be easily detached from the sub-wafer after thinning. The devices should be thinned by polishing, rather than dicing, due to the brittle nature of the silicon material.

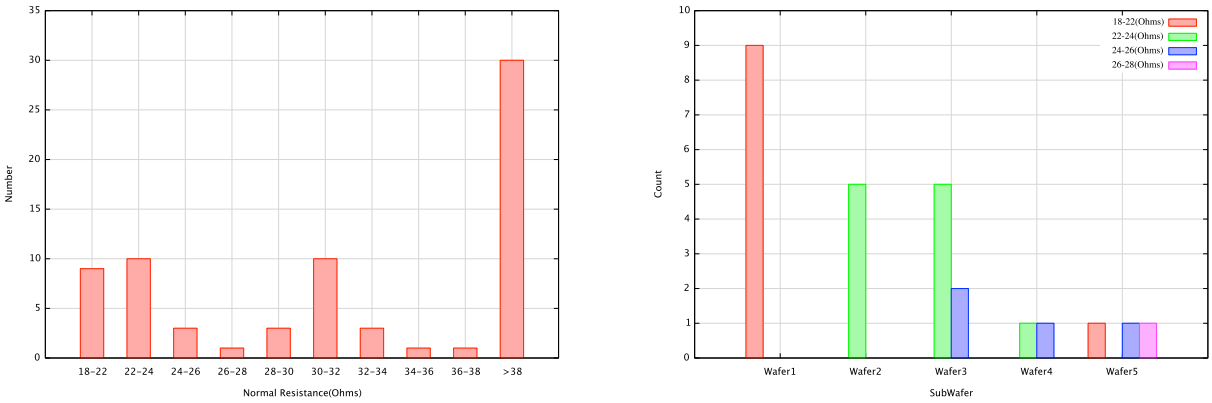

(a) (b)

Figure 4.15: (a) The distribution of normal resistance among devices on five SIS mixer sub-wafers. (b) The normal resistance distribution of the devices for each sub wafer.

separated from the wafer prior to testing, by either polishing or dicing the substrate. A photograph of the SIS devices on one sub-wafer is displayed in Fig 4.14. 9.4% of all 96 devices had a $\pm 10\%$ error in the normal resistance R_N while the other devices had a larger fabrication error in R_N. A 10% deviation in 20 Ω normal resistance shifts the tuning frequency by $\sim$20 GHz away from the expected value. Most of our devices had an SIS junction smaller than expected and were thus tuned higher than designed. Due to the fact that devices were spread over different locations on the wafer, different sub-wafers yielded different quality devices. 10 devices from the best sub-wafer (sub-wafer 1) had R_N in the range of 19 Ω to 21 Ω. The distribution of the normal resistance among all 96 devices is shown in Fig 4.15 (a), as well as the distribution for each individual sub-wafer (Fig 4.15 (b)).

In Fig 4.16 (a), we plot the leakage current as a function of normal resistance for all the fabricated

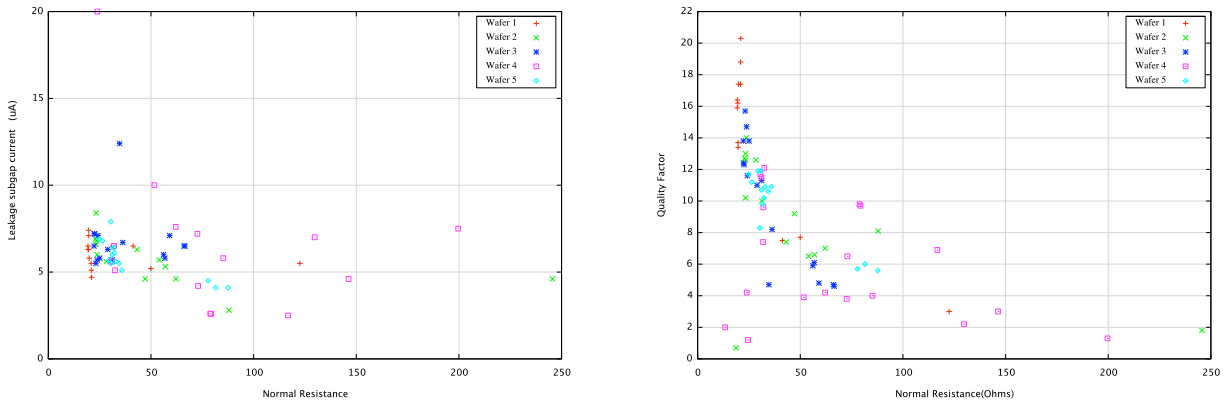

(a) (b)

Figure 4.16: (a) Leakage current as a function of normal resistance for mixer devices. (b) Quality factor Q as a function of normal resistance.

mixer devices. As indicated in following equation [46],

$$I_{\text{leakage}} = \frac{2}{R_N \cdot e} \cdot e^{-\frac{\triangle}{k_B T}} \cdot \sqrt{\frac{2\triangle}{eV + 2\triangle}} \cdot (eV + \triangle) \cdot \sinh(\frac{eV}{2k_B T}) \cdot K_0(\frac{eV}{2k_B T})$$

where K_0 is the 0^{th} order modified Bessel function. The leakage current I_{leakage} should be inversely proportional to the normal resistance R_{N}, which agrees with the DC data shown in Fig 4.16 (a). In Fig 4.16 (b), we plot the Q factor as a function of normal resistance for all the fabricated mixer devices. The quality factor Q , defined as $I_{\text{g}}/I_{\text{sub}}$, is the ratio of tunneling currents when the junction is biased above and below the gap voltage. In theory Q-factor should be independent of the junction area, as both the leakage current (I_{sub}) and the critical current (I_{g}) would scale with the junction area. However in the DC tests, we found that the Q-factor was a strong function of the normal resistance as shown in Fig 4.16 (b). This is because small amount of leakage current [43] is expected to flow at the edge of the SIS junction. In such a circumstance, smaller SIS junction has higher leakage current per unit area than the bigger junctions, resulting in a lower Q factor for smaller SIS junction. Our device selection criteria was based on selecting devices with the correct normal resistance (20 Ω), low leakage current (<8 μA)and high Q-factor (> 10). Further practical details for each sub wafer are listed in Tab 4.2.

Subwafer	Substrate Thickness	Thinning Method	Comments	Reported Devices
Wafer 1	~60 μm	Polish	The best wafer giving 10 devices with R_N approaching 20 Ω.	N/A
Wafer 2	~85 μm	Polish	Thick Si substrate (>80 μm) reduces RF power coupling to the unilateral finline, leading to mixer performance deterioration above 240 GHz.	A2N1 D2N1
Wafer 3	~60 μm	Dice	Dicing lines left on the back of substrate make the devices vulnerable for breaking.	D3N4 C3N1
Wafer 4	~85 μm	Polish	Thick Si substrate (>80 μm) reduces RF power coupling to the unilateral finline, leading to mixer performance deterioration above 240 GHz.	N/A
Wafer 5	~60 μm	Polish	Right thickness and robust structure. The best mixer device reported is from this sub-wafer.	C5N1

Table 4.2: Overview of each sub-wafer

4.4 Mixer test results

Summaries of the measurement results for a few representative mixers tested in the Wet Dewar and in the GUBBINS system are given in Tab 4.3 and Tab 4.4. The quoted DSB noise temperatures include the optical loss, the mixer transmission lines loss, the mixer quantum limited noise and the IF loss. The measurement data quoted in the table would have certain error bars that might be caused by slightly different LO pumped levels, slightly different magnetic fields that applied to the SIS junction and minor fluctuations in the IF amplifier gain in each time measurement. All the uncertainties mentioned above could lead to an error bar of $\sim \pm 6\% * T_{\mathrm{rec}}$ in the noise temperature measurement, where T_{rec} is the measured receiver noise temperature. The accuracy of the junction normal resistance R_{n} is limited by the linearity of the I-V curve above the gap voltage. Plots of the mixers performance measured across the RF band can be found in Fig 4.17 and Fig 4.18.

Table 4.3: Characteristics of the devices tested in the GUBBINS system.

No.	R_{N} (Ω)	f_{B} (GHz)	G_{RF} (dB)	T_{IF} (K)	T_{rec} (K)	IF (GHz)
A2N2	23.3	210	-5.6	13	214	4-6
D2N1	23	216	-5.4	8	79	4-6
C5N1	20.5	216	-4.5	19	103	4.5-5.5
C5N1	20.5	216	-4.2	16	71	4-6
D5N1	80	216	-2.2	9	111	4-6

Table 4.4: Overview of the characteristics of the devices tested in the Wet Dewar.

No.[0]	R_N[1] (Ω)	BS[2] (μm)	f_B[3] (GHz)	G_{RF}[4] (dB)	T_{IF}[5] (K)	T_{rec}[6] (K)	IF[7] (GHz)	LO[8]	Sub[9](μm)
A2N2	23.3	19	216	-3.4	15	130	4-6	GUB	85
A2N2	23.3	23	216	-4.1	15	130	4-6	GUB	85
A2N2	23.3	19	219	-4.1	15	130	4-6	Gunn	85
D2N1	23	12	216	-5.2	7	90	4-6	GUB	85
D2N1	23	12	219	-4.5	7	73	4-6	Gunn	85
D3N4	22.6	36	264.6	-0.7	9.8	90	4-6	GUB	60
C5N1	20.5	12/8	216	-3.2	16	74	4-6	GUB	60
C5N1	20.5	12/8	216	-0.8	10.1	64	3.75-4.25	GUB	60
C5N1	20.5	12/8	216	-0.6	8.6	51	3-4	GUB	60
C5N1	20.5	8	219	-0.1	16	71	4-6	Gunn	60
C5N1	20.5	8	219	-0.8	10.1	52	3.75-4.25	Gunn	60
C5N1	20.5	8	219	0	8.6	50	3-4	Gunn	60
C3N1	22.24	12	208.8	-3.8	9	75	4-6	GUB	60

[0] No.: the unique device identity number.

[1] R_N: the normal resistance of the device.

[2] BS: the thickness of the Mylar beamsplitter used in the optical assembly.

[3] f_B: the LO frequency at which the best noise temperature was obtained.

[4] G_{RF}: the conversion gain of the mixer at the frequency where the best noise temperature was measured.

[5] T_{IF}: the noise temperature of the IF system. Note that this figure has not been divided by the mixer conversion gain G_B.

[6] T_{rec}: the best noise temperature obtained for this device.

[7] IF: the bandwidth of IF filters used in the warm IF chain.

[8] LO: GUBBINS multiplier chain LO denoted by GUB or diode Gunn LO denoted by Gunn.

[9] Sub: the thickness of the silicon substrate.

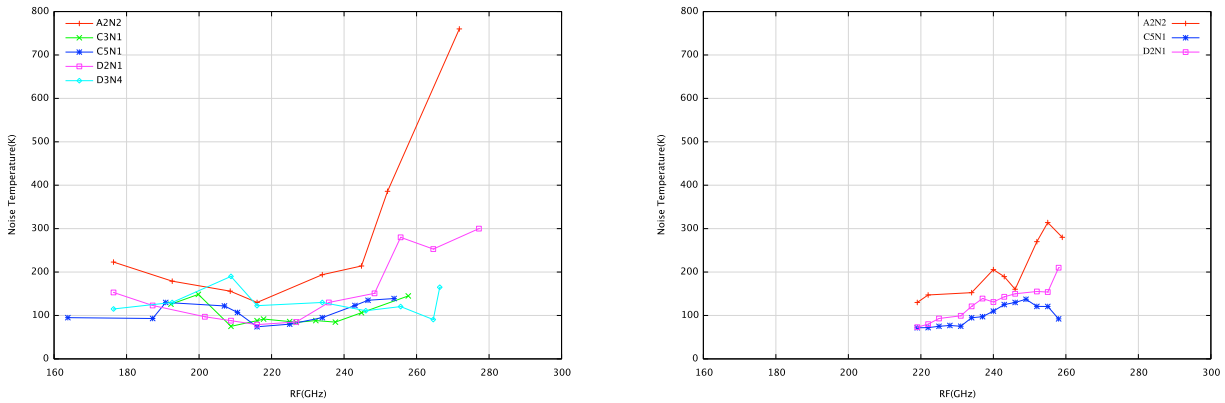

(a) (b)

Figure 4.17: (a) Summary of the mixer performance data for 5 tested devices in the Wet Dewar using the GUBBIN LO. (b) Summary of the mixer performance data for 3 tested devices in the Wet Dewar using the Gunn LO

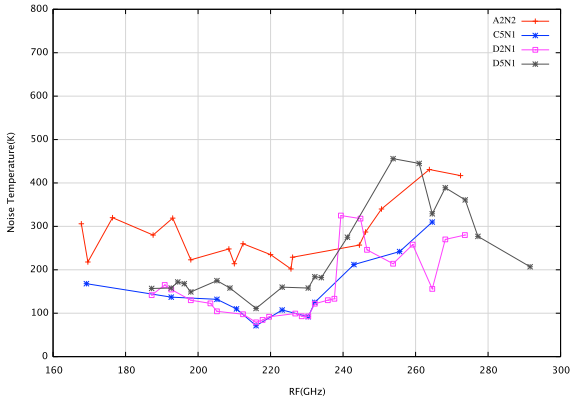

Figure 4.18: Summary of the mixer performance data for 4 tested devices in the GUBBINS system using the GUBBINS LO.

General behavior of the tested devices:

- The tested mixers showed reasonable performance over RF bandwidth ∼170 GHz–260 GHz with an average noise temperature of ∼100 K (Fig 4.17 (a)).
- The best measured device (C5N1) had an average noise temperature of ∼75 K over RF bandwidth 160 GHz–260 GHz and a best noise temperature of 50 K at 219 GHz.
- The substrate thickness has a profound influence on the mixer performance.
- For the same device, the noise temperatures measured in the GUBBINS system were ∼20 K higher than the noise temperatures measured in the Wet Dewar (Fig 4.18), especially at RF band edges.
- The higher harmonic signals in the GUBBINS LO enhanced the measured mixer noise temper-

ature. In Sec 4.4.1, we would discuss the influence of the higher order LO harmonics on the SIS mixer.

4.4.1 The influence of R_N on the mixer receiver performance

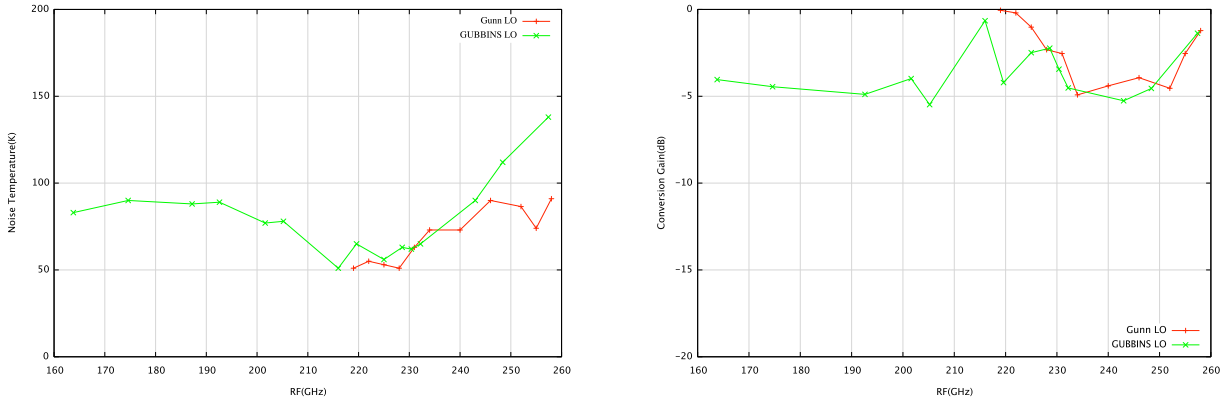

(a) (b)

Figure 4.19: (a) The receiver noise temperature measured for device C5N1 by the GUBBINS LO and the Gunn LO as a function of RF frequency using 3–4 GHz IF bandpass filter. (b) The conversion gain.

Fig 4.19 shows the performance of the best device we have ever measured. Device C5N1 had a normal resistance of 20.5 Ω, a leakage current of 6.9 μA, a Q-factor of 11.7 and a substrate thickness of around 60 μm. All the characteristic of device C5N1 satisfied the device selection criteria, i.e. a normal resistance approaching 20 Ω, a low leakage current, a high Q-factor and a silicon substrate thickness matching the design. Therefore the good performance measured for device C5N1 met our expectations, hence confirms the integrity of our mixer design and measurement system. The performance shown in Fig 4.19 was measured in the Wet Dewar over IF bandwidth of 3–4 GHz using either the Gubbins LO or the Gunn LO. The RF bandwidth cover was 163 GHz-258 GHz with an average noise temperature of 75 K. A best noise temperature of 50 K was measured at 219 GHz by the Gunn LO (red curve in Fig 4.19 (a)). Using the techniques described in Sec 4.2.4 and Sec 4.2.3, we calculated an IF noise temperature of 8.6 K and an RF contribution noise of ∼40 K at LO frequency 219 GHz. As the optical system would contribute 27 K noise, this leaves ∼13 K to the quantity $T_{\mathrm{SIS}}/G_{\mathrm{Optics}}G_{\mathrm{trans}}$. This 27 K optical noise is contributed by the Mylar beamsplitter and the vacuum window. The transmission loss of the Mylar beamsplitter could be referred to Fig 4.3 and the investigation on the loss of the vacuum window could be referred to Chapter 7. In the above expression, T_{SIS} is the quantum limited noise for the SIS junction, G_{Optics} is the optical loss and G_{trans} is the mixer planar circuit loss (i.e finline transition loss etc.). The quantum noise for the SIS junction T_{SIS} $(h\nu/k_{\mathrm{B}})$ was calculated

to be 11 K, and thus our measured mixer performance approaches the quantum limited noise for an SIS junction predicted by Tucker's theory [55]. In Fig 4.20 (bottom), we show the IV and IF characteristics measured at 219 GHz for device C5N1 and the noise temperature and conversion gain that were calculated from the IF power ratios as a function of the bias voltage in Fig 4.20 (top). Although we did manage to obtain noise temperature as low as 38 K (labelled by T_{lowest} in Fig 4.20) at the bias voltage 2.5 mV, there was only one single point that gave a noise temperate of 38 K. If the mixer is used in a practical telescope, it is hardly guaranteed that the mixer can be biased at exactly 2.5 mV. Therefore here we only accept 50 K (T_{peak} in Fig 4.20) as the noise temperature of the mixer, which is easy to locate (at the bias voltage that gave the peak IF power) and covers at least 0.1 mV bias voltage width.

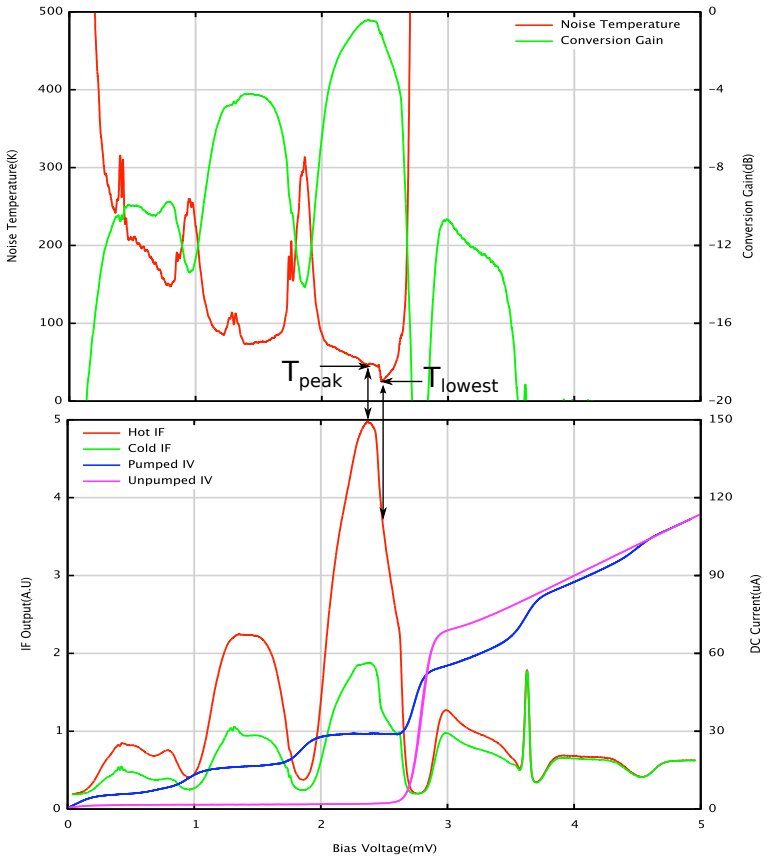

Figure 4.20: (Top) The noise temperature and conversion gain as a function of the bias voltage for device C5N1 measured at 219 GHz. (Bottom) The IV and IF characteristics of device C5N1 measured at 219 GHz.

In Fig 4.19(a), the noise temperatures measured by the GUBBINS LO and by the Gunn LO showed good agreement at some RF frequencies (i.e 225 GHz–240 GHz), but showed big divergence at other RF frequencies (i.e 220 GHz–225 GHz or 240 GHz–260 GHz). Fig 4.19 (b) shows that the mixer

conversion gains measured by both the GUBBINS LO and the Gunn LO were similar. Therefore the greater noise temperatures measured by the GUBBINS LO must have originated in the RF section. Using an FTS (Fourier Transform Spectroscope) we measured the spectrum of the GUBBINS LO at different RF frequencies [62]. The FTS measurement was done by Dr. Jamie Leech at RAL (Rutherford Appleton Laboratory). It was discovered that unwanted harmonic signals existed on the LO spectrum. Some harmonics even appeared at frequencies close to the fundamental LO signals and some harmonics had amplitude comparable to the fundamental signals. Fig 4.21 shows the measured FTS spectrum of the GUBBINS LO at 223.2 GHz and 250 GHz. At LO frequency 223.2 GHz, a harmonic signal existed at 240 GHz. At LO frequency 250 GHz, a harmonic signal existed at 290 GHz. The degradation of frequency down-conversion process of a DSB mixer by a higher harmonic signal is because the RF signals in the signal sideband and in the image sidebands would both be down-converted to the IF frequencies, by mixing with the fundamental LO signal. However if a harmonic LO signal existed and was very close to the fundamental signal in frequency, additional noise from its signal and image sideband would also be down-converted to the IF band and increase the total receiver noise temperature.

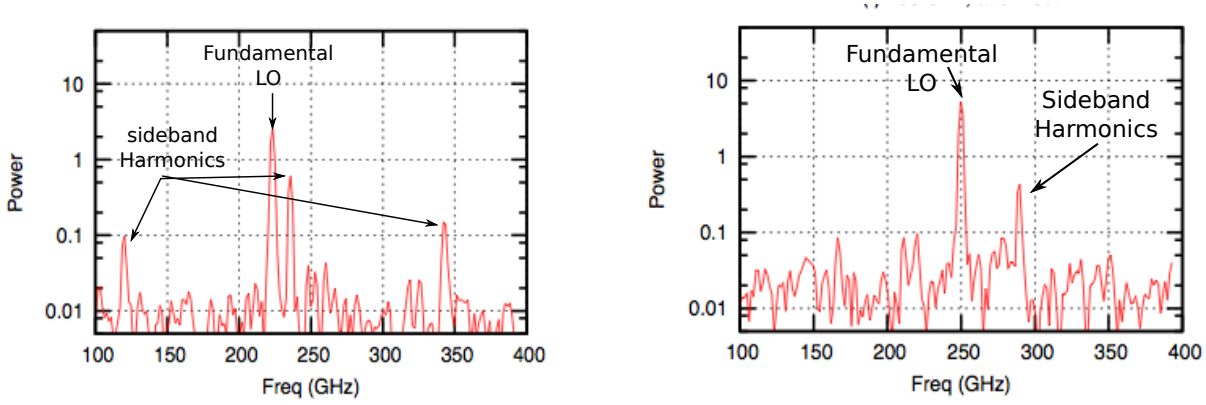

(a) (b)

Figure 4.21: (a) An FTS measurement for the GUBBINS LO measured at f=223.2 GHz (b) An FTS measurement for GUBBINS LO measured at f=250 GHz [62]

If we replace the noise temperature data taken with the GUBBINS LO by the ones taken with the Gunn LO at f >245 GHz, the new noise temperature spectrum would be the red curve shown in Fig 4.22 (a). The noise temperatures measured across the RF bandwidth were all below 100 K. Clearly, the noise temperature of the mixer was consistent which verifies the integrity of our RF simulation.

Although we did measure a noise temperature as low as 50 K at the center of the RF band, we also measured noise temperature as high as approaching 90 K at the edge of the RF band. The measured mixer conversion gain at the band edges was not low enough to explain the increase in the noise

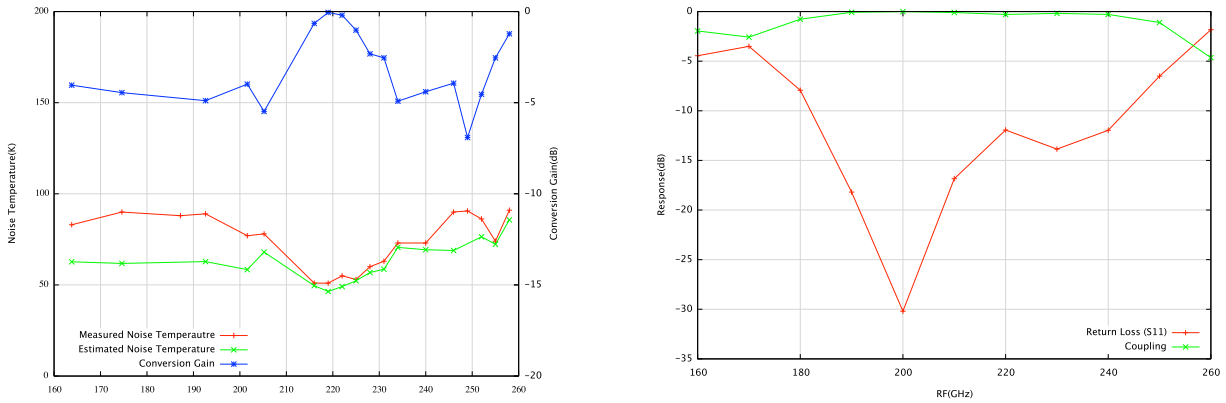

(a) (b)

Figure 4.22: (a) The measured noise temperature (red curve), the measured conversion gain (blue curve) and the estimated noise temperature (green curve) for device C5N1. The data presented at frequencies 160 GHz-220 GHz were measured using the GUBBINS LO and the data presented at frequencies 220 GHz-260 GHz were measured using the Gunn LO. (b) The HFSS simulated return loss (S11) and coupling for device C5N1

temperature. For instance, the conversion gain at 163.8 GHz was -4 dB (linear value: 0.4) and the IF noise was 8.3 K, so the overall IF contribution would be 8.3/0.4=21.5 K. The conversion gain at 219 GHz was -0.05 dB (linear value: 0.989) and the overall IF contribution noise would be 8.6/0.989=8.7 K. The IF contribution noise temperature difference between 219 GHz and 163.8 GHz is only ∼12.8 K, far less than the difference in the total noise temperature (83-50=33 K). Therefore the increment of the receiver noise temperature at band edges can not be accounted for by the conversion gain alone. In addition, we observe that the RF coupling deteriorated quickly at the band edges (Fig 4.22 (b), i.e only -5 dB at 260 GHz). The decrement in the coupling would enhance the noise temperature contributed by all the components that came after it. We have estimated the total receiver noise temperature through the receiver chain equation

$$T_{\rm rec} = (1/G_{\rm optics} - 1)T_{\rm phys} + \frac{T_{\rm trans}}{G_{\rm optics}} + \frac{T_{\rm SIS}}{G_{\rm optics}G_{\rm trans}} + \frac{T_{\rm IF}}{G_{\rm optics}G_{\rm trans}G_{\rm SIS}} \tag{4.16}$$

The first term of Eq 4.16, $G_{\rm optics}$ is determined by the thickness of the Mylar beamsplitter and the transmission loss of the vacuum window/IR filter. The thickness of Mylar beamsplitters was 8 μm and the transmission loss of the vacuum window/ IR filter was assumed to be 3.2% (the calculation of the transmission loss for vacuum window/IR filter is discussed in detail in Chapter.7). The second term $T_{\rm trans}$ can be calculated through $(1/G_{\rm trans} - 1) \times 4K$, where $G_{\rm trans}$ is the HFSS calculated junction coupling (Fig 4.22 (b)). The third term, $T_{\rm SIS}$ is the junction quantum noise which was assumed to be $h\nu/k_{\rm B}$. The fourth term, $T_{\rm IF}$ is the IF noise temperature in the IF chain, and $G_{\rm optics}G_{\rm trans}G_{\rm SIS}$ is the

mixer conversion gain. The IF noise T_{IF} (8.6 K) and the conversion gain $G_{\mathrm{optics}}G_{\mathrm{trans}}G_{\mathrm{SIS}}$ (Fig 4.19 (b)) can be calculated through the methods described in Sec 4.2.4. The estimated noise temperatures and the measured noise temperatures are compared in Fig 4.22 (a).

Term 2, 3 and 4 in Eq 4.16 are all affected through the junction coupling G_{trans}, that a lower SIS junction coupling can lead to an increase in noise temperature through term 2, 3 and 4. For instance, at 163.8 GHz, we have calculated that the optical noise contributed by the 8 μm Mylar beamsplitter is ∼13 K (term 1 in Eq 4.16), the optical noise contributed by the vacuum window/IR filter is ∼ 10 K (still term 1 in Eq 4.16), the noise contributed by the mixer planar circuit is ∼2.5 K (term 2), the noise contributed by the SIS junction is ∼17 K (term 3) and the IF noise is 21 K (term 4). The estimated total noise temperature at 163.8 GHz is 63.5 K, 10 K out of which is a result of the finite SIS junction coupling.

For the noise temperature measured at 219 GHz, the optical loss (Mylar and window/IR filters) is 25 K, the noise contributed by the mixer planar circuit is almost zero because of a coupling efficiency approaching 0 dB, the noise contributed by the SIS junction is 11.5 K and the noise contributed by the IF system is 8.8 K. The estimated noise temperature at 219 GHz summed up to 46.4 K, which is consistent with the measured noise.

We did similar calculations for the noise temperature at other RF frequencies (Fig 4.22 (a)) and found that the estimated noise temperature followed the trend of the measured noise temperature, however at both high frequency ($>$ 240 GHz) and low frequency ($<$ 205 GHz), the measured noise temperatures were ∼10 - 20 K greater than the estimated noise temperatures. We therefore suspecte that in the receiver chain, there must be some other frequency-dependent losses that haven't been taken into account. The HFSS simulation of the finline was idealized and did not take into account the groove loaded waveguide. In practice, higher order modes could degrade the mixer performance especially at the high frequency band. In addition it has already been established that the GUBBINS LO would result in higher noise temperatures than the Gunn LO. We therefore expect the mixer noise temperature to be slightly improved if the Gunn LO could cover the low frequency end. Last but not least, the smooth-walled horn might exhibit some level of transmission loss at band edges. As an optical loss, the loss in the horn would enhance the noise contribution by all the components that came after it.

As well as device C5N1, we also measured good noise temperatures for device C3N1. We list the measured noise temperature for both devices in IF bandwidth 4-6 GHz in Fig 4.23. Device C3N1 had a normal resistance of 22.2 Ω, a leakage current of 6.5 μm, a Q-factor of 13.8 and an ideal ∼60 μm thick silicon substrate. The normal resistance of device C3N1 was 8.5 % higher than the normal

resistance of device C5N1. In theory, this 8.5 % increment in normal resistance would shift the tuning frequency from 230 GHz to 250 GHz. However, from the Y-factor measurements (Fig 4.23), the bands with good noise temperature for both devices almost overlapped with each other and the center of the tuning bands for both devices existed at around 220 GHz. Therefore the tuning circuit designed in the finline SIS mixers can indeed tolerate a small range of fluctuations (±10%) in the junction size, without substantially affecting the mixer performance. The same conclusion can also be drawn by the summaries of the tested mixers in Fig 4.17 (a), that with the normal resistance ranging from 20.5 Ω to 23.3 Ω, the center of the operating RF bandwidth remained almost unchanged at around 220 GHz.

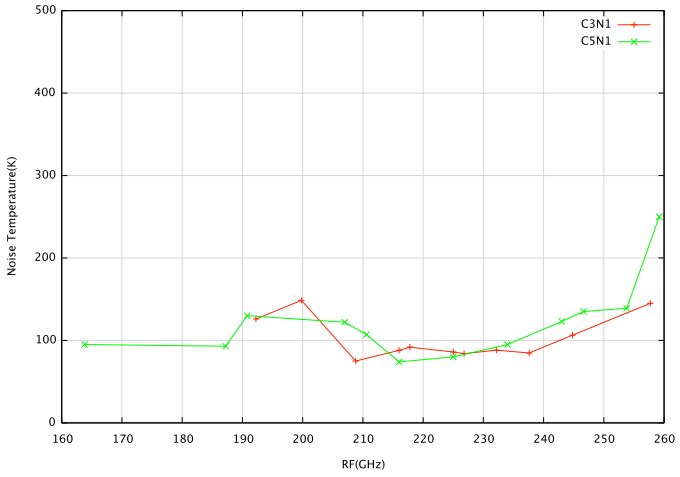

Figure 4.23: Comparison of the noise temperatures measured for device C3N1 and device C5N1 in IF bandwidth 4-6GHz.

4.4.2 Embedding admittance recovery

In Sec 2.4.3 we have shown the method of calculating the embedding admittance seen by the SIS junction when the mixer is mounted in the waveguide. The equivalent circuit showing the embedding admittance Y_ω is shown in Fig 4.24. The embedding impedance is strongly influenced by the parasitic capacitance of the SIS junction and its tuning circuit. A good knowledge of the embedding impedance is of great importance, because the match between the embedding impedance and the SIS junction determines the coupling of the LO and RF power into the SIS junction, and hence the sensitivity of the SIS mixer. For a perfectly tuned SIS junction, the normalized embedding admittance (normalized to mixer normal resistance R_n) should have a real part of unity and an imaginary part of zero. In the embedding admittance recovery calculation, we could calculate a theoretical pumped IV curve with a given embedding impedance, based on an experimental unpumed IV curve. Then we alterd the value of the embedding admittance that we were using in the code, to produce different theoretical pumped

IV curves until it matcheed the shape of the experimental pumped IV curve, especially at the location around the first photon step.

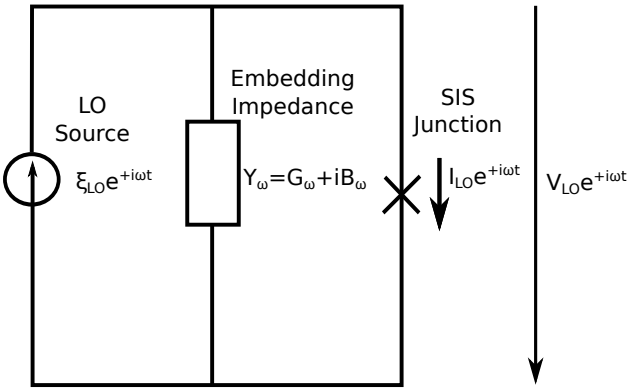

Figure 4.24: The equivalent circuit of an SIS mixer under the illumination of an external LO source. The embedding admittance is shown by Y_ω in the Figure.

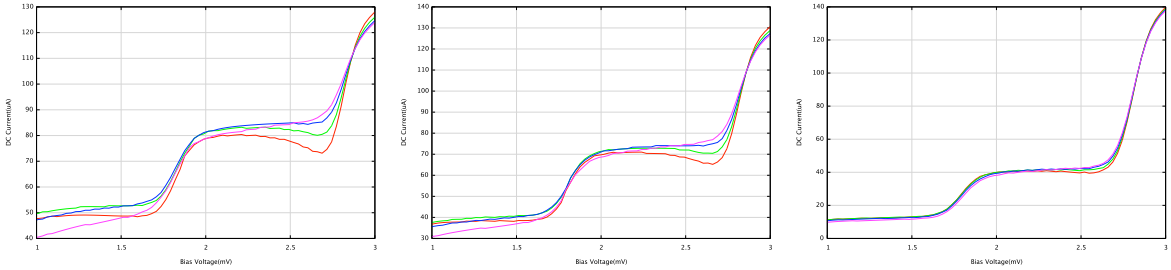

(a) G=0.8 (b) G=1.0 (c) G=2.0

Figure 4.25: Calculated pumped I-V curves with different embedding admittance. In plot (a) (b) (c), the assumed embedding susceptances are B=-0.45, -0.15, 0.15, 0.45 from red, green, blue to pink. The assumed embedding conductance are (a) G=0.8 (b) G=1.0 (c) G=2.0

In Fig 4.25, we investigate the influence of the embedding impedance on the shape of the first photon step of the pumped IV curves. It can be seen that the slopes of the first photon steps of the pumped I-V curves undergo a transition from negative to positive with increasing susceptance (B=-0.45 to B=0.45). And when the conductance (G) gets smaller (Fig 4.25(a)), the differences between the curves become larger. One example showing the calculated pumped IV curve using the embedding impedance recovery method is plotted in Fig 4.26 (b), for device C5N1 at LO frequency 216 GHz. The normalized recovered embedding admittance was (0.8+0.24 j). The imaginary part of the embedding admittance is therefore very small and the real part is close to unity hence the mixer is reasonably well tuned and matched at this frequency. The recovered mixer embedding susceptance across the RF bandwidth is also plotted in Fig 4.26 (a). We saw positive embedding susceptance across nearly the whole RF band, which indicated slightly capacitive tuning over most of the RF bandwidth [82]. This capacitive tuning can also be seen by the shape of the first photon steps on the pumped I-V curves

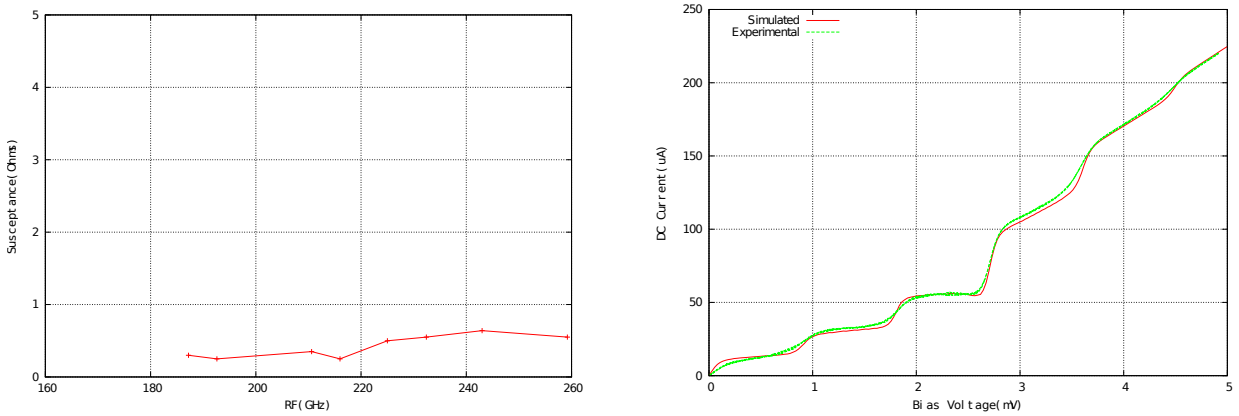

(a) (b)

Figure 4.26: (a) Recovered embedding susceptance as a function of the RF band. Note that the impedance recovery at frequencies below 190 GHz were not performed due to the irregular shapes on the first photon steps in the pumped IV curves. These irregular shapes at the photon steps were caused by the LO harmonics. (b) Example of the matching between the simulated pumped IV curve and the experimental pumped IV curve at 216 GHz. The embedding admittance recovered at 216 GHz is (0.8+0.24j).

(Fig 4.27). In fact, all of our pumped I-V curves have shown positive slopes on the first photon steps , which is the characteristic of a capacitive tuning.

4.4.3 The influence of the substrate thickness on the mixer performance

Devices A2N2 and D2N1 were both from sub-wafer 2, which was polished to a thickness greater than 60 μm. The mixer device is designed with a substrate thickness of 60μm. The substrate notches and the finline serrations are both designed according to this 60μm thickness. If the thickness is thicker than the nominal value, the guided wavelength will be longer than what it should be in the original design. Then the serrations at either sides of the substrate would be smaller than the quarter-wavelength of the propagating signal in the waveguide. In such a scenario, the serrations cannot completely short the finline to the waveguide, so higher order modes can be excited inside the groove and propagate along the waveguide, especially at frequencies close to the high band edge. Additionally the waveguide loading thicker substrate would also generate higher order mode excitations.

In Fig 4.28, we show HFSS simulations of the unilateral finline transmission that support this argument. The transmissions of the fundamental mode and for the 3rd order mode electromagnetic (EM) signals are plotted. It is interesting to note that below 240 GHz, the influence of the substrate thickness on the transmission of the fundamental EM signal is not significant. But above 240 GHz, the impact of the substrate thickness starts to appear and it becomes clear that a thicker substrate can reduce the transmission of the fundamental mode by almost 50%. For instance, at 270 GHz, the

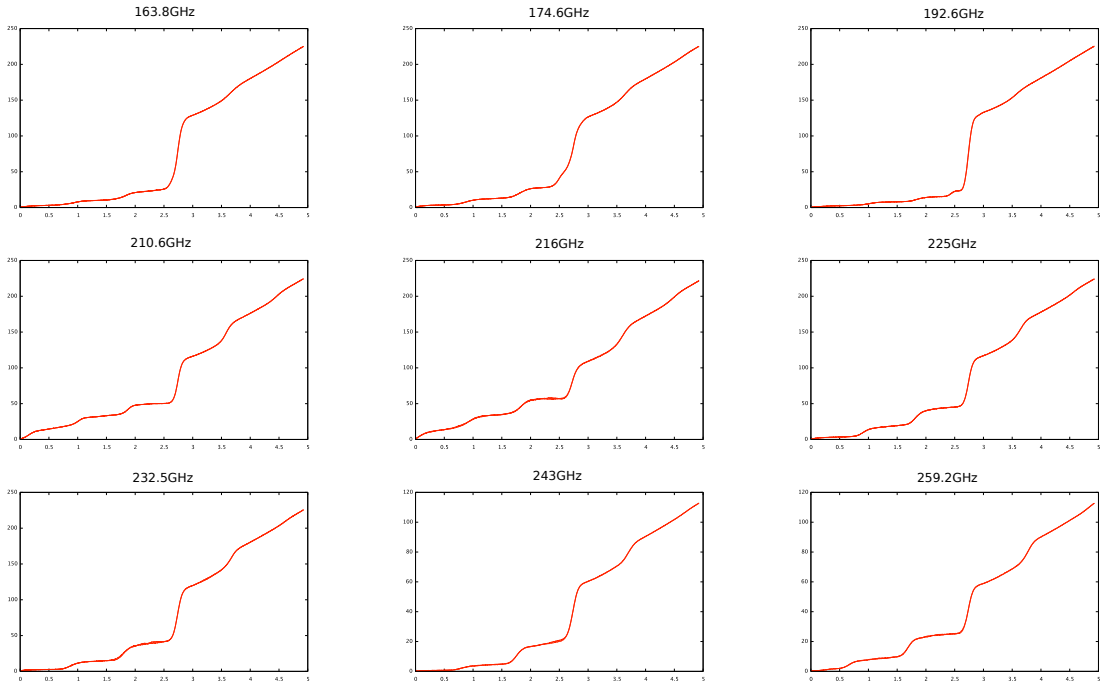

Figure 4.27: The measured IV characteristics for device C5N1 pumped by the GUBBINS LO, across the RF band. In the above plots, the X-axis represents the bias voltage in the unit of mV and the Y-axis represents the DC current in the unit of μA. The existence of harmonics in the LO output can be seen on some photon steps.

transmission for the fundamental mode is reduced from 77% to 34%, as the thickness increases from 60 μm to 80 μm. The reduction of signal propagation at the fundamental mode above 240 GHz is accompanied with propagation of higher modes signals as shown in Fig 4.28 (b). The effect of this on the mixer noise temperature is not only to slightly increase the noise temperature contributed by the planar RF circuits, but more substantially, it enhances the noise contribution by all the subsequent components through a smaller G_{trans}. For example when the noise temperature measured at 255 GHz using the Gunn LO was broken down to RF and IF components, it was found that 35 K was not accounted for in the RF contribution when the factor G_{trans} was calculated for substrate thickness of 60 μm. It is therefore likely that this excess 35 K noise have came from a lower G_{trans} corresponding to a substrate thickness of 80 μm or 90 μm. We compare the noise temperatures measured for the devices with 60 μm substrate thickness and for the devices with 80 μm substrate thickness in Fig 4.29. We notice that with a thicker substrate (A2N2 and D2N1), the noise temperature increase at high frequency (f $>$ 245 GHz) is more significant than a device with a thinner substrate.

In what follows we shall calculate the effect of the substrate thickness on receiver noise temperature (N_{T}) for device A2N2 and D2N1. The total receiver noise temperature can be expressed by the equation:

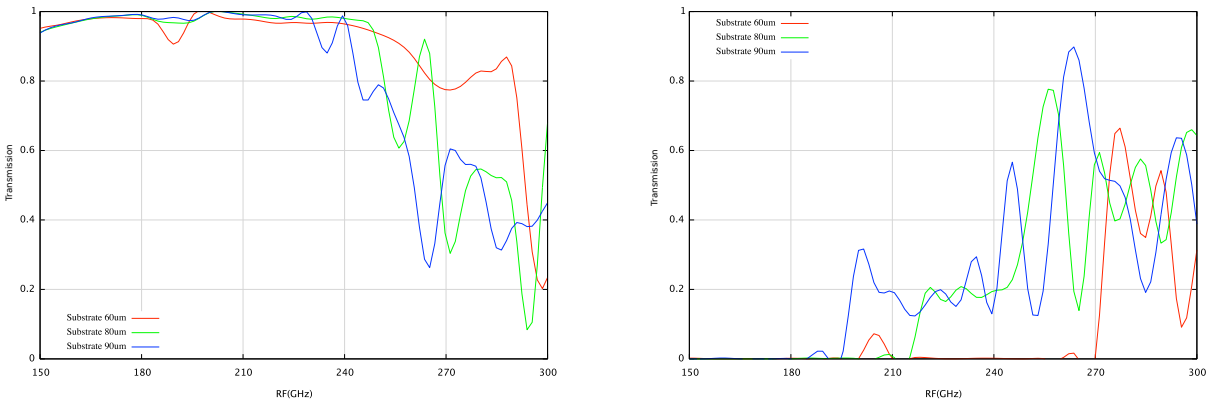

(a) (b)

Figure 4.28: Simulation plots showing the performance of unilateral finline tapers with 60 μm, 80 μm or 90 μm substrate thickness, with serrations included in the HFSS model. (a) Behavior of the fundamental EM mode and (b) the 3rd EM mode. It can clearly be seen that the transmission of the fundamental mode EM power decreased quickly with a thicker substrate, and at the same time higher order modes are excited.

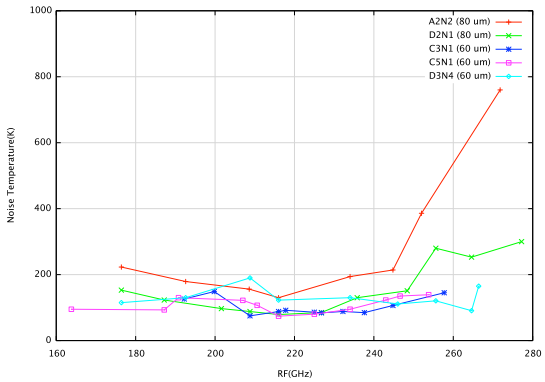

Figure 4.29: The noise temperatures measured for the devices with 60 μm substrate thickness (C3N1, C5N1 and D3N4) and for the devices with 80 μm substrate thickness (A2N2 and D2N1).

$$T_{\rm rec} = T_{\rm optics} + \frac{T_{\rm trans}}{G_{\rm optics}} + \frac{T_{\rm SIS}}{G_{\rm optics}G_{\rm trans}} + \frac{T_{\rm IF}}{G_{\rm optics}G_{\rm trans}G_{\rm SIS}} \tag{4.17}$$

where $G_{\rm trans}$ is the transmission gain of all the RF circuits including the unilateral finline before the SIS junction based on 80 μm silicon substrate. We can replace $G_{\rm trans}$ by $G'_{\rm trans}$,

$$G'_{\rm trans} = \frac{G_{\rm 60um}}{G_{\rm 80um}} * G_{\rm trans} \tag{4.18}$$

where $G'_{\rm trans}$ is the transmission gain based on 60 μm silicon substrate. $G_{\rm 60um}$ and $G_{\rm 80um}$ are the transmissions gains of a unilateral finline with silicon substrates thickness of 60 μm and 80 μm respectively. Therefore we can infer the noise temperature of an SIS mixer fabricated on a 60 μm substrate using

the measurement of a mixer fabricated on 80 μm substrate, by calculation the ratio $G_{60\mu m}/G_{80\mu m}$ from Fig 4.28.

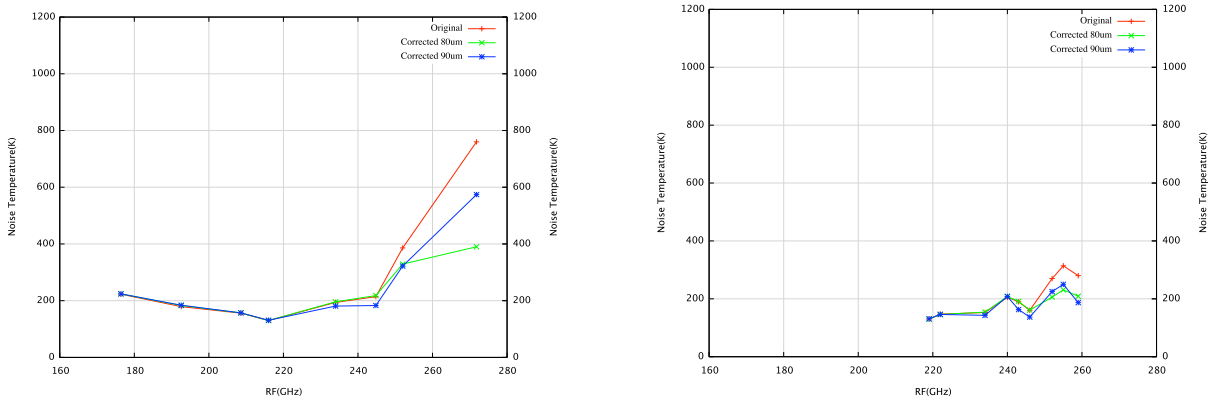

(a) (b)

Figure 4.30: The corrected noise temperatures measured for device A2N2 (a) by the GUBBINS LO with 23 μm beamsplitter and (b) by the Gunn LO with 19 μm beamsplitter.

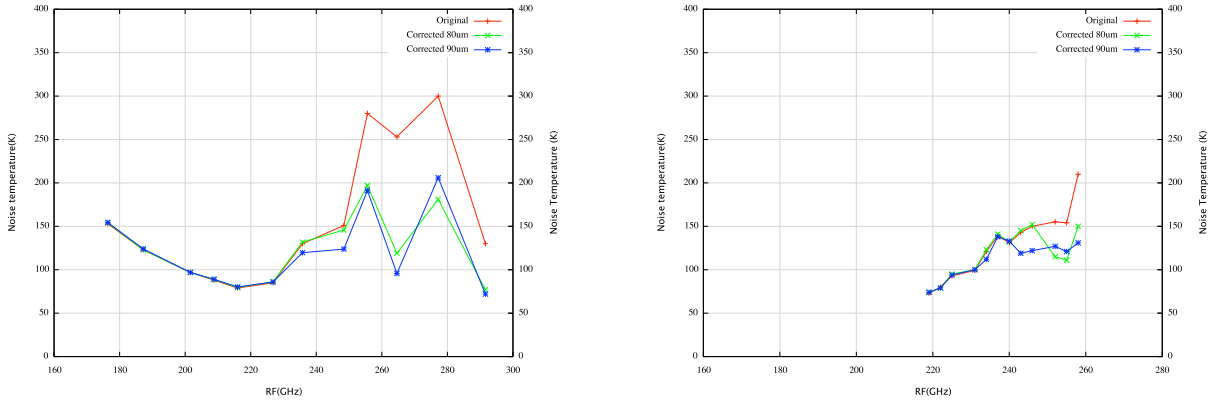

(a) (b)

Figure 4.31: The corrected noise temperatures measured for device D2N1 (a) by the GUBBINS LO with 23μm beamsplitter and (b) by the Gunn LO with 19μm beamsplitter (b) for device D2N1.

The measured receiver performance for device A2N2 and device D2N1 is shown in Fig 4.30 and Fig 4.31. The noise temperature corrections performed for the substrate thickness are also shown in Fig 4.30 and Fig 4.31. It can be seen that a reduction of 80 K $\sim$ 150 K in the noise temperature is obtained above 240 GHz by this correction. It is interesting to note that the reduction in the noise temperature is larger when the GUBBINS LO is used.

The above results show that thinning the substrate of finline devices to the correct thickness is crucial, especially for a substrate with a high dielectric constant (i.e ε_r=11.8 for Silicon). A small increase in the substrate thickness can result in a significant change in the guided wavelength of the

propagating signals, leading to the excitation of higher order modes. In addition, the input impedance of the silicon substrate is strongly dependent on the substrate thickness and the dielectric constant. The change in the substrate thickness is likely to affect the performance of the substrate notches, causing a mismatch between the empty waveguide and the loaded waveguide.

4.4.4 The influence of LO coupling on the mixer performance

The measurements discussed in the previous sections were performed in the wet Dewar where the LO power was coupled to the SIS mixer by the reflection of the Mylar beamsplitter. Other experiments, however, (i.e with device C5N1) were tested in the GUBBINS system, where a waveguide LO coupler was employed to couple LO radiation to the SIS mixer. The detailed description of the LO coupler can be found in Sec 6.6.2. The mixers tested in the GUBBINS system could be easily pumped across the RF band 160 GHz–280 GHz and presented reasonable noise temperature over most of the RF band, which meant that the directional coupler coupled enough power to pump the mixer.

To compare the performance of the two systems, the noise temperature for device C5N1 was also measured in the GUBBINS system over frequency 160 GHz–260 GHz with an IF band 4–6 GHz. The measured receiver noise temperatures and the mixer conversion gains are compared in Fig 4.32. It can be easily noted that the noise temperature measured in the GUBBINS system is higher than the ones measured in the Wet Dewar, especially near the edge of the RF bands. This behavior was observed for other devices measured in the two systems.

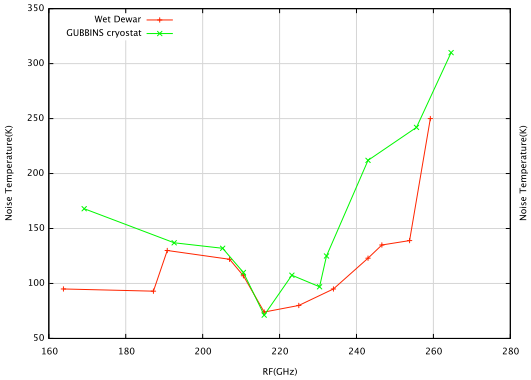

Figure 4.32: Comparison of the noise temperatures measured in the GUBBINS system and in the Wet Dewar for the same device.

In the GUBBINS system, the LO coupler is designed to provide a coupling efficiency of -17 dB, which is comparable to a 19 μm Mylar beamsplitter. However, we found that the mixers tended to be more easily pumped in GUBBINS system than in the Wet dewar while using a 19 μm beamsplitter. A possible explanation for this is that the LO coupling in the GUBBINS system was stronger than the

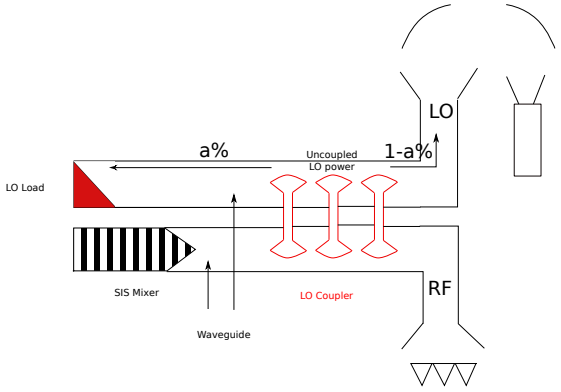

Figure 4.33: A schematic view of the LO/RF optics in the GUBBINS system. A fraction of the uncoupled LO signals are absorbed by the load, and the rest of uncoupled LO signals are reflected back to the room temperature environment.

expected -17 dB. In fact the measurements done in Sec 6.6.2 implied that the directional LO coupler provided a coupling efficiency of ∼-14 dB. The strong coupling of the LO coupler, which behaved as a thick beamsplitter to reflect/absorb the RF radiation, enhanced the optical noise and reduced the optical gain. In addition, since the GUBBINS LO suffered from excess noise at the band edges, further coupling increased the LO noise.

For a receiver chain with the LO coupler, the cascaded receiver noise temperature equation for the GUBBINS cryostat is,

$$T_{\rm rec} = (L_{\rm window} - 1) \times T_{\rm room} + \frac{(L_{\rm coupler} - 1)T_{\rm 4K} \times a + (L_{\rm coupler} - 1)T_{\rm room} \times (1 - a)}{G_{\rm window}} + \frac{T_{\rm trans}}{G_{\rm window}} + \frac{T_{\rm SIS}}{G_{\rm window}G_{\rm coupler}G_{\rm trans}} + \frac{T_{\rm coldIF}}{G_{\rm window}G_{\rm coupler}G_{\rm SIS}G_{\rm trans}} + \frac{T_{\rm warmIF}}{G_{\rm window}G_{\rm coupler}G_{\rm SIS}G_{\rm coldIF}G_{\rm trans}} \tag{4.19}$$

where a is a fraction that denotes the coupling weighting coefficient at the physical temperature of the LO coupler. Since the LO coupler is located at the 4 K stage, the noise contribution from the coupling loss in GUBBINS system should be rather smaller compared to the Wet Dewar, where the Mylar beamsplitter was placed at room temperature. However we can see that the physical temperature $T_{\rm phy}$ for the LO coupler cannot simply be taken as 4 K. Instead, for an LO coupler, only a fraction of the uncoupled LO power was absorbed by the LO load located at the end of the waveguide (4 K) and $1 - a$ of the uncoupled power was directly reflected back to the LO source (290 K, see Fig 4.33). So the LO coupler was in fact looking at both the 4 K stage and the 290 K room temperature. Therefore the effective physical temperature for the LO coupler that should be used in calculating the optical loss, is a weighted average of 4 K and 290 K. The coefficient a is determined by the matching between the LO load and the WR-4 waveguide, and also the matching

between the GUBBINS LO optics and the WR-4 waveguide. In Tab 4.5, we show the breakdown of noise temperature at three RF frequencies. Values of a are calculated such that the sum of the noise temperature is equal to the measured receiver noise temperature, assuming LO noise can be ignored and the quantum noise of SIS junction are identical in both the Wet Dewar and the GUBBINS system.

At 210.6 GHz and 216 GHz we measured similar noise temperature in both of the two systems, but at 243 GHz the noise temperatures measured in GUBBINS system was ∼88 K higher than the one measured in the Wet Dewar. Consequently the calculated weighting coefficient a was around 90% at 210.6 GHz and 216 GHz, and around 60% at 243 GHz. This implied the LO load was better matched to the LO couplers at frequencies around 220 GHz so that most of the uncoupled LO signals were terminated at 4 K. However at frequencies approaching the band edges, the matching between LO load and the mixer may have started to deteriorate and a substantial part of the uncoupled LO was reflected to the room temperature port, which greatly enhanced the optical noise contribution.

	Optics(K)	Mixer(K)	ColdIF(K)	Total(K)	a%
210.6GHz	11	67	32	110	89%
216GHz	10.5	30	34.5	75	93%
243GHz	41	84	80	210	62%

Table 4.5: The breakdown of the noise temperature measured at three RF frequencies, in GUBBINS and Wet Dewar system. At 210.6GHz and 216GHz, we measure similar receiver noise temperatures in the two systems, but at 243GHz we see a ∼90K noise temperature difference between them.

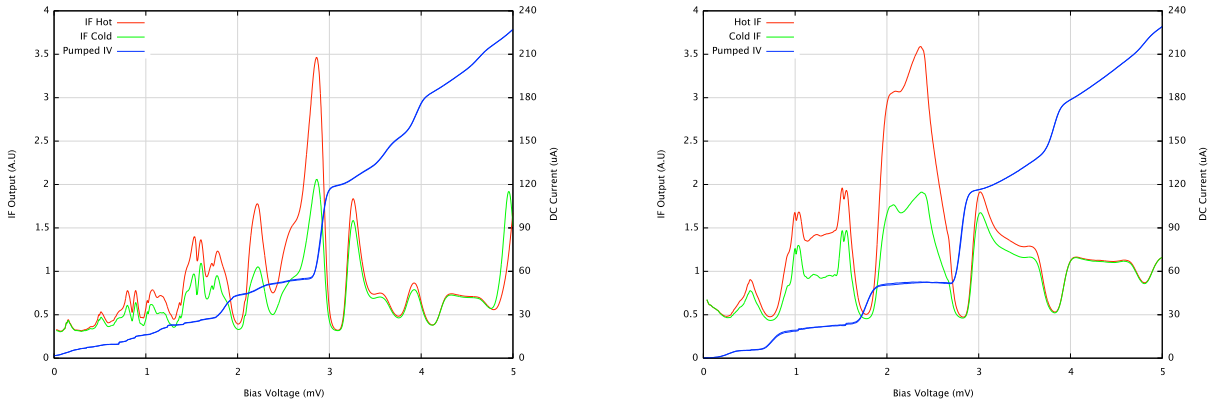

(a) (b)

Figure 4.34: The I-V and I-F characteristic curves for device C5N1 taken in (a) GUBBINS system and in (b) Wet Dewar.

Here we emphasized that the optical coupling loss may not be the only reason for the increase in the receiver noise temperature in the GUBBINS system. In GUBBINS system, higher harmonics

from the GUBBINS LO source were more difficult to suppress than in the Wet Dewar, especially at frequencies above 245 GHz, since we could not use a thin beamsplitter in GUBBINS system to reduce the LO noise. The pumped I-V and I-F curves recorded for device C5N1 in either the GUBBINS system or the Wet Dewar at 255 GHz, shown in Fig 4.34 are the evidences. Extra photon steps can be clearly seen on the first photon in the I-V curve taken in the GUBBINS system corresponding to the peaks shown in the IF curve. However in the Wet Dewar, we were able to suppress the harmonics as can be seen in both I-V and I-F curves. Since the Gunn LO could not be used in conjunction with the GUBBINS system, it was hard to determine how much the harmonics have affected the performance. We believe that if a clean LO was also available in the GUBBINS system, a lower noise temperature would have been measured at the higher frequency end.

4.5 Summary

We have presented the measured performance for silicon SIS unilateral finline mixers operating around 230 GHz, which were tested in two independent cryogenic systems. In general, the devices were very easy to pump and the best ones exhibited state-of-the-art performance. The electromagnetic modeling and the measured performance have demonstrated the integrity of the mixer design and also indicated that the design is tolerant of a small range of manufacturing errors in the SIS junction size and tuning circuits. The measured performance showed good agreement with computed predictions.

A best noise temperature of 50 K and an average noise temperature of 75 K over 80 GHz RF bandwidth were measured for one device. A mixer noise of 11 K, which is close to the quantum noise limit at 219 GHz, was achieved for the particular SIS device. For another two devices, best noise temperatures of 80 K and an average noise temperature of 100 K over 50 GHz RF bandwidth were measured. Following thorough analysis of the RF and IF contribution of the receiver noise, it was found that the thickness of the mixer substrate played an essential role in the receiver performance with a thicker substrate deteriorating the performance at the band edges. By correcting the measured receiver noise against substrate thickness for two devices with thicker substrates, significant improvements in the receiver noises could be obtained at RF frequencies above 240 GHz. The SIS mixers were also tested in the GUBBINS cryostat, in which an LO waveguide coupler was used to coupled the LO power into the SIS mixer. The mixers could be very well pumped in the GUBBINS system and reasonably good noise temperatures could be measured. However, higher noise temperatures were measured in GUBBINS cryostat than in the Wet Dewar around the band edges as a result of higher LO coupling and lack of spectral purity in the LO source.

An important conclusion for this chapter is that the silicon unilateral finline mixer, which is

featured by easy design and fabrication, can indeed deliver state-of-the-art performance over 160–260 GHz range.

Chapter 5

SIS Mixer IF performance tests

Overview: The IF system is the collective term given to the components that make up the pathway between the IF port of the SIS junction and the data acquisition system. Typical SIS mixers might have an IF bandwidth of ∼2 GHz which is usually sufficient for broad extragalactic spectral line observations. However for CMB observations where weak continuum sources are involved, SIS mixers with a wide IF band are desirable since a wide IF bandwidth enhances the instrument brightness sensitivity. With a wide IF bandwidth (∼15–20 GHz), SIS mixers can be as sensitive as TES bolometers but with the added advantages of orders of magnitude higher dynamic range and much easier fabrication, integration and readout. To broaden the IF bandwidth, SIS mixers must be designed with low lumped capacitance and inductance, and with the RF circuits effectively decoupled from the IF circuits. However relatively large capacitance and inductance can still be tolerated with rigorously designed IF matching circuits, which could perform the impedance matching between the SIS mixer and the LNA. In this chapter, we review the SIS mixer design, in particular the on-chip IF circuit design, and also introduce the design of IF matching circuits. To verify the mixer IF performance, we adopted two experimental setups to test the mixer performance either over the full IF bandwidth (i.e 0–16 GHz) or over several small IF bandwidths (i.e 3-4 GHz, 4-6 GHz).

5.1 The IF circuit design of SIS mixer

SIS based heterodyne receivers currently in use on major telescopes were usually built with limited IF bandwidths of a few GHz, although some recent work has extended the IF bandwidth up to 8 GHz [61]. If an SIS mixer is operated with a cryogenic amplifier (LNA) whose input impedance is 50 Ω, the impedance mismatch between the complex output impedance of SIS mixer and the LNA can cause the overall receiver gain and noise temperature to substantially deteriorate in particular at

high IF frequencies.

The deterioration is generated by two mechanisms: (i) IF signals emitted from the output of SIS mixer undergoing multiple reflections between the mixer and the LNA due to the mismatch; (ii) Noise waves outgoing from LNA input port being reflected at the mixer and returning to interfere and correlate with the ingoing noise wave [7]. To avoid the reflection, an isolator is usually inserted between the SIS mixer and the LNA. However the insertion of an isolator is not without price. The thermal noise from the internal termination of the isolator is partially reflected at the mixer and adds to the IF noise, which can significantly enhance the receiver noise temperature, even at an ambient temperature of 4 K [7]. Also the commercial isolators usually have limited IF bandwidths (e.g 4 GHz–6 GHz), the insertion of an isolator can limit the total bandwidth of the SIS mixer receiver. Consequently our IF system did not use an isolator.

To expand the mixer IF bandwidth, a variety of techniques have previously been attempted. For example, using multiple SIS junctions distributed in series [99], limiting the size of the planar circuits [7], directly integrating the mixer with the MMIC preamplifier [76][67] and applying a matching circuit between the SIS mixer and the LNA [100] are all the solutions previously attempted to maximize the IF bandwidth of SIS mixers. For the unilateral finline SIS mixer, there are mainly two factors that limite the IF bandwidth: (1) The mixer output inductance/capacitance which is determined by the SIS junction and the planar circuits on the device. The mixer output reactance directly dictates the degree of complexity of the IF matching circuit and also the quality of the IF matching; (2) A resonant circuit which could be generated by the lumped inductance/capacitance in the RF circuit before the SIS junction. If the resonant frequency of the resonant circuit is within the band it limits the useful IF bandwidth of the mixer. The mixer chip should therefore be designed to shift the resonant frequency outside the desired IF frequency band. The output inductance/capacitance should be kept as small as possible to ease the design of the matching network. It is clear from ongoing research that [7], in order to reduce the IF output capacitance of a waveguide SIS mixer, the capacitance of the RF matching circuits and the intrinsic capacitance of the SIS junction must be reduced. To obtain a 10 GHz IF bandwidth of the mixer without inserting any matching circuit between the mixer and the LNA, only 300 fF capacitance is allowed to exist on the device, including the intrinsic capacitance of the SIS junction [88]. Therefore, if no IF matching network is employed, the effective capacitance of the SIS junction must be substantially reduced by using several junctions in series to reduce the overall capacitance [88]. To reduce the output inductance, the inductance of the RF choke and the bonding wires must be kept at minimum.

In our mixer, we used planar circuits with small surface area and a single SIS junction with small

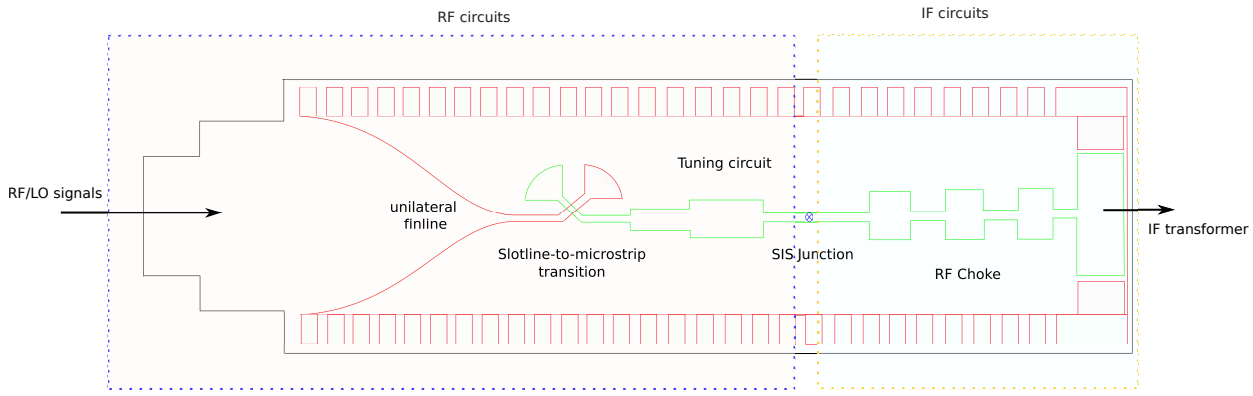

Figure 5.1: A schematic drawing of the SIS mixer design. The black line denotes the silicon substrate. The red line denotes the ground plane whose major structures are the finline taper. The green line denotes the wiring layer whose major structures are the microstrip lines. The blue cross represents the SIS junction. The dimensions in the Figure are not to scale for clarity.

intrinsic capacitance, to maintain low capacitance. Also an independent matching circuit was designed to match the mixer output impedance to the 50 Ω impedance of the LNA. A schematic drawing of the mixer planar circuit is illustrated in Fig 5.1. We use the blue dashed frame to enclose the RF circuits and the yellow dashed frame to enclose the IF circuits. The ground plane (labelled in red) contacts the mixer block through a direct contact and ground bonding wires, and the IF signal carried by the wiring layer (labelled in green) is transmitted to the IF transformer that closely follows the SIS mixer. The RF radiation propagating in the waveguide was coupled to the device by a unilateral finline and then coupled to the microstrip lines using two radial stubs. The SIS junction was fabricated across the microstrip line. The junction tuning circuit, consisting of several stages of microstrip transmission lines was used to tune out the intrinsic capacitance of the SIS junction, allowing the RF radiation to couple to the SIS junction over the widest possible RF bandwidth. The weak astronomical signal and the strong LO signal were combined in the SIS junction, and the IF signal with the difference frequency could then be generated. To block RF signals from leaking into the IF circuit and to transmit the IF signals over a wide IF bandwidth, we used a six-stage microstrip line RF choke. The surface area of the RF choke was relatively small and the total length of the microstrip line was short, to reduce the capacitance and inductance. The bonding pads were connected to an IF transformer circuit fabricated from copper microstrip on 0.254 mm thick Duroid by aluminum bond wires. To further minimize the inductance, the signal bond wires were kept as short (∼200 μm) as possible. Also, we often used more than one bond wire in parallel to further reduce the inductance.

However even by keeping the area of the planar circuit small to control the lumped capacitance and inductance, the output impedance of the SIS mixer is still not likely to be matched to the following LNA. This is because the embedding impedance is a strong function of the frequency of the junction

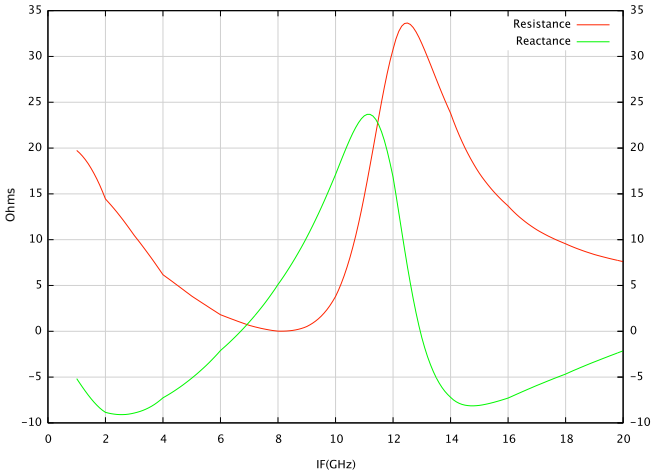

Figure 5.2: The output impedance of a unilateral finline SIS mixer.

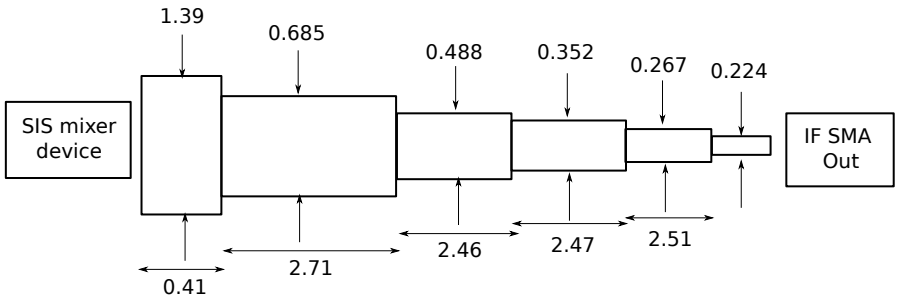

Figure 5.3: A schematic drawing of the resistance IF transformer. All the dimensions are in mm.

capacitance. The complex output impedance for a unilateral finline SIS mixer, calculated by *Ansoft* Designer, is presented in Fig 5.2. Directly connecting the IF output of the SIS mixer to a 50 Ω LNA would result in an IF return loss of about -3 dB over IF bandwidth 1 GHz –10 GHz and even worse at higher IF frequencies.

Therefore we designed an IF transformer to match the mixer output to the LNA, which has a 50 Ω input impedance. This IF transformer which we used in the first IF experiment was originally designed for another waveguide antipodal finline SIS mixer, which used a similar SIS junction and similar planar circuit design [58]. It consisted of a five stage quarter-wave transformer connecting the mixer bonding pads to input of the LNA. The transformer design was optimized in *Ansoft* designer in conjunction with the HFSS to match the 50 Ω input of the LNA to the bonding wires and normal resistance of the SIS junction. Consequently the reactance contributed by the radial stubs in our design was not taken into account in this transformer design.

The LNA we used in the experiment was manufactured by Caltech and has an operating bandwidth of 2–15 GHz. The performance of the LNA over the IF bandwidth is shown in Fig 5.4. In the

experiment, stainless steel coax cables were used to connect the mixer, the bias tee and the LNA. To reduce the losses at high IF frequencies, the cables used between the LNA and the mixer were made as short as possible.

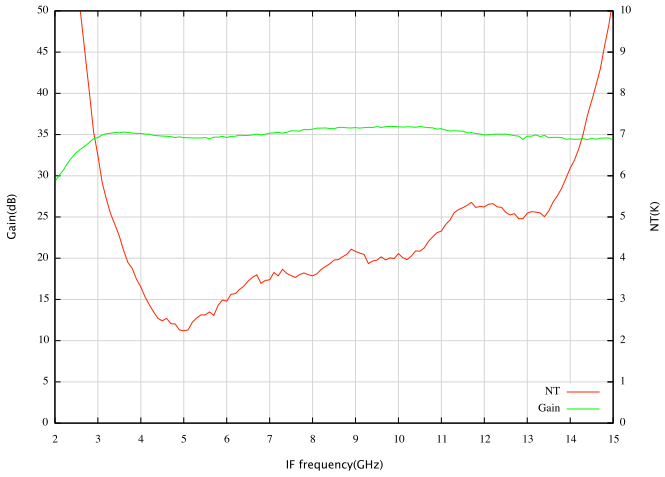

Figure 5.4: The noise temperature (NT) and gain measured for the LNA at ambient temperature of 9 K [81].

5.2 First IF tests of the mixer

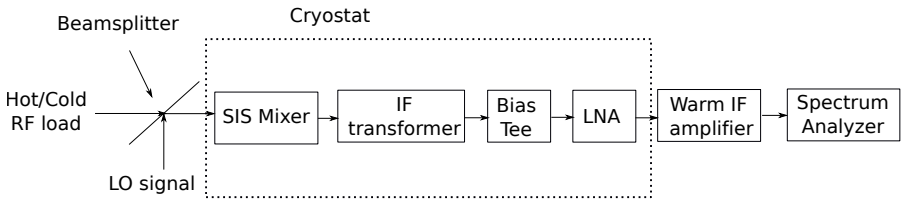

Figure 5.5: A schematic diagram showing the experimental layout used in the IF testing when a spectrum analyzer was used to measured the mixer IF performance over the full IF spectrum (2-16 GHz).

In this experiment, the IF performance of device C3N1 in conjunction with the IF transformer was measured using a spectrum analyzer over the IF bandwidth 2–16 GHz. The schematic diagram for the setup is shown in Fig 5.5. To test the broadband IF performance of the mixer, the IF filter was removed from the warm IF chain. The hot and cold IF power were directly measured by the spectrum analyzer and read by the computer through GPIB card under the Pylab environment. The noise temperatures could be calculated through the measured Y-factor ($Y = \frac{P_{\rm hot}}{P_{\rm cold}}$) at each sampled IF frequency. Thus we managed to obtain an IF performance of the SIS mixer over the full 2–16 GHz bandwidth. The measured IF noise temperature spectrums are shown in Fig 5.6, at RF frequencies of

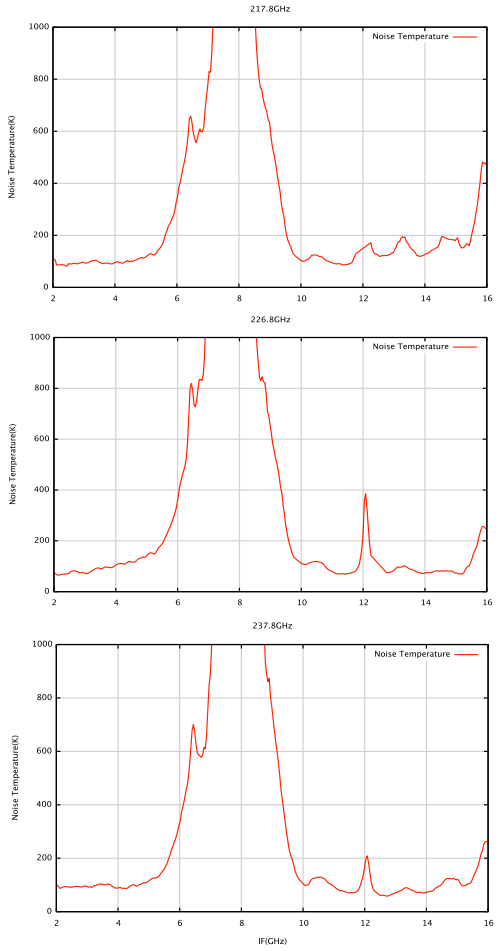

Figure 5.6: The IF noise temperature spectrums measured using a spectrum analyzer with LO radiation at frequencies of (Top) 217.8 GHz, (Middle) 226.8 GHz and (Bottom) 237.8 GHz.

217.8 GHz, 226.8 GHz and 237.8 GHz.

Over an IF bandwidth 2–15 GHz, the noise temperature measured for SIS mixer receiver was approximately flat below 100 K, apart from a strong deterioration at 8 GHz with a bandwidth of ∼4 GHz (Fig 5.6). We attribute this deterioration to an effective RLC resonant circuit with a resonance frequency at 8 GHz, existing before the SIS junction. The working IF bandwidth was therefore split into two separate sections: 2 GHz–6 GHz and 10 GHz–15 GHz. In the range 7 GHz–9 GHz, the noise temperatures were too high for any practical application. The mixer therefore had a useful performance over a 9 GHz bandwidth. We shall investigate in details the causes of the resonance circuit in Sec 5.4.1. In what follows, however we will focus on analyzing the mixer performance over 2–6 GHz, where the mixer performance is not strongly affected by the IF resonance.

We first simulated the performance of device C3N1 in conjunction with the IF transformer in HFSS software and in SuperMix package over 2–6 GHz and the results are shown in Fig 5.7. We also

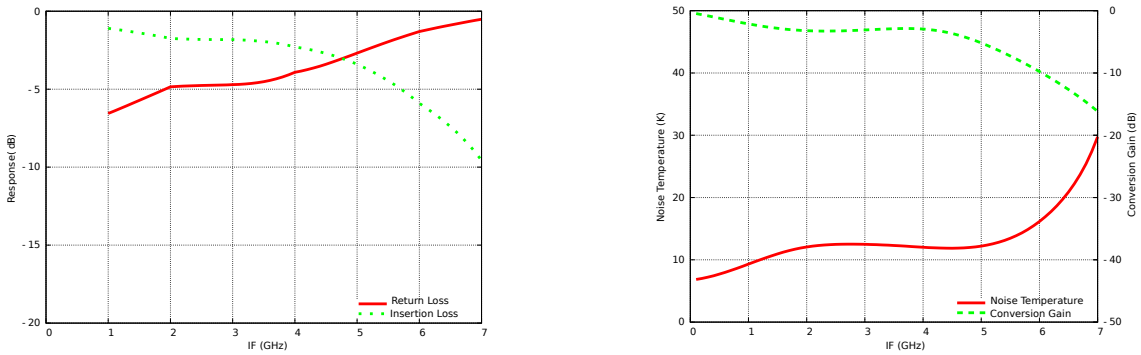

(a) (b)

Figure 5.7: (a) The HFSS simulated return loss and insertion loss for device C3N1 in conjunction with the first IF transformer. (b) The SuperMix simulated noise temperature and conversion gain.

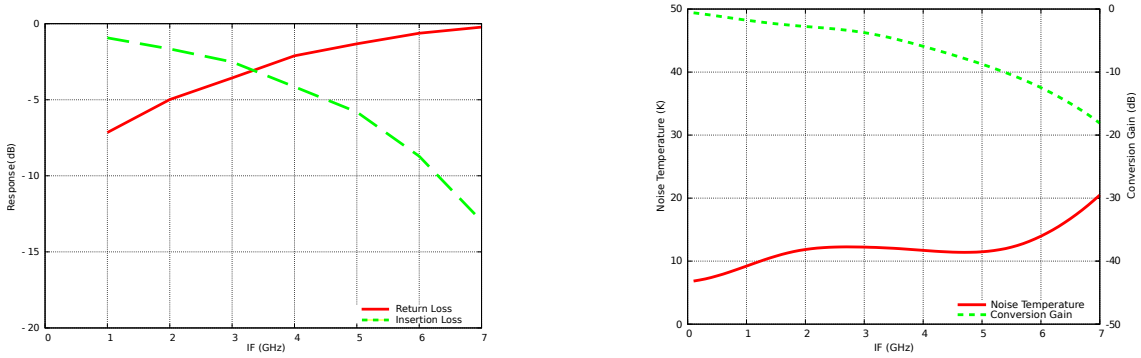

(a) (b)

Figure 5.8: (a) The HFSS simulated return loss and insertion loss for device C3N1 with no IF matching circuit. (b) The SuperMix simulated noise temperature and conversion gain.

show the simulated performance for device C3N1 itself, without any IF matching circuit in Fig 5.8, to illustrate the improvement brought by the IF transformer. It can clearly be seen from these figures that, the IF transformer only slightly improved the mixer performance over 2–6 GHz, reducing the mixer return loss by ∼2 dB and increasing the mixer conversion gain by ∼2 dB. This is because this IF transformer was not designed for this unilateral finline mixer and the planar circuits on the mixer device, in particular the radial stubs, were not taken into account in the IF transformer design. The mixer output impedance therefore was not well matched to the 50 Ω LNA. We will later present an alternative IF transformer design which is better suited to match this mixer device to the LNA.

Next, we measured the noise temperature contributed by the IF system, by using Woody's method (Sec 4.2.4). In Woody's method, we altered the LO power to change the mixer conversion gain, while the mixer noise temperature kept almost unchanged. A group of curves which showed the IF output power as a function of the input blackbody noise temperature can be collected. They had different

slopes which correspond to different LO power. These group of curves intersected at almost one point, and the temperature of this point indicated the RF noise temperature of the receiver system.

The IF noise temperature included the noise from the LNA and the noise from the IF mismatch. The results are shown in Fig 5.9, together with the noise temperature spectrum of the LNA. Over 2–4 GHz, the mixer IF noise is almost equal to the LNA noise which meant there is almost no IF mismatching in the circuit. Above 4 GHz however, the IF contributed noise started to become significantly higher than the LNA noise which meant the IF mismatch started to appear. This conclusion is consistent with the simulated mixer performance in HFSS and SuperMix (shown in Fig 5.7), that above 4 GHz the IF matching becomes very poor. Notice that the mixer performance at frequencies below 2 GHz was limited by the LNA performance degradation.

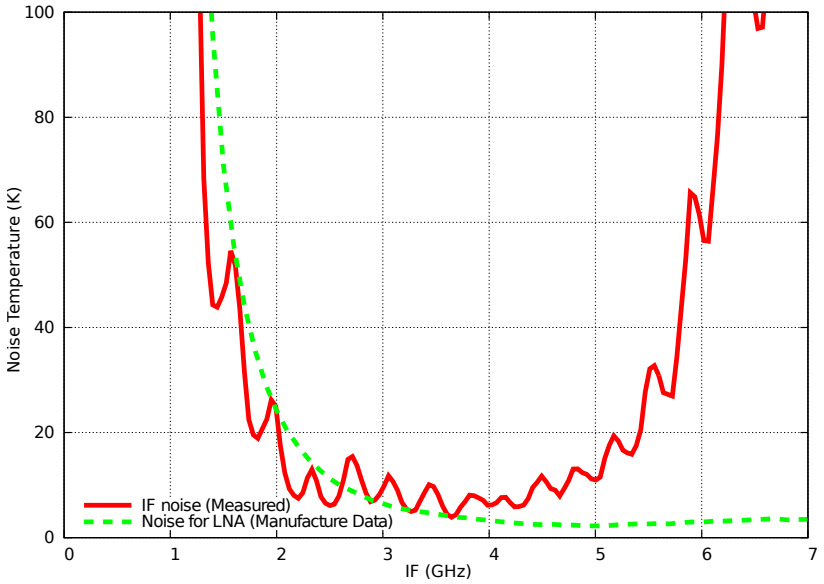

Figure 5.9: The noise temperature contributed by the IF system over 0–7 GHz measured by the spectrum analyzer (green line) and the LNA noise temperature performance provided by the manufacturer (red line).

Apart from measuring the mixer performance using the spectrum analyzer, we have also tested device C3N1 over the IF bandwidth 4–6 GHz using the conventional diode method, with a 4–6 GHz IF bandpass filter inserted in the warm IF chain. The schematic diagram for testing the mixer using the diode detector is shown in Fig 5.10. In Fig 5.11, we plot the measured noise temperature and the conversion gain as a function of the RF frequency integrated over an IF bandwidth of 4–6 GHz. The average noise temperature is around 100 K and the average conversion gain is around -5.5 dB. Noise temperatures of 91 K, 84 K and 85 K were measured at 217.8 GHz, 226.8 GHz and 237.8 GHz respectively. If we integrate both the hot and cold IF power spectrums measured by the spectrum analyzer from 4 GHz to 6 GHz and use the integrated hot and cold IF power to calculate the noise

temperature [63], we obtain 112 K at 217.8 GHz, 134 K at 226.8 GHz and 109 K at 237.8 GHz (shown in Tab 5.1). We therefore notice that the noise temperatures measured by the spectrum analyzer (Fig 5.6) were higher than the ones measured by the bandpass filter over the same IF bandwidth. This indicates that the spectrum analyzer could only provide a useful qualitative assessment of the mixer performance, but is not accurate enough to provide a high quality measurement.

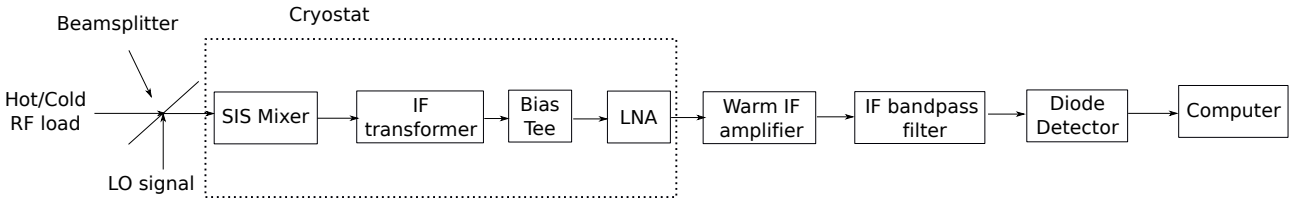

Figure 5.10: The schematic diagram showing the experimental layout in the IF testing when the IF bandpass filter was used in the IF chain to confine the IF bandwidth to 4–6 GHz.

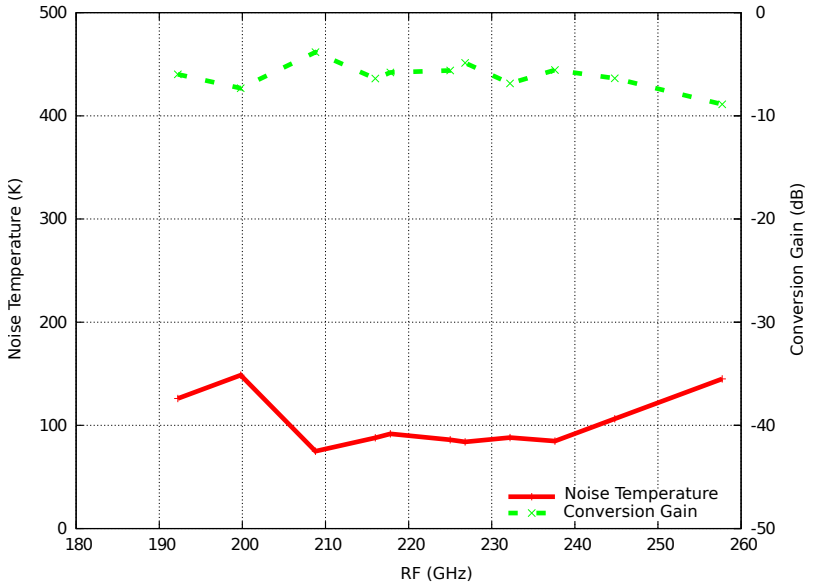

Figure 5.11: The noise temperature and conversion gain measured across the RF bandwidth of 190–260 GHz within an IF bandwidth of 4–6 GHz, using the diode detector.

Frequency (GHz)	IF Filter (K)	Spectrum Analyzer (K)
217.8	91.8	112
226.8	84	134
237.8	85	109

Table 5.1: Comparison of the measured noise temperature by the spectrum analyzer with them measured by the diode detector over an IF bandwidth of 4–6 GHz.

5.3 IF tests of the mixer with a 2–6 GHz transformer

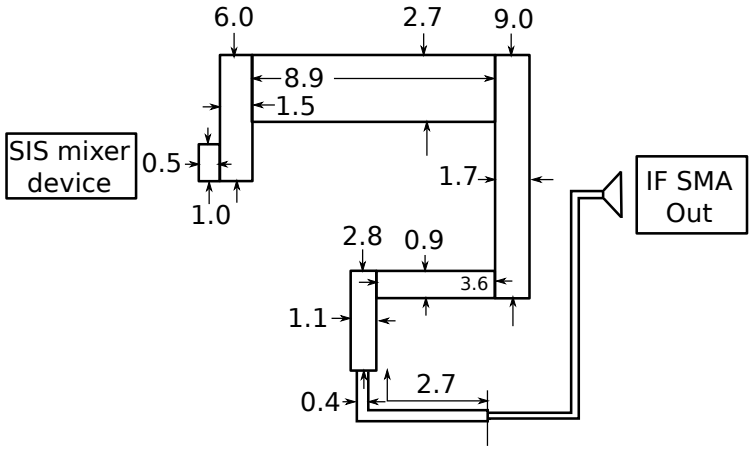

Figure 5.12: A schematic drawing for the IF transformer used in conjunction with device C5N1. All dimensions labelled here are in mm.

In the last experiment (Sec 5.2), device C3N1 was assembled with an IF transformer which could not effectively match the mixer output impedance across the desired IF band. In this experiment, we described the design of a new IF transformer to optimize the mixer performance over 2–6 GHz, matching both the mixer output resistance and reactance to the 50 Ω LNA. Since this transformer was designed to achieve the best matching only over 2–6 GHz, the mixer performance above 6 GHz was intentionally sacrificed. The new IF transformer consisted of eight stages of microstrip transmission lines deposited on 0.245 mm thick Duroid 6010 substrate. The first two stages tuned out the mixer output reactance at two frequencies and the later five stages, which were a 5-stage binomial transformer, performed the resistance matching. The last stage was a section of 50 Ω transmission line. At the end of the IF microstrip line, a triangular shaped island was fabricated to ease the soldering of the IF transformer to the SMA pin. The schematic drawing and the dimensions of the IF transformer are shown in Fig 5.12. Device C5N1 was used to test the mixer IF performance in conjunction with the new IF transformer.

We first simulated the performance of device C5N1 in conjunction with the new IF transformer in both HFSS software and the SuperMix package. In Fig 5.13, we show the S-parameter data and the noise temperature/conversion gain performance of the mixer. We also show the HFSS and SuperMix simulation for device C5N1 operating with no IF matching circuit in Fig 5.14 for comparison. It can clearly be seen that the new IF transformer improves substantially the mixer performance over 2–6 GHz, giving a ∼10 dB return loss across the bandwidth. The new IF transformer therefore achieved 5 dB better return loss and 2 dB better conversion gain than the previous transformer.

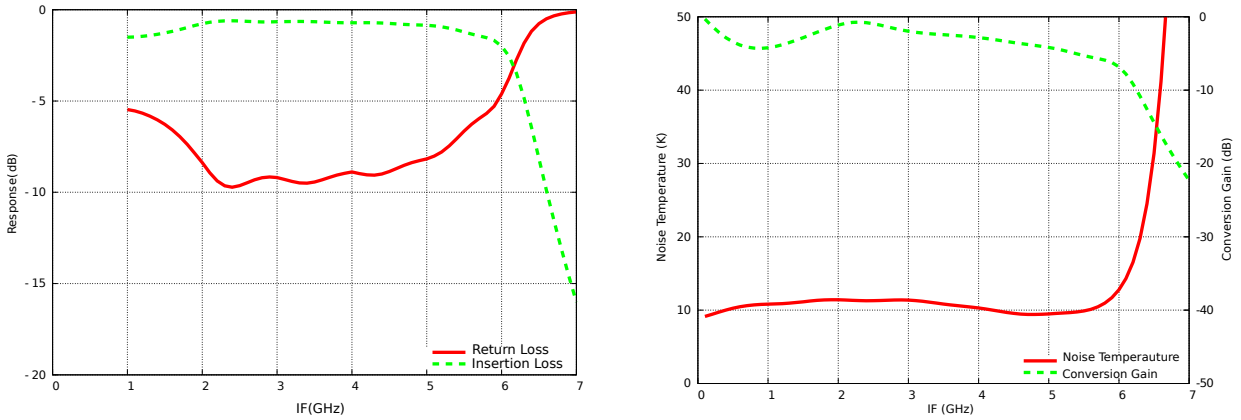

(a) (b)

Figure 5.13: (a) The HFSS simulated return loss and insertion loss for device C5N1 in conjunction with the new IF transformer. (b) The SuperMix simulated noise temperature and conversion gain.

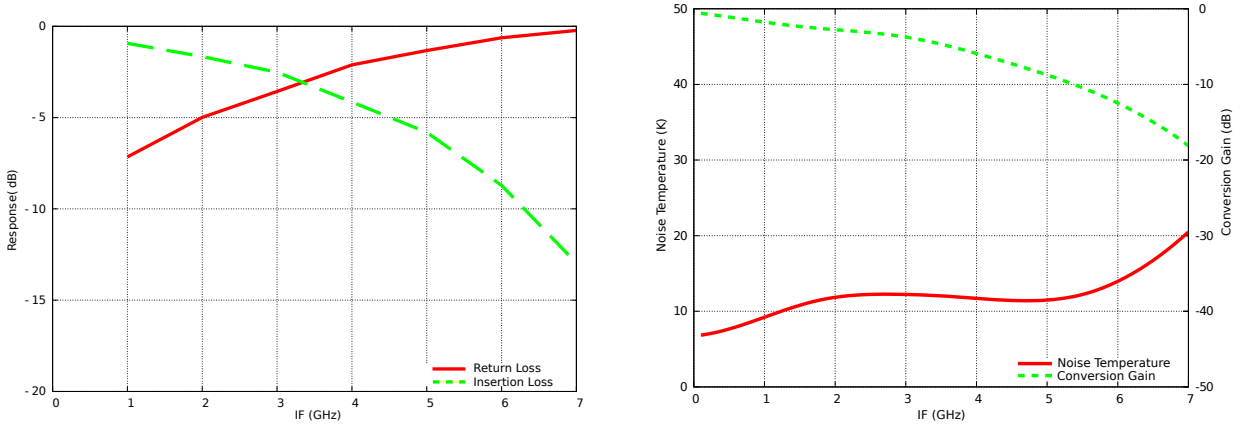

(a) (b)

Figure 5.14: (a) The HFSS simulated return loss and insertion loss for device C5N1 with no IF matching circuit. (b) The SuperMix simulated noise temperature and conversion gain.

Due to the uncertainties in interpreting the measurements made by the spectrum analyzer, we decided to improve the accuracy by measuring the IF performance using the conventional diode detector, over different small IF bands. These individual IF bands were defined by different IF bandpass filters. A schematic diagram illustrating the experimental layout is shown in Fig 5.10.

Three edged-coupled IF bandpass filters with bandwidth 3–4 GHz, 4–6 GHz and 3.75–4.25 GHz were designed and constructed by our group. We show the schematic drawing and the scattering parameter performance measured by a vector network analyzer (VNA) for the 3–4 GHz filter in Fig 5.15. This filter is a combination of a low-pass filter and an edge-coupled bandpass filter. The edge-coupled (or parallel-coupled) microstrip bandpass filter uses half-wavelength line resonators. The adjacent resonators are parallel to each other along half of their length. This design is particularly

suitable for constructing filters with a wide bandwidth, compared to the structure of the end-coupled microstrip filters [78].

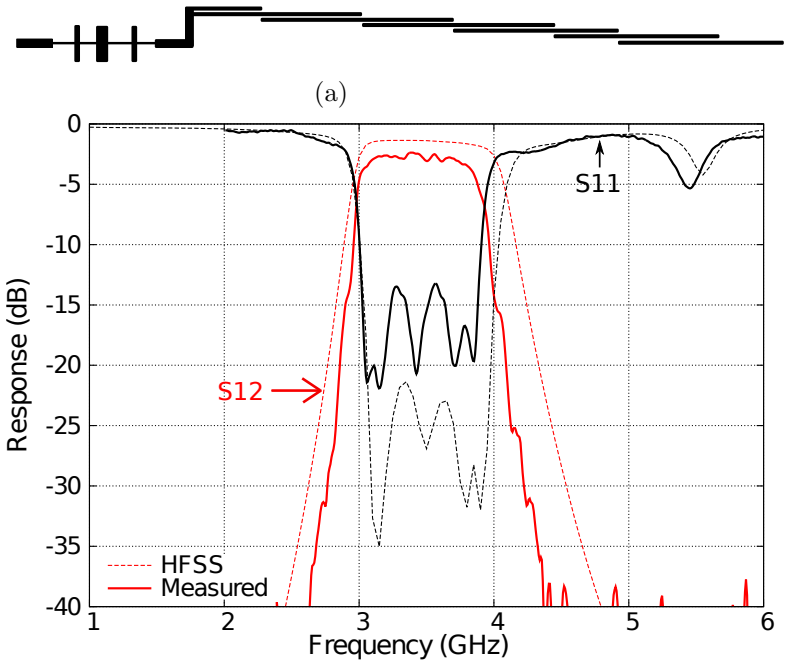

Figure 5.15: (a) A schematic drawing of a 3–4 GHz edge-coupled IF filter. The dimensions shown here are not to scale for clarity. (b) The simulated and measured performance of the 3–4 GHz bandpass filter. The solid line shows the measured performance and the dashed line shows the simulated performance. The filter was designed by Dr. Boon Kok Tan.

The noise temperatures measured over different IF bands are displayed in Fig 5.16. Over 3–4 GHz, which is the IF bandwidth with the best predicted performance (see Fig 5.13), we manage to measure noise temperatures below 100 K over an RF frequency range of 215 GHz–260 GHz and to obtain a best noise temperature of 50 K at 219 GHz. We can also observe clear improvement of the noise temperature and conversion gain as the IF bands was shifted from 4–6 GHz to 3–4 GHz at most of the RF frequencies. Within IF bandwidth of 3–4 GHz, the averaged noise temperature was 66 K. Within IF bandwidth of 4–6 GHz, the average noise temperature was 99 K. For the conversion gain, we could observe a ∼1–2 dB improvement in the 3–4 GHz IF band, compared to the 4–6 GHz IF band. This is in agreement with the SuperMix simulations which showed that the conversion gain between 3-4 GHz was ∼2 dB better than the gain between 4–6 GHz. Additionally, a T_{IF}=16 K IF noise temperature was measured over 4–6 GHz IF band while a T_{IF}=10.1 K IF noise temperature was measured over 3.75–4.25 GHz IF band and a T_{IF}=8.62 K IF noise temperature was measured over 3–4 GHz IF band. If we subtract the IF contribution ($T_{\mathrm{IF}}/G_{\mathrm{ConversionGain}}$) from the total receiver noise temperature, whatever was left should be attributed to the RF noise contribution. We therefore

plotted the RF contributions in Fig 5.17 for all three IF bands and we found that the RF contribution in three IF bands were very close to each other. This demonstrated that the increments in the noise temperature at the higher IF bands were indeed caused by the IF mismatch. This IF mismatch did not only degrade the conversion gain, but also increase the IF noise contribution at higher IF frequencies (i.e 16 K over 4–6 GHz, 10 K over 3.75–4.25 GHz and 8.6 K over 3–4 GHz).

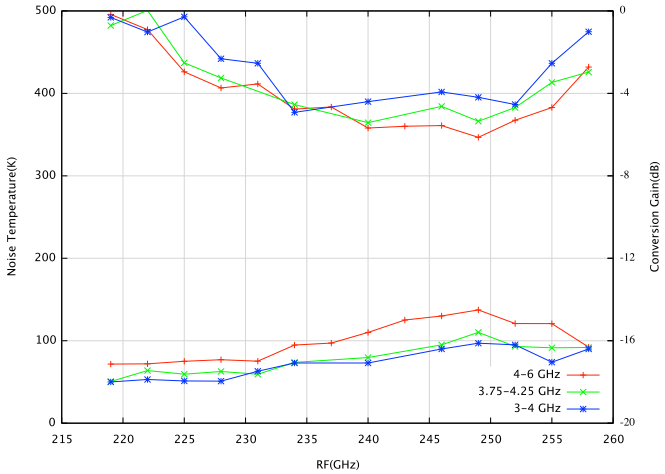

Figure 5.16: The noise temperature measured in various IF bands by using different IF band pass filters as a function of RF frequency (219 GHz–260 GHz).

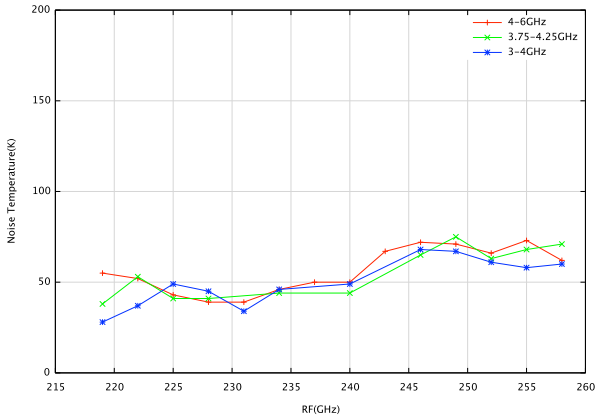

Figure 5.17: The calculated RF noise temperature using the equation $T_{\text{receiver}} - T_{\text{IF}}/G_{\text{ConversionGain}}$ in IF bands 3–4 GHz, 3.75–4.25 GHz and 4–6 GHz.

From this experiment, we were pleased to find that good matching (i.e -10 dB return loss over 3–4 GHz) could indeed substantially improve the mixer performance. It seems that -10 dB return loss is a bench mark to obtain a qualified IF matching, that does not restrict the conversion gain. Our IF transformer between 4–6 GHz was still not good enough because in the 4–6 GHz range the resonance at 8 GHz made the resistance over 4–6 GHz very low (∼2 Ω) and much lower than the resistance at

low IF frequencies (i.e 15 Ω at 2 GHz). The quality of the IF matching circuit is therefore limited by the large variance over the desired IF bandwidth. In the future design, the resonant circuit will be removed outside the desired IF band, hence the resistances across the IF band would become more uniform.

5.4 Design Modification

5.4.1 Analysis of the resonant circuit

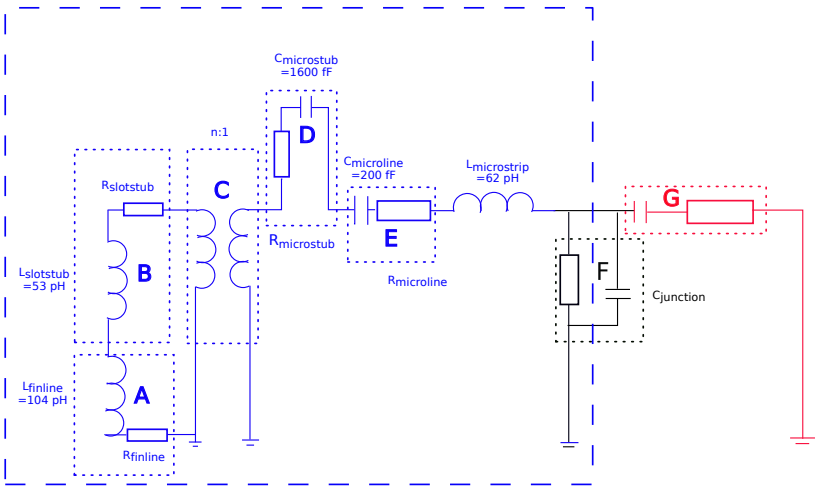

Figure 5.18: The equivalent RLC circuit for the unilateral finline SIS mixer in the IF band. A: unilateral finline. B: 90° slotline-stub . C: the mutual inductance between 90° slotline stub and 90° microstrip stub. D: 90° microstrip-stub. E: Tuning circuits before SIS junction. F: SIS Junction. G: Tuning circuits after SIS junction and RF choke. The circuits within the blue dashed frame are the resonant circuits. The estimated values for the lumped capacitance and inductance are labelled in the Figure.

In the IF band the propagating wavelength is far greater than the physical sizes of the planar circuits, hence the planar circuits of the mixer chip can be regarded as lumped element circuits, whose capacitance and inductance are largely determined by their physical geometry. Consequently we shall analyze the mixer IF performance using the RLC lumped element equivalent circuit of the mixer as shown in Fig 5.18 [101]. In the equivalent circuit, the finline and the 90° slotline stub are respectively represented by lumped inductances L_{finline} and L_{slotstub} in series with characteristic impedance R_{finline} and R_{slotstub}. As the finline and the slotline structure contribute very small capacitance (<50 fF), we shall ignore their capacitance in the equivalent circuit for simplicity. The power coupling between the slotline and the microstrip is achieved by a pair of 90° radial stub through electromagnetic field and this is represented by a mutual inductance with a transforming factor of n. The 90° radial stub and all the other microstrip structures before the SIS junction are respectively represented by

lumped capacitances $C_{\text{microstub}}$ and $C_{\text{microline}}$ and characteristic impedances $R_{\text{microstub}}$ and $R_{\text{microline}}$. The inductance of all the microstrip lines before the SIS junction is represented by $L_{\text{microstrip}}$. The SIS junction is represented by its intrinsic capacitance in parallel to its normal resistance. Since the unilateral finline acted as the ground plane for all the planar circuits including the SIS junction, a resonant circuit is formed by all the circuits between the unilateral finline (included) and the SIS junction, which is framed by the dashed line in Fig 5.18.

Rigorous analysis of the equivalent circuit was performed using the actual planar circuit and the finline taper in waveguide employing the HFSS software. To investigate the influence of various components on the resonant frequency we performed the following tests.

By removing the finline structure from the model (Test 1 and Test 2), the resonant frequency shifted from 8 GHz to 11 GHz. By gradually reducing the opening angle of the slotline radial stub from 90° to 2° (from Test 2 to Test 6), the resonant frequency only shifted from 11 GHz to 12 GHz. By completely removing the slotline structure from the model (Test 7), the resonant frequency shifted from 12 GHz to 15 GHz. This demonstrates that the slotline structure indeed contributes significantly to the inductance of the resonant circuit. This contribution is largely proportional to the length of the slotline but not very sensitive to the slotline width.

In Test 8, the opening angle of the radial microstrip line stub was reduced from 90° to 45° causing a large shift in the resonant frequency. This demonstrates that the 90° microstrip stub has the largest contribution to the lumped capacitance and their contributed capacitance is almost proportional to their surface area. The microstrip lines contribute very litter to the capacitance because of their small collective area. In addition, it is shown in the simulations that the parasitic capacitance C_{j} of the SIS junction was not included in the resonant circuit that the value of C_{j} does not affect the location of the resonate frequency.

	Finline	Slotline Stub (Open Angle)	Mirostrip Stub (Open Angle)	Resonant Frequency
Test 1	$\surd$	90°	90°	8 GHz
Test 2	×	90°	90°	11 GHz
Test 3	×	45°	90°	11 GHz
Test 4	×	15°	90°	11 GHz
Test 5	×	3°	90°	11.5 GHz
Test 6	×	2°	90°	12 GHz
Test 7	×	×	90°	15 GHz
Test 8	×	90°	45°	14.5 GHz

Table 5.2: Influences of individual planar circuits on the resonant frequency. $\surd$ means the structure was included in the model and × means it was not included in the model.

Since the resonant frequency is calculated using HFSS full wave analysis, lumped element ca-

pacitance and inductance values could be attributed to the various components. For a resonant frequency at 8 GHz, we approximated the total lumped capacitance C ($C = C_{\mathrm{MicroLine}} + C_{\mathrm{MicroStub}}$) in the resonant circuit to be 1798 fF, using the equation $C = \varepsilon_0 \varepsilon_r A/d$, where A is the total area of the microstrip transmission lines, d is the SiO substrate thickness, ε_0 is the free space permittivity and ε_r is the relative static permittivity. The total lumped inductance $L(L = L_{\mathrm{SlotStub}} + L_{\mathrm{Finline}} + L_{\mathrm{microstrip}})$ could be derived from equation $f = \frac{1}{2\pi\sqrt{LC}}$, where $C = 1798$ fF and f=8 GHz. A total inductance of $L = 220$ pH is then obtained. The removal of the finline structure lead to a shift in the resonant frequency from 8 GHz to 11 GHz and the removal of the slotline shifted the resonant frequency to 15 GHz. Therefore the inductance contributed by the finline (L_{finline}) is calculated to be 104 pH, by the slotline ($L_{\mathrm{MicroLine}}$) ~53 pH and which leaves 62 pH inductance to be contributed by the microstrip lines ($L_{\mathrm{microstrip}}$). This result is reasonable since the total length of finline is 0.90 mm and the length of the slotline is 0.40 mm, the ratio of which is approaching 104 pH/53 pH. Then using the same method, we calculated the capacitance contributed by the radial microstrip stub ($C_{\mathrm{microstub}}$) to be roughly 1600 fF and the capacitance contributed by all the rest microstrip lines in the circuit before the SIS junction to be 200 fF.

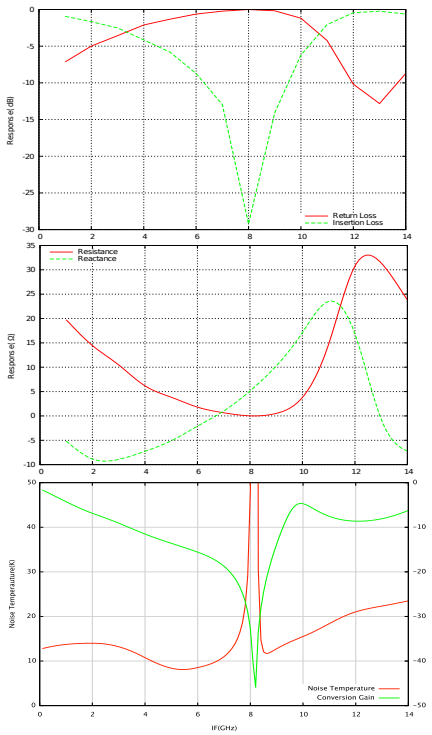

Figure 5.19: (Top) The S-parameter of the SIS mixer chip. The input port was the SIS junction and the output port was the IF port of the mixer chip. (Middle) The output impedance of the SIS mixer. (Bottom) The SuperMix simulated mixer performance. The noise temperature and the conversion gain shown here are only for the the SIS mixer chip itself, not including any optical noise or LNA noise.

The calculation performed above demonstrates that, to design a broad IF band SIS mixer, we should keep the surface area of microstrip structures as small as possible, and the total length of the slotlines and the microstrip line as short as possible. The problem caused by the RLC circuit is that the IF signals cannot propagate at frequencies close to the resonant frequency f_0 (f_0=8 GHz). This is because at frequencies close to the f_0, the IF output port would be shorted. Consequently it would be difficult to design an IF transformer to match the mixer output to the LNA 50 Ω at frequencies close to f_0, which is shown in Fig 5.19.

5.4.2 New mixer Design

To avoid the mixer degradation at the resonant frequency at 8 GHz, we modified the design of the SIS mixer with the aim of shifting the resonant frequency outside the targeted IF bandwidth 2 GHz–13 GHz. As discussed in the previous sections, it is mainly the long slotline and the large area of the 90° microstrip radial stub that lead to the presence of the resonant frequency at 8 GHz, owing to their large capacitance and inductance. Since the finline profile was rigorously calculated by the OTM method, it is not worthwhile to alter the structure of the unilateral finline. Also since changing the shape of the unilateral finline does not alter the lumped element impedance, we put more effort towards adjusting the shape of the radial stubs in the slotline-to-microstrip transition, aiming to reduce the capacitance by reducing the metallic surface area as much as possible without sacrificing the RF performance. We needed to take into account that the reduction of either the opening angle or the radius of the radial stub can narrow the bandwidth of RF power coupling and strongly affect the coupling efficiency. To investigate the sensitivity of the RF coupling to the angles and radii of the radial stubs, we constructed a back-to-back model for the slotline-to-microstrip transition which is shown in Fig 5.20 (a).

In the back-to-back model, the slotlines were joined together and we assigned the input and output ports to the microstrip lines. In the HFSS model (Fig 5.20 (b)), the angles of stubs were decreased from 90°, to 60° and then to 30° with an unchanged radius. Then the radius was reduced by a factor of 0.6 for the 60° stub. The HFSS simulated return losses for thesis cases are shown in Fig 5.20 (b). It was found that reducing the angles of the radial stubs only shifted the center frequency at which the return loss was minimum but the return loss remained better than -15 dB across most of the RF band. Changing the radius both shifted the center frequency and also slightly increased the return loss. However changing the radius is more effective in reducing the capacitance, since the area of the stub changes linearly with opening angle and quadratically with the radius. We therefore have chosen the new design to have an open angle of 60° and a radius reduced by a factor of 0.6. The total area of

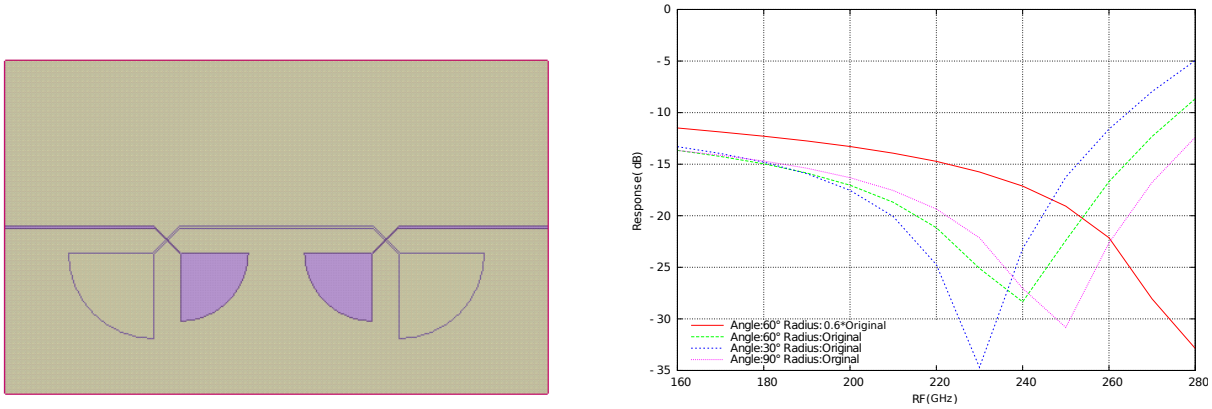

(a) (b)

Figure 5.20: (a) A schematic drawing for the back-to-back model of the slotline-to-microstrip transition (b) HFSS simulated return loss for the slotline-to-microstrip transition with various opening angles and radii.

the microstrip radial stub was reduced by ∼70% which shifted the resonant frequency to ∼18 GHz, as shown in Fig 5.21. Also the RF power coupling at the slotline-to-microstrip transition still maintained a return loss better than -12 dB across the whole RF band.

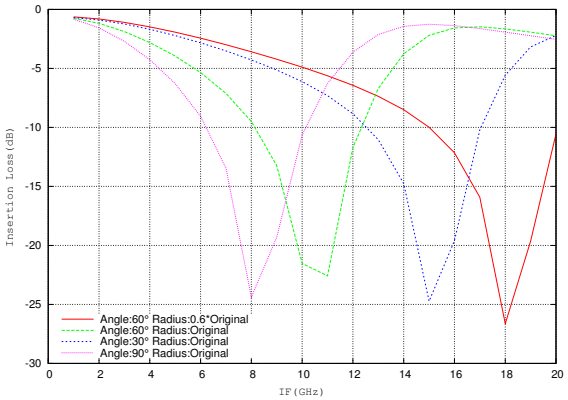

Figure 5.21: The simulated insertion loss for the entire device as a function of the IF frequency, with different opening angles and radii values for the radial stubs in the slotline-to-microstrip transition.

The modification of the slotline-to-microstrip transition causes a change to its output impedance, and hence to the matching to the tuning circuit. Therefore the tuning circuit and the RF choke design needed to be revised to match the new slotline-to-microstrip transition. The revised RF and IF performance of the entire mixer device are plotted in Fig 5.22 (a). It can be seen that a return loss lower than -10 dB is obtained across ∼85 GHz RF bandwidth with the IF resonant frequency shifting to 18 GHz. We attach the schematic drawing of the revised mixer design in Fig 5.23 and tabulated the dimensions for the critical planar circuits components in Tab 5.3.

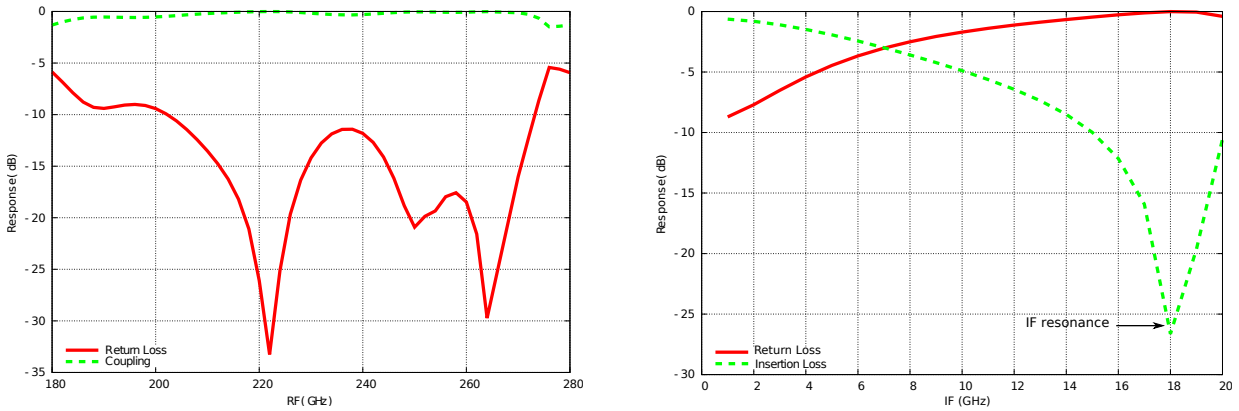

Figure 5.22: (a) The HFSS simulated RF performance for the revised mixer design. (b) The HFSS simulated IF performance for the revised mixer design.

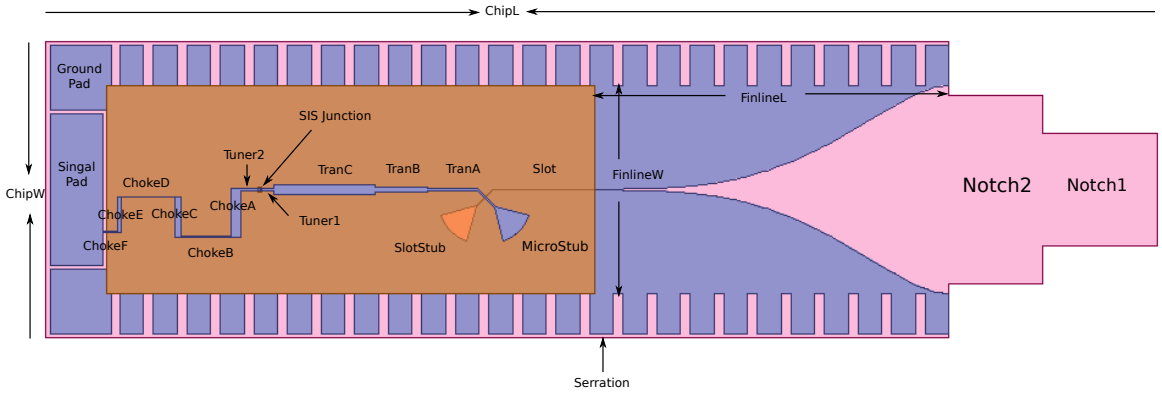

Figure 5.23: A schematic drawing for the modified device. The planar circuit components labelled in the figure are not to scale for clarity.

	TranA	TranB	TranC	Tuner1	Tuner2	ChokeA	ChokeB
width/length	2.2/130	6.43/164	14.27/67.5	2.2/38.4	2.2/56	14.25/122.2	2.2/154
	ChokeC	ChokeD	ChokeE	ChokeF	Notch1	Notch2	Serration
width/length	11/112	2.2/165	9.48/102	2.5/30	300/300	520/246	64.26/105.4
	Slot		SlotStub	MicroStub			
width/length	2.5/179	radius/angle	102/60°	81.6/60°			

Table 5.3: Dimensions of the revised mixer design. All the dimensions mentioned in the table are in units of μm

5.4.3 The IF Transformer

An IF transformer was designed for the new device, aiming at an IF bandwidth of 1-13 GHz. The IF transformer consists of 7 stages of microstrip transmission lines deposited on 0.635 mm Duroid 6010

substrate. The process of designing an IF transformer is summarized as follows:

- The mixer chip is first simulated in HFSS. The HFSS calculated S-parameter files are exported to *Ansoft* Designer or SuperMix package and combined together to calculate the output impedance.
- The imaginary part of the output impedance are tuned out at two different IF frequencies by the first two stages of the IF transformer. We choose these frequencies with reactance as small as possible to perform the tuning. Then a multi-stage Chebyshev transformer or a quarter-wavelength transformer is added to match the real part of the impedance to the 50 Ω LNA, especially at frequencies where the reactance parts are approaching zero.
- The S-parameter files of the entire passive circuit including the IF transformer are exported to SuperMix package to analyze the full mixer IF performance, considering the quantum mixing of SIS junction.

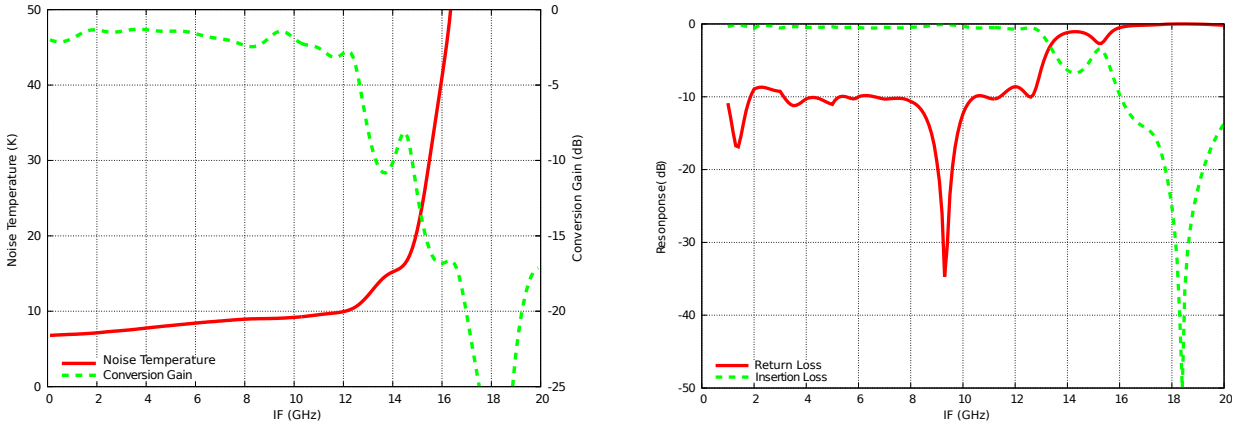

(a) (b)

Figure 5.24: (a) The SuperMix simulated mixer performance in conjunction with the IF transformer. (b) The HFSS simulated S-parameter for the revised mixer working in conjunction with the IF transformer.

Fig 5.24 shows the SuperMix and HFSS simulated performance of the mixer incorporating the IF transformer. The HFSS simulated return loss shows responses lower than -10 dB over the operating bandwidth. Also, SuperMix shows a simulated conversion gain of higher than -2 dB and a noise temperature of lower than 10 K. The dimensions of the IF transformers are tabulated in Tab 5.4.

IF transformer	1	2	3	4	5	6	7
Length (mm)	0.3	10.55	3.24	3.28	3.38	3.49	3.55
Width (mm)	4.5	3.00	2.55	2.08	1.35	0.82	0.62

Table 5.4: The dimension for the IF transformer.

5.5 Summary

We have performed a thorough investigation of the IF performance of an SIS mixer across the 2–15 GHz IF bandwidth. In particular, we investigated the influence of the lumped element impedance of the mixer chip and the influence of the IF matching on the mixer conversion gain. Our experimental measurement and simulations have shown that for an ultra-wide IF performance, an RLC resonance can exist in the design bandwidth that reduces the useful IF bandwidth of the mixer. These resonance however could be shifted outside the IF bandwidth with a carefully designed planar circuit on the mixer chip.

Our investigation also has shown that matching the output impedance of the mixer to the input of the LNA is crucial for high mixer performance. Here again we have demonstrated that this can be successfully accomplished by carefully designing a multi-stage transformer following the mixer.

Chapter 6

220 GHz Ultra-BroadBand INterferometer for S-Z effect (GUBBINS)

Overview: In this chapter, we introduce a 220 **G**Hz **U**ltra-**B**road**B**and **IN**terferometer for the **S**-Z effect (GUBBINS), which is a single baseline tracking interferometer operating in the frequency band 185-275 GHz. It is designed to observe the Sunyaev-Zel'dovich (SZ) effect in bright galaxy clusters, particularly at the 217 GHz null-frequency of the blackbody spectrum. It features high brightness sensitivity in the millimeter band, which is achieved by ultra-wide IF bandwidth SIS mixers and a complex Fourier correlator system. The Cosmic Microwave Background (CMB) and Sunyaev-Zel'dovich effect science is briefly reviewed. And the critical components in the GUBBINS instrument and the observational strategy are discussed.

6.1 CMB Science

6.1.1 The Cosmic Microwave Background (CMB) Radiation

The Cosmic Microwave Background radiation is the left-over radiation from the big bang, which is a very uniform thermal radiation that fills the observable Universe. It was predicted by Ralph Alpher and Robert Herman as a landmark test of the Big Bang Model [38][37][3] of the Universe, and accidentally discovered by Arno Penzias and Robert Woodrow Wilson [70]. Investigation of the CMB radiation allows us to observe the earliest era of the Universe.

Shortly after the Big Bang, the photons propagating through the Universe were repeatedly scattered by ionized hydrogen plasma. Thus the blackbody radiation field was thermally coupled with

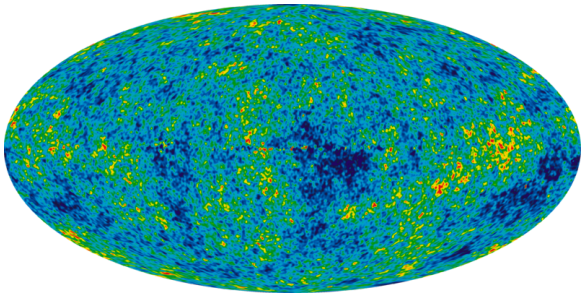

(a)

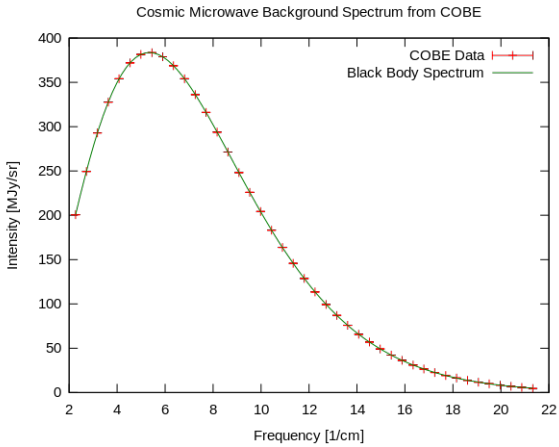

(b)

Figure 6.1: (a) All-sky map of the CMB, created from 9 years of WMAP data. Red color denotes the bright area and blue color denotes the faint area [24][22]. (b) Graph of CMB radiation spectrum measured by the FIRAS instrument on the COBE. Figures here were extracted from [92].

the plasma and was optically thick in the extremely hot and dense early Universe. As the Universe expanded, the density and temperature of the whole Universe decreased. When the Universe reached an age of 370,000 years, its temperature had dropped to ∼3500 K. At this point the ions and electrons of the primordial plasma were sufficiently cool to form neutral atoms and hence provided a nearly transparent medium for the propagation of photons. Under the influence of gravitational attraction, the baryonic matter which chiefly consisted of hydrogen and helium atoms could form stars, galaxies and even larger structures [36]. The moment of decoupling of radiation and matter is defined as the 'surface of last scattering'. At this early stage of evolution, the cosmic background radiation from the Big Bang had a wavelength of ∼1 μm and a temperature of 3,000 K. As the Universe kept expanding and cooling, the cosmic background radiation was cooled and the wavelength of the radiation was red-shifted torwards the microwave band. Observations from COBE's Far Infrared Absolute Spectrophotometer (FIRAS) revealed that the CMB spectrum was well fitted by a blackbody curve with $T \approx 2.728 \pm 0.004$ K over the region from 500 μm to 5000 μm [51] (Fig 6.1).

The CMB radiation is remarkably homogeneous over large scales across the sky, apart from the dipole moment anisotropy which is due to our relative motion with respect to the CMB rest frame. The homogeneity suggests that the Universe was close to thermal equilibrium in the past before the epoch of the 'surface of last scattering'. However we do observe tiny variations in temperature (anisotropy) on smaller scale ($\Delta T/T < 10^{-5}$) at angular scale of ∼1 degree. For example, the WMAP (Fig 6.1) measurement detected small anisotropy, at the level of one part in 100,000 Kelvin, in the temperature of the CMB radiation from place to place across the sky. For large scale structure to be formed during

the expansion of the Universe, there must have been a primordial perturbation in the early matter and energy distribution. This primordial fluctuation of matter density would leave imprints in the form of temperature anisotropies in the CMB, leading to the formation of large scale structures later. Researchers have been studying these anisotropies for more than two decades since they hold the key to understanding the origin of structure in the universe: how the primordial plasma evolved into stars, planets, galaxies and clusters of galaxies. Apart from these 'primordial anisotropies' of the CMB radiation which is known as the effect that occurred at the last scattering surface or even before, there also exists the 'secondary anisotropies'. 'Secondary anisotropies' are effects such as the interaction of the CMB radiation photons with the hot gas or the gravitational potential, which occurred between the last scattering surface and the observer, known as 'secondary anisotropy' [60].

6.1.2 Sunyaev Zel'dovich Effect

The Sunyaev Zel'dovich (S-Z) effect was first proposed in 1970 by Sunyaev and Zel'dovich [80] and was firstly reliably detected some 20 yrs later [13]. The S-Z effect occurs when CMB photons are inverse Compton scattered by the hot ionized gas within galaxy clusters. Galaxy clusters are the largest gravitationally bound structures in the Universe, whose abundance and structure provide us with a rich resource to explore the Universe. A rich cluster might have mass $> 3 \times 10^{14}$ solar masses and the intra-cluster gas has temperatures of $\sim 10^7 - 10^8$ K. A galaxy cluster is not simply a group of galaxies, instead most of the baryonic matter in a galaxy cluster is not in the galaxies themselves but in highly ionized gas which occupies the space between them. The hot electrons radiate thermal bremsstrahlung radiation in the X-ray range and also interact with 1%-2% of the CMB photons passing through the cluster, via inverse Thomson scattering, known as the 'thermal SZ effect'. Apart from this so called 'thermal SZ effect', a 'kinematic SZ effect' is caused by the peculiar movement of the intra-cluster (IC) gas with respect to the CMB rest frame. The kinematic SZ effect is weak if the peculiar velocity of the IC gas is less than 10^3 km/s and is usually much smaller than the thermal SZ effect.

On average, for the thermal SZ effect, the energy of the CMB radiation is boosted which results in a spectral shift of blackbody spectrum towards higher frequencies. The magnitude of thermal S-Z effect is proportional to the line integral of the electron pressure through the cluster, and hence directly proportional to electron number density n_e and the cluster temperature T_e. The equation describing the thermal S-Z effect is given by [80]

$$\frac{\Delta T_{SZ}}{T_{CMB}} = -2 \int n_e \frac{k_B T_e}{m_e c^2} \sigma_T dl \tag{6.1}$$

where k_B is the Boltzman constant, $m_e c^2$ is the rest mass energy of the electron, σ_T is the Thomson

cross section and the length l is the cluster diameter. The integral over length l is only evaluated over the cluster diameter because the contribution outside the cluster is negligible [28]. Fig 6.2 (a) shows the unperturbed CMB spectrum and the perturbed CMB spectrum along a line of sight through massive clusters of galaxies.

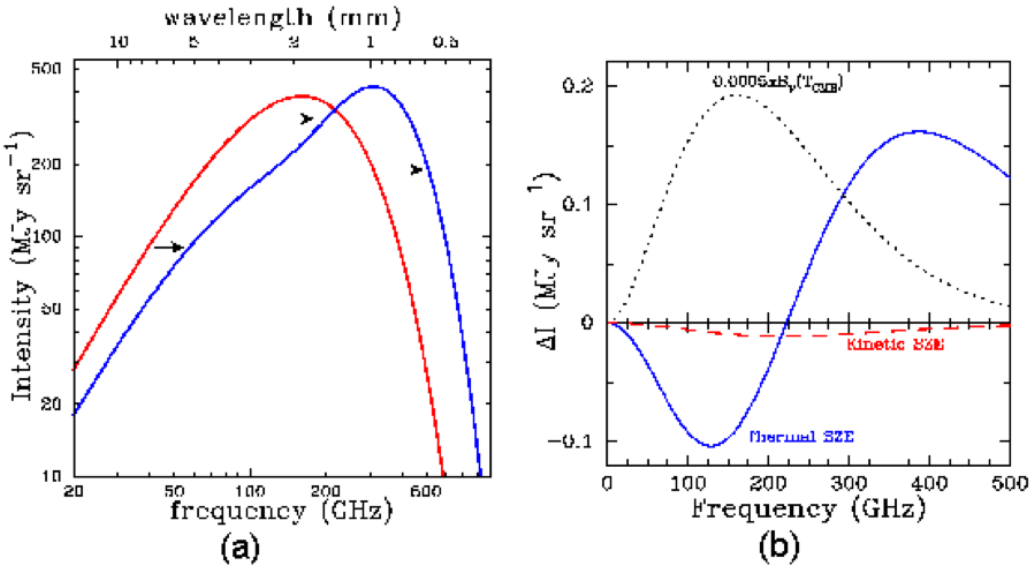

Figure 6.2: (a) The unperturbed CMB radiation (red) and the perturbed CMB radiation (blue) due to the SZ effect along the line of the sight. (b) The deviation from blackbody CMB intensity. The thermal SZ effect is denoted as a solid blue line and the kinetic SZ as a dashed red line. For comparison a scaled CMB radiation spectrum is shown as a dotted line. The figures shown above were extracted from [11].

The distortion in the CMB power spectrum due to the thermal SZ effect is in the order of 10^{-5}K in temperature. The SZ effect varies in strength over the surface of a given cluster because it depends on the depth of the cluster gas at each point in the cluster. The distortion is strongest at the center and decreases towards the edges. This is displayed in Fig 6.3 showing the observation of the SZ effect over a range of galaxy clusters with various redshifts. At high frequencies, the net result is an increment in the intensity whilst at low frequencies the net result is a decrement in the intensity. Near 217 GHz there is a point where there is no change in the intensity of CMB blackbody spectrum known as the 'null frequency'. The kinematic SZ effect, on the other hands, always weakens the intensity of the radiation at all frequencies for a cluster that is receding with respect to the Hubble flow, and boosts the intensity at all frequencies for a cluster that is approaching us. The kinematic SZ effect reaches its maximum at the null frequency of the thermal SZ effect, which offers us a tool to separate these two effects. The shift in the null frequency f_{null} due to the thermal S-Z effect is approximated by

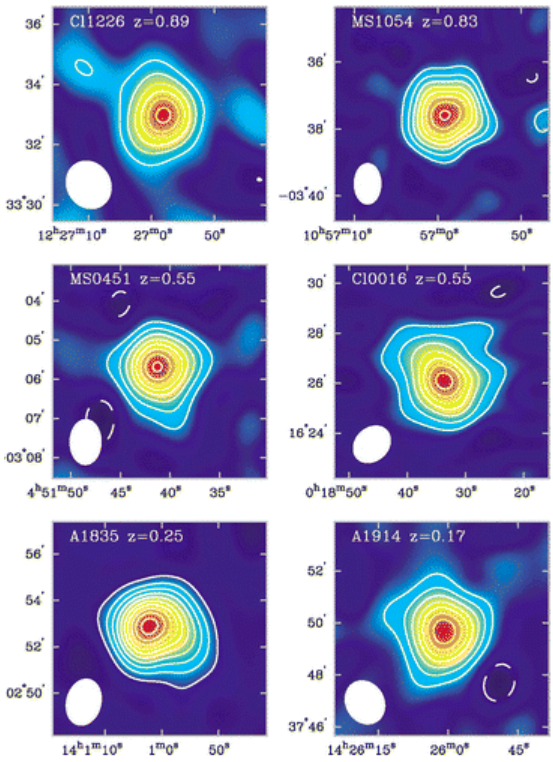

Figure 6.3: Sunyaev Zel'dovich effect images for a range of galaxy clusters with various redshifts (indicated by 'z' values). These interferometric images were made at a frequency of 30 GHz and were taken with the Owens Valley Radio Observatory and the Berkeley-Illinois-Maryland Association Array. These figures were extracted from [28].

$$f_{\text{null}} = 217 + 0.45\ T\ \text{(GHz)} \tag{6.2}$$

where T is the cluster gas temperature in keV. The gas temperature for a typically rich cluster ranges from 5 to 15 keV, resulting in a shift in the null frequency of 2.5-7.5 GHz [58]. Hence by measuring the SZ spectrum and finding the null frequency we can derive the cluster temperature without the need for X-ray spectral measurements. The SZ effect is particularly well suited for deep surveys because the size of the SZ effect is not sensitive to the redshift of the clusters. This remarkable property of SZ effect is due to the fact that the SZ effect is a distortion of the CMB radiation spectrum. Whereas the CMB suffers cosmological dimming with redshift, the ratio of the magnitude of the SZ to the CMB (Eq 6.1) does not. So we could expect, in principle, to observe very distant clusters even if they are invisible in the X-ray band. However the redshifts of the observed galaxy clusters could not be infinitely large, since the SZ effects with too large red shifts might be difficult to be distinguished from the CMB background due to their small angular sizes.

6.2 SZ Effect Observation

Accurate observations for the SZ effect are difficult due to the small amplitude of the effect and other sources of CMB temperature fluctuations (i.e primordial anisotropies). Two main techniques have been used for detecting and measuring the SZ effect: the single-dish technique and the interferometric technique. In what follows, the weaknesses and strengths of each technique and the types of systematic errors they suffer are discussed.

6.2.1 Single Dish Techniques

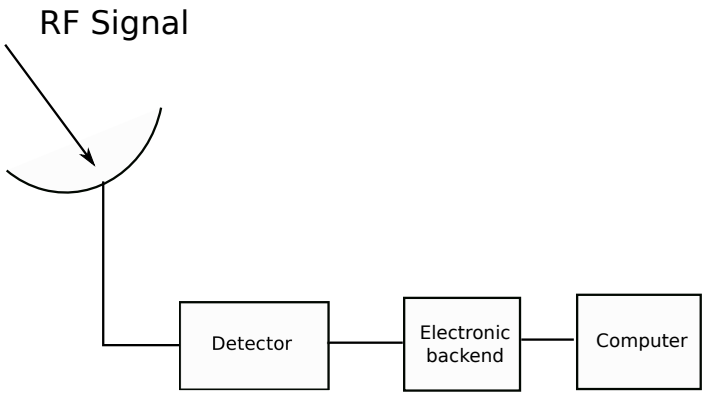

Figure 6.4: A schematic view of a single-dish radio telescope.

The first successful detection of the S-Z effect was accomplished by a 40 m single-dish telescope in Owens Valley Radio Observatory, pointing at relatively low redshift clusters (z<0.2) [14]. A single dish radio telescope consists of a parabolic mirror that collects the incoming radiation and focuses it onto the detector. If the signal is at a frequency above 100 GHz, mixers are usually used at the start of the detector chain to down-convert signal frequency to a few GHz, to allow the amplification by the following amplifiers. The amplified signals are then converted to an understandable format by the back-end electronics. Most of the early measurements suffered from systematic errors or atmospheric noises, leading to non-reproducible and inconsistent results [13]. Recently, due to the better understand of the single-dish data and the widely used high sensitivity radiometer arrays, more and more reliable SZ effect observations of high-temperature clusters (60 clusters) have been successfully achieved which only took a few hours per cluster, with random measurement errors <100 μK and low level of residual systematic errors, i.e SuZIE bolometer array, OVRO 5 m telescope, SEST 15 m telescope, IRAM 30 m telescope and Nobeyama 45 m telescope [15].

In the process of astronomical observation, the power received by the receiver is not only related to the brightness temperature of the astronomical target source T_{astro}, but can also include emission

from the atmosphere $T_{\rm atm}$ and the ground signal $T_{\rm gnd}$ as,

$$P = G(T_{\rm astro} + T_{\rm sys} + T_{\rm atm} + T_{\rm gnd}) = G(T_{\rm astro} + T_{\rm sys'}) \tag{6.3}$$

$T_{\rm sys}$ is the noise temperature of receiver system. The point-source sensitivity of a single dish telescope with effective collecting area $A_{\rm eff}$, bandwidth $\Delta\upsilon$ and integration time τ is [74]

$$\sigma_s = \frac{2k_B T_{\rm sys'}}{A_{\rm eff}[\Delta\upsilon\tau]^{1/2}} \tag{6.4}$$

Therefore single-dish telescopes with large dishes ($A_{\rm eff}$) and low noise receivers ($T'_{\rm sys}$) can have very high sensitivity, especially if the telescope is fitted with large array receivers. However, for the single-dish radio telescope, we cannot really expect the point source sensitivity σ_s to improve simply as $\tau^{-1/2}$, because of the varying ground and atmosphere contribution. Furthermore, it is difficult to extract weak astronomical source signal from data contaminated by atmospheric and ground signals. Therefore for a single-dish observation of weak signals, the observing directions have to be quickly switched between the target astronomical source and a reference background region, which should be close to the target astronomical source and certainly not have any emission. As most of the atmospheric and ground signals are slow functions of time and position, subtracting the reference power from the target power can provide an accurate correction for the sky temperature. However the integration time τ in the observation would then be at least cut down by half since half of the time is spent on the reference signal, therefore leading to a lower point-source sensitivity.

6.2.2 Interferometric Techniques

The simplest form of an interferometer (Fig 6.5) contains two identical dishes separated by a distance B. Assuming signals from a point radio source with monochromatic frequency ω arrives at the interferometer, the wavefront in direction θ is essentially planar because of the great distance travelled. It reaches the right-hand antenna at time τ_g ahead of the left-hand antenna. The signals collected by two antennas are correlated (first multiplied and then integrated over a time $\Delta t \gg (2\omega^{-1})$) so that signal $R(\widehat{s})$ is generated at the correlator output. The amplitude of $R(\widehat{s})$ is determined by the point-source flux density E and its phase depends on the delay τ_g and frequency ν, as indicated in the following equation [32]:

$$R(\widehat{s}) = \tfrac{1}{2}E^2\cos(2\pi\nu\widehat{B}\cdot\widehat{s}/c)) \tag{6.5}$$

where $\widehat{B}$ is the vector baseline from one antenna to the other and $\widehat{s}$ denotes the unit vector in the

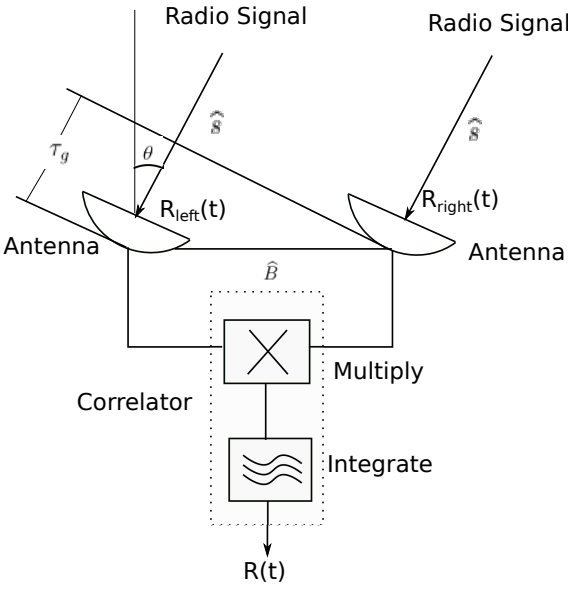

Figure 6.5: A schematic view of an idealized two-element interferometer. $\hat{B}$ is the vector baseline from one antenna to the other. $\hat{s}$ denotes the unit vector in the direction of a distant point source. (90°-θ) is the angle between the baseline and the wave front from radio source. τ_g is the wave propagation delay that varies in source tracking. The incident radio signals have a very narrow band centered at $\nu = \omega/2\pi$ [32]

direction of a distant sources. The time delay of radio signals reaching the two antennas changes due to the earth rotation, as $\tau_g = B\sin\theta/c$. The quasi-sinusoidal output fringe $R(\widehat{s})$ is caused by the source direction changing at a rate of $d\theta/dt$ and the broad Gaussian envelop shape of the fringe is caused by the pattern of the primary-beam when the radio source moves across the sky (Fig 6.6 (a)). Uncorrelated noise from the receivers and the atmosphere do not appear in the correlated output $R(\widehat{s})$. The process of correlation can be regarded as multiplying a sinusoidal fringe pattern (green curve in Fig 6.6 (a)) onto the convolution of the sky source and the primary antenna beam pattern (red curve in Fig 6.6 (a)). The result signal (blue curve in Fig 6.6 (a)) is then integrated over the sky. The fringe separation is set by the projected baseline length and the wavelength, λ/B, while long baseline gives close-packed fringes and short baseline gives widely-separated fringes [32].

The response of a spatially incoherent extended source with sky brightness distribution $I_\upsilon(\hat{s})$ near frequency $\nu = \omega/2\pi$ is regarded as the sum of independent points sources integrated over beam angle Ω

$$R_c = \int I_\upsilon(\hat{s})\cos(2\pi\upsilon\widehat{B}\cdot\hat{s}/c)d\Omega \tag{6.6}$$

The cosine function in the above equation is an even function that is only sensitive to the even part of any source brightness distribution, but averages out the odd part. To detect the odd part, a 90° phase delay is inserted into the output of one antenna to produce the sin output as,

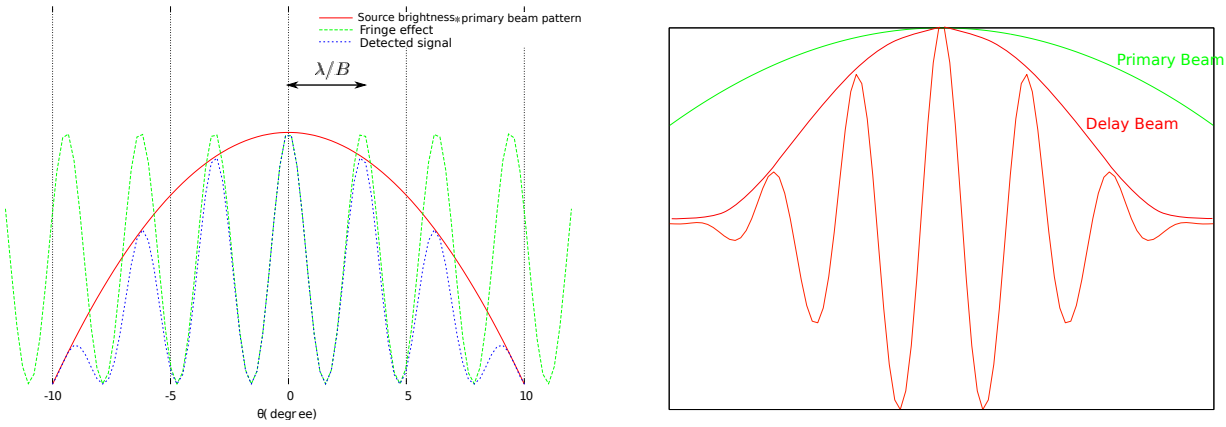

(a) (b)

Figure 6.6: (a)A diagram explaining the formation of fringes in an interferometer. (b) A diagram showing the time delay effect in an interferometer. The receiver bandwidth determines the width of the delay beam [32].

$$R_s = \int I_\upsilon(\hat{s})\sin(2\pi\upsilon\widehat{B}\cdot\hat{s}/c)d\Omega \tag{6.7}$$

We now define a complex visibility V to be the complex sum of the sin and cos correlator outputs [32]

$$V = R_c - iR_s = Ae^{-i\phi} = \int\int I_\upsilon(s)e^{-2\pi i\upsilon\mathbf{B}\cdot\mathbf{S}/c}\mathrm{d}\Omega \tag{6.8}$$

where $A = \sqrt{R_c^2 + R_s^2}$, $\phi = \tan^{-1}(R_s/R_c)$ and $I_\upsilon(s)$ is the source brightness. A complex correlator is developed to produce an output equal to Eq 6.8 and we see that V is related to the source brightness $I_\upsilon(s)$ through a Fourier transform (Eq 6.8).

Normally the receiver has a finite bandwidth and the incoming radiation is not strictly monochromatic but has a finite bandwidth $\Delta\nu$. If we assume the response of the interferometer and the source flux varies slowly across the pass band $\Delta\nu$, the single-frequency response in Eq 6.6 can be summed over the bandpass $\Delta\nu$ as [32]

$$V = \int[(\Delta\nu)^{-1}\int_{\nu_c-\Delta/2}^{\nu_c+\Delta/2} I_\nu(\hat{s})e^{-i2\pi\nu\tau_g}d\nu]d\Omega = \int I_\nu(\hat{s})\mathrm{sinc}(\Delta\nu\tau_g)e^{-i2\pi\nu_c\tau_g}d\Omega \tag{6.9}$$

Due to the finite bandwidth $\Delta\nu$, the sinc function derived in Eq 6.9 attenuates the response function V if the geometric time delay τ_g is comparable to the inverse of the bandwidth $1/\Delta\nu$, shown in Fig 6.6. Therefore an instrumental time delay τ_i, whose value is close to τ_g, is added to another antenna to compensate the time delay τ_g. As the earth rotates, the instrumental time delay τ_i must

be continuously adjusted to track τ_g, which is done by the analogue electronics in the back-end.

Here we define the angular radius of the usable field-of-view as $\Delta\theta$ offset from the wave-front direction $\widehat{s}$. Since $\Delta\nu\tau_g \gg 1$, we see that $\Delta\nu(B\sin\theta)/c \gg 1$. Substituting $\lambda\nu = c$ and the synthesized beam width $\theta_s = \lambda/B$, we find that [74]

$$\Delta\theta\Delta\nu \ll \theta_s\nu \tag{6.10}$$

For a broad band interferometer, to obtain broad field-of-view, the bandwidth of the correlators $\Delta\nu$ has to be divided into a number of sub-frequency channels each with bandwidth of no more than $\theta_s\nu/\Delta\theta$.

The observation of the SZ effect signal which is as weak as $\sim$300 μK, requires sophisticated observing techniques. Although the first SZ effect observation was performed using a single-dish radiometer, studies of the SZ effect are also done with interferometers [19]. Compared to the single-dish telescope, interferometers can take advantage of earth rotation to modulate the sky signal via a quasi-sinusoidal function on top of signal function, which helps distinguish the source signals from other interrupting signals, i.e crosstalk, ground-spill, constant atomspheric signals or the uniform components of the CMB radiation, via the correlation. Also by combining the long baseline with short baseline data, the SZ effect can efficiently be separated from the point source contamination. These provide significant advantages in deep space observations where the interrupting signals could be comparable to the source signals. Moreover, it can provide high spatial resolution without the need for excessive antenna size. However the angular scale of the S-Z feature is of the order of tens of arc-seconds to one arc-minute, so if the angular scale of an interferometer is smaller than this, the signal would get averaged out. Therefore a small interferometer with moderate spatial resolution, and hence a small baseline, is ideal for observing S-Z effect.

The point-source sensitivity of an interferometer with N dishes is [74]

$$\sigma_{\rm s} = \frac{2k_{\rm B}T_{\rm sys}}{A_{\rm eff}[N(N-1)\Delta\upsilon\tau]^{1/2}} \tag{6.11}$$

where $T_{\rm sys}$ is the system noise temperature, $A_{\rm eff}$ is the effective collecting area of the antennas, $\Delta\nu$ is the receiver bandwidth, τ is the integration time and $k_{\rm B}$ is the Boltzmann constant. Compared with the point source sensitivity of a single dish radiometer, the point source sensitivity of a two-element interferometer is $\sqrt{2}$ times better, if the sum of the effective collecting areas of the interferometer is equal to the effective collecting area of the single dish.

However, as the SZ effect is an extended source rather than a point source, it is the surface bright-

ness sensitivity (unit: Jy/per solid angle) that is important, rather than the point source sensitivity (unit: Jy). The synthesized beam width of an interferometer is λ/B where B is the maximum baseline for the interferometer, while for single-dish radiometer the beam width is λ/D where D is the diameter of the single-dish. So the beam solid angle of an interferometer is smaller by a factor $\sim (D/B)^2$, which is roughly equal to the filling factor of an interferometer, defined as [74]

$$f = (D/B)^2 \tag{6.12}$$

where D is the dish diameter, and B is the longest baseline. The relation between surface brightness sensitivity σ_T and the filling factor f is then approximately given as [74],

$$\sigma_T = \frac{\sigma_s f \lambda^2}{2k_{\rm B}\Omega_A} \tag{6.13}$$

where λ is the signal wavelength, Ω_A is the beam solid angle, σ_s the point-source sensitivity (Eq 6.11), f is the filling factor and $k_{\rm B}$ is the Boltzmann constant. To achieve better surface brightness sensitivity which is required by SZ effect observations, larger filling factors are preferred. So the surface brightness sensitivity of an interferometer might be worse than the one of a single-dish radiometer with the same total collecting areas. For the single-dish telescopes, $f = 1$ is the optimum value that can be achieved. However for interferometers, the filling factors are always smaller 1, and significantly so for those with long baselines. Therefore compact antenna configurations are preferred to approach a high filling factor, and hence a high brightness sensitivity.

The recent development in expanding the IF bandwidth of SIS mixer and the availability of components for broadband IF processing, however allowing the bandwidth of heterodyne interferometer to be extended (e.g 10 GHz), hence allowing the interferometer to have enough brightness sensitivity to detect the SZ effect and yet to benefit from the crucial advantage of clean interferometer detection.

6.3 GUBBINS specification

GUBBINS (220 **G**Hz **U**ltra-**B**road**B**and **IN**terferometer for **SZ**) is a prototype single-baseline 220 GHz tracking heterodyne interferometer for astronomical observations, featuring high surface brightness sensitivity and moderate spectral/spatial resolution in the mm band. As described above, the observation of the CMB radiation requires the instrument to have extremely high brightness sensitivity and excellent control of systematic and instrumental effects. The employment of the interferometer enables the power fluctuation from the atmosphere in both channels to be subtracted. The surface brightness sensitivity requirement is met by an ultra-wide instantaneous bandwidth (IF bandwidth)

SIS mixers and the novel design of the backend correlator [44].

Apart from carrying out observations of the Sunyaev-Zel'dovich effect in bright galaxy clusters and performing measurements on atmospheric phase stability at GHz, we have used GUBBINS as a prototype for stimulating the development of the new technology. GUBBINS uses two small antennas on a short baseline with a pair of ultra-wide IF bandwidth SIS mixers and ultra-wide IF bandwidth analogue correlators. The use of the heterodyne SIS mixers allows each receiver to be independently phase switched by phase switching the local oscillator (LO) in each channel, so that the individually modulated redundant baselines can be used to eliminate the systematic effects of the instrument [44].

The specifications of GUBBINS system are listed in Fig 6.1. The primary antenna in each channel has a diameter of 0.4 m, and is separated by 0.5 m. This compact configuration of the antenna yields a high filling factor (∼0.8), and hence high brightness sensitivity. A 0.5 m wide baseline gives an angular resolution that fits the size of the brightest S-Z cluster, with a primary beam having a FWHM of 11.4′. The SIS mixers for both antennas are located in the same cryostat, which are mounted between the antennas. The target noise temperature for the SIS receiver system is 50 K, with a total instantaneous bandwidth of $\Delta\upsilon$=10 GHz at each sideband. SIS mixer and LO source are required to have an RF bandwidth of 185-275 GHz, realizing a total DSB bandwidth of at least 20 GHz at either side of the nominal null frequency (217 GHz) in the S-Z effect. Derived from Eq 6.13 and Eq 6.11, a 350 $\mu K/\sqrt{s}$ surface brightness sensitivity can be achieved by T_{sys} of 50 K, $\Delta\upsilon$ of 10 GHz, A_{eff} of 0.125 m^2 and primary beam Ω_A of 11.4'. The complex correlator is designed with a bandwidth of 2-20 GHz, which is divided into 16 channels to achieve a wide field-of-view according to Eq 6.10.

Table 6.1: Specification for GUBBINS instrument

Frequency	185-275 GHz
Antenna aperture	0.4 m
Baseline	0.5 m
Primary beam	11.4' FWHM
IF band	3-13 GHz
Instantaneous bandwidth	2×10 GHz
Correlator channels	16
Correlator bandwidth	2-20 GHz
Channel bandwidth	1.125 GHz
Target system temperature	50 K
Brightness sensitivity per channel	1.5 $mK/\sqrt{s}$
Total brightness sensitivity	350 $\mu K/\sqrt{s}$

A block diagram showing the GUBBINS system is given in Fig 6.7. The astronomical signals collected from the sky are combined with the phase-switched LO signals in the SIS mixer. Then the

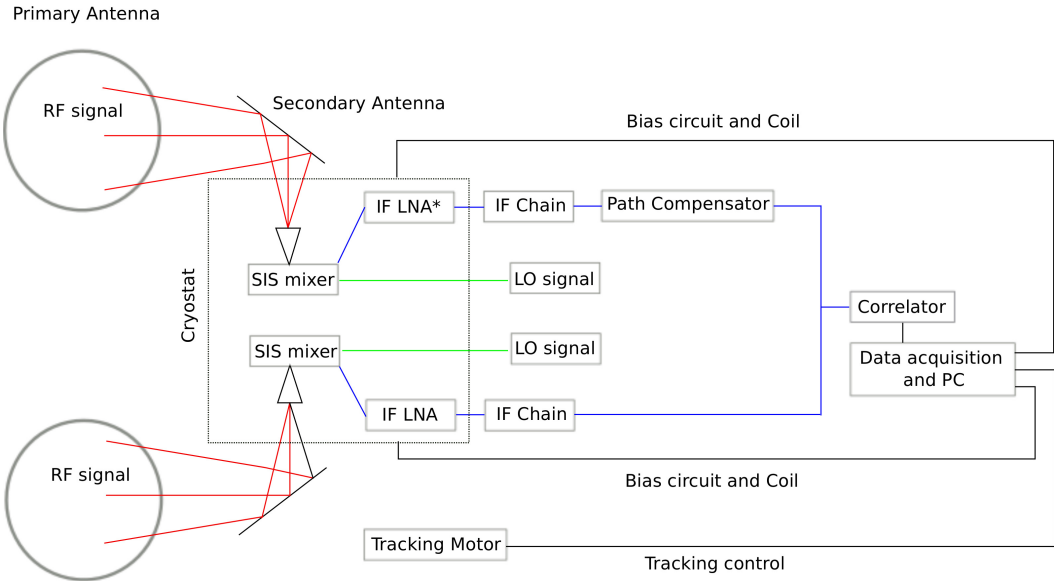

Figure 6.7: A system diagram for the GUBBINS instrument. Data and DC signals are shown in black lines, LO signals in green lines and the IF signals in red.

IF signals generated from both channels of the mixers are amplified and phase-compensated before entering the analogue correlator to perform the complex Fourier transform. The data acquisition system processes the correlated signals and a PC controls the tracking motors for the optics, cryostat and the bias/magnetic control for the SIS mixers. Two CAD models for the instrument are shown in Fig 6.8 and Fig 6.9. To save the cost, only one cryostat is used at the center of the instrument to house two mixers channels, which are symmetrically installed inside the cryostat with the optics for each antenna mounted on either side.

The mechanical design, optical design and fabrication of GUBBINS system were accomplished by several members of the astrophysics group at Oxford Physics department [44]. A significant amount of work mentioned here, including optical design, correlator design and data acquisition system design, were completed by our group colleagues. The part of the work that I was responsible for was to design, test and analyze the SIS receivers, and also integrate and test them in the GUBBINS cryostat.

6.4 Observation Strategy

The GUBBINS instrument was designed to be located in Chile and perform observations on the southern sky. We prepare to use the point-mode technique to observe the SZ effect in the GUBBINS instrument. Due to the earth rotation, the bright source is tracked by continuously rotating the pointing of both antennas. Each antenna tracks the radio source around axis between the center of the secondary mirror and horn reflector in elevation, around the axis between the center of the

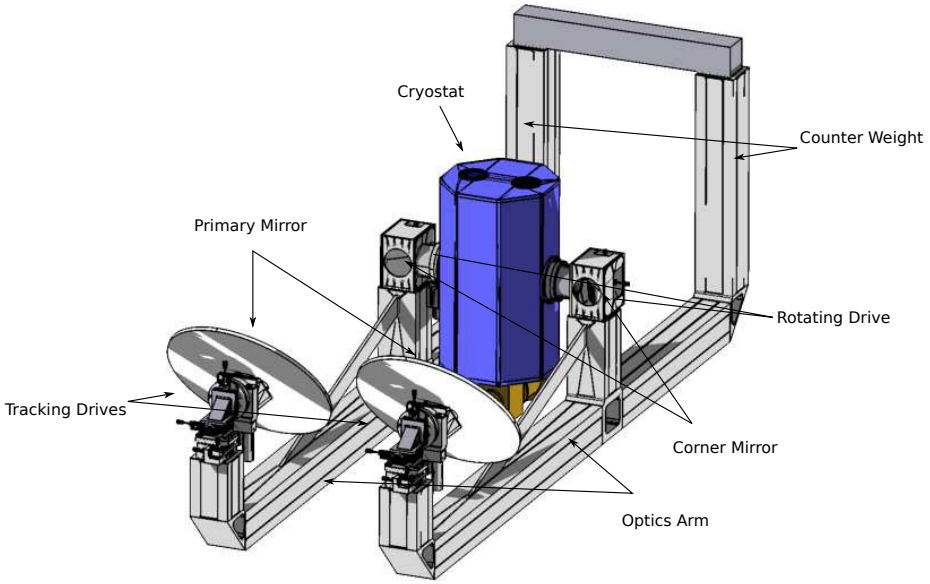

Figure 6.8: A CAD model for GUBBINS instrument. The figure is extracted from [44].

primary mirror and secondary mirror in azimuth. By tracking the radio source, the projected baseline changes when the position of radio source changes, which gives rise to phase variation between two signals. It is this phase difference that distinguishes the astronomical signals from the uncorrelated non-astronomical signals.

The celestial position of the bright radio source is calibrated and programmed into the control motor system. The tracking accuracy for a telescope beam is required to be $\theta/10$ where θ is the angular resolution of the telescope. Each antenna is equipped with an elevation/tracking unit to allow the antenna to be freely pointed. The tracking unit consists of a cubical bracket carrying the secondary mirror and two ring bearings, one fixed to the cryostat side plate providing the elevation motion, the other fixed to the main optics arm that carries the primary mirror. Both axes in the elevation/tracking motion are driven with rack and pinion drives from a DC motor/gearbox controlled by a servo-amplifier, and each axis carries an angle encoder to read pointings back to the control computer [86]. During observation, the time delay τ_i is automatically adjusted in the IF path according to the position of the radio source. Known radio sources (i.e Jupiter) with known brightnesses and known R.A. (right ascension) / declination will be used to calibrate the instrument.

6.5 Optical Design

The GUBBINS optical path is displayed in Fig 6.10, where the pink beams indicate the paths of the astronomical signals to the SIS mixer receives. The antennas are designed to have an off-axis prime

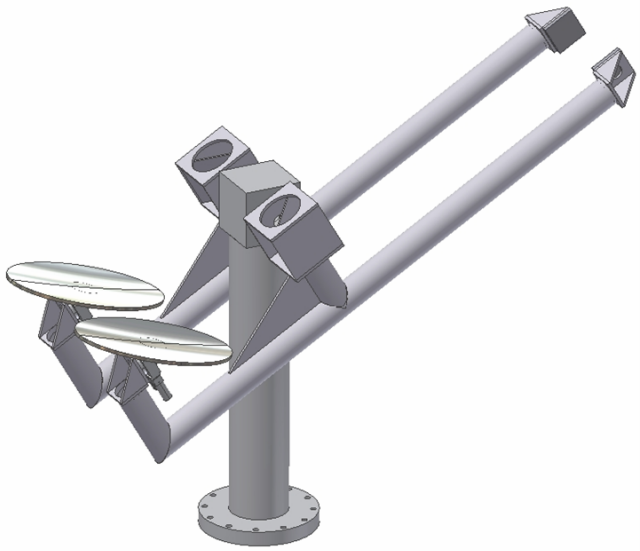

Figure 6.9: A CAD model showing GUBBINS instrument tracking a celestial source.

focus with the beam path folded by 90° by the secondary mirror. The primary mirror is an off-axis parabolic mirror with a focal length 1.02 m, an elliptical rim 0.57 m×0.4 m, providing a projected aperture towards the sky of 0.4 m diameter. The primary mirror is mounted on a 2-axis tip/tilt stage, and has been carefully designed to achieve a maximum filling factor. The configuration of the primary mirror allows the antennas to scan up to 45° from the zenith with no shadowing.

The astronomical signals are fed to the mixer through the side-window of the cryostat and a horn reflector antenna, while the LO signals are fed into the mixer through windows on the top of the cryostat, a smooth-walled horn and waveguide directional LO coupler inside the mixer block.

To enable the sharing of the cryostat by two mixer channels and also to allow reasonable freedom for the telescope to be pointed in both elevation and azimuth, the beam is folded by a 45° secondary mirror placed between the primary mirror and the horn-reflector feed. The secondary mirror is a convex paraboloid mirror with a focal length of 0.12 m that focuses the astronomical radiation to the SIS mixer through the windows on the opposite sides of the cryostat. This was done to reduce the total length of the telescope but at the expense of introducing slight aberration when the mirrors are pointed far from zenith. The secondary mirrors are mounted on 2-axis goniometers. The astronomical signals are eventually fed to the SIS mixer detector through this 90° secondary mirror, a horn reflector and then a corrugated horn. The corrugated horn has a semi flare angle of 15° and an aperture diameter of 15 mm. The combination of the horn-reflector and the corrugated horn ensures a collimated beam with high gain and good coupling to the optics. The beam truncation by the cryostat window is below -25 dB.

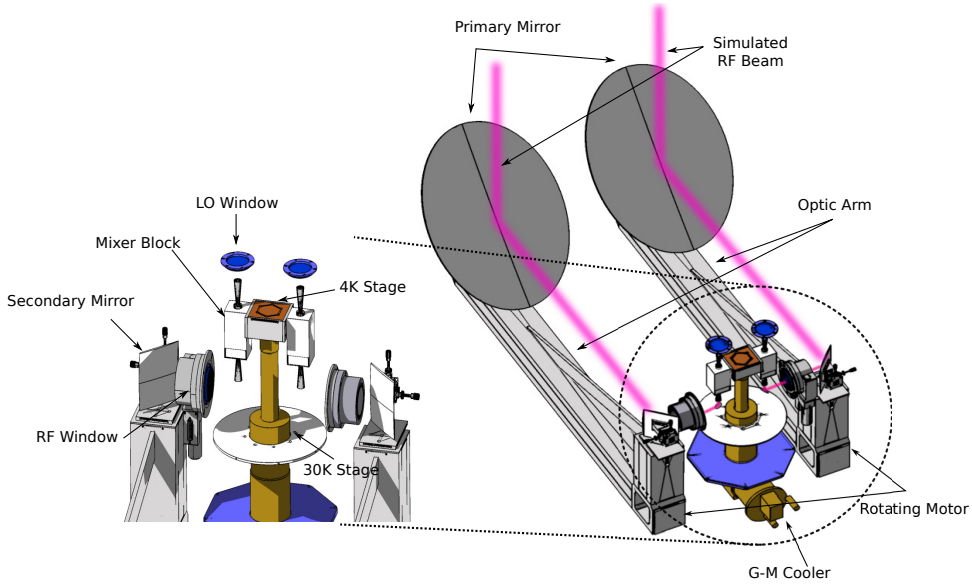

Figure 6.10: A schematic view of GUBBINS optics with the pink lines showing the RF beams [44].

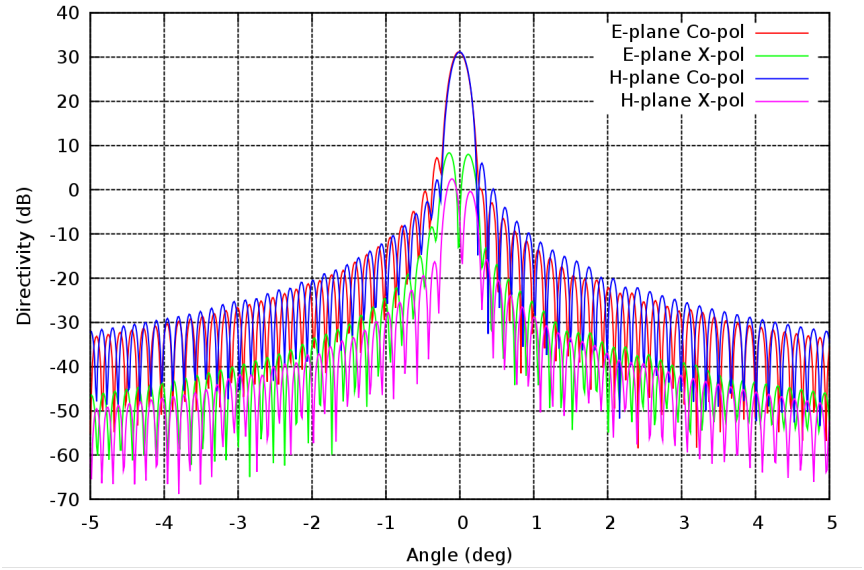

Figure 6.11: A GRASP simulation of the primary beam of the GUBBINS optics

Fig 6.11 (a) shows a GRASP simulated primary beam pattern for the GUBBINS optics. The optical system for GUBBINS system was designed by Dr. J. Leech and fabricated by the mechanical workshop in Department of Physics, University of Oxford.

6.6 The heterodyne receivers

6.6.1 Wide IF band SIS mixers

GUBBINS employs a single-ended ultra-wide IF band finline SIS mixer with the LO and RF radiations coupled to the SIS junction through the planar circuits. The mixer design and the analysis for the mixer RF/IF performance are discussed in Chapter 4, Chapter 5.

The SIS mixer (Fig 6.12) employs a unilateral finline taper on a 60 μm silicon substrate to transform the waveguide mode to the slotline mode. The unilateral finline structure allows wide band coverage in both RF and IF frequency, and also offers a large area for complicated on-chip planar circuits. The finline mixer does not require mechanical tuning or an accurately located back short, which eases the design and fabrication of the mixer block. The mixer was designed to work in conjunction with a circular 1 μm^2 Nb/AlO_x/Nb SIS junction embedded in a microstrip line. A wide RF band tuning circuit is connected to the SIS junction to tune out its intrinsic capacitance to allow the RF power over the maximum bandwidth to couple to the junction. To achieve wide-IF bandwidth, the on-chip planar circuits have been carefully designed to keep the lumped capacitance and inductance as low as possible. An IF microstrip transformer board is designed as an independent component to match the complex output impedance of the SIS mixer to the 50 Ω input impedance of the cryogenic LNA (Lower Noise Amplifier) with a target IF bandwidth of ~10 GHz. The best tested mixer could achieve an average noise temperature of 71 K over RF bandwidth 160 GHz-260 GHz, where the lowest measured noise temperature was ~50 K. An IF bandwidth of 2–15 GHz was obtained. In Fig 6.13 we show the noise temperatures measured for one SIS mixer as a function of RF band, and the corresponding IV/IF curves.

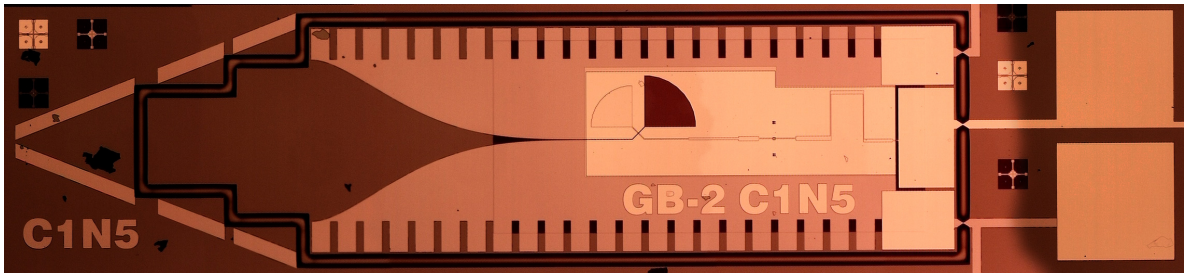

Figure 6.12: The SIS mixer device used in the GUBBINS system.

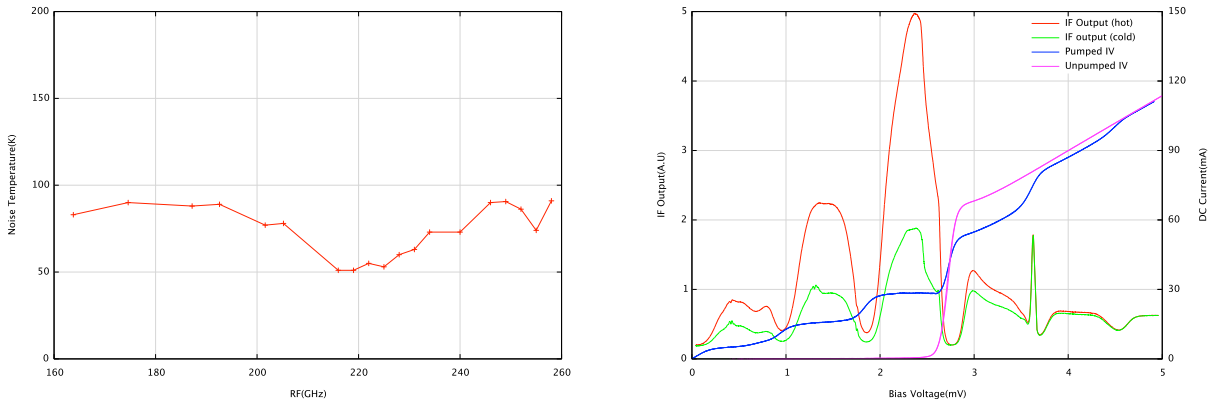

(a) (b)

Figure 6.13: (a)The measurement of noise temperature as a function of RF frequency for one tested SIS mixer over IF bandwidth 3–4 GHz. (b) The pumped IV/IF curves for one tested SIS mixer at RF frequency 219 GHz.

6.6.2 Mixer block

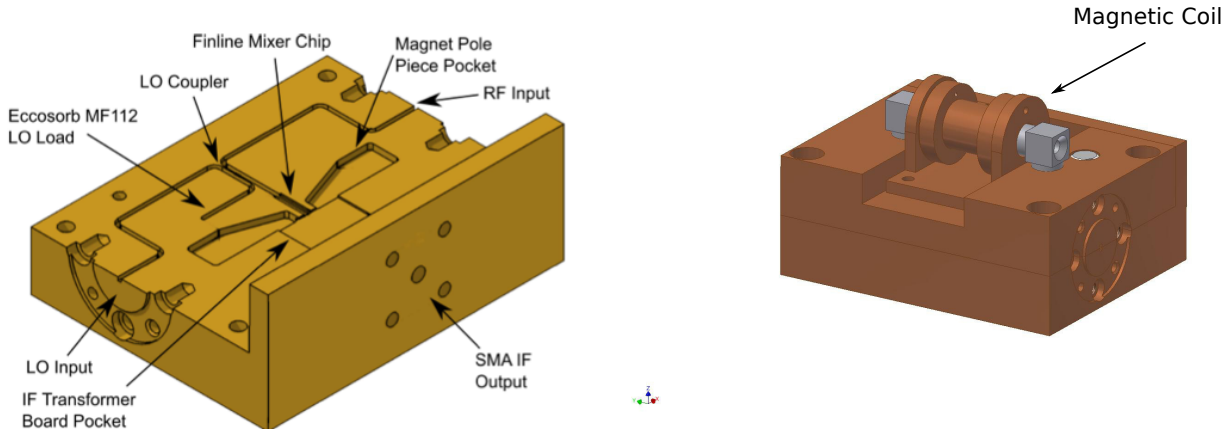

(a) (b)

Figure 6.14: (a) An AutoCAD model of the lower half of the mixer block. (b) An AutoCAD model of a complete GUBBINS mixer block.

The SIS mixer chip was mounted in the E-plane of the waveguide in a double-ended mixer block. The split block (Fig 6.14 (a)) contains a -17 dB directional coupler used to combine the LO radiation with the RF radiation into the SIS mixer. The uncoupled LO signals are terminated by a wedge shaped Eccosorb MF 112 load. The mixer block also contains an IF transformer board that is used to transform the complex output impedance of the mixer device to the 50 Ω input impedance of the

amplifier, and also enable the DC bias connection. A superconducting coil is mounted on the top of the block to suppress the Josephson current, by concentrating the magnetic field around the SIS junction. The DC bias circuits for each mixer, the magnetic control circuits for the coils and the voltage supply for the cold LNAs are connected to the room temperature control panel through a D-type connector.

Figure 6.15: The picture of the LO coupler sitting inside the waveguide.

The -17 dB directional coupler [44] (Fig 6.15) consists of three 0.4 μm thick gold radial probes connected by a suspended stripline deposited on 65 μm thick quartz chips. These probe chips couple the power between the LO waveguide and the RF waveguide, as shown in Fig 6.14 (a). The chips are glued down to the slots at the shared boundary of the LO and RF waveguides, spaced at quarter wavelengths along the waveguides. The HFSS simulated performance for the LO coupler (Fig 6.16 (b)) shows a coupling of around -17 dB, and a good isolation between the LO input port and the RF input port. In the HFSS simulation, we assumed the uncoupled LO power was totally absorbed by the LO load, so that we assigned perfectly matched ports to each end of the waveguides. The LO coupler design parameters are shown in Table 6.2. The LO coupler was designed by Dr. Paul Grimes.

Waveguide size	WR-4
Coupler spacing	350μm
Waveguide slot width	200μm
Waveguide slot height	130μm
Coupler chip thickness	65μm
Coupler chip width	190μm
Coupler chip length	600μm
Stripline width	20μm
Stripline length	275μm
Outer probe radius	100μm
Inner probe radius	130μm

Table 6.2: Dimensions of the waveguide directional LO coupler.

6.6.2.1 Measurement of the coupling efficiency

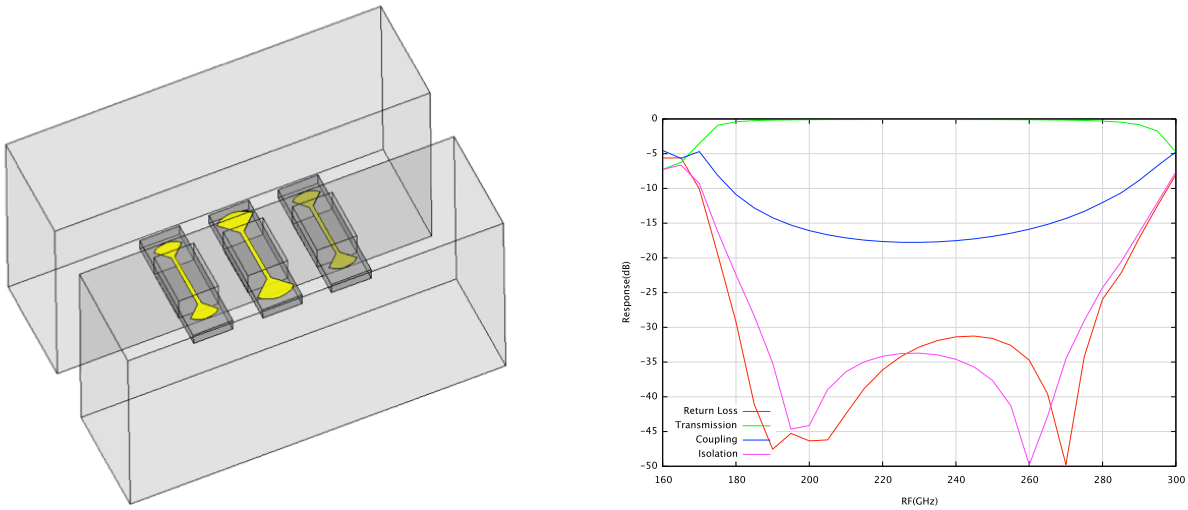

(a) (b)

Figure 6.16: (a) HFSS model of the waveguide directional coupler. The 60 μm thick quartz substrate chip (dark grey) with gold radial probes (gold) being supported in shallow slots (light grey). Three radial probes couple power between the LO waveguide and the RF waveguide via suspended stripline. (b) The HFSS simulation for the LO coupler. The 'Coupling' curve (blue) describes the coupling from the LO wavguide to the RF waveguide.

The LO coupling was designed to be -17 dB since a well-behaved mixer can be adequately saturated by our multiplier chain LO source with a -17 dB attenuation, and also the optics loss from a -17 dB LO coupler (G_{optics}) is quite acceptable with aspect to the receiver noise temperature. The coupling of a -17 dB LO coupler is equivalent to the coupling of a 19 μm thick beamsplitter. However, the experiments suggested that the LO coupler in the GUBBINS system provided higher coupling than -17 dB, since the mixer was much more easily saturated in the GUBBINS system than in the Wet Dewar while using a 19 μm beamsplitter. To calibrate the LO coupling, we made equal amounts of LO power couple to either the LO waveguide or the RF waveguide of the mixer block, which are graphically shown in Fig 6.17. By swapping the mixer block around by 180°, the LO power coupled through the RF waveguide would arrive at the mixer without any attenuation (if the mixer is well-matched to the waveguide), but the LO power through the LO waveguide would arrive the mixer with a -17 dB attenuation (Fig 6.17). If we define the amount of power arriving at the mixer chip through the RF waveguide to be P_1, and through the LO waveguide to be P_2. Then due to the attenuation of the -17 dB LO coupler, P_2 should be much lower than P_1 and its ratio (P_2/P_1) should be -17 dB.

To measure this ratio, we firstly rotated the mixer block by 180° and pumped the mixer through the RF waveguide. We tuned the LO power to make sure the mixer was well below saturation ($\sim$1/3

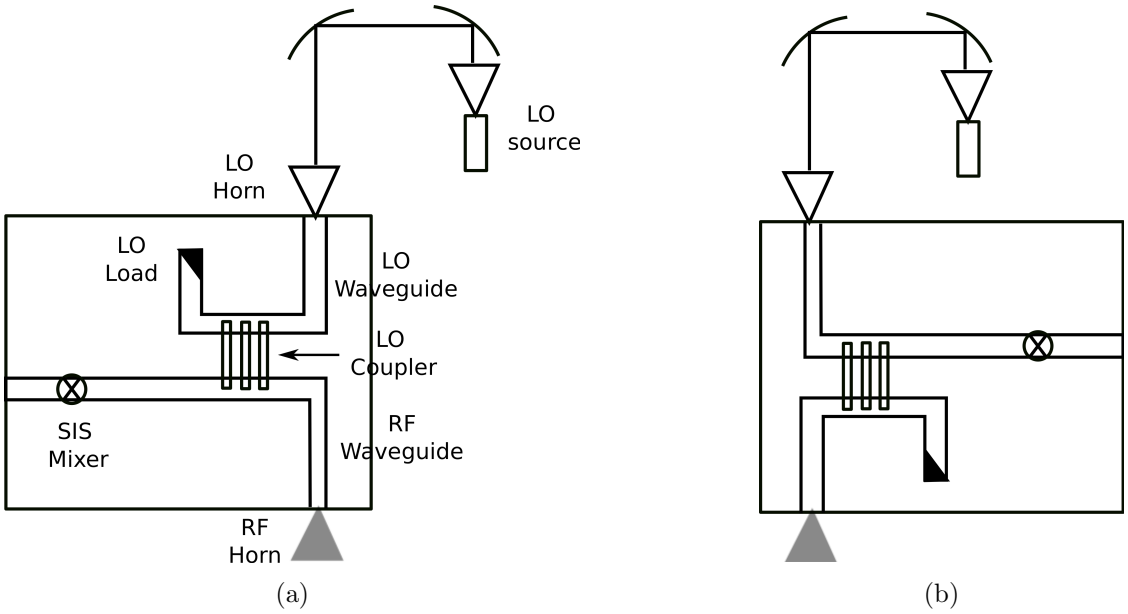

Figure 6.17: A schematic figure showing the two positions of the mixer block in the experiment of measuring the LO coupling, with the LO power coupled to the mixer through (a) the LO waveguide and (b) the RF waveguide.

gap current). The detected LO power P_1 was then proportional to the pumped current on the first photon step $A_1 - A_0$ (Fig 6.18 (a)), where A_1 is the current at the center of the first photon step and the A_0 is the leakage current of the unpumped IV curve. The mixer was then rotated 180° back and was pumped through the LO waveguide via the LO coupler, and the pumped current at the first photon step $A_2 - A_0$ was recorded. The coupling ratio is then given by $P_2/P_1 = (A_2 - A_0)/(A_1 - A_0)$.

The measured coupling efficiency for the LO coupler is displayed in Fig 6.18 (b), in comparison with the simulated LO coupling as a function of RF frequency. Since when the LO power was coupled through the LO waveguide, the pumped current was very weak that the I-V curve was very noise, we did have significant error bars on the calculated coupling. The LO coupler exhibited an average coupling of -14 dB across RF band, equivalent to a 36 μm Mylar beamsplitter. There are several reasons leading to this high measured LO coupling: (1) Due to a fabrication mistake, the stripline width came out to be 30 μm instead of the designed 20 μm. The HFSS simulation (Fig 6.19 (b)) shows that this imperfection results in an overall 2 dB increase in the LO coupling, (2) The LO harmonics deteriorate the measurement accuracy especially at band edges (i.e $>$ 250 GHz). With the existence of the higher order harmonics, the pumped current at the center of the photon step cannot correctly represent the real coupling power at the given frequency, (3) Validated by the tolerance test, the LO coupling is sensitive to the probe radius, that a $\pm$10 μm increment in radius could lead to 1-2 dB enhancement in the LO coupling, shown in Fig 6.19 (a). Given the fact that the strip width was

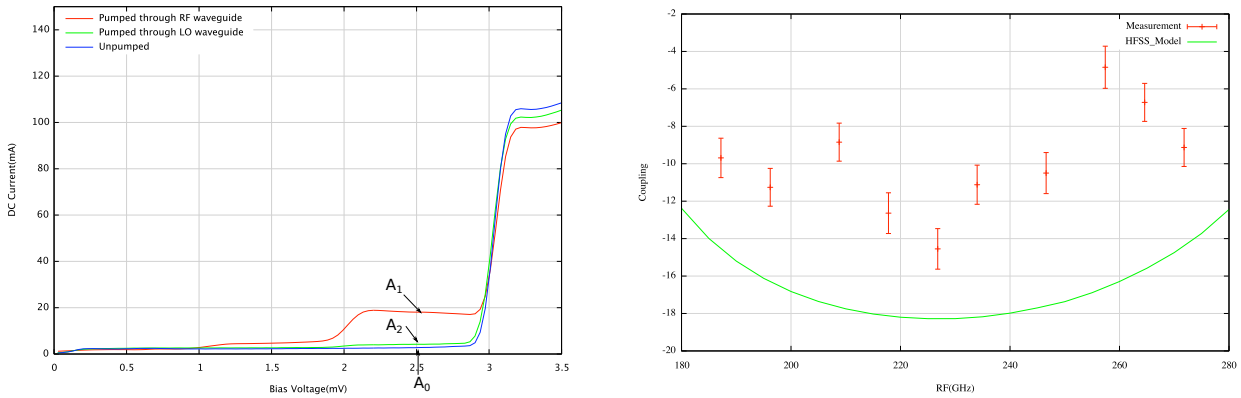

(a) (b)

Figure 6.18: (a) An example showing the measured pumped IV curves with LO radiation coupled through either the LO waveguide or the RF waveguide. The LO frequency is 246.6 GHz. (b) The measured coupling for the LO coupler with the error bars shown in red. HFSS simulation of the coupling is shown in green.

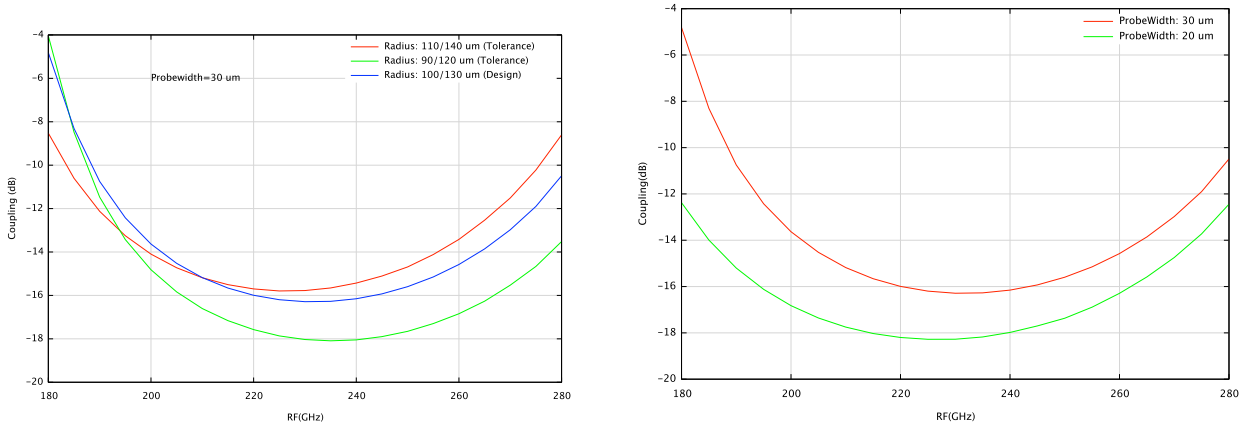

(a) (b)

Figure 6.19: (a) A tolerance test on the radius of the inner/outter radial probes. (b) The coupling with the probe width of either 20 μm (designed) or 30 μm (fabricated).

fabricated 10 μm wider, there exists a great chance that the probe might also be fabricated larger than expected. (4) In the HFSS model, we assumed all the four waveguide ports were perfectly matched. However in reality, this assumption is too optimistic since one port is loaded with an SIS mixer chip and the other port is loaded with an LO Eccosorb, both of which would have some level of mismatch. If, for example, the LO Eccosorb is not well matched to the waveguide, the reflected LO power from the Eccosorb would be again coupled by the LO coupler, hence might enhance the total coupling.

6.6.3 LO system

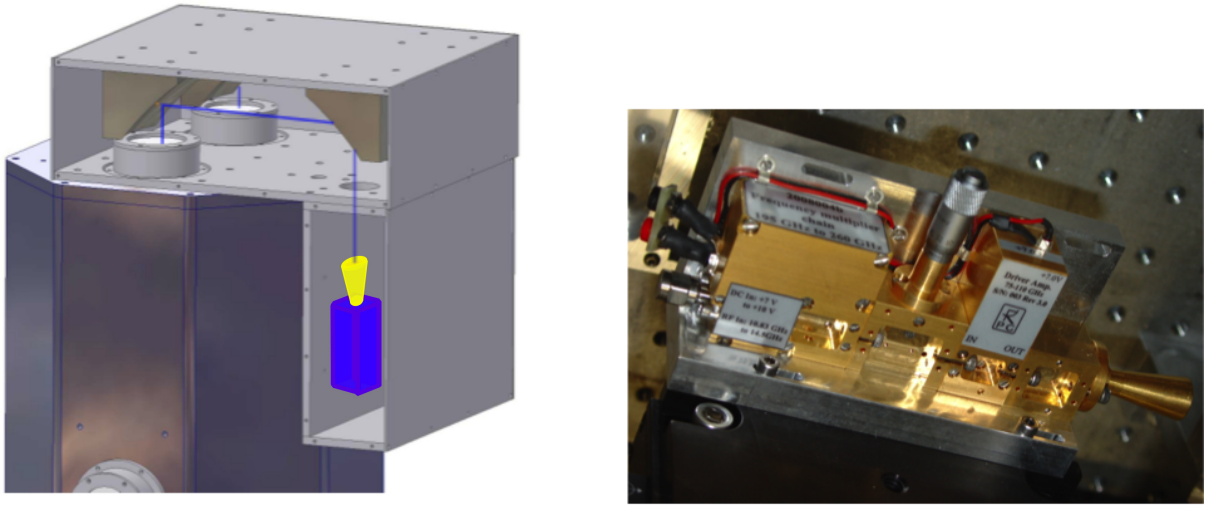

(a) (b)

Figure 6.20: (a) An AutoCAD diagram showing the LO optical path. (b) The GUBBINS multiplier chain LO.

The LO signals are coupled to the SIS mixer blocks via the optical path shown in Fig 6.20 (a) following the blue colored rays. Each smooth-wall feed horn on the mixer blocks receives the LO signal via a Gaussian beam telescope, consisting of two curved mirrors shown in Fig 6.20 (a) [44]. The LO signals are generated by two 195-260 GHz multiplied LO sources produced by Radiometer Physics GmbH, with a multiplication factor of 18 and an output power level of 100-500 μW. The picture of the LO source is shown in Fig 6.20 (b). Both LOs are driven by a single 10.8-14.5 GHz synthesizer. To facilitate the complex correlation at the back-end, the LO signals injected to one side of SIS mixer will be 180° phase switched with respect to LO signal on the other side by a 10° Schiffman phase switch [44]. The SIS mixer block assembly and the cold electronics inside the cryostat are shown in Fig 6.21 (b). The unpumped IV curves for the SIS mixers loaded in both channels of the GUBBINS system are shown in Fig 6.21 (a), together with a working 4 K GUBBINS system at the far end of the

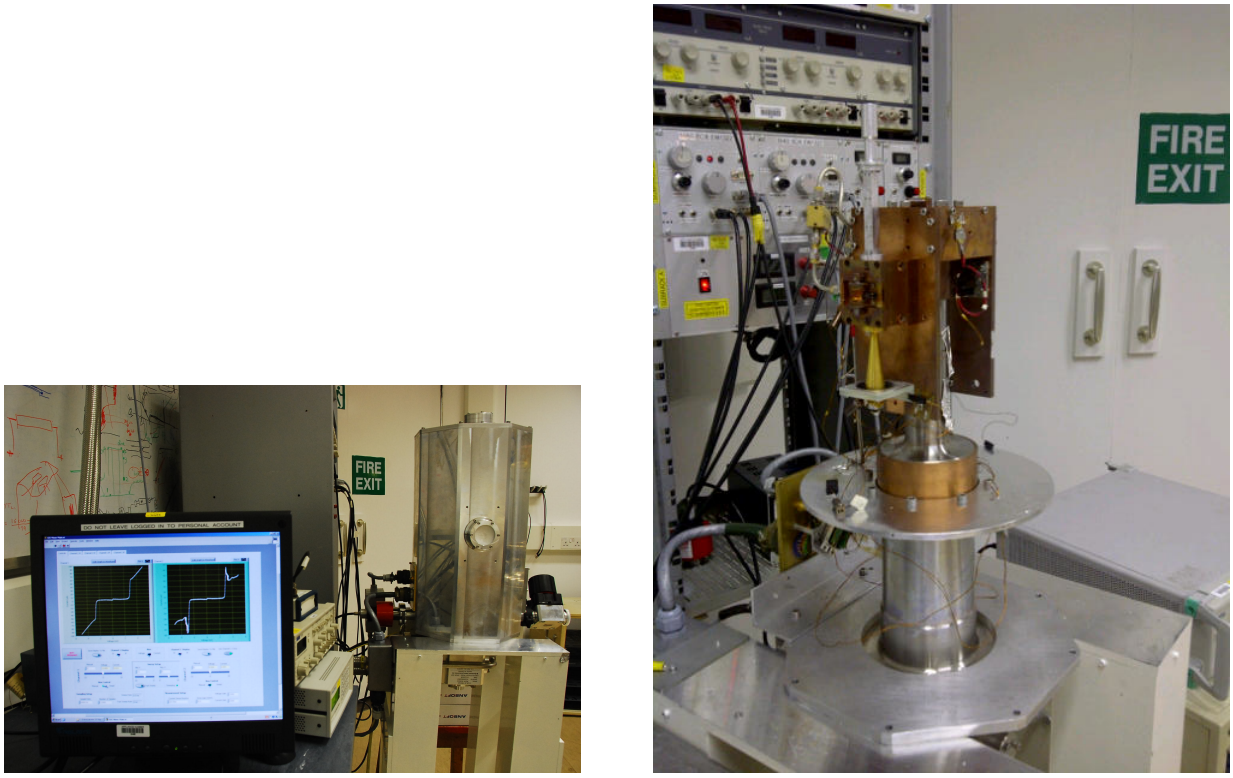

(a) (b)

Figure 6.21: (a) The GUBBINS cryostat loaded with working SIS mixers in both channels. The unpumped IV curves for the mixers in both channels are shown on the computer screen. (b) The SIS mixer block assembly loaded in one channel of the GUBBINS system. At the back of the cryostat, an electronic rack was built to house the mixer bias circuits, coils PSU and the power supply for the LOs and the LNAs.

picture.

6.7 Cryogenics

The cryostat used in the GUBBINS system (Fig 6.22 (a)) was custom designed and fabricated in the Department of Physics, University of Oxford. We provide a schematic view for the components inside the cryostat in Fig 6.22 (b). The cryostat is cooled by an air-cooled two-stage Gifford-McMahon (G-M) cooler purchased from Sumitomo Heavy Industries. It provides 1 W of cooling power at the 4 K cold stage where the SIS mixer blocks, the LNAs and the bias tees are mounted, and 40 W at the 30 K stage where the 30 K warm amplifiers will be mounted. A 30 K shield is included in the cooling system to prevent radiation from the outer walls from placing too much heat load on the receiver block and the 30 K stage cold head. The surface of the mixer blocks, which are tightly bolted on the cold plate, can achieve a temperature of 3.85 K. With all the cold electronics switched on, the block

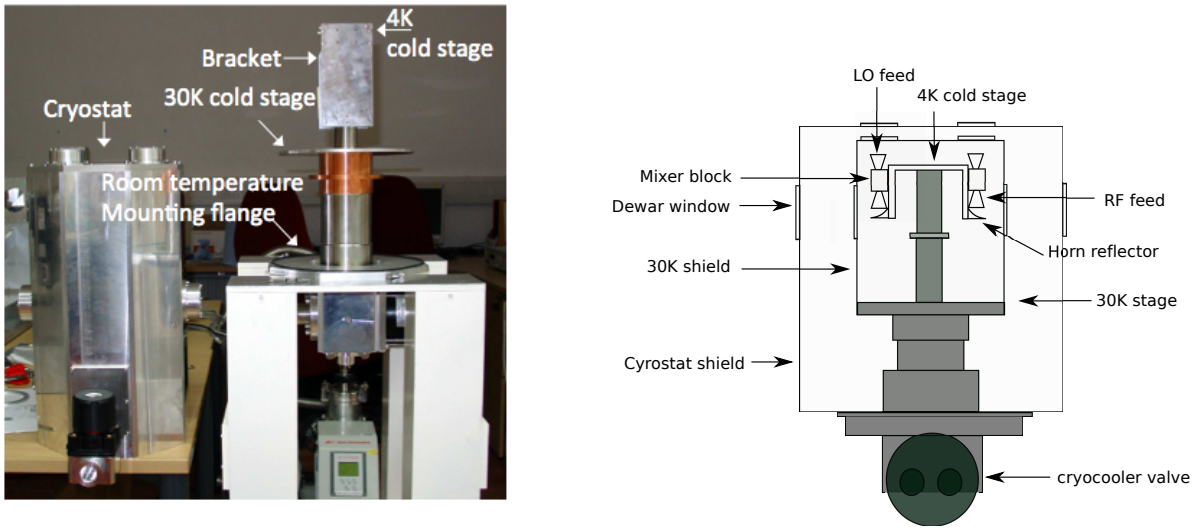

(a) (b)

Figure 6.22: (a)The custom designed cryostat for the GUBBINS system. (G-M cooler is supported by a temporary aluminum pillar). Brackets holding GUBBINS cold electronics (mixer blocks, cold amplifiers and etc.) and 4 K/30 K cold stages are also shown here. (b) Diagram of the cryostat layout.

temperature would rise up to around 4.0 K. G-M coolers are mechanical refrigerators that do have significant level of vibration. As SIS mixers are not as sensitive as bolometers to the microphonic pickup, they can tolerate small ranges of mechanical vibration. However, special attention had to be paid to the DC/AC connections of the SIS mixers, especially to delicate connections inside the mixer block (i.e bonding wires or the SMA pins solder joints), to avoid any cryogenic cracking.

6.8 IF chain

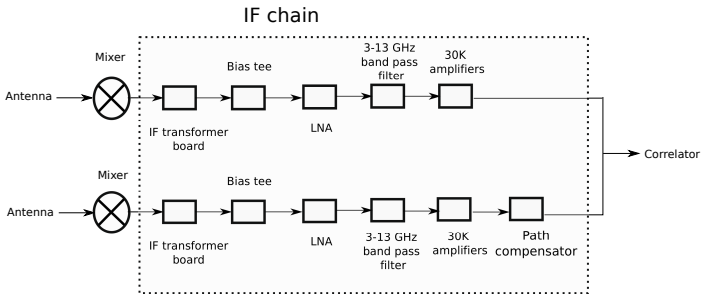

Figure 6.23: A schematic diagram showing the IF chain for the GUBBINS system, from the IF board to the correlator.

Fig 6.23 shows the block diagram of the GUBBINS IF chain. The IF output from the SIS mixer is matched to the LNA by an IF transformer board. The IF transformer board is a multi-stage

microstrip transformer printed on 0.635/0.254 mm thick Duroid 6010 substrate. A commercial bias tee is connected to the mixer block to supply the DC bias voltage to the SIS junction while passing the IF signals to the LNA. The performance of the receiver chain is largely determined by the SIS mixer and the first stage cryogenic LNA. The cryogenic LNA used in GUBBINS is identical to the one used in the Wet Dewar, which is a 3-13 GHz InP LNA supplied by the Sander Weinreb (Caltech). The noise temperature and gain performance of the LNA in cryogenic environment is shown in Fig 4.5. The IF amplifier provides a bandwidth >10 GHz with noise temperature below 5 K. Before entering the complex correlator, the IF signal from the cryogenic LNA is then further amplified by another amplifier which is installed at 30 K stage. Although we have plenty of gains in the cryogenic LNA, the latter stages of IF amplification will still be mounted on the 30 K stage on the final telescope, to minimize the noise figure and also minimize the gain drifting. The 30 K amplifier will consist of a number of gain blocks, each of them using two Hittite HMC462LP5 2-20 GHz, 13 dB cascaded amplifiers in surface mount packages. The noise of these amplifiers can be significantly reduced by cryogenic cooling, and 80 K noise temperature was measured for the gain blocks at an ambient temperature of 4 K [44].

After being amplified, a 3-13 GHz band pass filter is inserted into the IF chain to define the IF bandwidth. Before the correlator, path compensation will be applied to the IF signal to remove the path delay introduced by scanning the two antennas of the telescope. The path compensator is made up of seven time delay switches, providing 2.5, 5, 10, 20, 40, 80 and 160 mm of path compensation, and made up of differential lengths of microstrip line switched by Hittite HMC547 0-20 GHz FET surface mount package switches [44].

6.9 Correlator and data acquisition

The design and fabrication of the correlator was lead by Prof. Mike Jones and completed by colleagues in his group (Dr. Angela Taylor, Adam Coats, etc.) [21]. The correlator is an essential part of any interferometric radio telescope, where the signals from each antenna are combined to form the complex visibility measurements from which the image of the sky can be derived. The correlator used here is a double-side band complex Fourier Transform correlator, that consisting of two identical circuits with a broadband 90° phase shift at one input. Fig 6.24 shows a schematic diagram for the GUBBINS correlator. On each correlator board, the splitter trees of broadband Wilkinson dividers split the incoming signals into 16 identical channels, each with a bandwidth of 1.25 GHz. All the signals are then correlated after appropriate time delays using the custom-made Gillbert cell multipliers MMIC chips [21]. 16 Gillbert multiplier chips are placed between two splitter tree. Due to delay steps, the multiplier chips are arranged diagonally to the delay lines. The signal from the microstrip lines of

the dividers are directly wire bonded to the input pads of the multiplier chips. On either side of the multiplier chip, there are two metal feed-through pins. One is used for the bias supply to the multiplier and the other for the low frequency IF output signal from the multiplier. The single-layer microstrip and the multiplier chips of the correlator board are fabricated on a 10-mil alumina substrate with a dielectric constant of 9.9. The multiplied signals are then transmitted to a FR4 circuit board, containing further analogue gain, buffering and filter. The signals are then passed via a backplane to a 16 channels digitizer board where the signals are sampled at 14-bits resolution and 2.8 Msamples/sec, and integrated in an FPGA.

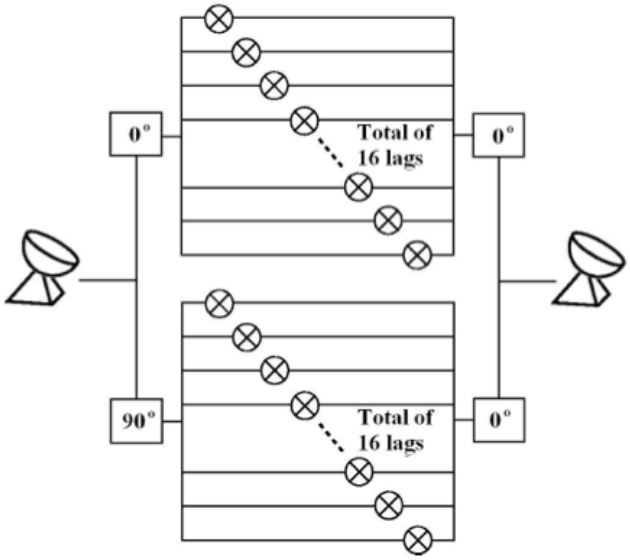

Figure 6.24: The schematic diagram for GUBBINS complex correlator.

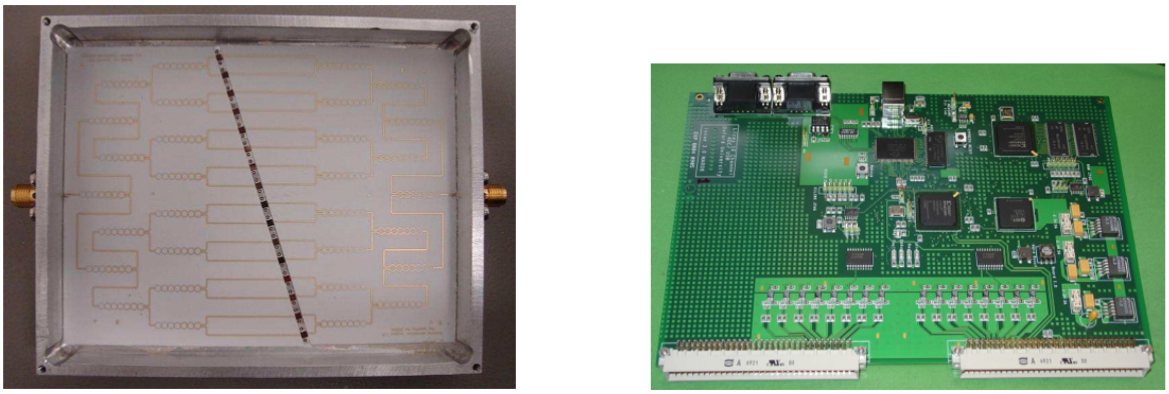

(a) (b)

Figure 6.25: (a) The prototype GUBBINS correlator board. (b) GUBBINS correlator readout board.

The first prototype 16 lag correlator board has now been fabricated and tested [12] (Fig 6.25 (a). The multiplier chips are read by low noise amplifiers and an A-to-D conversion board developed by the Oxford Central Electronics Group (Fig 6.25 (b). This board uses 2.8 MSps ADCs feeding an FPGA processor that demodulates the phase switching of the signals and provides a USB output to the data acquisition computer (Fig 6.25 (b)).

6.10 Summary and future work

GUBBINS is a prototype single-ended mm-wave heterodyne interferometer, built to observe the S-Z effect in the CMB background. It features a high brightness sensitivity and moderate spectral/spatial resolutions. This instrument has lead to the development of several new technologies, including the ultra-wide IF band SIS mixer and the ultra-wide band analogue correlators. Reasonably low noise temperatures have been measured for the SIS mixer devices used in the GUBBINS system. The SIS mixers installed on both channels deliver promising performances and could work well individually. The IF system and the correlator have also been tested separately and given excellent results.

In the future, 180° phase-switching system has to be built on the LO system. The waveguide LO coupler might have to be either re-designed or re-fabricated to figure out the high coupling issue. Once the new-batch of SIS mixer with an undisturbed 10 GHz bandwidth is fabricated and tested, the SIS mixer detector system has to be assembled with the backend 30 K amplifier/correlator system to form a real radio interferometer. All the lab tests towards the complete telescope instruments should be commissioned. The optical system has also to be tested and calibrated toward a known planet to measure the beam patter.

Chapter 7

Variable Temperature Load

Overview: In this chapter, we demonstrate the use of a cryogenically-cooled variable-temperature load for the noise temperature measurements of an SIS mixer inside the cryostat. To achieve an accurate measurement, the design of the variable-temperature load needs to have a large temperature range, a short thermal time constant and a good thermal isolation from the SIS mixer block. The variable temperature load was made of an aluminum cone coated with blackbody paint, the temperature of which was controlled by a Lakeshore® temperature controller. The temperature of the blackbody load could be driven from 9 K to 24 K within one minute and stabilized within ±0.01 K. The motivation in using this arrangement is that in the receiver chain, optical loss generated by the vacuum window and the IR filter could be avoided when the RF load is mounted. Experimental measurements have shown a ∼15 K decrement in noise temperature of the SIS mixer using the temperature load inside the cryostat with respect to the hot/cold temperature load external to the cryostat.

7.1 Variable Temperature Load

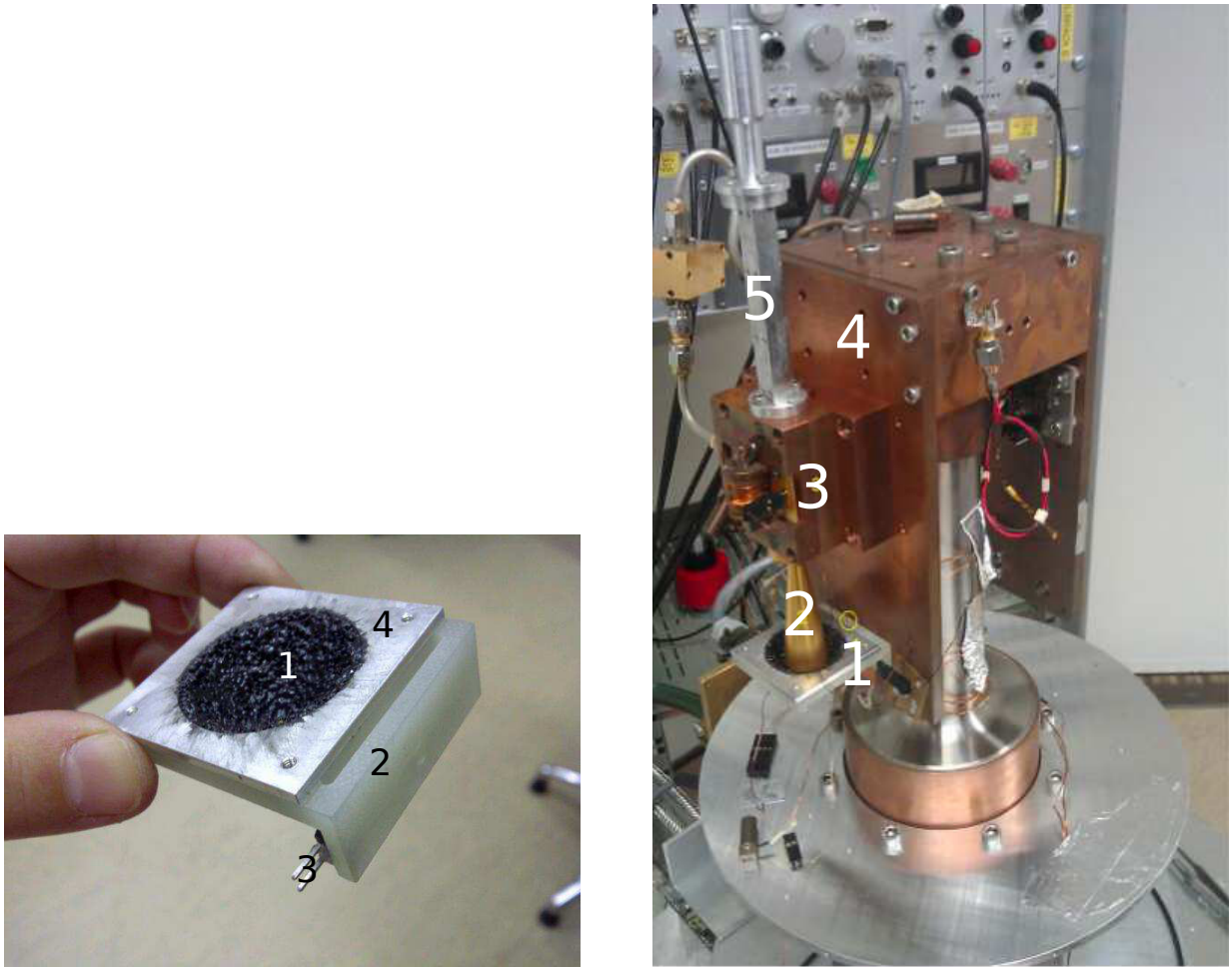

(a) (b)

Figure 7.1: (a) The variable-temperature load: (1) Blackbody paint, (2) Fiber glass bracket, (3) Connector for 32 AWG heating wires, (4) Aluminum cone. (b) A picture showing the variable-temperature load assembled with the GUBBINS receivers: (1) Blackbody load, (2) RF horn, (3) SIS mixer block, (4) 4 K cold stage, (5) LO horn. (The copper heat sink is emphasized by a yellow circle.)

An expression for the noise temperature of a mixer receiver is given by,

$$T_{\mathrm{N}} = (1/G_{\mathrm{window}} - 1)T_{\mathrm{room}} + \frac{(1/G_{\mathrm{filter}} - 1)T_{\mathrm{filter}}}{G_{\mathrm{window}}} + \frac{T_{\mathrm{optics}}}{G_{\mathrm{window}}G_{\mathrm{filter}}} + \frac{T_{\mathrm{SIS}}}{G_{\mathrm{filter}}G_{\mathrm{window}}G_{\mathrm{optics}}} + \frac{T_{\mathrm{LAN}}}{G_{\mathrm{filter}}G_{\mathrm{window}}G_{\mathrm{optics}}G_{\mathrm{SIS}}} + \frac{T_{\mathrm{WarmIF}}}{G_{\mathrm{filter}}G_{\mathrm{window}}G_{\mathrm{optics}}G_{\mathrm{SIS}}G_{\mathrm{WarmIF}}} \tag{7.1}$$

In the expression above, the noise configuration of the LD 45 Zotefoam vacuum window is calculated at room temperature environment T_{room} and the noise configuration of the IR filters is calculated at $T_{\mathrm{filter}} = 30$ K, both of which are lossy components and could potentially contribute significant optical

noise to the total receiver noise. These two components can also enhance the noise contribution via the conversion loss factors $1/G_{\text{window}}$ and $1/G_{\text{filter}}$ in the receiver chain.

To investigate the impact of the window/filter on the receiver noise temperature, we constructed a variable-temperature blackbody load which was installed inside the cryostat to allow RF radiation with various brightness temperatures to directly couple to the SIS mixer without passing through vacuum windows or IR filters. The load temperature in the cryogenic environment was controlled by a Lakeshore® temperature monitor. The load consisted of an aluminum cone coated with blackbody paint (stycast 2850) to provide the radiating surface, a FR-4 fiber glass bracket to support the cone and several windings of 30 AWG manganin wires wound on the back of the aluminum cone to act as a heater. The internal arrangement is shown in Fig 7.1 and the schematic diagram for the load is shown in Fig 7.2.

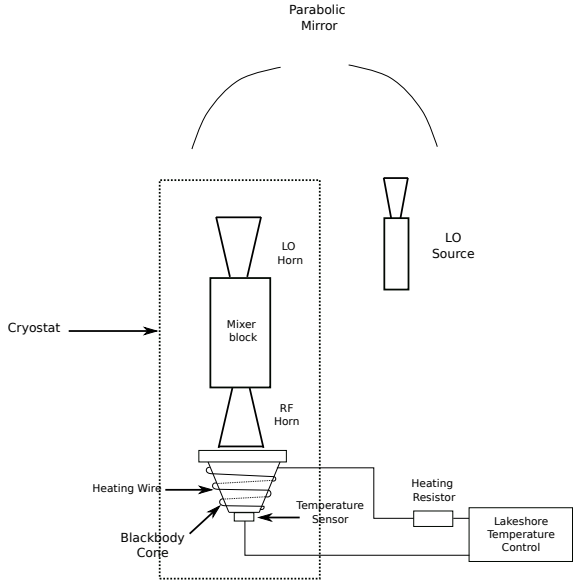

Figure 7.2: A schematic diagram showing the blackbody load system inside the cryostat.

In Fig 7.1 (b), the central pillar is the 4 K cold-head onto which the mixer block containing the SIS chip is mounted. A corrugated feed horn receives the incoming RF radiation and a smooth-walled feed horn receives the LO radiation. The blackbody load was bolted to the bottom of the 4 K stage cold plate, ∼4 cm away from the SIS mixer block. The blackbody cone was very close to the RF feed horn (1 mm) to ensure the beam is filled by the source. Care was taken in designing the shape of the blackbody cone to ensure the radiated RF source was well matched to the RF beam. By careful design and optimization [41], resistivity in the range of 200-400 Ω for the blackbody paint yields a good RF match to the SIS device [95][39]. An FR-4 fiber glass bracket was used to support the blackbody cone and was connected to the 4 K stage, because of its low thermal conductance and high heat capacity

at low temperature. Ideally, direct contact between the blackbody load and the 4 K stage should be avoided to prevent heating of the mixer block which is also mounted on the 4 K stage. However in our experiment, some contact was inevitable since the blackbody load needed to be heat sunk to the 4 K stage to reach a low base temperature (i.e < 10 K). A heat sink (labelled by a yellow circle in Fig 7.1) consisting of copper tape was used to connect the blackbody load to the cold plate to control the temperature of the load. The dimensions of the copper tape determined the speed at which the temperature load attained its final value in the 'hot' and 'cold' configuration. We aimed at a short thermal time constant since the drifting of the IF system could be significant over time $t > 10$ min, thus it was critical to drive the temperature load from low temperature to high temperature as quickly as possible. The size of the heat sink tape was crucial in determining the thermal time constant. A heat sink with too large a thermal conductance lengthens the heating up time and causes the heating of the SIS junction, whilst a heat sink with too small a thermal conductance lengthens the cooling down time and enhances the base temperature of the blackbody load. A compromise therefore had to be made in choosing the dimension of the copper strip to reach a balance between cooling and heating processes. The heating resistor, which controls the current of the power supply, can influence the temperature range of the blackbody load. The heating resistor we used in load system was 50 Ω which could heat up the blackbody load up to a stable temperature of 20 K from a base temperature of 9.0 K within 1 min. Heat resistance lower than 50 Ω could heat up the blackbody load even higher, but not without significantly heating of the SIS junction.

Fig 7.2 shows the diode temperature sensor which was bolted down to the bottom of the blackbody cone. The wires used for the temperature sensor were 35 AWG cryogenic wires made of phosphor bronze, which has high electrical conductance and low thermal conductance. A twisted pair of wires was used to reduce the effect of the electrical noise. All the cryogenic wires used on the blackbody load were adhered to the cold surface to cool the leads to a temperature close to the sensor. The heating wire and the diode temperature sensor formed a closed feedback loop with the Lakeshore temperature monitor to control the temperature. A proportional-integral-derivative (PID) control loop with heater outputs of 25 W was configured to drive a 25 Ω load for optimal cryocooler control flexibility. A PID algorithm calculated a control output based on temperature set-point and feedback from the control sensor. As we shall see later in the optimum arrangement of our system, the load temperature could be driven from 9.0 K to 20 K within $t <$60 seconds with the mixer block temperature rising up from 4.0 K to 4.15 K. The temperature of the load could stabilize within ± 0.01 K. With the heater off, the heat of the blackbody load dissipated through the heat sink to the 4 K stage, cooling the load from 20 K to 9 K in approximately 3 mins.

7.2 Y-factor measurements

7.2.1 C & W approximation

As we have stated in Chapter 4, the noise temperature of the mixer is calculated by measuring the Y factor ($Y = P_{\rm h}/P_{\rm c}$) using the expression,

$$T_{\rm rec} = (T_{\rm h} - YT_{\rm c})/(Y-1) \tag{7.2}$$

In the Y-factor method used throughout this thesis, the noise temperature of the blackbody radiation $T_{\rm h}$ or $T_{\rm c}$ was defined by the Rayleigh-Jeans (R-J) approximation which equals the brightness temperature to the physical temperature of the blackbody load,

$$T^N_{R-J} = T \tag{7.3}$$

where T is the physical temperature of the blackbody load. However the R-J approximation can only be used in the limit of small $h\nu/k_BT$. A more accurate way to evaluate the noise temperature is to use Collen & Welton (C&W) approximation,

$$T^N_{C-W} = \frac{h\nu/k_B}{e^{h\nu/k_BT}-1} + \frac{h\nu}{2k_B} \tag{7.4}$$

Collen & Welton approximation [17], which is a form of the Planck formula with an additional zero-point fluctuation, gives a more accurate noise temperature value. It can give a receiver noise temperature consistent with the quantum mixer theory and with the constraints of the uncertainly principle [6]. In Fig 7.3, we plotted the R-J approximation and the C & W approximation for a blackbody load in the temperature range of 0 K-20 K at 230 GHz. We can easily notice that the difference between R-J approximation and C & W approximation strongly depends on the physical temperature of the hot and cold loads ($T_{\rm h}, T_{\rm c}$), and also on the frequency ν. R-J approximation and C & W approximations only become similar for $h\nu/k_{\rm B}T << 1$, which means a low operating frequency ν or a high load temperature. In Fig 7.4, we compare the noise temperatures of one mixer, which was measured with T=20 K and T=9 K temperature loads, by either the C & W approximation or the R-J approximation. The calculated noise temperatures using C & W approximation are ∼6 K lower than the ones calculated using R-J approximation across the RF band, which is a significant portion of the total noise temperature (∼ 65 K). The conclusion therefore is that at 230 GHz, the R-J approximation is not accurate with low temperature loads (i.e 20 K or 9 K), instead the C & W approximation should be used. In this chapter, therefore the noise temperature calculation will be

based on the C & W approximation. However in the noise temperature measurements performed in the previous chapters, the blackbody loads are located either at room temperature (T=279 K) or at the boiling point of liquid nitrogen (T=77 K). Thus Rayleigh-Jeans approximation is accurate enough to use in relating the physical temperature to the noise temperature simply because $h\nu/k_BT \ll 1$

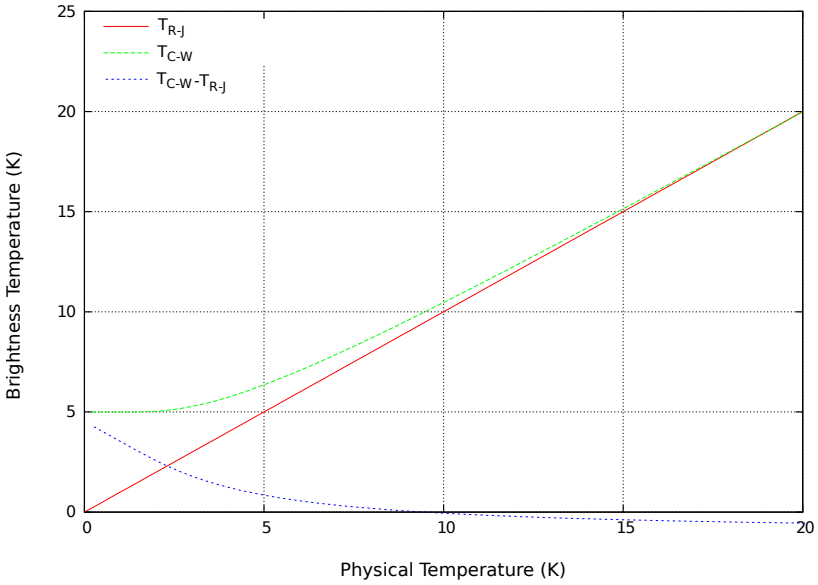

Figure 7.3: Brightness temperature as a function of physical temperature for blackbody radiation at 230 GHz, according to R-J approximation and C & W approximation. Also shown is the difference in the brightness temperature between the two. The R-J approximation converges to the C & W approximation only at high load temperatures.

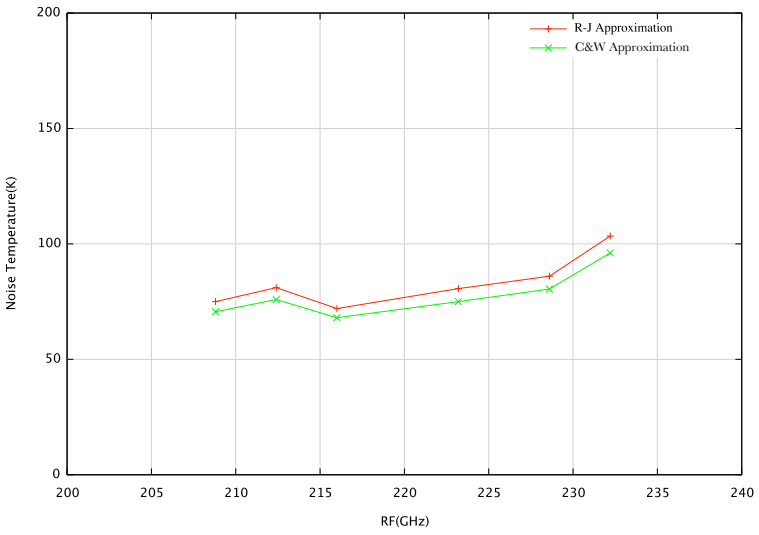

Figure 7.4: Comparison of noise temperatures calculated by R-J approximation or C&W approximation.

7.2.2 Optimization of the temperature load system

The noise temperature of SIS mixer is usually calculated by the measured Y factor ($Y = P_{\rm hot}/P_{\rm cold}$), as

$$\begin{aligned} T_{\rm N} &= (T_{\rm hot} - YT_{\rm cold})/(Y-1) \\ &= f(T_{\rm hot}, T_{\rm cold}, Y) \end{aligned} \tag{7.5}$$

The error deduced in the noise temperature ΔT_N can be expressed as

$$\begin{aligned} \Delta T_{\rm N} &= \frac{\partial f}{\partial T_{\rm hot}}\Delta T_{\rm hot} + \frac{\partial f}{\partial T_{\rm cold}}\Delta T_{\rm cold} + \frac{\partial f}{\partial {\rm Y}}\Delta Y \\ &= \Delta T_{\rm hot} + \frac{-Y}{Y-1}\Delta T_{cold} + (T_{\rm cold} + T_{\rm N})^2/(T_{\rm hot} - T_{\rm cold})\Delta Y \\ &= -\Delta T + (T_{\rm cold} + T_{\rm N})^2/(T_{\rm hot} - T_{\rm cold})\Delta Y \end{aligned} \tag{7.6}$$

where ΔT is the error in the load temperature ($\Delta T = \Delta T_{\rm hot} = \Delta T_{\rm cold}$), and ΔY is the error in the Y-factor. Eq 7.6 indicates that ΔT_N could be effectively reduced by a larger $T_{\rm hot} - T_{\rm cold}$ and a lower $T_{\rm cold}$. Thus a wider dynamic range ($T_{\rm hot} - T_{\rm cold}$) and a lower base temperature ($T_{\rm cold}$), (in addition to the shorter thermal time constant and less heating of the mixer block, as we discussed earlier) were important targets for the variable temperature load.

The Y-factor measurements using the variable temperature load were performed on device D2N1 across an RF bandwidth 208.8 GHz to 232.2 GHz. The load was tested for accurate measurements using the specification listed in Tab 7.1.

Round	Heat Sink Dimension	Heat Resistor	Temperature Range	Thermal Time Constant	block heating
Round 1	N/A	140 Ω	40-60 K	60 mins	4.0 K->4.1 K
Round 2	0.3 mm^2×2 mm	140 Ω	7.5-13 K	2 mins	4.0 K->4.3 K
Round 3	0.3 mm^2×2 mm	100 Ω	7.5-17.8 K	1 mins	4.0 K->4.3 K
Round 4	0.15 mm^2×2 mm	60 Ω	9-20 K	1 min	4.0 K->4.15 K
Round 5	0.15 mm^2×2 mm	40 Ω	9-24 K	1 min	4.0 K->4.2 K

Table 7.1: Tests for optimizing the load specification.

The noise temperature measurements as a function of frequency based on different versions of the temperature loads are displayed in Fig 7.5. For comparison, we also show the noise temperatures measured by the external 77 K/297 K load.

In round 1, no head sink was used hence it took ∼60 mins for the load to be heated from 40 K to 60 K and another 15 mins for the temperature to stabilize within ±0.1 K. The cooling time was even longer. The mixer response was measured as a function of bias voltage with the load regulated at 42 K, 45 K, 49 K, 52 K, 54 K, 59 K. The I-F curves recorded for all load temperatures and the measured noise temperatures are shown in Fig 7.6. The noise temperatures were calculated using

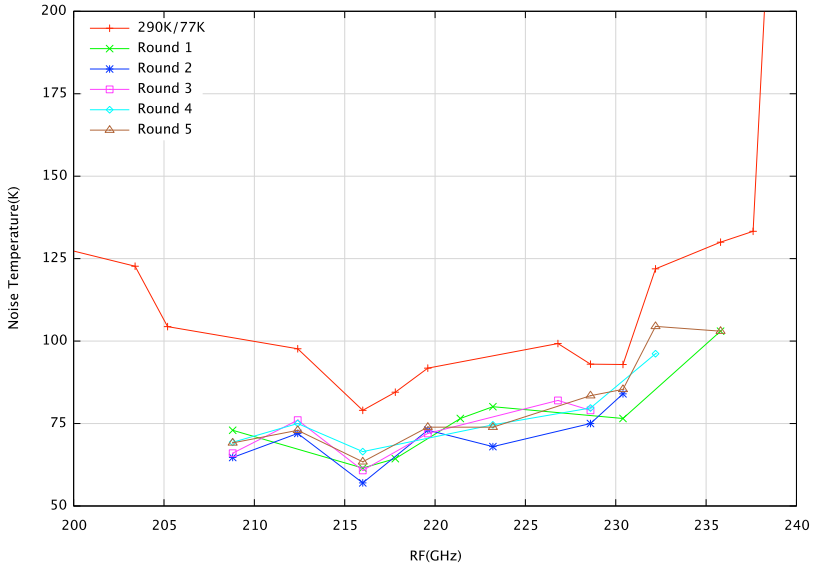

Figure 7.5: The noise temperatures measured with different variable temperature loads in the process of the load modification and with the hot/cold (290 K/77 K) load installed external to the cryostat. The details for the different temperature loads can be found in Tab 7.1.

a single cold load measurement at 42 K. There existed significant variation in the measured noise temperature ($\sim$ 10 K) corresponding to different load temperatures. To investigate the reason for the variations, we recorded the IF outputs of the receiver chain over half an hour with an interval of 5 mins (Fig 7.7). It was found that the IF output signal had a significant drift (1%) with a period of $\sim$15 mins. The drift degraded the accuracy of the noise temperature by $\pm$4 K. Due to the drift, it was hard to decide when the IF data should be measured. This drift could be caused by the instability of the temperature load and also the drifts in the gain of the IF system. As there was no heat sink attached to on the load, the cold load temperature $T_{\rm cold}$ was 40 K, which was too high and too close to $T_{\rm hot}$ for accurate Y-factor measurement. Both the significant drift in the load system and the high base temperature $T_{\rm cold}$ led us to add a heat sink to the load to reduce the base temperature $T_{\rm cold}$, to reduce the thermal time constant and to increase the dynamic range in the Y-factor measurement.

In round 2 (Tab 7.1), a copper strip heat sink connected the load (Fig 7.1) to the 4 K stage cold plate. The copper heat sink had a cross section of 0.3 mm^2 and a length of 2 mm. As a result, the base temperature of the load was reduced to 7.5 K and it took it only 2 min to rise up to 13 K. Once the target temperature was reached, significant temperature fluctuation stopped within 3 seconds and the temperature stabilized at $T_{\rm target}$ $\pm$0.01 K. The IF outputs as a function of time as well as the calculated noise temperatures are plotted in Fig 7.8, showing a much smaller drift in the IF output and an increased accuracy in the noise temperature measurement, despite the small range in $T_{\rm hot} - T_{\rm cold}$.

To increase the temperature difference between the hot and the cold loads, the heating resistor was

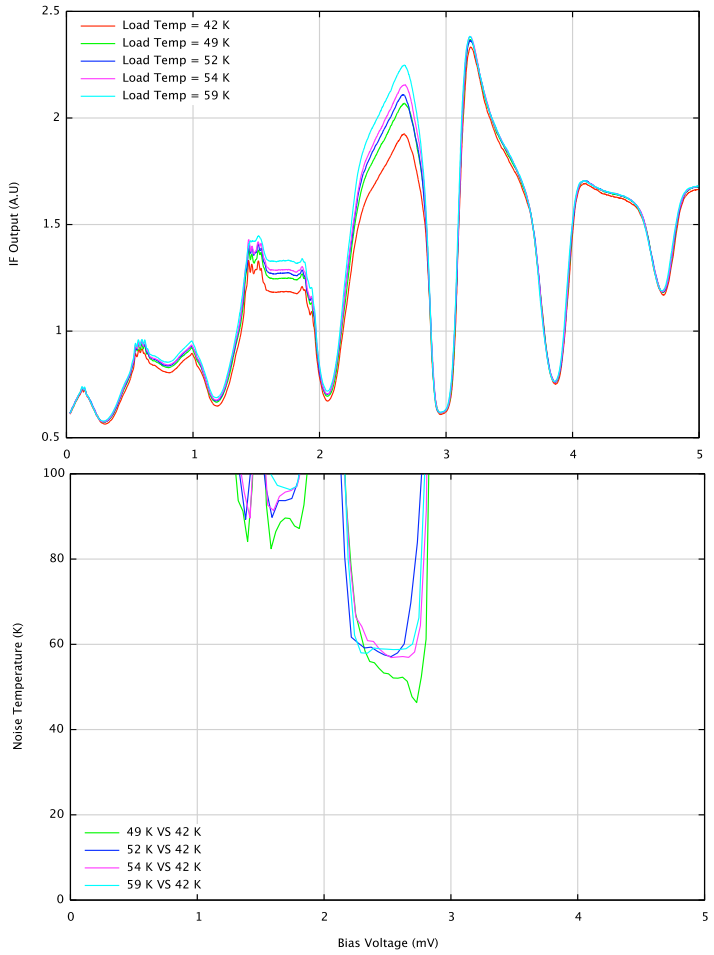

Figure 7.6: Receiver test at 216 GHz using the hot load with temperatures at 42 K, 45 K, 49 K, 52 K, 54 K and 59 K. The cold load temperature was at 40 K. In the top panel, we show the measured IF curves as a function of the bias voltage with the different hot load temperatures and in the bottom panel, the corresponding measured noise temperatures.

reduced from 140 Ω to 100 Ω, causing the temperature of the hot load to increase to 17.8 K within only 1 min. However this increase of the cold plate loading caused the mixer block to be heated from 4.0 K to 4.3 K which could potentially have had a large impact on the accuracy of the measurement. We therefore modified the system by reducing the width of the copper strip, to decrease the amount of heat flowing to the 4 K stage. As a result, the heating of the SIS mixer was mitigated, and the mixer block temperature was slightly increased from 4 K to 4.15 K. The hot load temperature could then be driven from 9 K to 20 K within 1 min. In round 5, we intended to reduce the heat resistor further to expand the temperature range (9 K->24 K) but this resulted in an unwanted increment of the mixer block temperature (4 K->4.2 K). The temperature load in round 4 was therefore taken as be the best setup for our experiment, since it provided a large temperature range (11 K), a short thermal time constant (1 min) and a relatively small heating of the mixer block (0.15 K) . Therefore

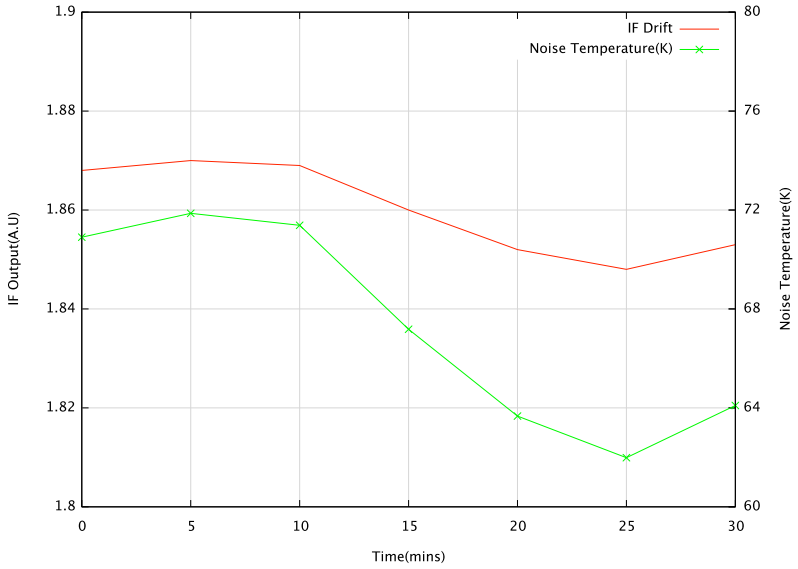

Figure 7.7: The IF output with RF radiation at 37 K recorded over half an hour and the measured noise temperature. IF output was recorded after the temperature variation of the load became less than ±0.1 K.

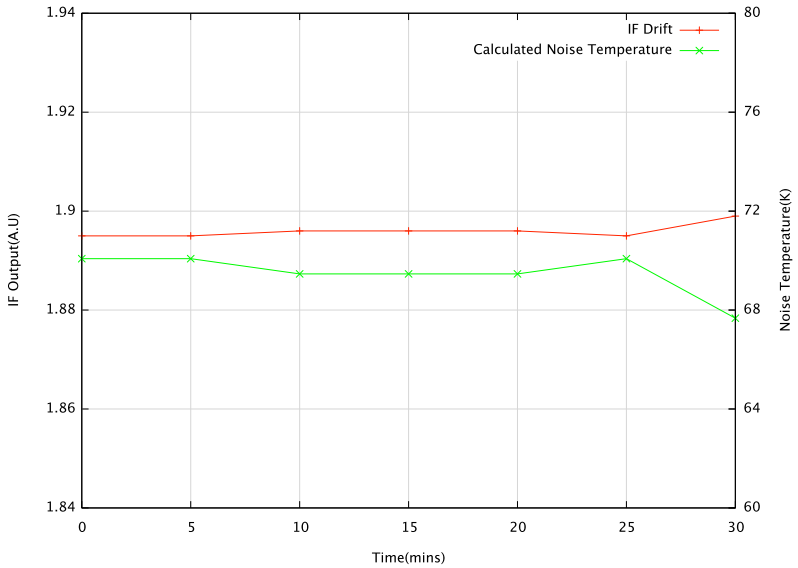

Figure 7.8: The IF output and the measured noise temperature with input RF radiation at 13 K recorded over half of an hour. and also the measured noise temperature at each time spot. We started to record the IF output after the temperature variation of the load became less then ±0.1 K.

the following discussion will focus on the results obtained in round 4. Fig 7.9 shows the IF mixer response measured as a function of the bias voltage at LO frequency 216 GHz, with the input loads at 9.0 K and 20 K. Notice that at 216 GHz, the measured receiver noise temperature was reduced from 79 K to 66 K as a result of using the internal cryogenic load rather than 77 K/297 K external load. This is a very significant improvement in the noise temperature which justifies the effect in using an internal load in this Y-factor measurement.

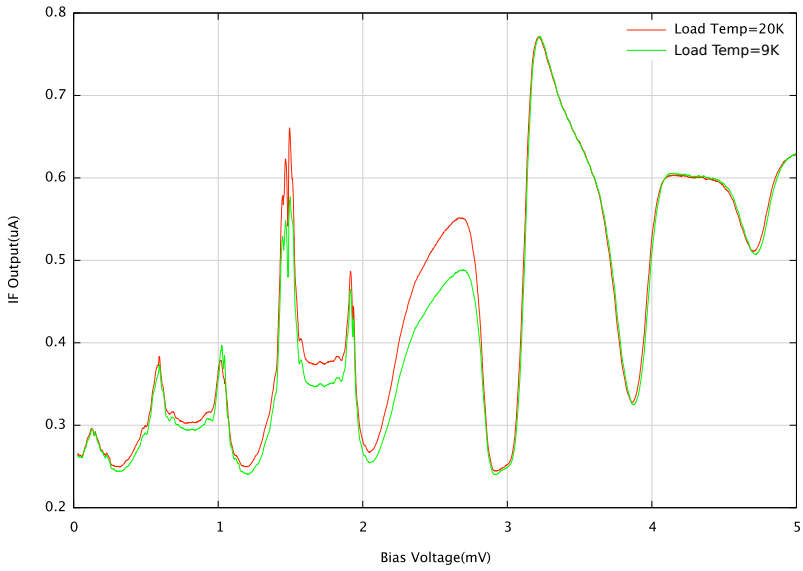

Figure 7.9: The IF response curves with RF radiation at 8.9K and 20K at LO frequency of 216GHz.

To investigation the validity of this result we recall that the noise temperature equation for the receiver chain in the GUBBINS system using the variable temperature load can be written as,

$$T_{\mathrm{N}} = T_{\mathrm{LO-Coupler}} + \frac{T_{\mathrm{SIS}}}{G_{\mathrm{LO-Coupler}}} + \frac{T_{\mathrm{LNA}}}{G_{\mathrm{LO-Coupler}} G_{\mathrm{SIS}}} + \frac{T_{\mathrm{Warm}}}{G_{\mathrm{LO-Coupler}} G_{\mathrm{SIS}} G_{\mathrm{LNA}}} \tag{7.7}$$

Since the RF load was installed inside the cryostat, the optical loss due to the room-temperature vacuum window and the Zitex IR filters were no longer present, as well as the loss $1/G_{\mathrm{window}} G_{\mathrm{filter}}$ that used to multiply all the components after the window (Eq 7.1). If we assume that window and filters contribute a loss of 3.2% ($L_{\mathrm{window}} L_{\mathrm{filter}} = 1.03$), this corresponds to a noise temperature of $T_{\mathrm{window/filter}} = 10.2\ K$. If the 79 K noise temperature which was measured with the hot/cold load external to the cryostat, is corrected against the variable temperature loads, the noise contributed by all the components post to the window/filter is (79-10.2)*0.968≈66.5 K, agreeing with the measured noise temperature by the internal load. We should point out however that the estimated $L_{\mathrm{window}} L_{\mathrm{filter}}$ is slightly higher than expected since the loss of the LD45 foam window and the IR filter obtained from FTS measurements was negligible at around 230 GHz. Therefore the high loss in the vacuum

window/IR filter might have been increased by the existence of the standing waves between the window and the RF horn reflector.

7.2.3 Heating of the SIS junction

The dependence of the SIS mixers performance on the ambient temperature has been extensively investigated by researchers [65]. It was found that the Nb SIS mixer can maintain a similar and reasonable performance at ambient temperatures as high as 80% of the superconducting transition temperature [65]. Therefore the deterioration of the quantum limited noise and the mixer conversion gain of an SIS mixer would be negligible, if the SIS junction was heated by only 0.2 K. However, in the context of the temperature load experiment, an increase of 0.2 - 0.3 K in the ambient temperature did have some impact on the measured mixer performance. For example, as the load temperature rose from 9 K to 20 K, the block temperature rose from 4.0 K to 4.15 K. We therefore measured $P_{9\mathrm{K}}$ when the SIS junction was cold (4 K), but we measured $P_{20\mathrm{K}}$ when the SIS junction was heated to 4.15 K. The noise temperature of the SIS mixer calculated through the measured Y factor $Y = P_{20\mathrm{K}}/P_{9\mathrm{K}}$ would then become inaccurate since the junction was not at a constant temperature. We want to emphasize however that the measurement shown in Fig 7.5, Fig 7.8 and Fig 7.9 demonstrate that the impact of the change in junction temperature on the measurement accuracy is not significant.

To evaluate the impact of the junction heating, we recorded two sets of pumped IV/IF responses in the process of the junction heating, with the block temperature respectively at 4.10 K and 4.15 K and with the load temperature fixed at 20 K. We could then assess the accuracy of our experiment by comparing with theoretical calculations.

The dependence of the SIS junction gap voltage V_{gap} on the ambient temperature T is given by the BCS theory [23] as

$$\frac{1}{VN(E_F)} = \int_0^{\hbar\omega_D} d\xi(\xi^2+\Delta^2)^{-1/2}\mathbf{tanh}[\frac{1}{2k_BT}(\xi^2+\Delta^2)^{1/2}] \tag{7.8}$$

By solving this equation, we can find the dependence of Δ on temperature as shown in Fig 7.10. From the plot, we notice that a temperature increment from 4.0 K to 4.15 K leads to a ΔV_{gap} of 0.015 mV, agreeing with what was observed in the experiments (Fig 7.11).

In Fig 7.12, we plotted the experimental IF/IV responses of the SIS mixer with junction temperatures at 4.10 K and 4.15 K with load temperature at 20 K, and the IF/IV responses with junction temperature at 4.0 K with load temperature at 9 K. It can be seen that from the unpumped IV curves that, the gap voltage was slightly suppressed at higher temperatures. Due to the shift in V_{gap} (Fig 7.12), the IF response curve of the hotter junction was shifted downwards towards zero bias

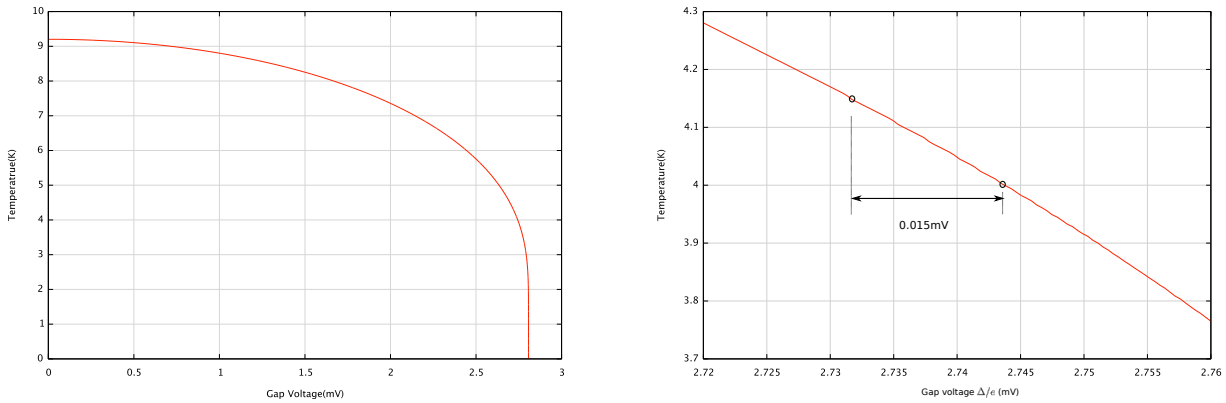

(a) (b)

Figure 7.10: (a) The relation between the junction gap voltage and the ambient temperature. (b) Same relation zoomed around T=4 K.

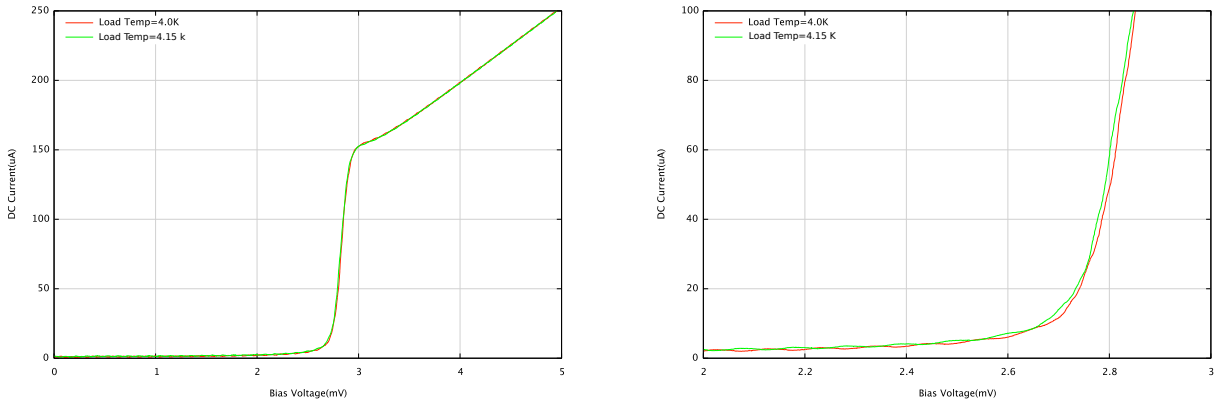

(a) (b)

Figure 7.11: (a) The measured unpumped IV curve with block temperature at 4.0 K and 4.15 K (b) The IV curve zoomed at bias voltage from 2 mV to 3 mV.

voltage and also the amplitude on the first photon step was slightly reduced.

It can clearly be seen from Fig 7.12, that the IF curve did not change significantly over a wide range of bias voltages (i.e remained almost unchanged between bias voltages 2.2 mV and 2.6 mV), apart from the IF curve at the bias voltage near both step edges (i.e between bias voltages 2.6 mV and 2.7 mV). We could therefore choose to measure the noise temperature almost anywhere across the first photon step. This is also confirmed by the calculated noise temperature in Fig 7.12 (bottom) where the values given by the blue and green curves are identical for 2.2 mV$< V_0 <$2.6 mV. We therefore conclude that measuring the noise temperature with an load inside the cryostat using the setup in round 4 gives accurate results.

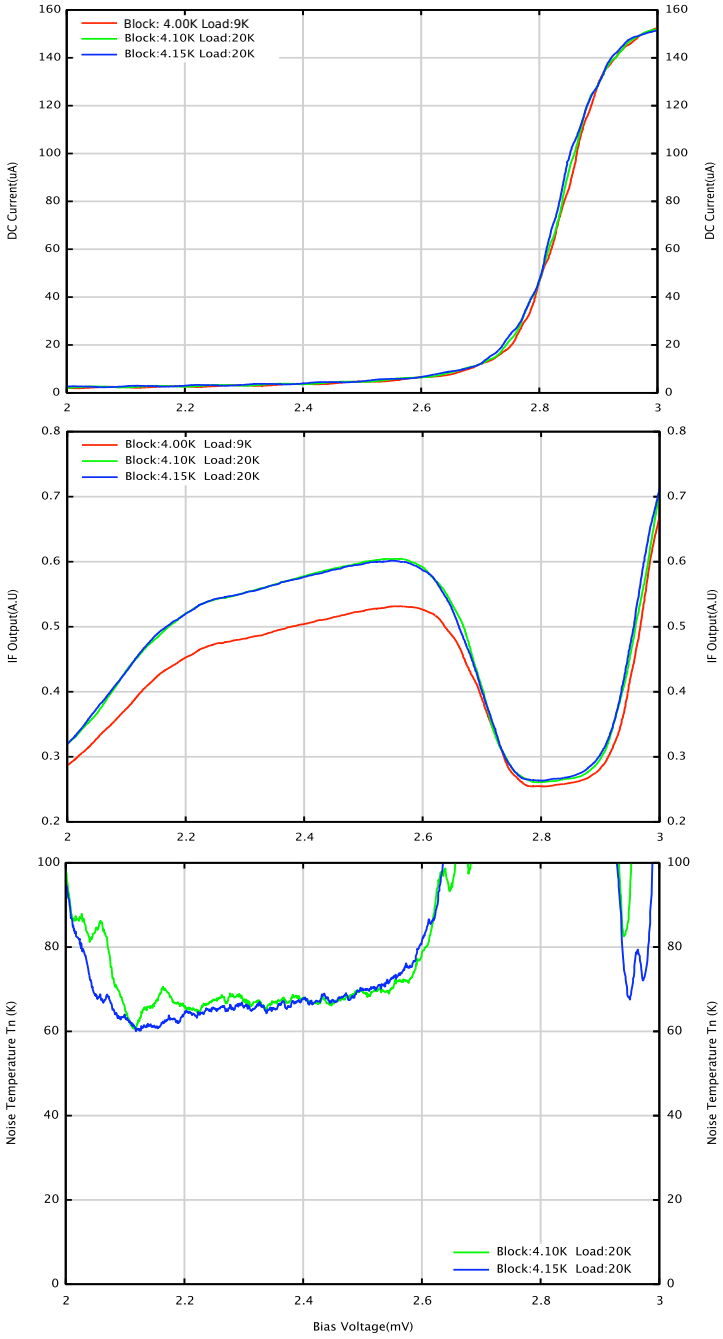

Figure 7.12: (Top) The IV curves as a function of bias voltages at different block temperatures. Notice that the gap voltage was reduced as a consequence of junction heating. (Middle) The IF curves as a function of bias voltage at different block temperatures. Notice that the shape of the IF curve at the first photon step was only slightly changed as a result of junction heating. (Bottom) The calculated noise temperature at different junction temperatures as a function of the bias voltage.

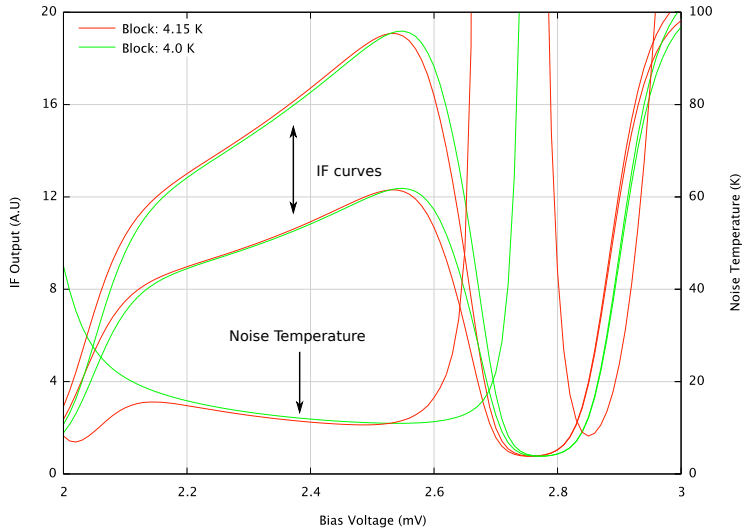

Figure 7.13: The SuperMix simulated IF curves at bias voltage ranging from 2.0 mV to 3.0 mV. With a heated SIS junction, the shape of the IF curve at the first photon was slightly distorted. We also show the SuperMix calculated noise temperature with different junction temperatures.

As an additional confirmation of the integrity of our method and experiment results, we simulated the mixer performance in SuperMix. In fig 7.13, we show the simulated pumped IF curves (with RF radiation at either 9 K or 20 K) with SIS junctions at 4.10 K and 4.15 K respectively. These simulation show that by slightly heating up the SIS junction, the IF curve has slightly shifted towards the zero bias voltage. This shift results in a slight decrease in the amplitude of the IF curve at band edges but almost unchanged amplitude across the middle of the photon step. The behavior of the computed IF curves agrees with the experimental observations.

In summary, experimental tests and simulations have clearly shown that, the heating of the SIS junction by 0.15 K did not effect the mixer noise temperature measurements, provided these measurements were taken at bias voltages away from the photon step edges, and data was recorded as quick as possible after the temperature was stabilized.

7.3 Summary and Conclusion

We constructed a cryogenically variable temperature load to investigate the impact of the room temperature optical components on the receiver chain noise. The blackbody load was installed at the 4 K stage and directly filled the beam of the RF feed horn of the SIS mixer. Using this load, the noise temperature was measured across the RF band and ∼15 K decrement in noise temperature was measured relative to the measurement done using an external 77 K/297 K load.

The cryogenic variable temperature load delivers very good performance in conjunction with the SIS mixer system, however one small defect is that the current apparatus caused heating of the 4 K stage by the temperature load. For the future improvement, we could consider detaching the temperature load from the 4 K stage and remove it to the 30 K stage and heat sink the load to the 30 K stage. The base temperature of the temperature load would be around 40 K. However as the mixer block is then entirely isolated from the temperature load, we could feel free to reduce the heat resistor from 50 Ω to much lower value to expand the dynamic temperature range. The sacrifice of a higher base temperature T_{cold} would then be compensated by a larger temperature range and less heating of the SIS mixer block.

Chapter 8

Summary and Future Work

8.1 Summary

Superconductor-Insulator-Superconductor (SIS) heterodyne receiver has been successfully used for radio astronomy at the (sub)millimeter wave band for decades, because of its high sensitivity, high dynamic range and stability of operation. However the successful operation of SIS mixers is never trivial since it requires rigorous circuit design, accurate sub-micro device fabrication, good coordination with the supporting electronics and extensive cryogenic testing. The development of Niobium SIS receivers at frequencies well below the superconducting gap (f<680 GHz) has matured; the noise temperature of state-of-art detectors can achieve 3 to 5 times the quantum limited noise ($\hbar\omega/k_{\mathrm{B}}$) over ∼40% of the RF bandwidth. However the detectors in most of the telescopes can only offer an IF bandwidth of a few GHz, although some of the recently designed ones might extend it to 8 GHz. Therefore expanding the IF bandwidth recently became another important solution to further enhance the receiver sensitivity, apart from merely reducing the detector noise temperature. With a wide IF bandwidth, the surface brightness sensitivity of the heterodyne receiver would be effectively enhanced for observations towards the faint continuum source. Additionally detectors with a wide IF bandwidth could cover more spectral lines in the spectroscopy observation, reducing the required amount of LO setting and greatly reducing the observing time.

This thesis focuses on the theoretical modeling, design and experimental verification of Nb SIS mixers operating around 230 GHz with a wide IF bandwidth. The mixer is based on a novel design that using the unilateral finline and other planar superconductivity circuits to couple the electromagnetic signals from the waveguide to the SIS junction. The full mixer chip is deposited on the silicon substrate, which is mounted in the E-plane of the waveguide. This design provides a wide RF bandwidth, reduces the demanding requirement for the mixer block and allows elegant integration of the on-chip planar

circuit.

The SIS mixers are employed in a novel heterodyne interferometer (GUBBINS). GUBBINS is built to perform demonstration observations on the Sunyaev-Zel'dovich effect in the Cosmic Microwave Background (CMB) radiation, especially at the null frequency around 217 GHz. CMB observation requires extremely high brightness sensitivity and very good control of the systematic and instrumental effects. Apart from the SZ effect observation, GUBBINS will also carry out measurements of atmospheric phase stability, as well as other tests of ground based interferometry.

This thesis concentrates on the underlying physics concerning SIS junctions and the investigation of quantum mixing theory (Chapter 2), the rigorous electromagnetic design of the SIS mixer (chapter 3), the SIS mixer performance tested in the RF and IF band (chapter 4 and chapter 5), the description of the GUBBINS instrument (Chapter 6) and the development of a variable temperature load system (Chapter 7). In what follows we shall summarize and comment on the key contents of each chapter:

- Chapter 1: Introduction

- Chapter 2: we described the physical principle of quantum tunneling in the SIS junction, i.e Cooper pair, quasi-particle tunneling and photon-assited quasi-particle tunneling. Also we outlined the quantum mixer theory developed by Tucker [55], which helps to predict the performance of the SIS tunnel junction mixer. Several practical techniques/softwares were introduced which could predict the mixer performance, i.e embedding impedance recovery, SuperMixer package and rigorous 3-D electromagnetic simulation software (HFSS). In addition, we also briefly introduced the fabrication techniques for the SIS mixer device: the photolithography technique was used in fabricating the planar circuits and the Reactive Ion Etching (RIE) technique was used to define the SIS junction.

- Chapter 3: we presented the design of a unilateral finline SIS mixer based on the silicon substrate. HFSS was extensively used to design and optimize the planar circuits in the SIS mixer device, such as the finline transition, the slotline-to-microstrip transition and the tuning circuits, etc. The RF/LO electromagnetic signals could be coupled from the waveguide to the SIS mixer chip through the unilateral finline and further coupled to the SIS junction through simple planar circuits. The performance of the SIS mixer was fully simulated using rigorous electromagnetic software HFSS, imported to SuperMix package to predict its full chip heterodyne behavior. An operating RF bandwidth of $\sim$80 GHz was predicted, defined by a HFSS simulated return loss below of -10 dB. The design has several attractions that can be summarized as follows: (1) The device does not interact with the waveguide mode since the electromagnetic field is

concentrated in the finline slot and then in the microstrip lines. Therefore the mixer block does not require complicated and high precision machining; (2) The substrate area is large compared to the dimension of the superconductive planar circuits, which allows elegant integration of useful planar circuits. For instance, this allows the possibility of using the chip in a back-to-back configuration, where RF and LO radiation signals are injected to the device from either sides, that avoiding the beamsplitter losses; (3) Unilateral finline could realize a wide bandwidth RF signal coupling. And the silicon substrate could yield a better signal coupling from the slotline structure to the microstrip structure than other commonly used materials, i.e Quartz, due to its high dielectric constant.

- Chapter 4: the experimental setups for testing the mixer performance are described. And the techniques for assessing and analyzing the RF performance of the mixers are discussed. Most of the device could be easily pumped and showed promising performance. The RF tests for several representative devices are discussed here and analyzed. The receiver noise temperatures are broken down to different contributions from various components in the receiver chain to highlight the performance of each component in the receiver chain and facilitate the improvement of the mixer detector. A best noise temperature of 50 K and an average noise temperature of 75 K over an RF bandwidth of 160 GHz to 260 GHz was measured for the best device. The HFSS simulations were compared with the experimental results, to investigate the influence of different parameters of the SIS mixer, e.g normal resistance, substrate thickness, on the mixer performance. The embedding admittance was also recovered across the RF band to examine the performance of the tuning circuit. As two test systems had been employed through the mixer testing, namely a wet cryostat system and a G-M (Gifford-McMahon) cooler system, investigations were carried out to find the reasons for the difference in the measured noise temperature between the two systems.

- Chapter 5: we investigated the IF performance of the finline SIS mixer. We performed Y-factor measurements for the unilateral finline devices across the IF bandwidth to evaluate the IF performance. The mixer presented reasonably flat noise temperature across 2–15 GHz but with an IF resonance located at 8 GHz. The IF transformers were designed and integrated with the SIS mixer to optimize the mixer performance over bandwidth 2–6 GHz. The mixer performance was successfully improved over 2–6 GHz by the IF transformer. Rigorous simulations were performed to explore the reasons for the IF resonance. Then the mixer design was revised to reduce the area of the microstrip lines before the SIS junction, which could remove the IF resonant frequency out of the IF band. The new mixer could achieve a continuous IF bandwidth

of 0-13 GHz in conjunction with a new IF transformer.

- Chapter 6: we described a prototype single-ended mm-wave heterodyne interferometer (GUBBINS). It is built to observe the Sunyaev-Zel'dovich (SZ) effect in the Cosmic Microwave Background (CMB) radiation, especially at around the 217 GHz null frequency of the thermal SZ effect. GUBBINS features a high brightness sensitivity and moderate spectral/spatial resolutions. The high brightness sensitivity of the GUBBINS instrument is achieved by the ultra-wide IF bandwidth SIS mixers and the backend correlators, and also by the special optical design which yields a large filling factor. The SIS mixer detectors described in the above chapters were integrated in the GUBBINS system with other supporting electronics. Low noise temperatures have been measured for the SIS mixer devices used in the GUBBINS system. The coupling efficiency of the LO coupler in GUBBINS system was experimentally verified and the reasons for high coupling were investigated. The back-end electronics, which were designed and fabricated by my colleagues, are also discussed.

- Chapter 7: A variable-temperature load was developed, which was installed inside the cryostat and used to investigate the impact of the room temperature optical components upon the receiver chain noise. The blackbody load was installed at the 4 K stage and directly filled the beam of the RF feed horn of the SIS mixer. Using this load, the blackbody radiation could directly be coupled to the mixer feed without passing through any optical components, therefore eliminating the optical losses. The noise temperatures were measured across the RF band and ∼15 K decrement in noise temperature was measured relative to the noise temperature measured using an external 77 K/297 K load. This is a very significant improvement in the noise temperature, which justified the effect of using an internal load in the Y-factor measurement. As the temperature load was attached to the 4 K stage, the load would heat up the SIS mixer block by 0.15 K when the load was heated from 9 K to 20 K. The impact of the junction heating was then analyzed and it was confirmed that a 0.15 K temperature increment would not impose a substantial effect on the measurement accuracy.

8.2 Future Work

- (1) A new batch of SIS mixers, which remove the IF resonant frequency out of the IF band, will be fabricated in the near future. Extensive cryogenic experiments have to be carried out to test the RF/IF performance. The mixer behavior in different IF bandwidths, i.e 6 - 8 GHz, 8 -10 GHz and 10 -12 GHz, could be tested using the available IF bandpass filters. If a mixer

design with an IF bandwidth of 20 GHz is desired in the future, we might think of replacing the 90° radial-stub slolinte-to-microstrip transition by other alternatives, e.g CPW circuits, or replacing the finline transition by the probe coupling, to further reduce the lumped inductance and capacitance.

- (2) A 180° phase-switching system has to be built on the GUBBINS LO system. The waveguide LO coupler might have to be either re-designed or re-fabricated to solve the high coupling issue. Also, the SIS mixer detector system has to be assembled with the backend 30 K amplifier and the correlator to form a real radio interferometer. All the laboratory tests towards the complete telescope instruments should be commissioned. The optical system also has to be tested and calibrated towards a known planet to test its beam pattern.

- (3) The internal variable temperature load could be removed from the 4 K to the 30 K stage to be thermally isolated from the SIS mixer block. Thus the temperature span of the load could be further expanded without seriously heating up the SIS junction.

AppendixA: SIS mixer device under Scanning Electron Microscope (SEM)

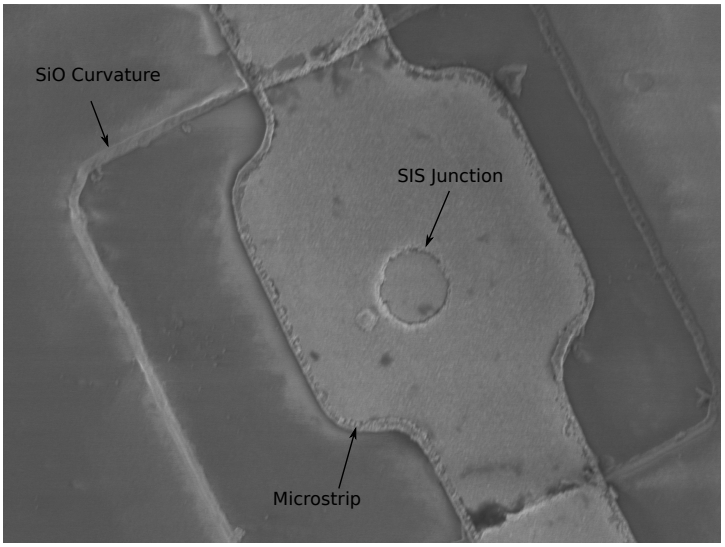

Figure 1: An SEM picture of an SIS junction

The picture of an SIS junction was captured by a scanning electron microscope (SEM) and shown in Fig 1. The SIS junction has a nearly perfect circular shape and a smooth edge. The SIS junction is embedded in the center of the microstrip and a 10 μm $\times$ 10 μm curvature was formed in the SiO dielectric layer around the SIS junction, to allow better contact between the niobium layer of the SIS junction and the microstrip.

Bibliography

[1] A.B.Pippard. Trapped flux in superconductors. *Philosophical transactions of the Royal Society of London*, **248**:97:129, 1955. 19

[2] Nabila Aghanim, Subhabrata Majumdar, and Joseph Silk. Secondary anisotropies of the CMB. *review paper for ROP*, **71**:66:69, 2008. 2

[3] R.A. Alpher and R.C. Herman. On the relative abundance of the elements. *Physics Review*, **74**:1737:1742, 1948. 1, 112

[4] P. W. Anderson and J. M. Rowell. Probable observation of the Josephson superconducting tunneling effect. *Phys. Rev. Lett.*, **10**:230–232, Mar 1963. 17

[5] S Andree, M. Justen, M. Schultz, C.E. Honingh, K. Jacobs, and J. Stutzki. Characterisation of SIS array mixers on Si substrates at 350 GHz. *Infrared Millimeter and Terahertz Waves*, **2**:1:2, 2010. 13

[6] A.R.Kerr, M.J.Feldman, and S.-K.Pan. Receiver nosie temperature, the quantum noise limit, and the role of the zero-point fluctuations. research report, National radio astronomy observatory, Charlottesville, Virginia,USA, 1996. 144

[7] A.R.Kerr, S.-K.Pan, A.W.Lichtenberger, and H.H.Huang. A tuneless SIS mixer for 200-280 GHz with low output capacitance and inductance. *9th International Symposium on Space Terahertz Technology*, March 17-19, 1998. 92

[8] A.R.Kerr, S.-K.Pan, E.F.Lauria, A.W.Lichtenberger, J.Zhang, M. W. Pospieszalski, N. Horner, G. A. Ediss, J. E. Effland, and R. L. Groves. The ALMA band 6 (211-275 GHz) sideband- separating SIS mixer-preamplifier. *International Symposium on Space THz Technology*, 2004,Northampton. 13

[9] J. Bardeen, L. N. Cooper, and J. R. Schrieffer. Microscopic theory of superconductivity. *Phys. Rev.*, **106**:162–164, Apr 1957. 20, 23, 24

[10] A.M. Baryshev, F.P. Mena, J. Adema, R. Hesper, B. Jackson, G. Gerlofsma, M. Bekema, K. Keizer, H. Schaeffer, J. Barkhof, C.F.J. Lodewijk, D. Ludkov, T. Zijlstra, E. van Zeijl, T.M. Klapwijk, and W. Wild. ALMA band 9 cartridge. *19th*

International Symposium on Space Terahertz Technology, 2008,Groningen. 13

[11] Frank Bertoldi. Sunyaev-Zel'dovich effect surveys: from Hubble to APEX. http://www.astro.uni-bonn.de/~bertoldi/projects/sz/ringberg/. 115

[12] E.V. Bezuglyi, A.S. Vasenko, E.N. Bratus, V.S. Shumeiko, and G. Wendin. Subgap current in superconducting tunnel junctions with diffusive electrodes. *Physical Review*, **73**, 2006. 27

[13] M. Birkinshaw, S.F. Gull, and H. Hardebeck. The Sunyaev-Zel'dovich effect towards three clusters of galaxies. *Nature*, **309**:34:35, 1984. 3, 114, 117

[14] M. Birkinshaw, S.F. Gull, and H. Hardebeck. Observations of the Sunyaev-Zeldovich effect. *Astrophysics and Space Science Library*, **164**:77:94, 1990. 117

[15] Mark Birkinshaw. The Sunyaev-Zel'dovich effect. *Physics Reports,*, **310, 97.**, 1999. 117

[16] Bernard F. Burke and Francis Graham-Smith. *An introduction to Radio Astronomy*. The Cambridge University Press, 2003. 8

[17] Herbert B. Callen and Theodore A. Welton. Irreversibility and generalized noise. *Phys. Rev.*, **83**:34–40, Jul 1951. 144

[18] Caltech. http://www.submm.caltech.edu/supermix/default.html. 36

[19] John E Carlstrom, Marshall Joy, and Laura Grego. Interferometric imaging of the Sunyaev-Zeldovich effect at 30 GHz. *THE ASTROPHYSICAL JOURNAL*, **456:L75-L78**, 1996, Jan. 121

[20] P.K. Grimes C.E. North, G. Yassin. Rigorous analysis of antipodal finline tapers for high performance millimetre and sub-millimetre detectors. *17th Interna- tional Symposium on Space Terahertz Technology*, 2006. 46

[21] C.Holler, M.E.Jones, A.C.Tayloar, A.I.Harris, and S.A.Maas. 2-20 GHz analogue lag-correlator for radio interferometry. *IEEE Transactions on instrumentation measurement*, **61**, 2011. 137

[22] Whitney Clavin and J.D. Harrington. Planck mission brings universe into sharp focus. *NASA*, 2013. 113

[23] Michel Cyrot and Davor Pavuna. *Introduction to Superconductivity and High-Tc Material*. World Scientific, 1999. 25, 151

[24] WMAP data. http://www.flickriver.com/photos/tags/cerrotoco/interesting/. 113

[25] A. J. DiNardo and E. Sard. Superconducting microwave mixers utilizing Josephson junctions. *Journal of Applied Physics*, **42**:105, 1974. 18

[26] P. Dindo, D. Erickson, F. Jiang, K. Yeung, D. Derdall, D. Duncan, D. Garcia,

D. Henke, B. Leckie, A. Lichtenberger, P. Niranjanan, M. Pan, S.K.and Pfleger, G. Rodrigues, K. Szeto, P. Welle, and K. Caputa. The band 3 receiver (84-116 GHz) for ALMA. *Infrared and Millimeter Waves*, **2**:407:408, 2005. 13

[27] D.Rogovin and D.J.Scalapino. Fluctuation phenomena in tunnel junctions. *Annals of Physics*, **86**:1:90, 1974. 68

[28] John E.Carlstrom, Gilbert P. Holder, and Erik D. Reese. Cosmology with the Sunyaev-Zel'dovich effect. *Ann.Rev.Astron.Astrophys*, **40**:643:680, 2002. 115, 116

[29] John E.Carlstrom, Gilbert P.Holder, and Eric D.Reese. Cosmology with the Sunyaev-Zel'dovich effect. *Annual Review of Astronomy and Astrophysics*, **40**:643–680, 2002. 2

[30] ESA. http://sci.esa.int/. 1

[31] ESA. http://background.uchicago.edu/~whu/courses/ast305_10/ast305_08.pdf. 3

[32] Armin Falb. Basic of radio interferometry. http://www.eracnet.org/workshop/doc/basics.pdf. 118, 119, 120

[33] F.A.Padovani and R.Stratton. Field and thermionic-field emission in Schottky barrier. *Solid-State Electron*, **9**:695:707, 1966. 28

[34] F.Rice, J.Ward, J.Zmuidzinas, and G.Chattopadhyay. Fast harmonic balance of SIS mixers with multiple junctions and superconducting circuits. *10th International Symposium on Space Terahertz Technology*, 1999. 28

[35] Harald T. Friis. http://en.wikipedia.org/wiki/Friis_formulas_for_noise. 65

[36] George F.Smoot. Cosmic Microwave Background radiation anisotropies: their discovery and utilization, Lawrence Berkeley National Laboratory. Space Science Laboratory, Department of Physics, University of California, Berkeley, CA94720, USA. 113

[37] G. Gamow. The evolution of the universe. *Nature*, **162**:680:682, 1948. 1, 112

[38] G. Gamow. The origin of elements and the separation of galaxies. *Physical Review*, **74**:505:506, 1948. 1, 112

[39] G.Engargiola and R.L.Plambeck. Wideband 3 mm SIS mixers operated with partial saturation. *SPIE's International Symposium on Astronomical Telescopes and Instrumentation*, **3357**, July 31,1998. 142

[40] P.F Goldsmith. *Quasiparticle Systems: Gaussian Beam Quasipartical Propagation and Applications*. Wiley-IEEE Press, 1997. 66

[41] Paul K. Griems. Variable temperature load. Private communication. 142

[42] Paul Grimes. Double ended GUBBINS block. Private Communication. 64

[43] Paul Grimes. *Design and analysis of 700 GHz finline mixers*. PhD thesis, University of

Cambridge, 2006. 22, 28, 69, 71

[44] Paul Grimes, M.J.R.Brock, C.M.Holler, J.John, M.E.Jones, O.G.King, J.Leech, A.C Taylor, G.Yassin, K.Jacobs, and C.Groppi. GUBBINS: A novel millimeter-wave heterodyne interferometer. *20th International Symposium on Space Terahertz Technology*, Charlottesville,20-22 April 2009. 3, 62, 63, 123, 124, 125, 127, 130, 134, 137

[45] G.Yassin, R.Padman, S.Withington, K.Jacobs, and S.Wulff. Broadband 230 GHz finline mixer for astronomical imaging arrays. *Electronics Letters*, **33**:498:500, 1997. 28, 43, 44

[46] H.A Hamid and D.P Hampshire. Critical current density of superconductors as a function of strain in high magnetic fields. *Cryogenics*, **38**:1007:1015, 1998. 27, 71

[47] W Heisenberg. The actual content of quantum theoretical kinematics and mechanics. *Z. Phys*, **43/172**, 1927. 7

[48] I.Giaever. Electron tunneling between two superconductor. *Physics Review Letter*, **5**:464:466, 1960. 28

[49] I.Giaever. Energy gap in superconductors measured by electron tunneling. *Physics Review Letter*, **5**:147:148, 1960. 28

[50] J.Bardeen. Tunneling from a many-particle point of view. *Physics Review Letter*, **6**:57:59, 1961. 28

[51] J.C.Mather, E.S.Cheng, D.A.Cottingham, R.E.Eplee, D.J.Fixsen Jr., T.Hewagama, R.B.Isaacman, K.A.Jensen, S.S.Meyer, P.D.Noerdlinger, S.M.Read, L.P.Rosen, R.A.Shafer, E.L.Wright, C.L.Bennett, N.W.Boggess, M.G.Hauser, T.Kelsall, S.H.Moseley, R.F.Silverberg Jr., G.F.Smoot, R.Weiss, and D.T.Wilkinson. Measurement of the cosmic microwave background spectrum by the COBE FIRAS. *The Astrophysical Journal*, **420**:439:444, 1994. 113

[52] J.G.Simmons. Electric tunnel effect between dissimilar electrodes separation by a thin insulation film. *Journal of Applied Physics*, **34**:2581:2590, 1963. 28

[53] B. D. Josephson. Possible new effects in superconductive tunnelling. *Physics Letters*, **1**:251:253, 1962. 17

[54] B.D. Josephson. The discovery of tunnelling supercurrents. *Rev.Mod.Phys*, **46**:251:254, 1974. 17

[55] J.R.Tucker. Quantum limited detection in tunnel junction mixers. *Quantum Electronics*, **15**:1234–1258, 1979. 8, 13, 28, 32, 66, 76, 157

[56] A. Karpov, J. Blondel, K. H. Gundlach, and D. Billion-Pierron. Low noise SIS mixer for 230 GHz receivers of Plateau de Bure interferometer. *International Journal of Infrared and*

Millimeter Waves, **18**:301:317, 1997. 13

[57] A. R Kerr. Some fundamental and practical limits on broadband matching to capacitive devices, and the implications for SIS mixer design. *IEEE Transactions on Microwave Theory Techniques*, **43**:2:13, 1995. 50

[58] Paul K.Grimes, Ghassan Yassin, Karl Jacobs, and Jamie Leech. Design of SIS finline mixers with ultra-wide IF bands. *19th International Symposium on Space Terahertz Technology*, 28-30 April,2008. 50, 94, 116

[59] J. W. Kooi, G. Chattopadhyay, S. Withington, F. Rice, J. Zmuidzinas, C. Walker, and G. Yassin. A full-height waveguide to thin-film microstrip transition with exception RF bandwdith and coupling efficiency. *Infrared and millimeter waves*, **24**, 2003. 11

[60] Anthony Lasenby. CMB anisotropies: recent measurements and interpretation. *Classical and Quantum Gravity*, **19**:3469:3485, 2002. 114

[61] E.F. Lauria, A.R.Kerr, M.W.Pospieszalski, S.K.Pan, J.E.Effland, and A.W.Lichtenberger. A 200-300 GHz SIS mixer-preamplifier with 8 GHz IF bandwidth. *ALMA Memo 378*, 2001. 91

[62] Jamie Leech. FTS measurement for GUBBINS multiplier chain LO. Private Communication. 77

[63] Jamie Leech. Spectrum analyzer measurement. Private communication. 99

[64] Chao-Te Li, Tse-Jun Chen, Tong-Liang Ni, Wei-Chun Lu, Chuang-Ping Chiu, Chong-Wen Chen, Yung-Chin Chang, Ming-Jye Wang, and Sheng-Cai Shi. Development of SIS mixers for SMA 400-520 GHz band. *20th International Journal of Infrared and Millimeter Waves*, 2009, Charlottesville. 13

[65] Jie Liu, Wenlei Shan, and Shengcai Shi. Temperature-dependent performances of Nb SIS mixers at millimeter and submillimeter wavelength. *Microwave and Millimeter Wave Technology*, pages 1–4, 2012. 151

[66] Sylvain Mahieu, Doris Maier, Bernard Lazareff, Alessandro Navarrini, Gaelle Celestin, Julien Chalain, Daniel Geoffroy, Fabrice Laslaz, , and Guillaume Perrin. The ALMA band-7 cartridge. *IEEE transactions on Terahertz science and technogloy*, **2**:29:39, 2012. 13

[67] D. Maier, D. Billon-Pierron, J. Reverdy, and M. Schicke. 100 GHz sideband separating mixer with wide IF band. *18th International Symposium on Space Terahertz Technology*, March 21-23, 2007. 92

[68] M.H.Cohen, L.M.Falicov, and J.C.Philips. Superconductive tunneling. *Physics Review*

Letter, **8**:316:318, 1962. 28

[69] N.R.Werthamer. Nonlinear self-coupling of Josephson radiation in superconducting tunnel junctions. *Physics Review Letter*, **147**:225, 1996. 17, 29

[70] A.A Penzias and R.W. Wilson. A measurement of excess antenna temperature at 4080 mc/s. *Astrophysical Journal*, **142**:419421, 1965. 1, 112

[71] P.Grimes, G.Yassin, K.Jacobs, and S.Withington. A 700 GHz single chip balanced SIS mixer. *16th Internation Symposium of Space Terahertz Technology*, 2005. 44

[72] P.Kittara. *The development of 700 GHz SIS mixer with Nb finline devices: Nonlinear mixer theory, design techniques and experimental investigation.* PhD thesis, University of Cambridge, 2002. 45

[73] P.Kittara, P.Grimes, G.Yassin, Withington, K.Jacobs, and S.Wulff. A 700-GHz SIS antipodal finline mixer fed by a Pickett-Potter horn reflector antenna. *IEEE Transactions on Microwave Theory and Techniques*, **52**:2352:2360, 2004. 44

[74] National radio observatory. Interferometers. http://http://www.cv.nrao.edu/course/astr534/Interferometers2.html. 118, 121, 122

[75] R.Blundell, R.E.Miller, and K.H.Gundlach. Understanding noise in SIS receivers. *International Journal of Infrared and Millimeter Waves*, **13**:3:14, 1992. 66

[76] S.-K.Pan, A. R. Kerr, M. W. Pospieszalskil, E. F. Laurial, W. K. Cradyl, N. Homer Jr, S. Srikanthl, E. Bryertonl, K. Sainil, S. M. X. Claude, C. C. Chin, P. Dindo, G. Rodrigues, D. Derdall, J. Z. Zhang, and A. W. Lichtenberger. A fixed-tuned SIS mixer with ultra-wide-band IF and quantum-limited sensitivity for ALMA band 3 (84-116 GHz) receivers. *15th International Symposium on Space Terahertz Technology*, 2004, 27-29 Apr, Northampton, Massachusetts. 92

[77] Y. Sekimoto, Y. Iizuka, N. Satou, T. Ito, K. Kumagai, M. Kamikura, M. Naruse, , and W. L. Shan. Development of ALMA band 8 (385-500 GHz) cartridge. *19th International Symposium on Space Terahertz Technology*, 2008,Groningen. 13

[78] Girraj Sharma, Patel Shreyas Navin, Yogesh Bhati, and Yash Walia. Half-wavelength parallel edge coupled filter simulation using MATLAB. *International Journal of Innovative Research in Computer and Communication Engineering*, **1, Issue 2**, April,2013. 102

[79] H. Smith, J. Buckle, R. Hills, G. Bell, J. Richer, E. Curtis, S. Withington, J. Leech, R. Williamson, W. Dent, P. Hastings, R. Redman, B. Wooff, K. Yeung, P. Friberg, C. Walther, R. Kackley, T. Jenness, R. Tilanus, J. Dempsey, M. Kroug, T. Zijlstra, and T. M. Klapwijk. HARP: a submillimetre heterodyne array

receiver operating on the James Clerk Maxwell Telescope. *SPIE*, 2003. 8

[80] R.A.AND YA.B.ZEL'DOVICH SUNYAEV. Small-scale fluctuations of relic radiation. *Astrophysics and Space Science*, **7**:3:19, 1970. 114

[81] S.WEINREB. Private Communication. 59, 60, 95

[82] BOON-KOK TAN. *Development of coherent detector technologies for sub-millimeter wave astronomy observation.* PhD thesis, University of Oxford, 2012. 19, 34, 63, 81

[83] BOON-KOK TAN, GHASSAN YASSIN, PAUL GRIMES, AND KARL JACOBS. Designs of broadband unilateral finline SIS mixers employing 15 m silicon-on-insulator substrate at THz frequencies. *21ST INTERNATIONAL SYMPOSIUM ON SPACE TERAHERTZ TECHNOLOGY*, 23-25 March, 2010. 11

[84] BOON-KOK TAN, GHASSAN YASSIN, PAUL GRIMES, KARL JACOBS, AND CHRISTOPHER GROPPI. Performance of a 700 GHz unilateral finline SIS mixer. *21th international symposium on Space Terahertz Technology*, 2011. 28

[85] BOON-KOK TAN, GHASSAN YASSIN, PAUL GRIMES, JAMIE LEECH, KARL JACOBS, AND CHRISTOPHER GROPPI. A 650 GHz unilateral finline SIS mixer fed by a multiple flare-angle smooth-walled horn. *IEEE Transactions on Terahertz Science And Technology*, **2**:40:49, 2012. 62

[86] ANGELA TAYLOR AND MIKE JONES. A novel ultra-wideband millimeter interferometer for astronomical and atmosphere observations. Proposal of GUBBINS instrument to Royal Academy of Society. 125

[87] MICHEAL TINKHAM. *Introduction to Superconductivity.* McGraw-Hill Inc., 1996. 20, 23, 24, 25

[88] EDWARD TONG. Ultra-wide if operation for SMA. http://www.cfa.harvard.edu/sma/meetings/Advisory/2010/Presentations/Tong/tong-IF-3.pdf. 92

[89] Y UZAWA, M KROUG, T KOJIMA, M TAKEDA, M CANDOTTI, Y FUJII, K KANEKO, W SHAN, T NOGUCHI, AND Z WANG. A sensitive ALMA band 10 SIS receiver engineering model. *SUPERCONDUCTOR SCIENCE AND TECHNOLOGY*, **22**, 2009. 13

[90] V.AMBEGAOKAR AND A.BARATOFF. Tunneling between superconductors. *Physics Review Letter*, **11**:1364, 1963. 29

[91] V. VASSILEV, D. HENKE, I. LAPKIN, O. NYSTROM, R. MONJE, A. PAVOLOTSKY, AND V BELITSKY. Design and characterization of a 211 275 GHz sideband separating mixer for the APEX telescope. *Microwave and Wireless Components Letters*, **18**:58–60, 2008. 11

[92] M. WHITE. Anisotropies in the CMB. *Los Angeles Meeting*, 1999. 113

[93] S. WITHINGTON, J. LEECH, G. YASSIN, K. G. ISAAK, B. D. JACKSON, J. R. GAO, AND T. M.

Klapwijk. A 350 GHz radial probe SIS mixer for astronomical imaging arrays. *International Journal of Infrared and Millimeter Waves*, **22**:1305:1312, 2001. 11

[94] D.and Miller R. Woody and M. Wengler. 85-115 GHz receivers for radio astronomy. *IEEE.Trans.Microwave Theory Tech*, **32**:90:95, 1985. 66, 68

[95] W.R.McGrath, A.V.Risnen, and P.L.Richards. Variable-temperature loads for use in accurate noise measurements of cryogenically-cooled microwave amplifiers and mixers. *International Journal of Infrared and Millimeter Waves*, **7**:543:553, 1986. 142

[96] G. Yassin, P.K. Grimes, O.G. King, and C.E. North. Waveguide-to-planar circuit transition for millimetre-wave detectors. *Electronics Letters*, **44**:866–867, 2008. 12, 45

[97] Ghassan Yassin, Stafford Withington, Matthew Buffey, K. Jacobs, and S. Wulff. A 350 GHz SIS antipodal finline mixer. *IEEE TRANSACTIONS ON MICROWAVE THEORY AND TECHNIQUES*, **48**:662:669, 2000. 11, 28, 44

[98] S Yassin, G.and Withington. Electromagnetic models for superconducting millimeter-wave and sub-millimeter-wave microstrip transmission lines. *Journal of Applied Physics*, **28**:1983:1991, 1995. 66

[99] Cheuk yu Edward Tong, Paul K. Grimes, Arnaud Barbier, Karl Schuster, and Ming jye Wang. Design and performance of a 3-junction series distributed SIS mixer for wide IF applications. *IEEE TRANSACTIONS ON APPLIED SUPERCONDUCTIVITY*, **23**, 2013. 12, 13, 92

[100] Yangjun Zhou, Ghassan Yassin, Paul Grimes, Jamie Leech, Karl Jacobs, and Christopher Groppi. Performance of a 230 GHz finline SIS mixer with a wide IF bandwidth. *21th International Symposium on Space Terahertz Technology*, 2012, 2-4 Apr, Tokyo, Japan. 92

[101] M. M. Zinieris, R. Sloan, and L. E. Davis. A broadband microstrip- to-slot-line transition. *Int. Conf. Computation in Electromagnetics*, **Publ. 350**, 1991. 104

[102] H. G. Zmuidzinas, J.and Leduc and J. A. Stern. Slot antenna SIS mixers for submillimeter wavelengths. *3rd International Symposium on Space Terahertz Technology*, 1992. 11